Title
Searching for Sub-GeV Dark Matter with Liquid Xenon and Superfluid Helium

Author
Biekert, Andreas

Publication Date
2023

Peer reviewed|Thesis/dissertation

Searching for Sub-GeV Dark Matter with Liquid Xenon and Superfluid Helium

by

Andreas Biekert

A dissertation submitted in partial satisfaction of the

requirements for the degree of

Doctor of Philosophy

in

Physics

in the

Graduate Division

of the

University of California, Berkeley

Committee in charge:

Professor Daniel N. McKinsey, Chair
Professor Matt C. Pyle
Professor Eric B. Norman

Fall 2022

Searching for Sub-GeV Dark Matter with Liquid Xenon and Superfluid Helium

Abstract

Searching for Sub-GeV Dark Matter with Liquid Xenon and Superfluid Helium

by

Andreas Biekert

Doctor of Philosophy in Physics

University of California, Berkeley

Professor Daniel N. McKinsey, Chair

Astrophysical evidence for dark matter is abundant; one of the great open problems in physics is its particle identity. In this dissertation we discuss two different detectors, LZ and HeRALD, designed to detect dark matter interactions. LZ is a recently assembled 10 tonne two-phase xenon time projection chamber. We discuss the first search for Weakly Interacting Massive Particles (WIMPs) from LZ, which set world-leading limits on the WIMP-nucleon interaction cross section. We present an extension of this search to lower masses via the Migdal effect, and suggest an alternative path for calculating the Migdal signal model for smaller recoil energies. We also show the design of a low energy photoneutron calibration source for LZ and data from its first deployment. The HeRALD detector is in active development, with R&D on different aspects of the superfluid helium-based design. We present an overview of this design and signal modeling work underlying projections of its sensitivity to low mass dark matter. We also discuss two experiments to probe this signal model by measuring helium scintillation from neutron and gamma ray interactions. Finally, we return to the photoneutron concept by presenting a source design that will serve as a path forward for even lower energy nuclear recoil calibrations important for further development of HeRALD.

Contents

Acknowledgments

I am extremely grateful to Dan for being my graduate advisor, an opportunity which would probably not have materialized without his willingness to take me on as an undergraduate researcher one summer after a cold email. Working on PIXeY at Yale that summer sparked a wonderful journey into the dark matter direct detection field, which was followed up by the undeniably cool HeRALD detector concept drawing me to grad school at Berkeley. Dan has helped me improve as a scientist immensely over the years and frequently encouraged me to recognize my own expertise when working on difficult calculations or analysis projects.

I also thank Rick and Matt for helpful feedback during my qualifying exam and on drafts of this dissertation, improving the work it describes.

Thank you to Junsong, who was my direct collaborator on almost all of the projects described in this thesis and a wonderful research mentor. You taught me how to set up an experiment, be careful in my measurements, and think through analysis choices to be confident in my conclusions. I think your dedication to making CAD drawings far surpasses mine and I'm glad we had such a complementary workflow to enable some cool science over the years.

Peter's influence on the photoneutron project was substantial; his wisdom was equally impactful on how I approached technical analysis problems and how I framed communicating the project's importance to others. I can't overstate how much I learned from Quentin, from the fine arts of C++ to the fine arts of cursing at C++. I want to thank Scott Ha for his close guidance and support during the LZ SR1 analysis final rush. Of course, there are many individuals that made UCB and LBL a wonderful place to work, and I thank Kevin, Simon, Aaron, Scott K, Shilo, Ibles, Hao, Suerfu, Vetri, Reed, Ryan S, Roger, Jose, Ryan G, Yue, Ethan, Evan, Brian, Elizabeth, Lucie, Kate, Kelsey, Jayke, Anisha, Elliot, Eve, Saumya, Lanqing, and Eric for keeping the environment vibrant, fun, and productive.

Through LZ and HeRALD I've had the opportunity to meet and work with a wide range of wonderful individuals, virtually, at collaboration meetings, and onsite at SURF. The future of both experiments is extremely bright (or maybe dark), and I'm eagerly looking forward to what they uncover in the future. Scott He was a critical source of guidance for me in both collaborations, and I thank him for providing me with insight and good humor along the way. I also wish to thank Alvine for her diligence in keeping the LZ photoneutron source on track to enable the first deployment. I had a great time working on weaving wire grids and photoneutron data analysis alongside Madan, and working on SR1 dark matter analyses with Dan K. It was a pleasure working with Doug and Pratyush on HeRALD R&D, and I'm glad we had a chance to catch up in person after all these years.

I am extremely grateful for receiving support from the NSF in the form of a graduate research fellowship, and to Dan, Qimin, Richard, and Tom, who wrote my letters of reference for it. I am indebted to those letter writers, research mentors in my formative undergraduate years who helped me find my path in physics. I also thank the staff who keep the graduate

program and research at UCB and LBL running, with a particular thanks for a great amount of help to Anne, Joelle, Carlos, Melissa, and Tami.

Thank you to the PhysCal soccer team for putting up with my low effort naming decision and making it a blast to play IM soccer for six years. The pinnacle of my time on the team was obviously the championship we won in the summer of '18, and I am immensely grateful that Nikola, Philipp, Matthew, Mauricio, Bryan, Nick, and Aashrita helped me achieve this lifelong goal. Photographic evidence aside, there were many other cherished team members playing for multiple seasons: Caleb, Fabio, Francisco, Pratik, Tomo, Chris M, Chris K, Adrian, and Lorenzo–and I apologize if I left anyone out. I want to thank Max for taking over as captain and leading PhysCal into a new era.

Thank you to Micah, who was always available for an afternoon coffee and made the world of the Graduate Assembly enjoyable for three years, even if the meetings were way too long. Brad and Bryce, thanks for keeping it real about quantum computing, and also for instigating all those trips to fun places. To Stephan, Owen, Andrew, Will, and Casey: I am glad to have had you around in the Bay Area at various times in the last six and a half years and I'll always be thankful for the special trip to Shasta Lake, even if pickup basketball didn't work out as planned.

Ann, Marek, and Elizabeth took me in without question, and drowned me in Polish food on many occasions. Mom and Dad, I am deeply thankful for the support you've provided me throughout my academic career. I'm not sure I could have made it this far without your encouragement when things got tough. I also fondly remember virtual game nights with you and Nick as a good outlet in the height of the pandemic, especially since I always won.

I would like to thank my three lap warmers, Gandalf, Pixie, and Lux, for keeping me company in front of the computer. Finally, I am most indebted to Emily, who is my partner in everything I do. I will always be your number one fan and most eager audience member.

Chapter 1

Searching for Dark Matter

In this chapter we introduce dark matter and some of the observational evidence of its existence from cosmology and astronomy. We briefly introduce these concepts to motivate the search for dark matter experimentally. While there are several methods to search for dark matter, the one relevant to this thesis is direct detection, where a dark matter particle interacts with a target material leaving behind some signal of the interaction.

We also review some theories for the formation of dark matter in the early universe which have lead to a widening field of interesting parameter space for dark matter direct detection. While historically dark matter direct detection has focused on weakly interacting massive particles (WIMPs) [1, 2] and axions [2–4], the loosening of theoretical constraints on what constitute interesting dark matter models has motivated a broader scientific search moving forward [5–8]. Finally, we discuss some fundamental assumptions behind dark matter direct detection experiments searching for nuclear interactions and provide a broad overview of the state of these searches.

1.1 Observational evidence

The evidence for the existence of particle dark matter exists on several scales, ranging from measurements of the entire universe to measurements of individual galaxies.

1.1.1 Cosmological scale

The history of the universe is currently understood via a model of cosmology called Lambda Cold Dark Matter (ΛCDM). As the name suggests, dark matter is an integral piece of this model, which contains separate parameters estimating the energy density of baryonic matter like nucleons, dark matter, and dark energy. Structure formation simulations of the universe show results consistent with the requirement that dark matter is "cold", or nonrelativistic [9].

The most stringent constaints on ΛCDM come from Planck measurements of the Cosmic Microwave Background (CMB). The CMB consists of photons originating in the era of 'last scattering', where baryonic matter transitioned out of thermal equilibrium with photons. This transition, occurring at $z \simeq 1100$, or when the universe was about 370,000 years old, propagated small changes in the local density of matter, baryonic and non-baryonic. The universe has since expanded so that these photons have a mean temperature of $T = 2.7255$ K, with small fluctuations remaining because of the matter density variations during recombination. The Planck satellite measured the temperature fluctuations (shown in Figure 1.1) and polarization of CMB photons.

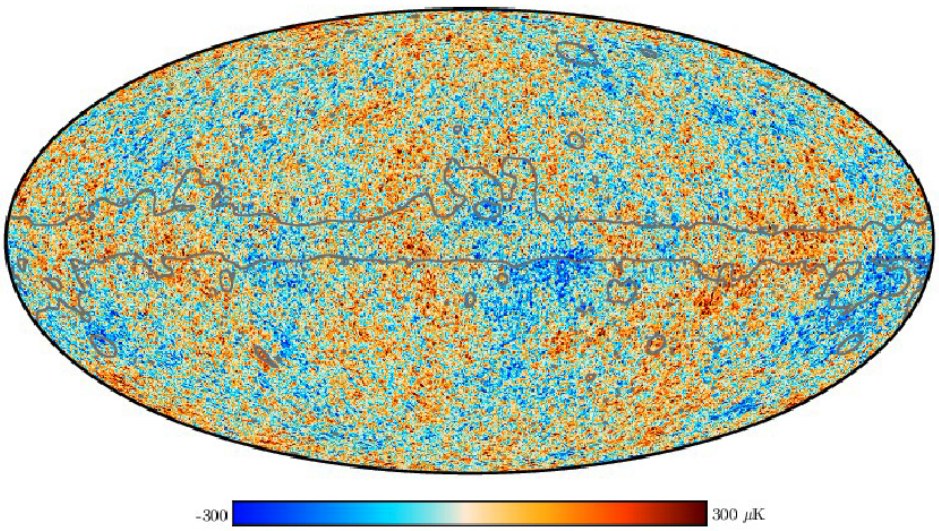

Figure 1.1: The Planck map of temperature fluctuations in the CMB. Figure copied from [10].

Parameters for ΛCDM are extracted from a fit to the power spectrum of the Planck map, as in Figure 1.2. The quantity plotted is

$$D_l^{TT} = \frac{l(l+1)}{2\pi} C_l, \tag{1.1}$$

where C_l are the coefficients of spherical harmonics Y_{lm} integrated over m [11]. The matter and dark energy density parameters from the Planck fit to the CMB temperature fluctuations with additional cosmological inputs are reported in Table 1.1 [12]. From these values, we see that dark matter makes up 84% of the matter density in the universe and 26% of the total energy density, while baryonic matter makes up just 5% of the total energy density.

The Planck power spectrum has some intuitive features related to the density parameters of interest [13]. It is physically attributed to the plasma shortly before recombination

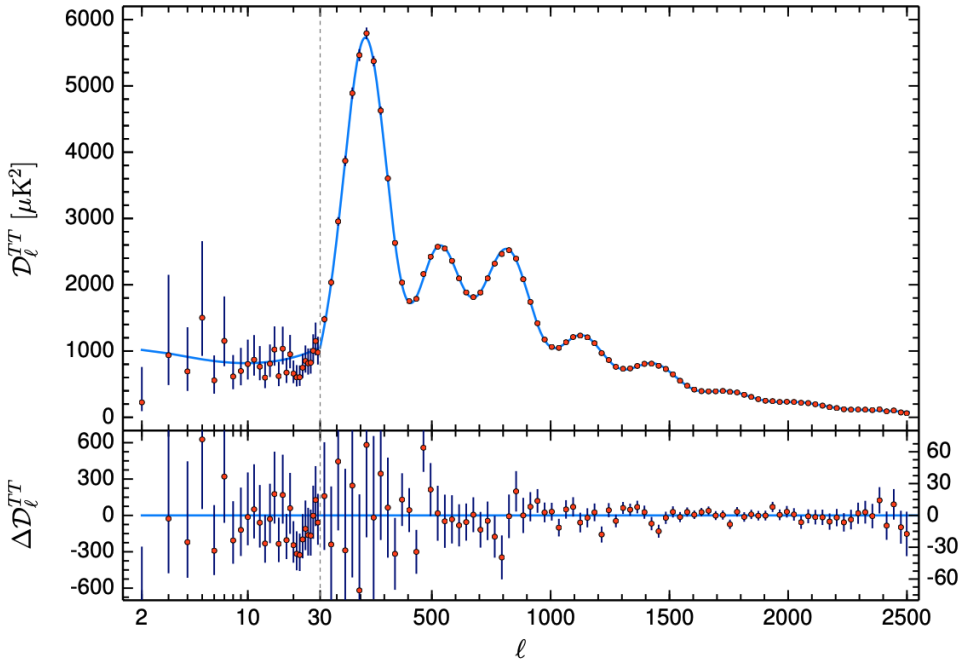

Figure 1.2: A multipole fit to angular correlations in the temperature spectrum of the CMB measured by Planck, constraining parameters of the ΛCDM cosmological model. Figure copied from [12].

Table 1.1: Best fit values for the different density parameters from ΛCDM as reported by the Planck collaboration [12]. The fit parameters are Ωh^2, where $h = H_0/[100 \text{ km s}^{-1} \text{ Mpc}^{-1}]$. Ω_Λ and H_0 are derived quantities and not direct parameters in the fit. Errors are 68% intervals from the fit.

Parameter description	Symbol	Best fit value
Baryonic matter density	Ω_b	0.04947 ± 0.00014
Cold dark matter density	Ω_c	0.26502 ± 0.00201
Matter density	Ω_m	0.3111 ± 0.0056
Dark energy density	Ω_Λ	0.6889 ± 0.0056

acting like an oscillator, where the attractive forces are gravitational from baryonic and non-baryonic matter, while the repulsive force is attributed to fluid pressure from baryonic self-interaction. Even-numbered peaks in the spectrum are associated with expansion, so the only the baryonic fluid pressure contributes to these. Conversely, the odd-numbered peaks are associated with compression, so these are a function of the total graviational force from both baryonic and non-baryonic matter. Thus, the overall scale of the power spectrum is dependent on the total matter density, while even-numbered peaks scale with the baryonic matter density. The variation of the power spectrum with different parameters is plotted graphically in Figure 1.3.

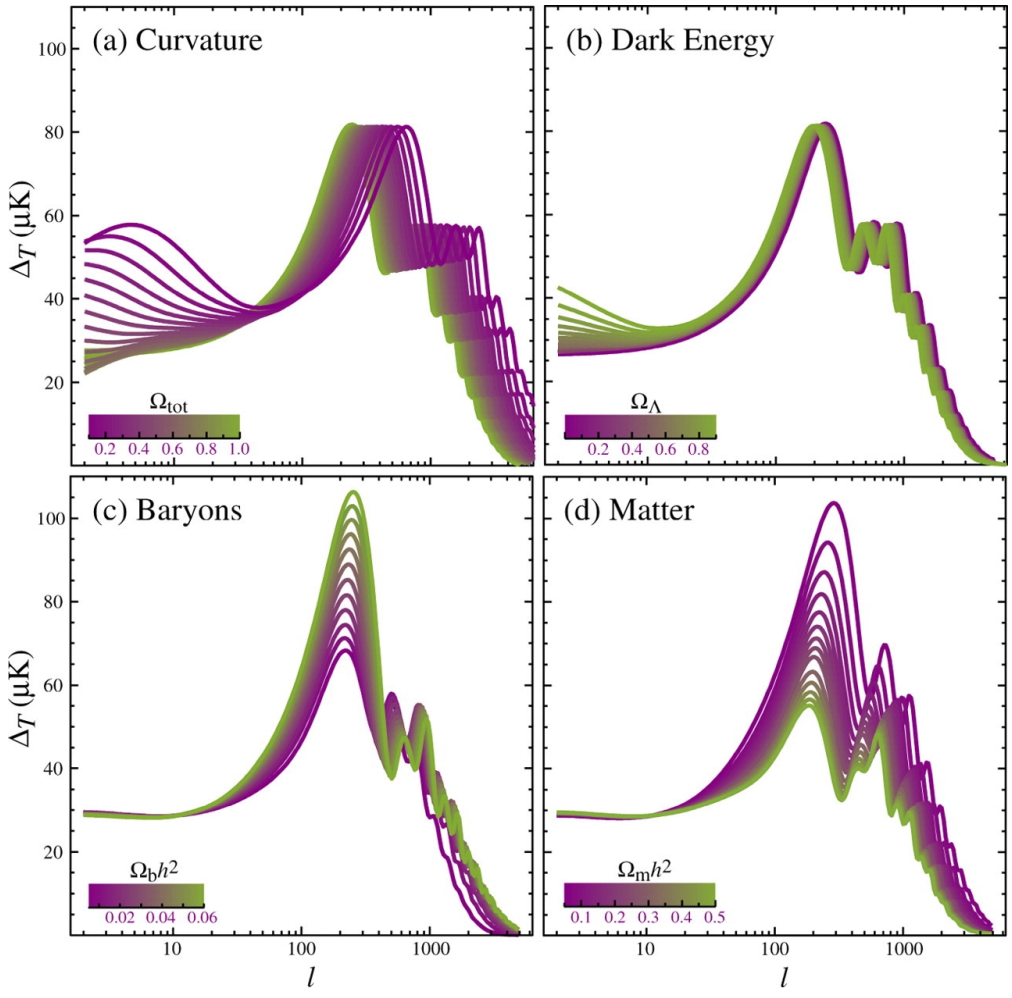

Figure 1.3: The different panels show the effect of various parameters in the ΛCDM prediction of the CMB power spectrum. Figure copied from [14].

Other cosmological observations can contribute constraints to the matter density parameters of interest. For example, the model of Big-Bang nucleosynthesis (BBN) describes the

production of light elements such as D, ^{3}He, ^{4}He, and ^{7}Li based on the ratio of baryons to photons [11]. The prediction of the formation of these elements probes cosmological physics at some of the earliest times in the universe; the predicted ratios are approximately fixed by the age of the universe $t \sim 180$ s, although astrophysical processes can alter these ratios. The produced ratio is a function of the baryon to photon ratio η, which can be independently probed by CMB measurements. From BBN, $5.8 \times 10^{-10} \leq \eta \leq 6.5 \times 10^{-10}$, in agreement with the independently constrained CMB value of $\eta = (6.105 \pm 0.055) \times 10^{-10}$. BBN and CMB constraints on η are shown in Figure 1.4. The agreement is seen as a great triumph of cosmological modeling, although it should be noted that the ^{7}Li prediction from BBN does not align with the CMB, possibly due to astrophysical uncertainties.

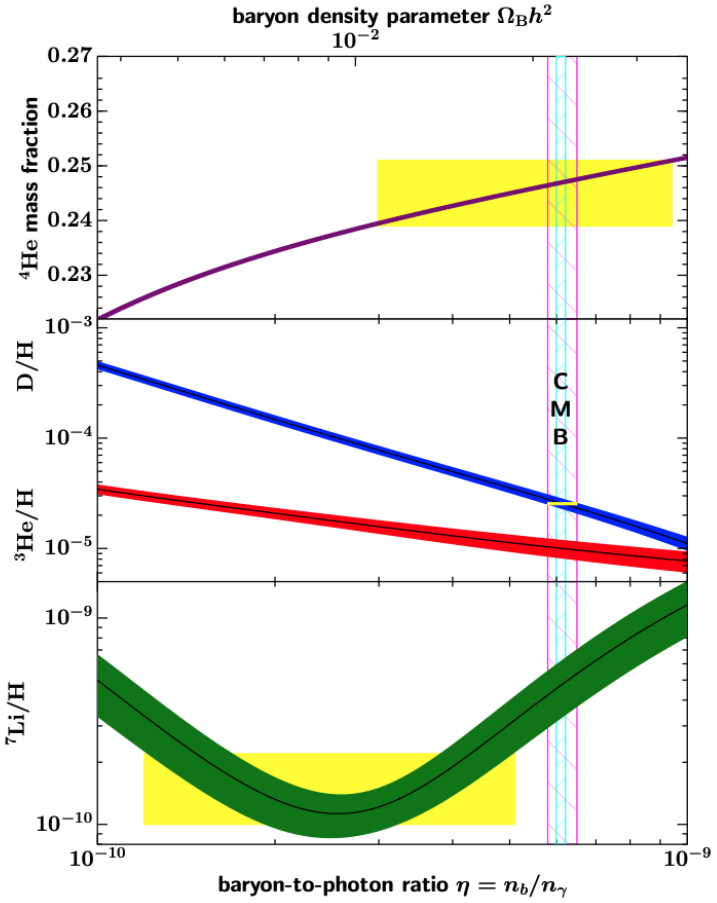

Figure 1.4: Primordial abundances of various nuclei according to the model of Big-Bang nucleosynthesis, providing alternate tests of ΛCDM parameters. Figure copied from [15].

1.1.2 Cluster scale

The phrase "dark matter" was coined by Fritz Zwicky, who applied it to explain cluster-scale inconsistencies in the velocities of nebulae in the Coma cluster in 1937 [16]. More recently, the so-called Bullet Cluster[1] was put forth as strong evidence for the gravitational effects of dark matter in the collision of two galaxy clusters [15]. The observation takes the form of two separate measurements, shown in Figure 1.5. The Chandra Observatory provides the X-ray measurements from luminous matter in the clusters, shown as the heat map in the right panel. This distribution is compared with the gravitational lensing reconstruction of the mass distribution from the Magellan Telescope optical data in the left panel, shown as green contours in both panels, revealing that the bulk of the matter is not self-interacting and also non-luminous. While this is a striking example, at least 72 more such objects have been observed with similar features [17].

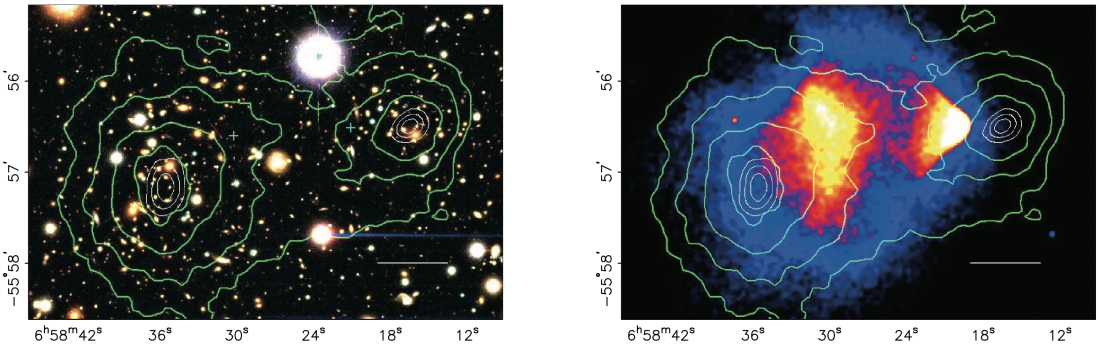

Figure 1.5: The left shows optical data from the Magellan telescope of the Bullet Cluster used to infer the gravitational profile shown in green contours with weak lensing. The right shows a heatmap of X-ray data taken with the Chandra X-ray observatory. Figure copied from [15].

1.1.3 Galaxy scale

Evidence for dark matter has also been observed in measurements of galactic rotational velocities. Measurements of the rotational velocity profile of galaxies by Rubin *et al* showed a flat behavior out to large distances, inconsistent with the Newtonian expectation [18]. The measurements made by Rubin *et al* are shown in Figure 1.6. According to the visible matter distribution in these galaxies, the velocity profile should fall roughly as $1/r$, but the flat behavior can be recovered with the presence of additional nonluminous matter out to larger radii.

[1] Alternatively, the catchy 1E 0657–558.

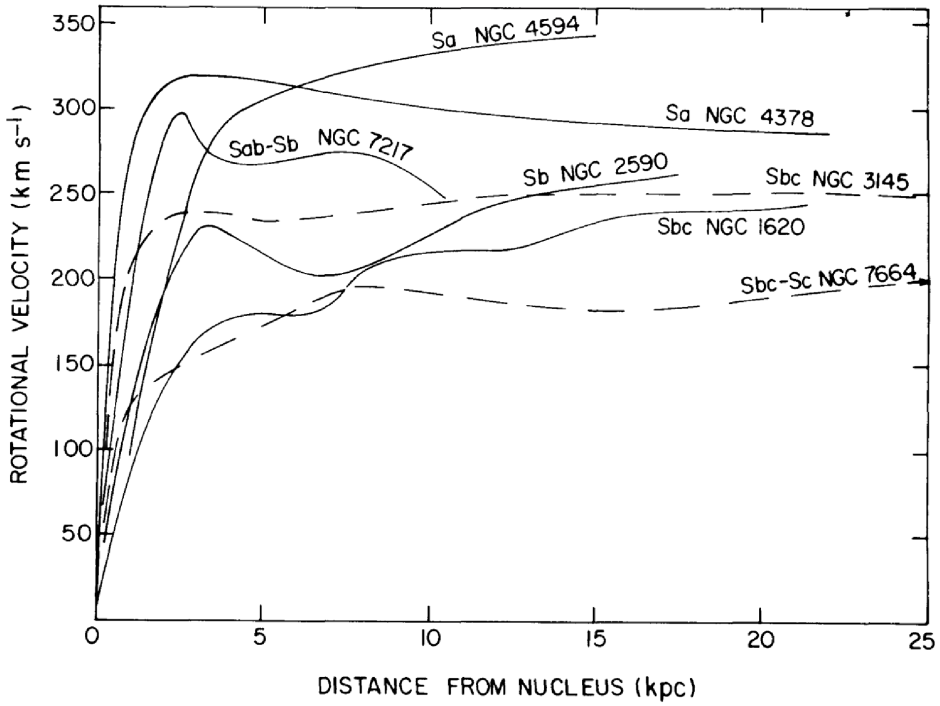

Figure 1.6: Measurements of galaxy rotational speeds as a function of radial distance. The approximately flat behavior is an additional piece of evidence pointing to the presence of dark matter. Figure copied from [18].

1.2 Dark matter production mechanisms

Taken together, the cosmological and astronomic pieces of evidence for particle dark matter are extremely compelling. Particularly, it must satisfy a few well-established criteria. It can only minimally interact via the electromagnetic force (or not at all), it must be long-lived compared to the scale of the universe, and its non-gravitational self-interaction is expected to be small. Additionally, it should be non-relativistic, ruling out the light standard model neutrinos, whose mass sum is constrained to < 0.12 eV from CMB parameters [11].

These criteria generally rule out standard model particles from being the dark matter. Still, there is room for a variety of models of exactly how the dark matter particle fits into the evolution of the universe, with several possible production mechanisms. First we consider the freeze-out mechanism, the mode of dark matter production most traditionally assumed. Suppose a particle χ exists in equilibrium with baryonic matter in the early universe such that $\chi\bar{\chi} \leftrightarrow SM$. Then the evolution of its number density is given by the relation

$$\frac{\mathrm{d}n_\chi}{\mathrm{d}t} + 3Hn_\chi = -\langle v\sigma_\chi \rangle \left[n_\chi^2 - (n_\chi^{\mathrm{eq}})^2 \right], \tag{1.2}$$

where H is the Hubble parameter governing the expansion of the universe, $\langle v\sigma_\chi \rangle$ is the

thermally-averaged annihilation cross section, n_χ is the time-evolving dark matter number density, and $n_\chi^{\rm eq}$ is the dark matter equilibrium number density. Qualitatively, this equation relates the expansion of the universe on the left with the annihilation of dark matter, balanced by the inverse process, on the right. Once the expansion of the universe takes over and the self-annihilation rate is suppressed, the dark matter density "freezes out" to a relic density. This is shown in the left panel of Figure 1.7, where the axes have been recast into the variables $Y \equiv n_\chi/s$ and $x \equiv m_\chi/T$, where s and T are the entropy density and temperature of the visible sector heat bath [19]. One can estimate a weak scale annihilation cross section as $\langle v\sigma_\chi\rangle \sim \alpha^2/(100\text{GeV}^2\ 10^{-25}\text{cm}^3\text{s}^{-1})$, which, in combination with the relic density expression $\Omega_c h^2 \simeq 3\times10^{-27}\text{cm}^3\text{s}^{-1}\langle v\sigma_\chi\rangle$ yields approximately the correct value for $\alpha \sim 10^{-2}$ [20]. This has been called the "WIMP Miracle," because it was seen as a major coincidence that the dark matter relic density in a freeze-out scenario was reproduced by a weak-scale interaction—hence "weakly interacting massive particles." It was also shown that the WIMP was constrained to a mass > 2 GeV/c^2 [21], providing an appealing overlap with supersymmetric particles as the candidate WIMPs. WIMP dark matter in the 10's of GeV/c^2 mass scale has been thoroughly probed, although there are still models which favor it [1].

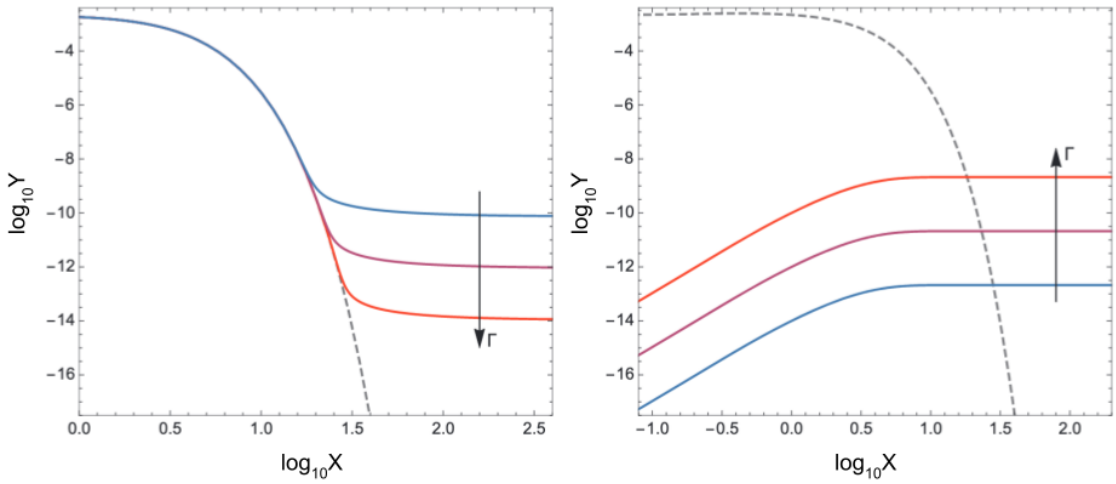

Figure 1.7: (Left) Freeze-out dark matter, where the dark matter starts in thermal equilibrium with the visible sector but the expansion of the universe eventually overrides the coupling, leading to a relic density after a certain age of the universe. (Right) Freeze-in dark matter, where the dark matter and visible sector are so weakly coupled that they are never in thermal equilibrium. Visible sector particles decay to dark matter particles, building their density over time, but eventually the expansion of the universe suppresses the decay process, leading to a fixed dark matter relic density. Figure copied from [22].

An alternative to freeze-out is the freeze-in mechanism [19]. In this scenario, the coupling between the dark matter and standard model sector is extremely weak, leading to the name

feebly interacting massive particles (FIMPs), and the dark matter exists in small to non-existent amounts in the early universe. Then there is never thermal equilibrium between the dark matter and the visible sector. Instead, dark matter is produced by visible sector decays like $\sigma \to \chi\chi$ or 2-to-2 interactions. In the decay case case, the time evolution of n_χ is

$$\frac{\mathrm{d}n_\chi}{\mathrm{d}t} + 3Hn_\chi = 2\Gamma_{\sigma\to\chi\chi}\frac{K_1(m_\sigma/T)}{K_2(m_\sigma/T)}n_\sigma^{\mathrm{eq}}, \tag{1.3}$$

where K_j are Bessel functions, $\Gamma_{\sigma\to\chi\chi}$ is the decay width, and n_σ^{eq} is the equilibrium number density of σ. In a freeze-in scenario, the abundance of dark matter gradually builds up, until the expansion of the universe causes the number density of σ to be Boltzmann-suppressed, $n_\sigma \propto \exp(-m_\sigma/T)$, assuming σ obey Maxwell-Boltzmann statistics. This process is shown in the right panel of Figure 1.7, with the variable substitution $x \equiv m_\sigma/T$ in this case ($Y \equiv n_\chi/s$ is the same). Estimates for the coupling parameter compared to the observed dark matter energy density yield compatibly small values for this scenario. It should also be noted that the particle χ in the freeze-in scenario does not have to be the final state dark matter, so this production mechanism is compatible with a dark sector of multiple dark matter particles. Some freeze-in models can be probed by direct detection experiments, and allow for a larger range of plausible dark matter masses than the traditional WIMP hypothesis [5].

The are yet more ways to generate the observed relic density of dark matter. In the strongly interacting massive particle (SIMP) scenario, dark matter interacts with itself in $3 \to 2$ processes while in weak contact with the visible sector. In this case, the correct relic abundance can be achieved for a SIMP of the MeV to GeV mass scale, within range of modern direct detection experiments [5, 23, 24]. The last case we mention here is asymmetric dark matter [25]. In this case the dark matter is postulated to have a matter-antimatter asymmetry comparable to the baryonic sector $n_\chi - n_{\bar{\chi}} \sim n_b - n_{\bar{b}}$. This leads to a natural estimate of $m_\chi \sim 5m_p \simeq 5$ GeV, since the dark matter density is about five times the baryonic matter density, but inclusion of a dark sector in asymmetric dark matter models can modify this mass to a wider range [5, 25].

This review of possible production mechanisms is clearly not detailed or exhaustive. It does however emphasize that there are a wide range of cosmologically-allowed dark matter models of interest for direct detection experiments, particularly at lower masses than the traditional 10's of GeV predicted for WIMPs. A nice collection of theory papers for low mass dark matter can be found in [7].

1.3 Dark matter nuclear recoils

While not strictly necessary for the dark matter models discussed in the previous section, we will assume the dark matter we want to detect is weakly interacting and primarily recoils off of nuclei in a target material, for which we follow a few different references [11, 26–28]. A summary of the calculation for the interaction rate follows. For a dark matter particle scattering off of a target nucleus, the most general way of writing the differential recoil

spectrum as a function of recoil energy is

$$\frac{\mathrm{d}R}{\mathrm{d}E_r} = \frac{\rho_0}{m_\chi m_A} \int_{v_{\min}} v f(\mathbf{v}) \frac{\mathrm{d}\sigma}{\mathrm{d}E_r} \mathrm{d}^3 v, \tag{1.4}$$

where $\rho_0 = 0.3$ GeV/c^2/cm^3 is the local dark matter density [29], m_χ is the dark matter mass, and m_A is the nuclear mass of the target.

We can write a general definition of the dark matter-nucleus differential cross section as

$$\frac{\mathrm{d}\sigma}{\mathrm{d}E_r} = \frac{m_A}{2\mu_A^2 v^2} \left(\sigma_0^{SI} F_{SI}^2(q^2) + \sigma_0^{SD} F_{SD}^2(q^2) \right) \tag{1.5}$$

where we use the reduced dark matter-nucleus mass

$$\mu_A = \frac{m_\chi m_A}{m_\chi + m_A}, \tag{1.6}$$

the momentum transfer

$$q = \sqrt{2 m_A E_R}, \tag{1.7}$$

σ_0 is the zero momentum transfer cross section, and $F^2(E_R)$ are the nuclear form factors associated with spin-independent and spin-dependent nuclear interactions. Let us first focus on spin-independent interactions. To facilitate comparison between experiments using different nuclear targets, we can decompose the nuclear cross section

$$\sigma_0^{SI} = \frac{4\mu_A^2}{\pi} [Z f_p + (A - Z) f_n]^2, \tag{1.8}$$

where f_p and f_n are the nuclear couplings and typically $f_p \approx f_n$. For a single nucleon

$$\sigma_{0,n}^{SI} = \frac{4 m_n^2 f_n^2}{\pi}, \tag{1.9}$$

so we can write the SI part of the differential rate from Equation 1.4 as

$$\frac{\mathrm{d}R_{SI}}{\mathrm{d}E_r} = \sigma_{0,n}^{SI} \frac{\rho_0}{2 m_\chi \mu_n^2} A^2 F_{SI}^2(q^2) \int_{v_{\min}} \frac{f(\mathbf{v})}{v} \mathrm{d}^3 v. \tag{1.10}$$

A common choice for the form factor function $F^2(q)$ is the Helm form factor computed for various targets in [26].

The function $f(v)$ describes the dark matter velocity distribution, and the corresponding integral starts at a minimum velocity

$$v_{\min} = \sqrt{\frac{2 m_A E_{\mathrm{thr}}}{2\mu_A^2}}, \tag{1.11}$$

where E_{thr} is a minimum energy threshold for detecting a recoil. The function $f(v)$ is typically assumed as a Maxwellian velocity distribution with a hard cutoff at an escape velocity,

but several astrophysical models of differing levels of detail exist. The most commonly used model is called the standard halo model (SHM). A recent inter-collaboration whitepaper suggested fixing the SHM parameters to specific values despite their uncertainties, so that dark matter experiments can compare against each other without different astrophysical assumptions [29]. The function $f(v)$, the effect of these uncertainties, and the scale of annual modulation related to the Earth's orbit around the sun is shown in Figure 1.8. Since we have rewritten the differential recoil rate in a way that isolates the effects of the function $f(v)$, this astrophysical modeling does not make any further assumptions about the nature of the dark matter.

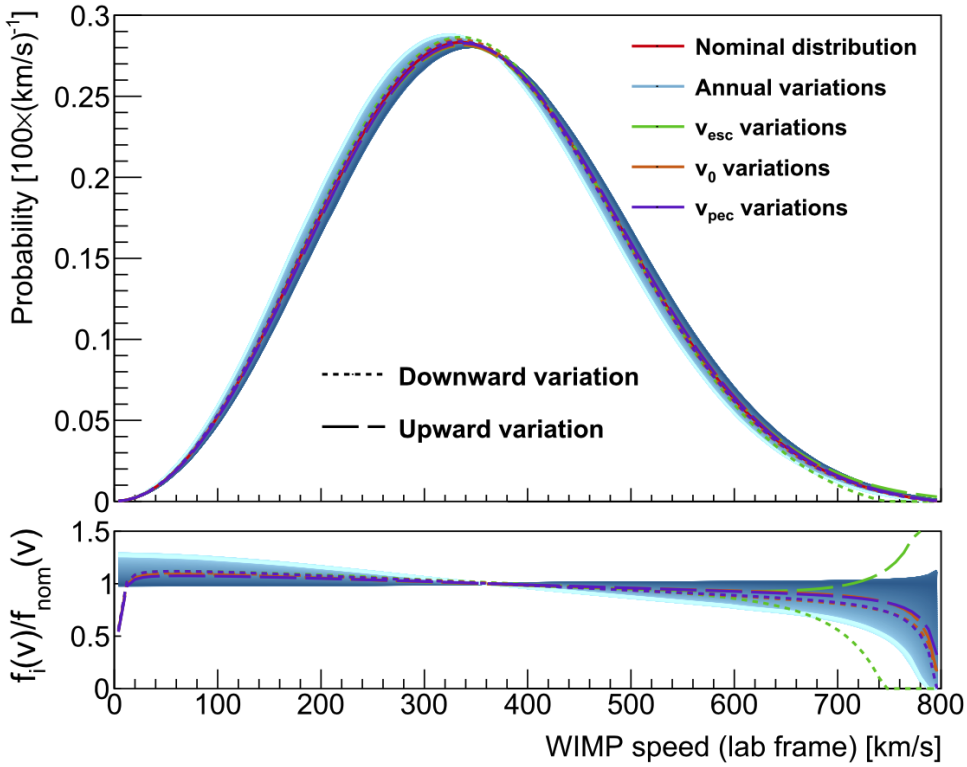

Figure 1.8: Possible dark matter velocity distributions in the standard halo model for dark matter due to uncertainties in the astrophysical parameters and variations over the course of the year. Figure copied from [29].

The spin-independent scattering spectrum of various masses of WIMP on xenon nuclei is shown in Figure 1.9. As the WIMP mass increases, so does the maximum recoil energy. The effects of the form factor can be easily seen for the three heavier WIMPS. The recoil energy imparted by an elastically scattering dark matter particle onto a target nucleus is

$$E_R = \frac{m_\chi^2 m_A}{(m_\chi + m_A)^2} v^2 (1 - \cos\theta). \tag{1.12}$$

This quantity is optimized when $m_\chi \sim m_A$, so matching the dark matter mass to the experimental target brings some advantages.

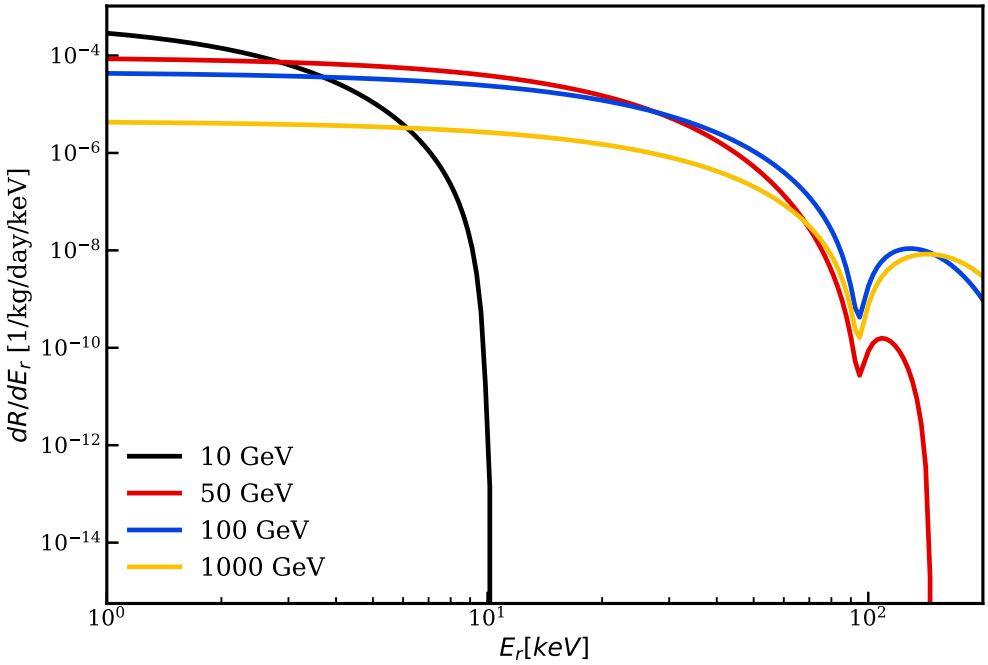

Figure 1.9: Recoil spectra for several masses of WIMPs scattering on xenon. The coupling was assumed to be spin independent with cross section $\sigma = 10^{-45}$ cm^2.

The spin dependent term in Equation 1.5 depends on more complicated nuclear physics calculations. For example, the structure functions describing coupling to nucleon spin are calculated for xenon in [30–33]. These were used to calculate the spin-dependent WIMP spectra used in the analyses in Chapters 3 and 4.

1.4 Direct detection technologies

Understanding the nuclear recoil spectrum of WIMPs scattering in a detector target material is only one piece of the experimental puzzle. Detector technologies are based on a variety of signal readout schemes, summarized in Figure 1.10. There are many advantages and disadvantages associated with each detector design, and we do not attempt to discuss them all here; for a fairly comprehensive review see [28]. One important point stressed by the community in recent years is the complementarity of different search approaches. Given the expanded field of theoretical models probed by modern experiments, a dark matter signal in one experiment is likely insufficient to completely identify the particle properties of its source, and confirmation with one or more additional approaches is a crucial step [5–7].

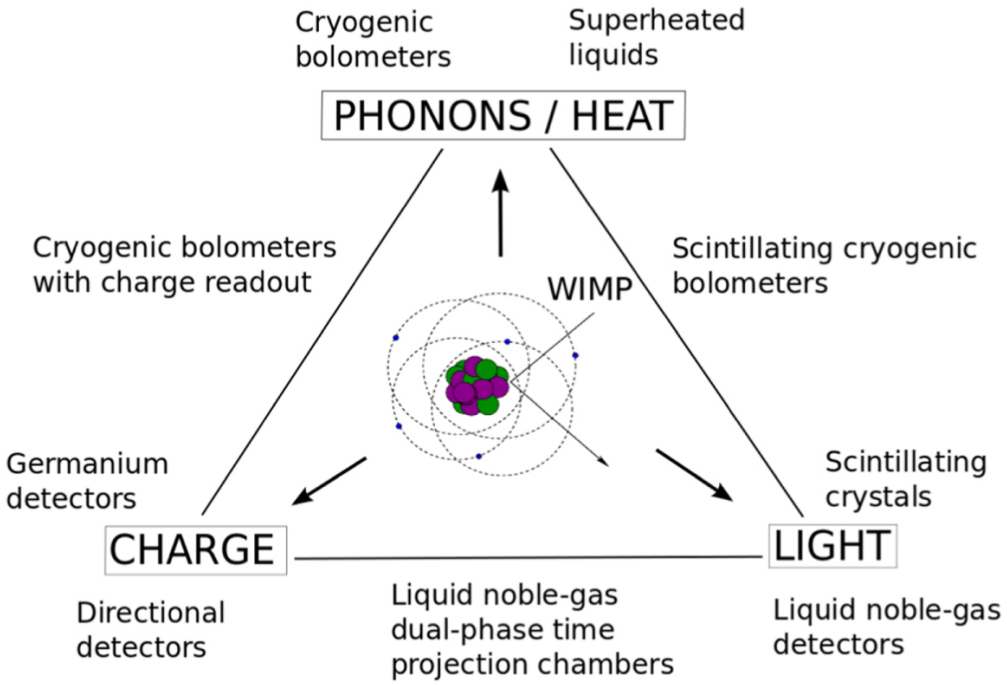

Figure 1.10: Technologies associated with different sets of signal readout channels. Some technologies (or analyses searching for dark matter) focus only on one signal channel, while others read out multiple for enhanced background rejection and/or energy reconstruction. Figure copied from [28].

So far there have not been any firm positive signals in dark matter direct detection experiments.[2] Instead, experiments report upper limits on the WIMP-nucleon cross section by analyzing collected data against the WIMP spectrum from Equation 1.4. Figure 1.11 shows a generalized view of how experimental limits can be improved, either by lowering the experimental threshold to smaller energy deposits or by increasing the exposure with a larger experiment and/or a longer data-taking time. These limits depend on the detailed understanding of background events appearing in the dataset, which are generally particle interactions or detector-specific signals not caused by dark matter. Equation 1.10 also reveals the relationship between the scattering rate and the dark matter mass. Since the local dark matter density is known, the relative rate of interactions for a fixed cross section increases inversely with the dark matter mass, and experiments probing lighter dark matter masses require comparatively less exposure for limits on similar cross sections.

The landscape of the spin independent dark matter-nucleon coupling parameter space is shown in Figure 1.12, with a selection of recent upper limits on the cross section and the

[2]The DAMA/LIBRA experiment claims evidence for dark matter via a modulating annual signal in their sodium iodide detector target, but these results are inconsistent with most of the limits shown in Figure 1.12, and the COSINE-100 experiment using the same target material has not seen the same signal [34].

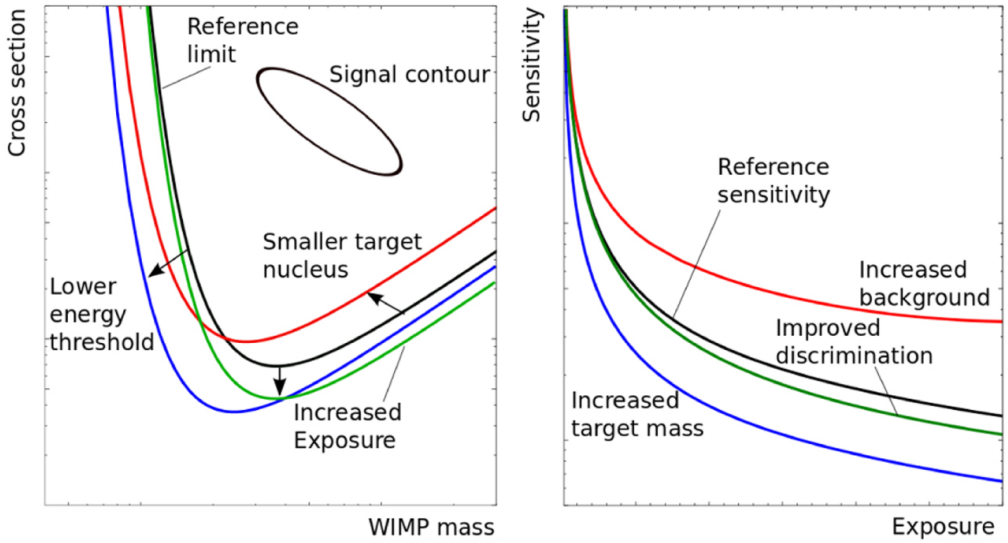

Figure 1.11: (Left) Generalized view of dark matter limits in the cross section-mass parameter space, and ways that experiments can exclude new parameter space. (Right) The relationship between dark matter sensitivity and exposure, and how it varies with backgrounds in the data. Figure copied from [28].

overall excluded parameter space shaded in grey. This figure is not a comprehensive display of all dark matter experiments setting limits on this parameter space but rather highlights recent developments in the last few years. There are two further features on this plot that warrant commentary. The yellow region marked as the neutrino fog is a region where the coherent scattering of astrophysical neutrinos with the detector target material presents a significant background. These are difficult to distinguish from dark matter signals, although in principle it is possible to make headway into the fog with extra work [35]. Still, this region marks a change in regime for dark matter experiments, necessitating specific strategies for making further progress distinct from historical developments to increase constraints in this parameter space. On the other end of the spectrum, some limits are shown with a maximum cross section boundary. This detail is important for experiments setting limits for sub-GeV masses and beyond, because the overburden may actually shield the dark matter away from the detector when the cross section is large enough [36]. Thus, there is motivation for collecting data both near the surface of the Earth and deep underground.

In this dissertation we discuss two different dark matter direct detection experiments. Chapters 2–5 focus on the LZ detector, a liquid-gas xenon time projection chamber (TPC). Xenon TPCs are a detector technology that has proven dominant for testing the traditional WIMP parameter space in masses in the 10's of GeV/c^2. They have also extended their reach into sub-GeV masses by searching for signals generated via the Migdal effect. Many of the leading limits in Figure 1.12 were set with xenon detectors, and LZ represents the next generation of this approach. The second half of this thesis, Chapters 6–9, concern the

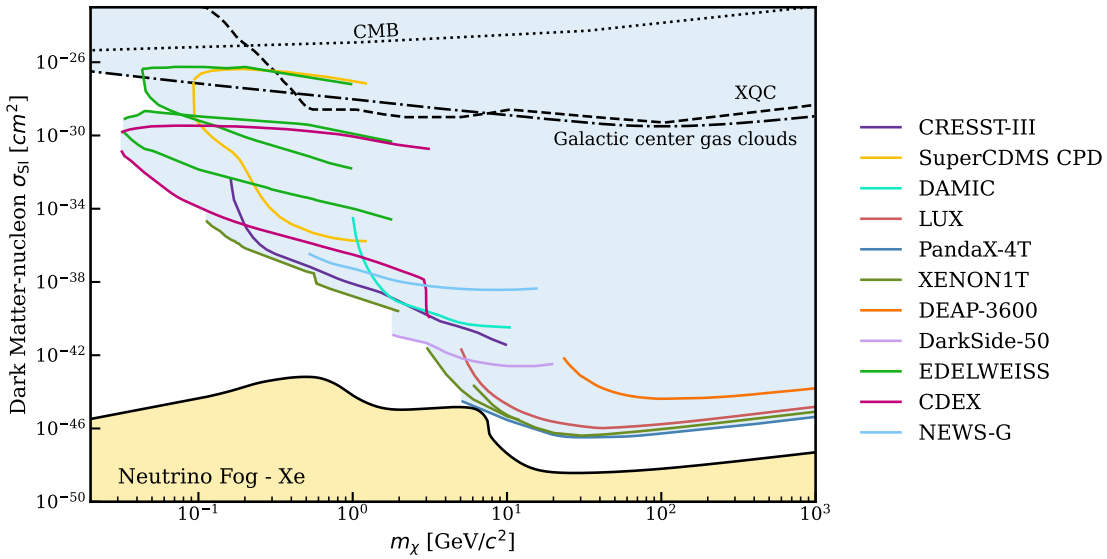

Figure 1.12: Spin independent dark matter-nucleon scattering cross section limits for a selection of recent experiments: CRESST-III [37], SuperCDMS CPD [38], DAMIC [39], LUX [40], PandaX-4T [41], XENON1T [42–44], DEAP-3600 [45], DarkSide-50 [46], EDELWEISS [47, 48], CDEX [49], and NEWS-G [50]. Also shown is the neutrino fog calculated for xenon [35] and dark matter limits from the CMB [51, 52], galactic center gas clouds [53], and the XQC experiment [54].

HeRALD detector. HeRALD is a superfluid helium target with signal readout via superconducting transition edge sensors. While it is still in the R&D phase, sensitivity projections show access to large amounts of sub-GeV parameter space. Studies in this thesis concern a signal generation model used in these sensitivity studies and experimental measurements testing those predictions. HeRALD is developing rapidly as a new detector technology to probe dark matter in the near future.

Chapter 2

The LZ Experiment

In this chapter we introduce the LZ experiment, a xenon two-phase liquid-gas time projection chamber (TPC) designed chiefly to detect WIMP dark matter. We first introduce the basic detector principles informing the design of a TPC before describing the LZ detector directly, as well as calibration strategies and sources of backgrounds for dark matter searches. We focus on mainly on topics informing the first science run (SR1) used to search for dark matter, collected between December 23rd, 2021 and May 11th, 2022, since these detector conditions apply to the analyses presented in subsequent chapters: the first WIMP search in Chapter 3, extending the WIMP sensitivity to lower masses in Chapter 4, and the design of a low energy neutron calibration source and its first dataset in Chapter 5. The material presented in this chapter includes results produced by other members of the LZ collaboration informing the SR1 analysis, some of which are available in the pre-print describing the result [55].

2.1 TPC operating principles

The basic construction of a two-phase xenon TPC is designed to detect two separate signals for every particle interaction in the active volume. A particle recoil generates prompt scintillation light and ionizes some xenon atoms. An electric field is applied to the target volume of the TPC so that some of these electrons drift to the liquid surface in the detector. When the drifted electrons pass into the gas phase, they produce light in a process called electroluminescence. Photomultiplier tubes (PMT) at the top and the bottom of the TPC detect the light from both of these signals; LZ has 253 top PMTs and 241 bottom PMTs, of which 12 were shut off for detector operation during SR1. Xenon is transparent to its own 178 nm scintillation light, allowing for the detection of the small prompt scintillation signal even in large detectors. This detection scheme provides three dimensional position reconstruction; the electrons are drifted at a uniform velocity, so the time separation between the prompt scintillation (S1) signal and the extracted electron (S2) signal provides information about the interaction depth in the detector, while the PMT hit pattern can be used to reconstruct

its XY position [56]. These steps to event measurement and reconstruction are shown in Figure 2.1.

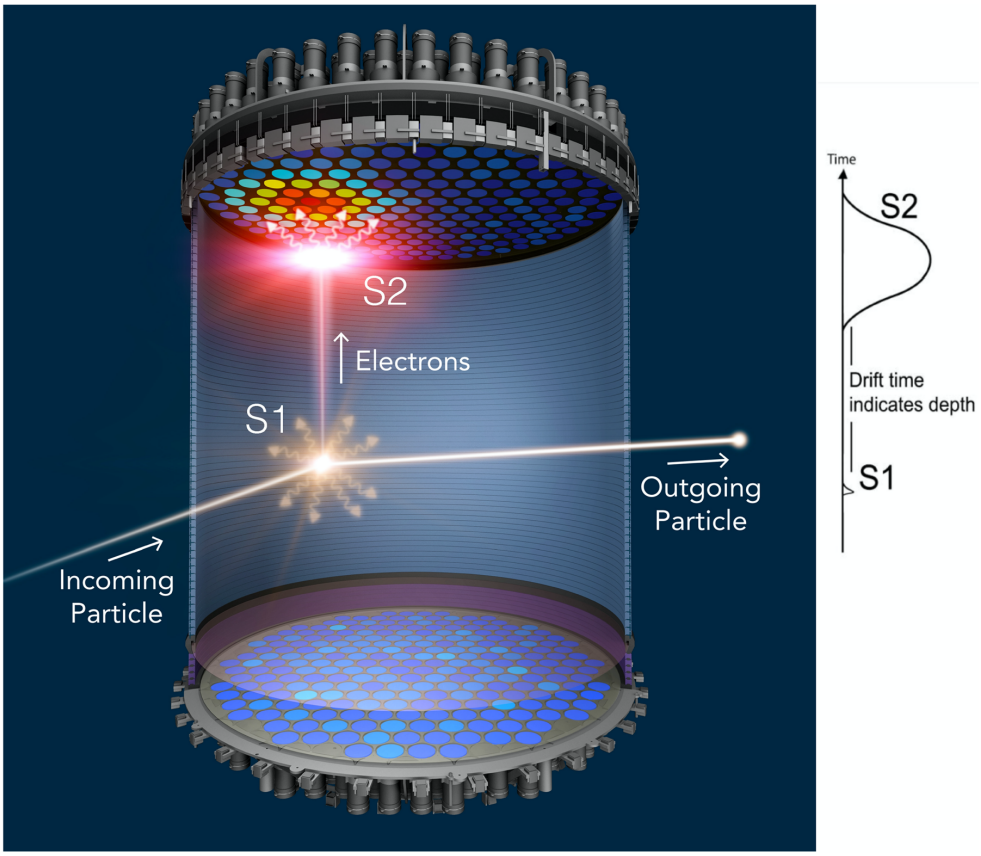

Figure 2.1: A rendering of a particle interaction in the LZ TPC. Prompt scintillation light (S1) precedes a larger scintillation signal from electrons (S2) extracted with a drift field applied to the liquid xenon target. The time separation of S1 and S2 indicates the depth of the interaction, and the PMT hit pattern is used to reconstruct its position in the horizontal plane. Figure copied from [57].

Since xenon is relatively dense and MeV-scale gamma rays have a mean interaction length of only a few centimeters, the medium is said to be self-shielding [57]. Combined with the position reconstruction capabilities of the TPC, events near the detector edges can be rejected for substantial background reduction. Another advantage of this detector design in the context of dark matter detection is that it allows for the reconstruction of multisite interactions, which are unlikely to be caused by WIMPs. For context, LZ has a horizontal position resolution between a few millimeters and a centimeter, contingent on the number of photons in the S2 signal and a slight reduction in resolution near detector walls, compared

to its diameter of 1.456 meters.[1]

The relative size of the S1 and S2 signals provide information about the type of particle interaction that generated them. The WIMP recoils of interest are those which scatter off of the xenon nucleus, so the ability to discriminate away backgrounds which interact with the xenon electrons is another significant benefit to the TPC design. This discrimination power is the result of the fundamental signal-generating process in the xenon, and depends on many factors like the amount of energy deposited in the detector and the electric field used in the TPC. Experimental data from many sources, with varying temperature, electric field, and detector configurations, have been compiled into a global model and simulation software called NEST [59, 60]. While we provide a very basic review of the quantities relevant for understanding fundamental behaviors of S1 and S2 signals, the NEST model is complex and covers a wide range of physics models and use cases.

Schematically, the signal generation process is outlined in Figure 2.2. When a particle deposits energy in the detector, the recoiling xenon track is populated by a number of excited and ionized xenon atoms

$$E_{\text{dep}} = fW(n_{\text{ion}} + n_{\text{ex}}) \tag{2.1}$$

where $W = 13.5$ eV [61][2], f is the quenching factor accounting for variation in the amount of energy lost to heat, and n_{ion} and n_{ex} are the number of ions and excited state xenon atoms produced, respectively.

Despite the applied electric field in a TPC, some number of electrons recombine with xenon ions in the recoil track, forming more excited states as a result. The fraction of these that recombine, r, modifies the detectable number of electrons

$$n_e = n_{\text{ion}}(1 - r) \tag{2.2}$$

and the detectable number of photons

$$n_\gamma = n_{\text{ex}} + r n_{\text{ion}}. \tag{2.3}$$

We define the yields L_y and Q_y as n_γ/E_{dep} and n_e/E_{dep}, respectively. Recombination is assumed to yield one-to-one conversion between ions and excited state xenon atoms, so $n_{\text{ex}} + n_{\text{ion}} = n_e + n_\gamma$. Thus, we can also write the deposited energy as

$$E_{\text{dep}} = fW(n_e + n_\gamma). \tag{2.4}$$

The inverse of f is the Lindhard factor L, taken to be unity for electronic recoils (ERs) and a function of the recoil energy for nuclear recoils (NRs) [61]. It represents signal quenching,

[1] The performance of the same position reconstruction methods were studied in detail for the LUX detector [58].

[2] The is some disagreement in the literature for measured values of W [62–64]. A different W value in Equation 2.1 could for the most part be absorbed into detector-specific quantities discussed later in Section 2.3, so while its true value remains an open question, we adopt the value used in current versions of NEST.

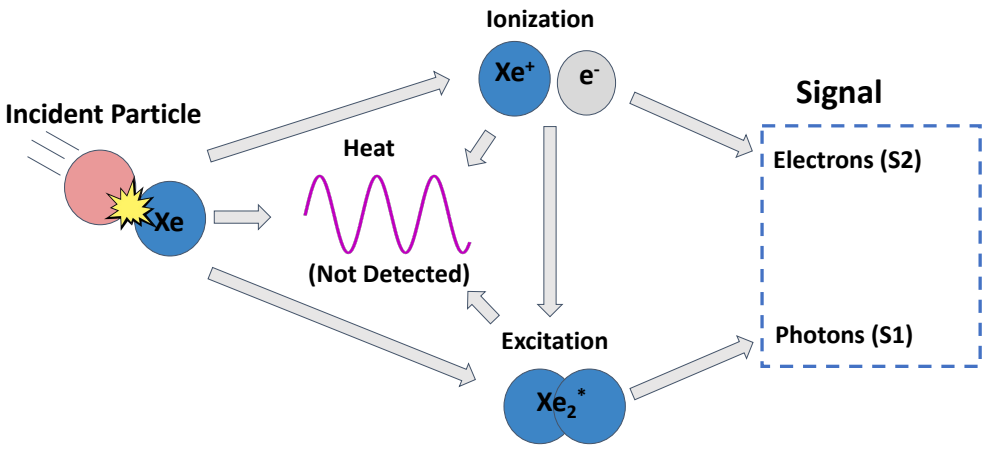

Figure 2.2: An overview of signal generation in a liquid xenon TPC. Particle recoils ionize and excite helium atoms. Ionized xenon atoms recombine with their electrons into more excitations, which quickly decay to xenon scintillation light forming the S1 signal. Some ionized electrons are extracted with the drift field and generate the S2 signal. Energy is lost to undetectable heat in every step.

reducing the number of detectable quanta in the nuclear recoil case. The difference in signal leads to two different energy scales, keV_{ee} and keV_{nr}, depending on which treatment of f is applied. Nuclear and electronic recoils have different values of L_y and Q_y as a result of f, different values of r, and several other physical processes modeled by NEST. An example of the NR and ER light yields, and their differences, from the NEST model is shown in Figure 2.3. NEST is actively maintained and incorporates new data regularly, leading to updated models as the global understanding of particle interactions in xenon grows.

2.2 LZ detector systems

The LZ detector and its many systems have been documented in detail in the technical design report (TDR) [57] and after its assembly [66]. The LZ experiment actually consists of several nested detectors, with the aforementioned liquid xenon TPC at their center. Outside of the TPC, a layer of liquid xenon called the skin is instrumented with 93 PMTs with a diameter of 2.54 centimeters and 38 PMTs with a 5.08 centimeter diameter (of which two were disabled during the first science run). The skin provides an extra layer of xenon shielding material as well as an active veto that can be used to veto events also scattering in the TPC.

The liquid xenon is contained in the inner of two nested titanium cryostats: the inner cryostat vessel (ICV) and the outer cryostat vessel (OCV). Surrounding the OCV is the outer detector (OD), a set of acrylic tanks filled with gadolinium-loaded liquid scintillator designed to efficiently veto neutrons scattering in the TPC [67]. All of these systems are submerged

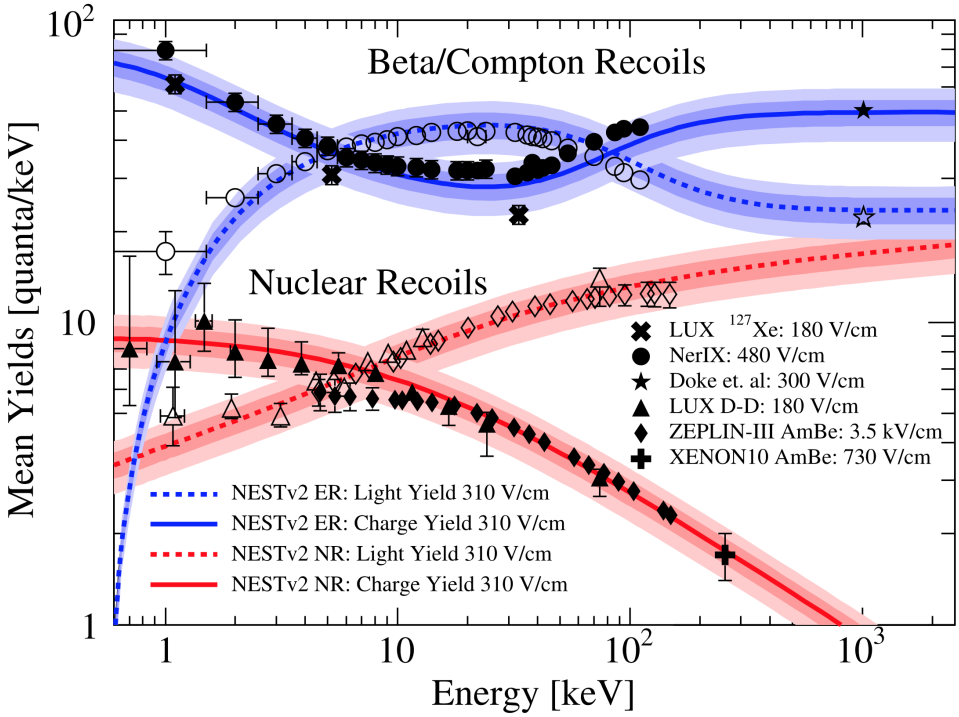

Figure 2.3: Collected experimental data of xenon light and charge yields for nuclear and electronic recoils, and the NEST model associated with each [59]. For the most up to date yields models, see the most recent version: NESTv2.3.11 [60]. Figure copied from [65].

in a water tank filled with 238 tons of ultra-pure water, serving as an additional shield for ambient radioactivity. 120 PMTs with a 20 centimeter diameter monitor the OD tanks and water to serve as a combined OD veto detector. A rendering of the nested detector system is shown in Figure 2.4. LZ is located deep underground in the Davis Cavern of the Sanford Underground Research Facility (SURF) in Lead, South Dakota, with 4850 feet of rock serving as an additional layer of shielding from cosmic ray muons and other astrophysical radiation.

The electric fields in the LZ TPC are set by four woven wire grids serving as transparent electrodes [68]. These were used to establish a drift field of 193 V/cm in the TPC for SR1 operations. The gas extraction field was determined to be 7.3 kV/cm at the center of the gas just above the liquid surface, where the enhanced field relative to the drift field is critical in generating the electroluminescence signal forming the S2. The reverse field region is a region of liquid xenon below the cathode, where the field from the high voltage cathode is reduced by the bottom grid in front of the bottom PMTs. This is a region of xenon where electrons cannot be extracted to the surface, so it serves as an additional xenon layer for shielding. Figure 2.5 shows a photo of the assembled TPC and highlights the positions of the different grids.

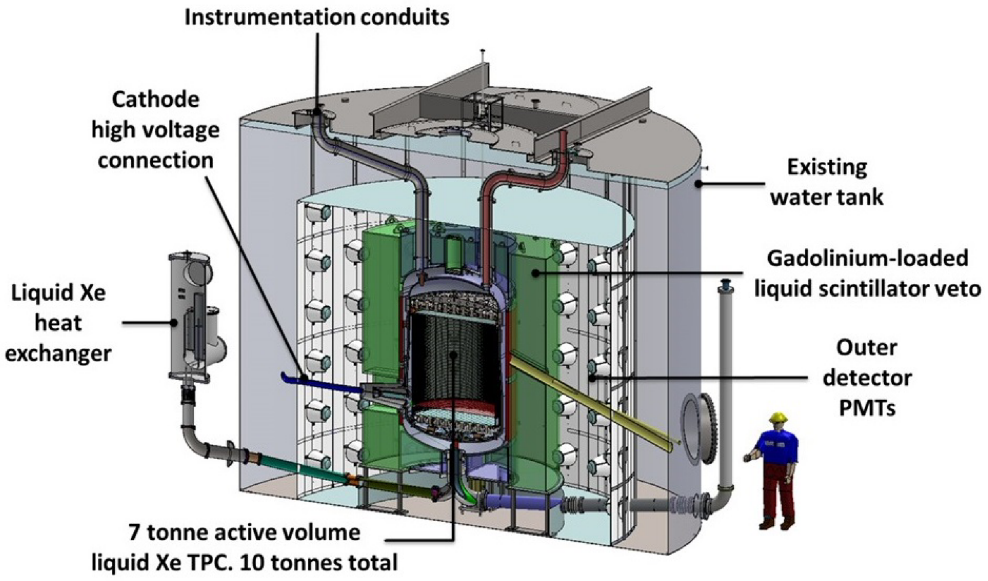

Figure 2.4: A rendering of the LZ TPC and its associated systems. The TPC is housed inside two titanium cryostats, surrounded by a set of acrylic vessels filled with gadolinium-loaded liquid scintillator forming the outer detector, all of which is inside of a large water tank for extra shielding. The are several feedthroughs through these layers for high voltage delivery, instrumentation connections, xenon circulation and temperature control, and calibration access. Figure copied from [57].

Data are recorded as zero-suppressed waveforms for each PMT in the TPC, skin, and OD. Events are triggered on the S2 pulse, with 100% trigger efficiency for pulses corresponding to 6 extracted electrons or larger. Each event consists of a time window with 2 ms of pre-trigger and 2.5 ms post trigger bounds. Once recorded, events are processed according waveform timing and pulse sizes, computed in terms of photons detected (phd) accounting for the double photoelectron effect [69, 70]. Pulses are classified as S1 or S2 signals based on their shape, area, and hit pattern, where S1 pulses are required to have photons identified in at least 3 separate PMTs. Events are classified as single scatter or multiple scatter interactions based on the number and ordering of S1 and S2 pulses. The top panel of Figure 2.6 is an example of a good single scatter-like event. This reconstruction step can also classify events as the pileup of multiple interactions in a single event window or identify events for which there is not a clear classification. One common pathological event type consists of many delayed electron emissions after a large energy deposit in the detector [71]. An example of this type of event is shown in the bottom panel in Figure 2.6

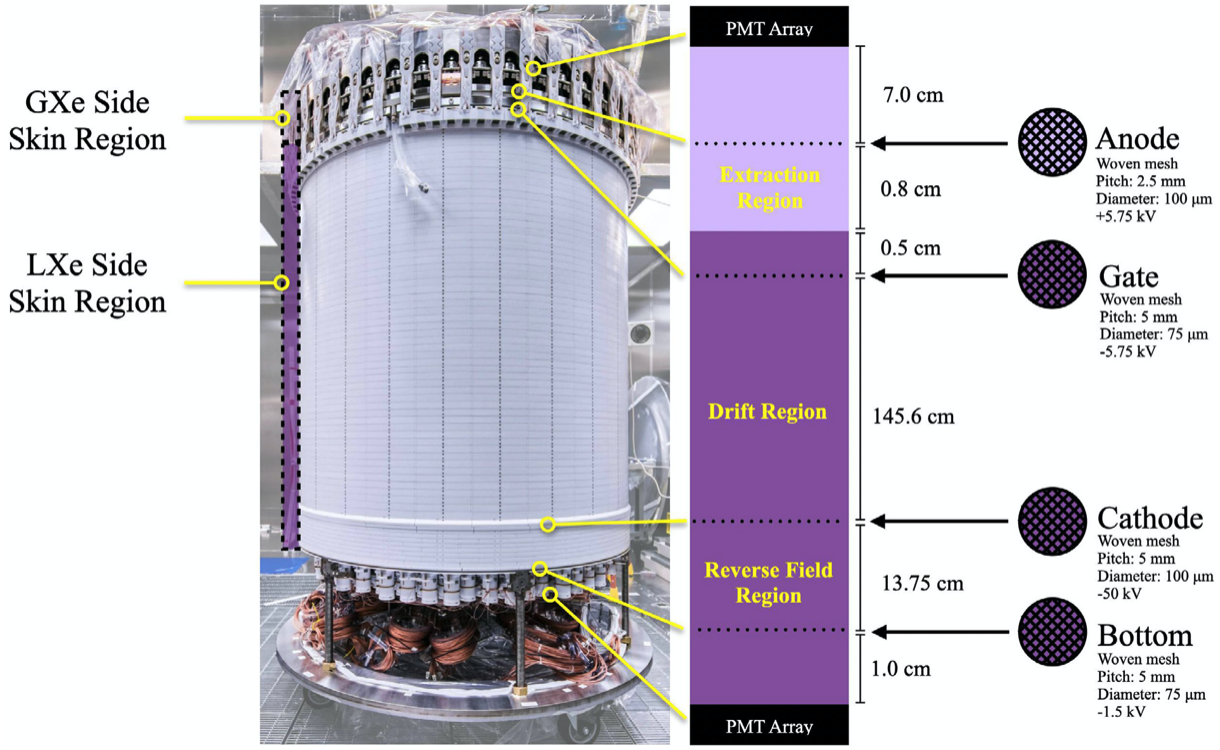

Figure 2.5: A photo of the assembled LZ TPC alongside a diagram marking the different electric field regions set by the four woven wire grid electrodes. Dark purple indicates liquid xenon and light purple represents gaseous xenon. Figure copied from [68].

2.3 Calibrations

A crucial step for comparing the data taken by LZ to the expected dark matter spectrum from Equation 1.4 is converting the recorded signals to the corresponding energy deposited in the detector. Equation 2.4 is an expression for the number of detectable electrons and photons produced as a function of energy for nuclear and electronic recoils. What we measure in the detector is the related quantity

$$E_{\text{reco}} = W\left(\frac{\text{S1}c}{g_1} + \frac{\text{S2}c}{g_2}\right), \tag{2.5}$$

where S1c and S2c are the detected S1 and S2 signal corrected for spatial variations in the detector response and g_1 and g_2 are the detector-specific gain functions for the S1 and S2 signals. It is also possible to define an electron-energy scale based purely on Q_y, but the nonlinearity in this quantity makes the resulting energy estimate less reliable [61]. S2-only analyses have been employed in previous liquid xenon experiments to dramatically lower the threshold for event detection, extending the detector reach to smaller energies [43, 72].

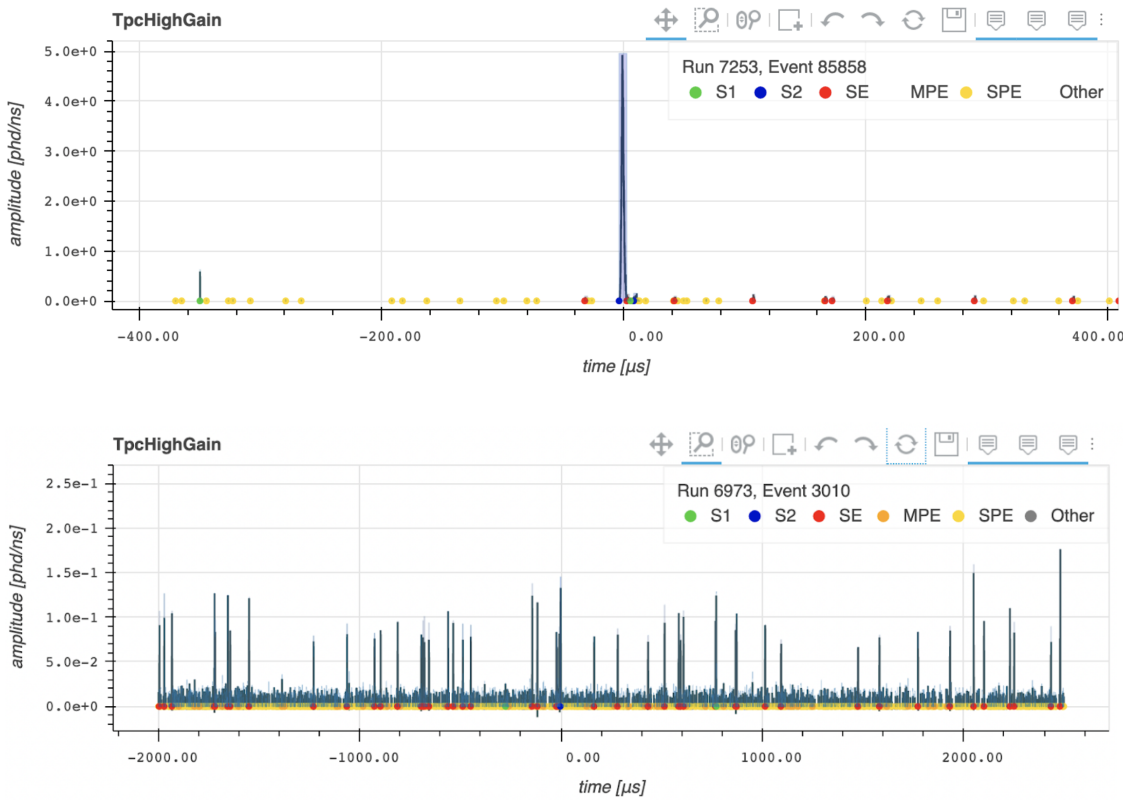

Figure 2.6: Two events recorded with LZ. The top event is an example of a clean single scatter event, consisting of a single S1 marked in green and a single S2 marked in blue. Additional single electron pulses are marked in red, while the yellow markers show single photons, though these are too small to see on this scale. The bottom event is an example of an electron train event, where there are many single- and few-electron pulses in close succession. Additionally, the elevated single photon rate can lead to a mis-identification of an S1. These events are excluded at the analysis level.

The spatial variation corrections used to obtain S1c and S2c are derived from radioactive calibration sources dispersed in the liquid xenon, including ^{83m}Kr [73] and ^{131m}Xe [57]. These were injected in advance of SR1 and decay quickly, with half-lives of 1.8 h and 11.9 days respectively [57]. Additionally, their decays are relatively high energy, 41 keV and 164 keV respectively, and do not enter the final analysis signal region. Correction maps can be constructed from these decays because they spread out into the full TPC volume, serving as standard candles for the S1 and S2 response in three dimensions.

Since S1 signals are generated in the liquid xenon, the measurement of these photons is affected by their probability to reflect off of the teflon walls of the detector, their probability to cross the interface at the liquid surface or reach the bottom PMT array, and the probabilities associated with the various steps in the PMT detection mechanism. S1 corrections are

applied simultaneously in x, y, and drift time to normalize the signal to the geometric center of the TPC. The scale of corrections extends from factors of 0.8 to 1.25, with an average correction size of 9%.

S2 corrections account for two separate effects. Variation in x and y occurs due to switched-off PMTs and nonuniformities in the extraction field near the wires of the grids. The average scale of this correction is 11%. Electrons drifting through the TPC can also capture on impurities, reducing the S2 signal size as a function of the depth of an interaction in the detector. The average probability of this capture is quantified with the electron lifetime in units of milliseconds, but it should be noted that this quantity is drift velocity dependent. Figure 2.7 shows the measured electron lifetime over the course of SR1, as well as the maximum correction factor associated with this lifetime on the second y-axis. SR1 values for the electron lifetime were between 5000 and 8000 μs, yielding an average correction for this effect of 7%.

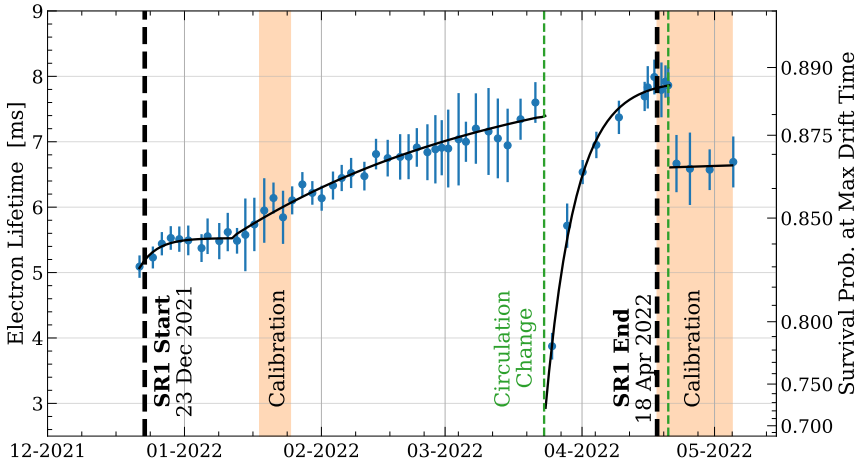

Figure 2.7: The measured electron lifetime during SR1. The corresponding maximum correction factor applied to S2 signals is shown on the right axis. Plot by J. Genovesi and M. Timalsina.

These corrections help normalize the detected S1 and S2 signals, but they are still not equivalent to the more fundamental n_e and n_γ. The relationship between Equations 2.5 and 2.4 is captured via the gain functions, which map the detected signals S1c and S2c to the yields from the NEST model. The factor g_1 is dependent on the light collection efficiency of the detector and the quantum efficiency of its PMTs, yielding an average detection probability for an emitted photon. Thus, it is typically much less than 1; in SR1, LZ's $g_1 = 0.1136$ phd/photon. The factor g_2 is dependent on the average number of photons emitted during

the electroluminescence process and the average efficiency of extracting an electron from the liquid surface. Since electroluminescence is a multiplicative process generating many photons per electron, g_2 is typically at least a factor of 10 or more.

In addition to modeling fundamental properties of xenon, NEST models detector-specific quantities to reproduce the effects of signal detection in addition to the signal production effects described in Section 2.1. LZ employed a second class of calibration sources to tune the NEST response model to accurately simulate the LZ detector. Two broad spectrum sources, tritium as CH_3T for beta decay electron recoils [74] and a DD neutron generator for nuclear recoils [75, 76], were used to populate the detector response for a range of S1c and S2c covering the region of interest for the WIMP search. Tritium has a half-life of 12.3 years, so it was injected after the collection of SR1 data and was actively purified from the detector via the circulation system [66, 74]. The DD generator is an external source, creating 2.45 MeV neutrons that are directed through the water tank to the TPC via a small conduit. Energy deposits from these sources were simulated in a model of the LZ detector using the LZ software BACCARAT [65], a package extending the functionality of GEANT4 [77–79] for LZ specific applications. The NEST model for LZ was tuned by matching the simulated response to the tritium and DD data in S1c and S2c. The datasets from these calibrations are shown in Figure 2.8, as are the simulated 10-50-90 percentile bands associated with the best tuning parameters. The detector response parameters that best fit the data from this tuning procedure are provided in Table 2.1, and they ultimately required that the recombination model previously developed for LUX [80] was modified to adequately match the tritium data. Future tritium calibrations will target higher statistics to probe this discrepancy further.

Table 2.1: NEST tuning parameters corresponding to the LZ detector conditions during the first science run. The top half are direct inputs to NEST and the bottom half are useful quantities derived from the resuling NEST model.

Parameter	Value
g_1^{gas}	0.0921 phd/photon
g_1	0.1136 phd/photon
Effective gas extraction field	8.42 keV/cm
Single electron	58.5 phd
Extraction efficiency	80.5%
g_2	47.07 phd/electron

Additional NR calibration data were taken with an americium-lithium neutron source to provide another dataset for consistency checks of the data analysis code, detector response model, and data selection cuts described in the next chapter. Many more sources with different calibration targets and physics implications are planned [57]. One of these is a low

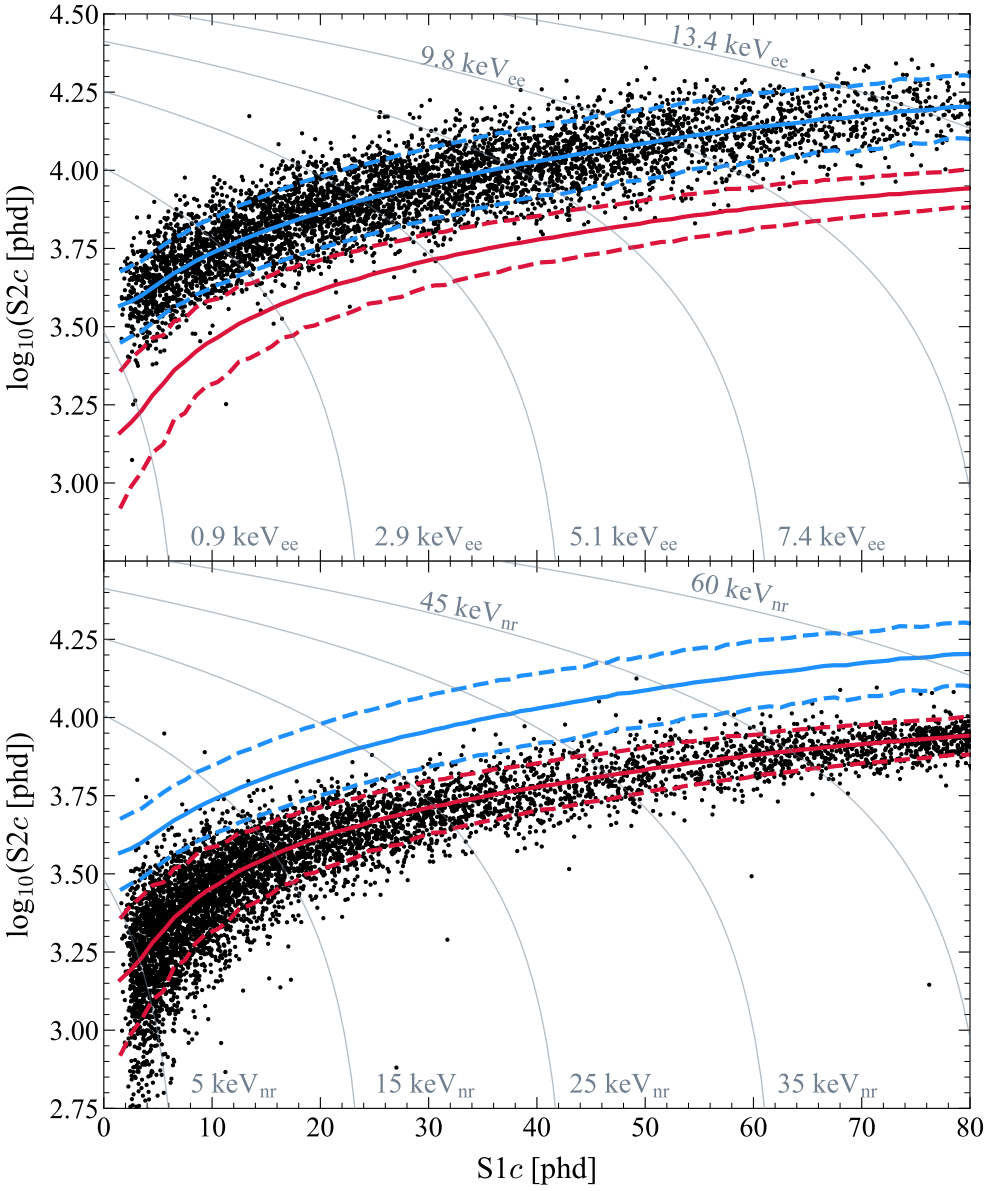

Figure 2.8: Calibration data used to tune the detector response model for SR1. The top panel contains electronic recoils from tritium decays injected as CH_3T via the circulation system. The bottom panel events are nuclear recoils from DD neutrons. The solid lines are the median S2c response of ERs (blue) and NRs (red) as a function of S1c. They grey lines show contours of constant energy in both ER and NR energy scales. Plot made by G. Rischbieter.

energy photoneutron source which was deployed before SR1. The design of this source and analysis of the first dataset are discussed in Chapter 5.

2.4 Sources of background events

The self shielding of xenon and event discrimination power of the TPC design are crucial in combating a range of background sources that induce particle interactions in the detector. Many of these backgrounds are well-known from previous generations of experiments and their impact on the LZ WIMP sensitivity was projected with a detailed simulation analysis [81], while some others are relevant only because of the specific parameters of the SR1 dataset. In this section we will provide an introduction to the backgrounds of interest for SR1. The rate estimates for these backgrounds, specific to the analysis of SR1 data in the context of dark matter limit setting, will be discussed in the next chapter.

The vast majority of backgrounds events are electronic recoils from a variety of sources, for which a low energy recoil spectrum is shown in Figure 2.9. Due to the larger energy scale associated with ERs, the region of interest in SR1 was limited to a maximum ER recoil energy of about 20 keV_{ee}. The largest contribution from ER sources in this energy range is due to dispersed ^{222}Rn contamination. Particularly, the isotope ^{214}Pb in its decay chain undergoes beta decay without emitting any associated gamma rays, yielding a flat ER spectrum at low energies. ^{212}Pb from the ^{220}Rn decay chain constitutes a similar background at a reduced rate. The third dispersed beta decay source in Figure 2.9, ^{85}Kr, was removed from the xenon via chromatography [82] before its delivery to the underground LZ detector. ^{222}Rn and ^{220}Rn can be introduced into the xenon in two ways: emanation from materials and components used to build the detector and emanation from dust introduced during its assembly. Radon backgrounds from detector components were controlled for via an extensive assay campaign [83, 84], while dust was minimized via strict cleanliness protocols employed while assembling the detector. Other decays modes in the ^{220}Rn and ^{222}Rn chains, such as alpha decays, contribute background events depositing energy in the detector, but these are generally at MeV scales far outside of the region of interest for the main WIMP search. Near the detector walls, these decays can produce a reduced signal size approaching the smaller energy scales of the main signals of interest, providing an additional motivation for using an inner fiducial volume for the data analysis. Measurement of the rates of the alpha decays in these chains provided a method for constraining the expected beta decay backgrounds in the region of interest for the SR1 WIMP search analysis discussed in Chapter 3 [85].

There are various sources of gamma rays which can induce recoils in the TPC. Detector components contain their own trace radioactivity. These contaminants were also measured via radio assay to ensure a subdominant contribution in the region of interest. High energy gamma rays from the cavern walls can also penetrate into the TPC. While the probability for such gamma rays to make it to the central TPC volume is small, the flux was measured experimentally to validate assumptions about their rate [86]. Finally, surface contaminants are another source of trace radioactivity, but the relatively short SR1 duration and the

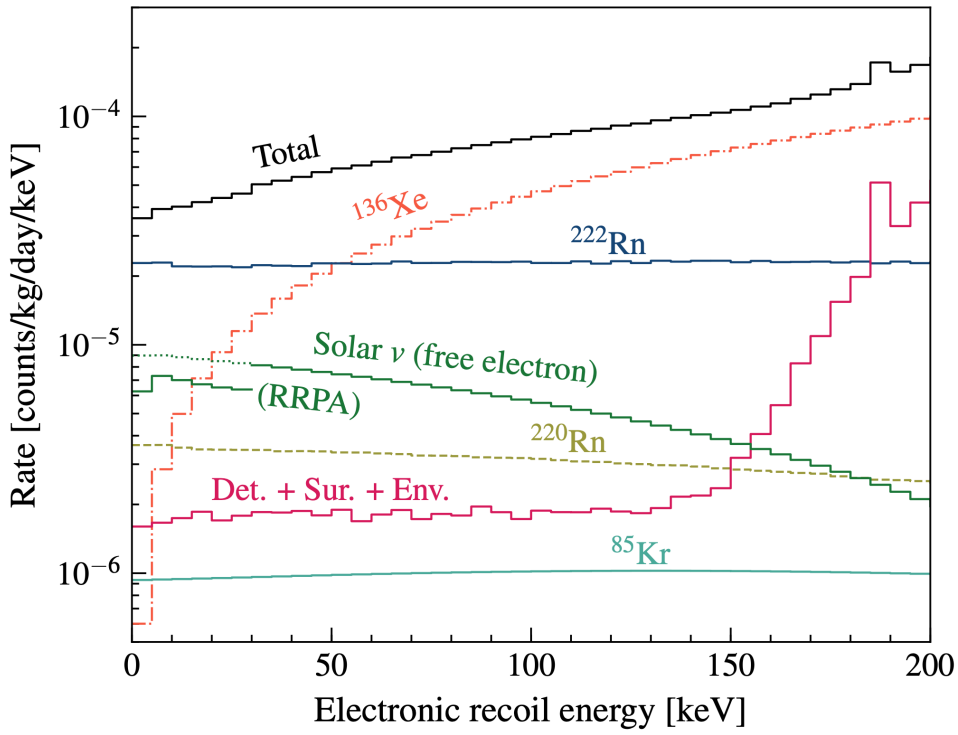

Figure 2.9: Simulated electron recoil backgrounds for the projected 1000 day full exposure of LZ. Figure copied from [81].

fiducial cut used to eliminate events close to the detector walls minimized the impact of these backgrounds. These three components are grouped together in Figure 2.9 and land at rates well below other ER backgrounds.

Two naturally occurring isotopes of xenon contribute backgrounds via rare decays. The double beta decay of ^{136}Xe actually serves as a potential source of signal of physics beyond the Standard Model, leading to its use for neutrinoless double beta decay searches [71]. In the energy range of interest for a WIMP search this background is subdominant, but it grows with recoil energy and takes over as the dominant background source for energies above about 50 keV in Figure 2.9. After Figure 2.9 was made, it was recently measured that ^{124}Xe undergoes the extremely rare process of double electron capture [87]. For a detector the size of LZ, a few such events are expected as backgrounds even in the relatively short SR1 duration.

The final ER background component shown in Figure 2.9 is due to solar neutrino scattering. The solar and other astrophysical neutrino spectrum is shown in Figure 2.10 according to the recommendations in [29]. These neutrinos can also generate nuclear recoils via coherent neutrino-nucleus scattering (CEνNS) which has been observed from spallation sources [40] but not astrophysical ones [44]. CEνNS is a background of concern particularly for low

mass WIMPS as the spectra overlap, limiting sensitivity [35].

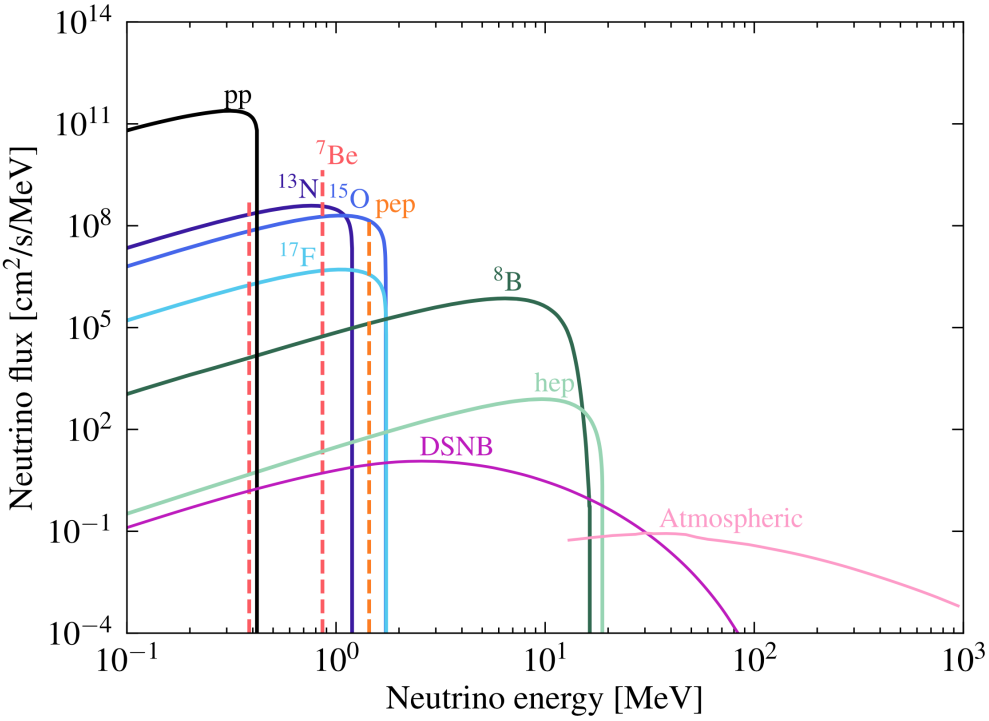

Figure 2.10: Astrophysical neutrino spectrum contributing to backgrounds in LZ. Figure copied from [88].

Neutrons can be introduced into the TPC via (α, n) processes in the detector components or outside of the water tank in the cavern walls [89]. The OD neutron veto, with measured tagging efficiency $88.5 \pm 0.7\%$, helps combat these backgrounds. The projected number of neutron single scatters after the application of vetoes was just 1.03 in the 1000 day exposure [81], but this background was still considered for the SR1 analysis due to its spectral overlap with the WIMP signal of interest.

The relatively short duration of SR1 as the first dataset taken with the LZ detector meant that the short-lived cosmogenic activation products ^{37}Ar and ^{127}Xe, with half-lives of 35 days and 36.3 days respectively, were a larger fraction of the background rate than they would be in a 1000 day exposure. ^{127}Xe is less of a concern as the K-shall captures fell outside of the WIMP-search region of interest and could be leveraged to constrain the rate. The contribution from ^{37}Ar is more concerning since most decays are K-shell captures which release 2.82 keV of Auger electrons and X-rays [90]. The expected activity of ^{37}Ar due to activation during the xenon shipment to SURF is shown in Figure 2.11, but the estimates were subject to fairly large uncertainties of a factor of about 3 [90].

Of the "nonstandard backgrounds" considered in [81], the one deemed most concerning

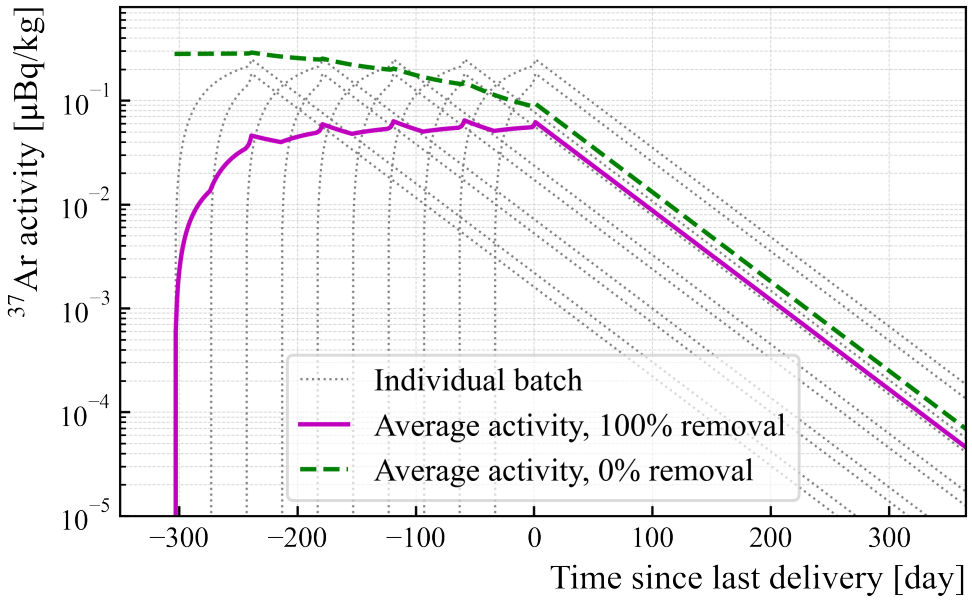

Figure 2.11: Estimated ^{37}Ar activity in the LZ liquid xenon due to cosmogenic activation. The xenon was delivered underground to the detector in several batches, shown by the different dashed lines. The total activity of ^{37}Ar is shown assuming it is perfectly removed via purification before shipment (magenta) and not removed all by purification (dashed green). It decays with a half-life of 35 days. Figure copied from [90].

during SR1 was formed from accidental coincidences of isolated S1 and S2 pulses falling in the same event window to produce single scatter-like events. The spectrum of these events was studied using events with an unphysical drift time (UDT) greater than the maximum 951 μs for true recoils in the TPC. A spectrum of accidental coincidence events derived from UDT events is shown in Figure 2.12.

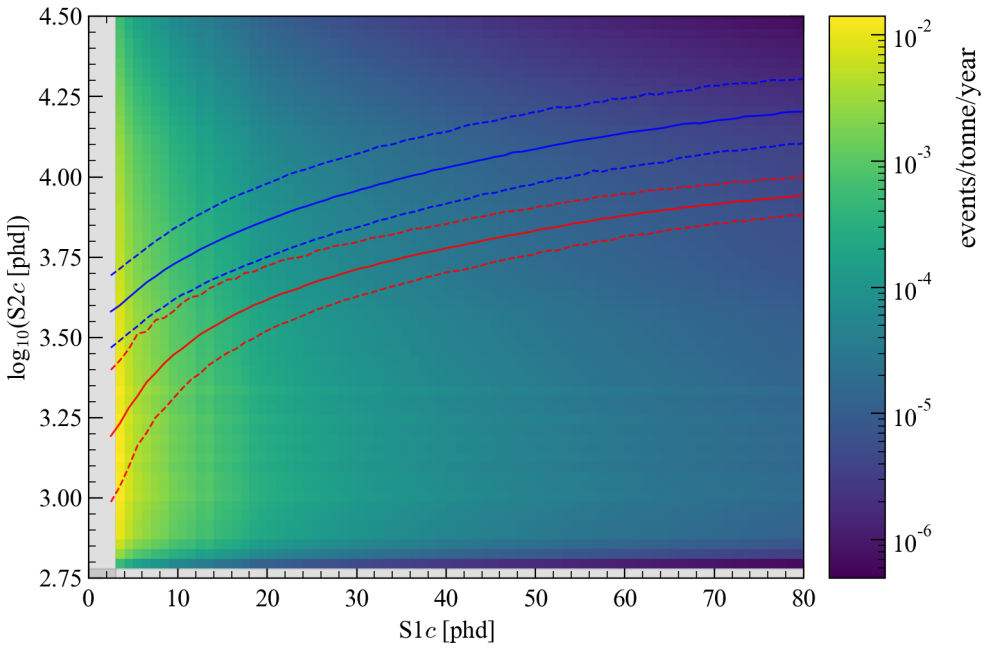

Figure 2.12: The spectrum of accidental coincidence events formed by isolated S1 and S2 pulses for the SR1 detector conditions. The ER and NR bands from Figure 2.8 are shown for context. Figure by I. Olcina.

Chapter 3

First WIMP Search Results from LZ

This chapter describes the first WIMP search conducted with the LZ detector which was introduced in Chapter 2. A pre-print of this analysis is currently available on the arXiv [55]. The dissertation author primarily contributed to the statistical analysis of the final dataset to set limits on both spin independent and spin dependent WIMP-nucleon interactions, working closely with S. Haselschwardt, A. Manalaysay, A. Kaboth, and H. Lippincott to do so. Due to the dissertation author's role, we focus on the statistical analysis of the data, briefly summarizing the building blocks to get to the final dataset. However, we emphasize the full analysis of the SR1 dataset was the collective work of many scientists which we do not attempt to describe completely.

3.1 First science run

The first LZ dataset used to search for dark matter, labelled science run 1 (SR1), was collected between December 23rd, 2021 and May 11th, 2022. The live time of the detector in this period, that is the time during which data were actively able to be recorded and therefore dark matter could be detected, is shown by the blue line in Figure 3.1. Not included in this live time are periods where the detector was under maintenance, active calibration periods, and times where the data acquisition system was not live or subject to anomalous trigger rates. Some of these events were vetoed at the analysis level, yielding the active search live time shown by the dashed orange curve, amounting to 60 ± 1 days of exposure. Details of data selection are provided in the next section. The active volume used in the analysis consisted of 5.5 ± 0.2 tonnes of liquid xenon, for a total search exposure of 0.91 ± 0.04 tonne years.

3.2 Data selection

A total of 1.1×10^8 events were recorded in the total SR1 dataset during the 89 live days. In order to reduce these events to the final WIMP search candidates, a series of data selection

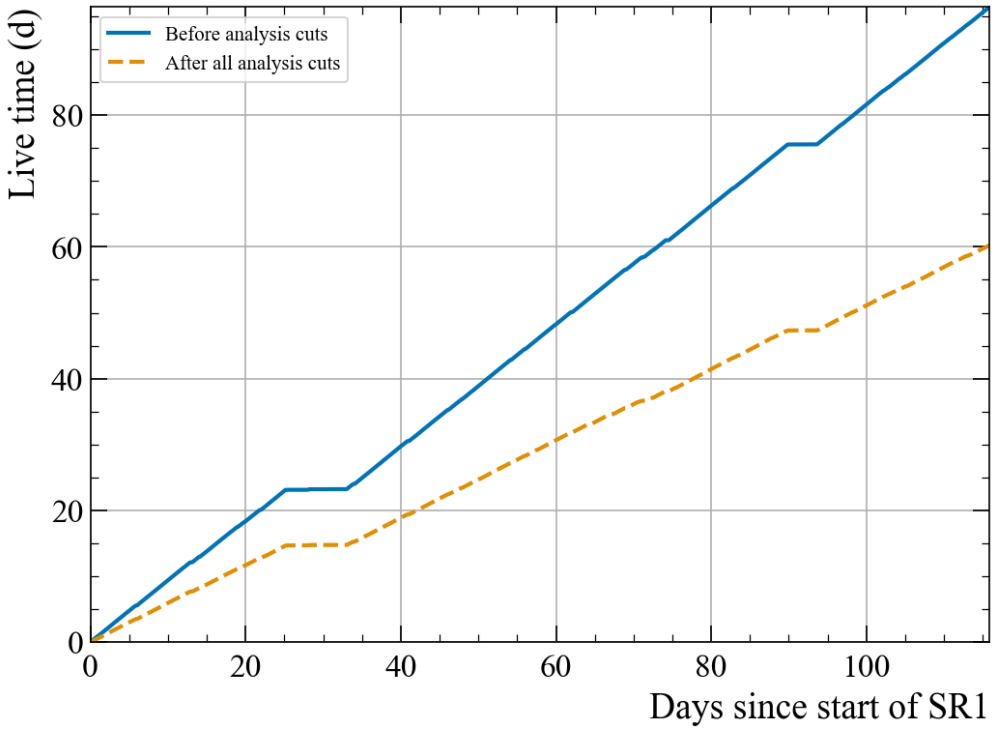

Figure 3.1: The live time of the LZ detector during the first science run (SR1) data used to search for dark matter. The blue curve shows the live time corresponding to all collected data while the dashed orange curve is the live time after the application of analysis level vetoes. Plot made by M. Buuck and A. Fan.

vetoes and cuts were applied. Events containing an elevated rate of single electrons, like the one shown in the bottom panel of Figure 2.6, follow large S2s and cosmic ray muons interacting the TPC [71]. An analysis-level time holdoff was implemented to discard these events from the dataset.

Events identified as multiple scatters in the TPC were removed, as well as events with anomalies otherwise interfering with the reconstruction of single scatter interactions. Single scatter events were considered inside of the WIMP search region of interest (ROI) if they had an S1c in the range 3 – 80 phd, an S2 greater than 600 phd, and an S2c less than 10^5 phd.

A suite of data quality cuts were implemented to identify accidental events and other improperly reconstructed single scatter events. These were constructed to ensure both the S1 and S2 were self-consistent in their drift time, top-bottom light asymmetry, pulse width, pulse timing, and PMT hit pattern. Efficiency for removing events formed by accidental coincidence between an S1 and an S2 was tested against unphysical drift time events known to be accidentals and by simulating them from isolated S1 and S2 waveforms. It was found that the cuts removed more than 99.5% of accidental coincidence events upon their application.

The efficiency curves for events to pass the S2 trigger, S1 threshold, and single scatter and analysis cuts are shown in Figure 3.2. Application of the ROI introduces the rolloff on the upper side of the recoil energy range. The uncertainty on the total event selection efficiency was estimated using AmLi and tritium calibration data.

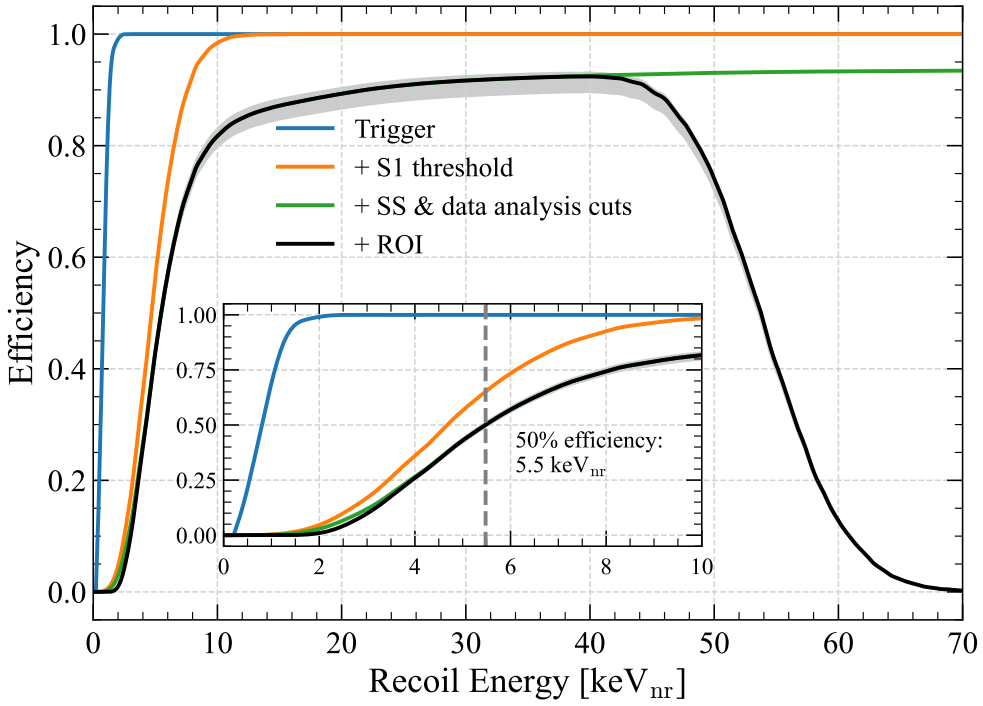

Figure 3.2: The efficiency for detecting events as a function of nuclear recoil energy. The blue curve is the efficiency of the S2 trigger for recording events. Application of the three-fold S1 threshold during data processing reduces the efficiency to the orange curve. Data selection cuts, including the identification of single scatter events, give the efficiency in green. Finally, application of the region of interest gives the black curve, presented with uncertainties for all steps in grey. Plot made by S. Kravitz.

A central fiducial volume was defined by excluding events less than 4 cm from the detector walls, with additional cutouts at the top and bottom corners. It also used to reject events near the gate and cathode grids by selecting for events with drift times $936.5\mu s < t_{\text{drift}} < 86\mu s$. The fiducial volume, as well as all of the events passing the analysis cuts up to this point, are shown in Figure 3.3. A final veto was applied to events which were coincident with signals inside of the skin or outer detector. These are shown as red crosses and blue circles, while the 335 events passing all analysis cuts are shown in black circles.

As described in Section 2.3, the detector response to particle interactions was simulated with BACCARAT [65] which is built on GEANT4 [77–79]. LZ software leveraging NEST [60] was used to process BACCARAT simulations to apply event level clustering and detector

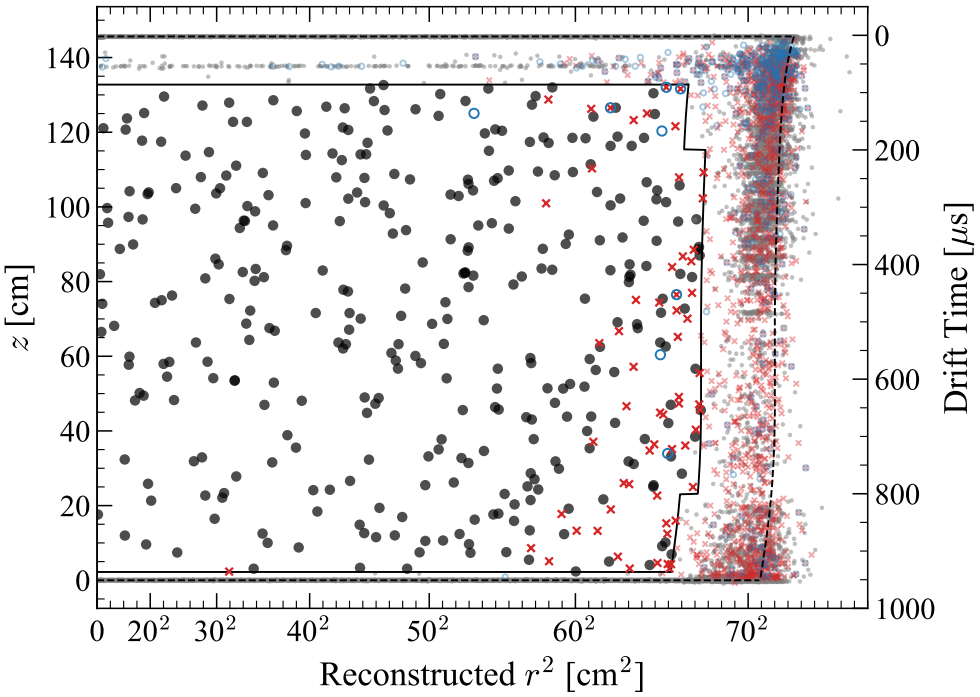

Figure 3.3: The reconstructed r^2 versus z distribution of events in the final WIMP search data set in black. Grey points are those outside of the fiducial volume shown as a solid black line. Red crosses show events vetoed by the liquid xenon skin detector and blue squares are those vetoed by the liquid scintillator outer detector. The physical extent of the detector volume is shown as a dashed black line. Plot made by A. Fan.

response according to the parameters from Table 2.1 and with the recombination skewness model [80] disabled. Analysis cuts were reproduced on simulations of WIMP interactions and the major background components expected in SR1 to construct signal and background PDFs in S1c and $\log_{10}(\mathrm{S2}_c)$. The PDFs for a 30 GeV/c^2 WIMP spectrum and the background model, as well as the 335 candidate events passing all cuts, are shown in Figure 3.4.

3.3 Background estimates

In this section we briefly summarize the background model and expected counts associated with the different components, some of which were introduced in Section 2.4. More detail on the extensive work that went into producing the predicted background rates and their constraints is available in a separate LZ publication pre-print [85]. Because the SR1 data were not blinded, rate estimates and selection cuts were developed on data outside of the ROI or events otherwise failing to pass the selection cuts.

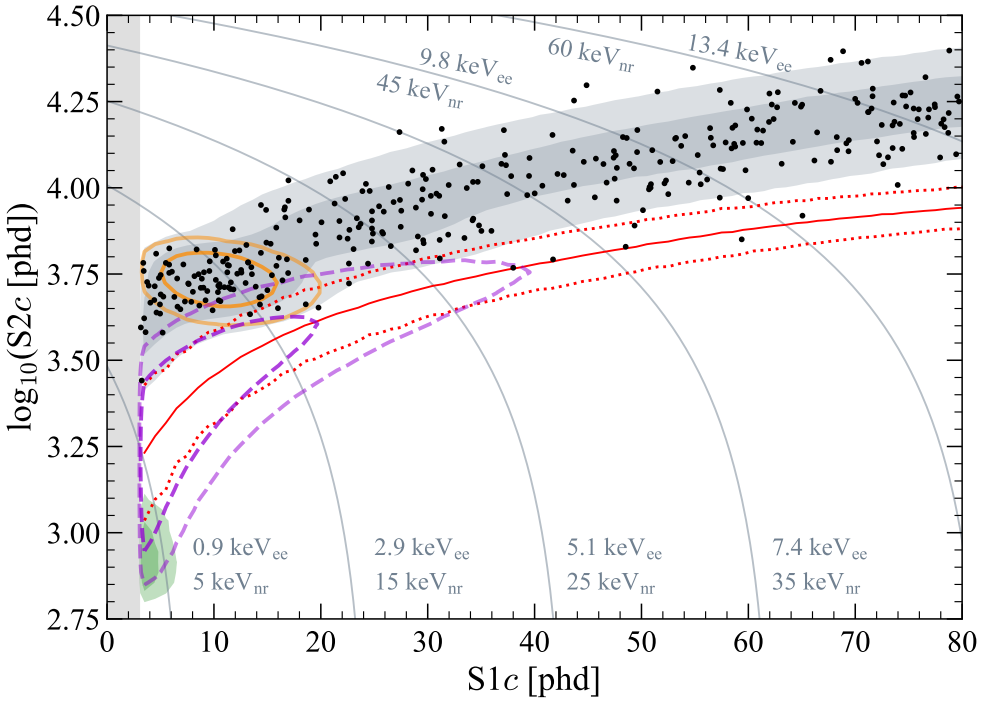

Figure 3.4: The final dataset and models used for the WIMP search. 68% and 95% contours of the background model are shown in grey. The green contour is the expected ^{8}B neutrino coherent scattering region. ^{37}Ar events are are expected inside of the orange curves. The dashed purple lines correspond to the expected signal from a 30 GeV/c^2 WIMP. The solid and dashed red lines are the same nuclear recoil band from Figure 2.8. Also shown in grey is the minimum 3 phd cut applied to the data and models.

The dominant source of background events in the WIMP search ROI is electronic recoils from beta decay of various radioisotopes contaminating the xenon. These are ^{214}Pb from the ^{222}Rn decay chain, ^{212}Pb from the ^{220}Rn decay chain, and ^{85}Kr from natural krypton. The rates of ^{214}Pb and ^{212}Pb were found by fitting peaks produced by other steps in the ^{222}Rn and ^{220}Rn decay chains which fall outside of the ROI. The ^{85}Kr rate was derived from sampling measurements of the liquid xenon in the LZ system. Since these beta decay recoil spectra are all flat in the ROI, they are grouped together into a single component in the model. A flat ER spectrum representing recoils from gamma rays originating in the detector components [84] and the surrounding cavern walls [86] accounts for an additional small number of counts in the total beta decay and detector ER component.

Neutrino fluxes are included according to the recommended procedure in [88], where the experimentally measured rates are used for ^{7}B [91] and ^{8}B [92], and otherwise the rates are from the predictions in [93]. Solar neutrinos also contributed a flat ER spectrum in the ROI, but we leave this component separate in the fit due to the precise prediction of the rate. We

also expect a small rate of nuclear recoils from coherent elastic neutrino-nucleus scattering (CEνNS) from ^{8}B solar neutrinos.

There are several types of xenon isotopes with decay processes that contribute ER events in the ROI. Double electron capture in naturally occurring ^{124}Xe is a recently observed rare process [87], and an additional source from natural xenon is the double beta decay of ^{136}Xe [94]. The expected counts from these were estimated via the known isotoptic abundances and lifetimes associated with these processes [95]. ^{127}Xe decays via electron capture with a relatively short half life of 36.3 days [96], but it was produced by cosmogenic activation before the xenon used in LZ was transported to the underground facility. L- and M-shell captures of ^{127}Xe fall within the WIMP search ROI, and their rates were constrained by the rate of K-shell captures outside of the ROI. De-excitation gamma rays from these events were tagged by the skin veto, reducing the rate by a factor of 5.

The rate of accidental events formed by the pairing of isolated S1 and S2 pulses was constrained applying the data selection cuts to the population of unphysical drift time events. The PDF for these events is shown in Figure 2.12. All of the backgrounds described so far were assigned Gaussian constraint functions with mean and σ equal to the estimated number of counts and uncertainties from the "Expected Events" column of Table 3.1, above the subtotal row.

Background components below the subtotal row were those with non-Gaussian constraint functions. An additional source of backgrounds due to cosmogenic activation are electron capture decays of ^{37}Ar. The activity of ^{37}Ar present in the detector during SR1 was estimated prior to its start [90]. Since the uncertainties on this estimate were relatively large, ^{37}Ar was assigned a flat constraint between 0 and three times the predicted 96 events. Radiogenic neutrons from detector components and the cavern walls can create single scatter nuclear recoils that look like WIMP signals when evading the neutron veto outer detector. The rate of neutron scatters in the WIMP search data was constrained by a likelihood fit to the OD-tagged data that passed the other selection cuts. The result was consistent with no neutron single scatters, and the constraint function was constructed from the likelihood of the fit and the OD neutron tagging efficiency of $88.5 \pm 0.7\%$.

3.4 Statistical inference

The data, consisting of 335 candidate events, were fit to the background model in Figure 3.4 using the maximum likelihood method. The extended[1], unbinned likelihood function was

[1] An extended likelihood accounts for Poisson fluctuations in the number of events in the dataset, as in the first term in Equation 3.1.

Table 3.1: The pre- and post-fit event model used to analyze the SR1 dataset. The expected counts for each background component were determined using data outside of the WIMP search ROI. Non-Gaussian constraints were used for ^{37}Ar and detector neutrons, so they were excluded from the subtotal.

Source	Expected Events	Fit Result
β decays + Det. ER	215 ± 36	222 ± 16
ν ER	27.1 ± 1.6	27.2 ± 1.6
^{127}Xe	9.2 ± 0.8	9.3 ± 0.8
^{124}Xe	5.0 ± 1.4	5.2 ± 1.4
^{136}Xe	15.1 ± 2.4	15.2 ± 2.4
^{8}B CEνNS	0.14 ± 0.01	0.14 ± 0.01
Accidentals	1.2 ± 0.3	1.2 ± 0.3
Subtotal	273 ± 36	280 ± 16
^{37}Ar	[0, 288]	$52.5^{+9.6}_{-8.9}$
Detector neutrons	$0.0^{+0.2}$	$0.0^{+0.2}$
30 GeV/c^2 WIMP	–	$0.0^{+0.6}$
Total	–	333 ± 17

defined as

$$\begin{aligned}\mathcal{L}(\mu_s, \boldsymbol{\theta}) = \text{Poiss}(N_0|\mu_{\text{tot}}) \\ \times \frac{1}{\mu_{\text{tot}}} \prod_{i=1}^{N_0} \left(\mu_s f_s(\text{S1}c_i, \log_{10} \text{S2}c_i) + \sum_{b=1}^{9} \mu_b f_b(\text{S1}c_i, \log_{10} \text{S2}c_i) \right) \\ \times \prod_{b=1}^{9} g_b(\mu_b|\nu_b),\end{aligned} \tag{3.1}$$

where the inputs consist of the expectation value of the number of signal events, μ_s, and a vector of the expectation value of the number of counts associated with each component of the background model, $\boldsymbol{\theta} = \{\mu_{b=1},\ ...,\ \mu_{b=9}\}$. The observed dataset consisted of $N_0 = 335$ events and $\mu_{\text{tot}} = \mu_s + \sum_{b=1}^{9} \mu_b$ is the total number of signal and background events expected according to the model. The signal and background PDFs, f_s and f_b respectively, were defined in the signal space $\{\text{S1}c, \log_{10} \text{S2}c\}$. Constraint functions $g_b(\mu_b|\nu_b)$ were defined for each background component according to the constraints ν_b, listed in Table 3.1. The likelihood is maximized for the estimators $\hat{\mu}_s$ and $\hat{\boldsymbol{\theta}}$. These maximum likelihood estimators and associated errors for a 30 GeV/c^2 WIMP model are shown in the "Fit Result" column of Table 3.1. Many of the post-fit values do not deviate much from the input model because

the external meaurements represent stronger constraints than those that can be derived from the SR1 dataset. A visualization of the correlation matrix for this fit is shown in Figure 3.5. The best fit signal value was 0 for all tested signal masses between 9 GeV/c^2 and 10 TeV/c^2.

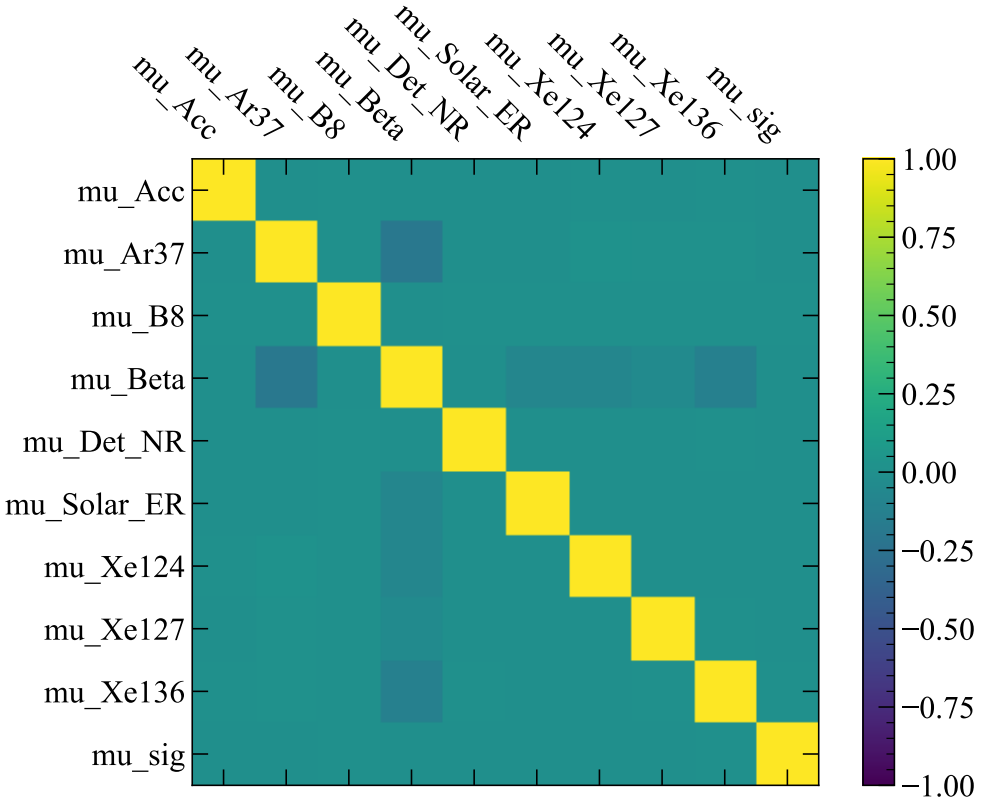

Figure 3.5: A visualization of the correlation matrix for the best signal plus background model fit to SR1 data for a 30 GeV/c^2 WIMP.

Limits on the number of dark matter events in the SR1 exposure, and therefore the dark matter interaction cross section, were calculated using the profile likelihood ratio (PLR) method. This analysis approach has become fairly widespread in the dark matter direct detection field, and a set of recommendations for how to construct the analysis in a standardized way is offered in [88]. We provide a summary of the method here, but there are many more details available in [11, 88, 97, 98] and elsewhere. The PLR is defined as

$$\lambda(\mu_s) \equiv \frac{\mathcal{L}(\mu_s, \hat{\hat{\boldsymbol{\theta}}})}{\mathcal{L}(\hat{\mu}_s, \hat{\boldsymbol{\theta}})}, \tag{3.2}$$

where $\hat{\hat{\boldsymbol{\theta}}}$ maximizes the likelihood for a set value of μ_s. Since $\mathcal{L}(\hat{\mu}_s, \hat{\boldsymbol{\theta}})$ is by definition the maximum value of the likelihood for the dataset, $\lambda(\mu_s)$ takes on values between 0 and 1,

where 1 signifies good agreement between the data and the value μ_s. The test statistic

$$t_\mu \equiv -2 \log \lambda(\mu_s) \tag{3.3}$$

is a simple conversion of the PLR where smaller values indicate good agreement between the data and μ_s, although [88] recommends the modified

$$\tilde{t}_\mu = \begin{cases} -2 \log \frac{\mathcal{L}(\mu_s, \hat{\hat{\boldsymbol{\theta}}})}{\mathcal{L}(\hat{\mu}_s, \hat{\boldsymbol{\theta}})} & \hat{\mu}_s \geq 0, \\ -2 \log \frac{\mathcal{L}(\mu_s, \hat{\hat{\boldsymbol{\theta}}})}{\mathcal{L}(0, \hat{\boldsymbol{\theta}}(0))} & \hat{\mu}_s < 0, \end{cases} \tag{3.4}$$

since the dark matter signal cannot be negative.

In the construction of setting limits on dark matter in the dataset, our null hypothesis H_0 is the combined signal and background model for a given signal count parameter μ_s. The p-value associated with this hypothesis is the probability that the test statistic value computed from a dataset produced by the model is greater than or equal to the one from the observed data:

$$p = P(\tilde{t}_\mu \geq \tilde{t}_{\mu,\text{obs}} | \mu_s) = \int_{\tilde{t}_{\mu,\text{obs}}}^{\infty} f(\tilde{t}_\mu | \mu_s) \mathrm{d}\tilde{t}_\mu. \tag{3.5}$$

The distribution of test statistic values for the model, $f(\tilde{t}_\mu|\mu)_s$, is estimated by generating toy datasets from the signal and background model and fitting the likelihood from Equation 3.1 to each toy. The distributions $f(\tilde{t}_\mu|\mu_s)$ for a few different values of μ_s are shown in Figure 3.6.

What remains is to compute an upper limit on the number of dark matter events in the observed data at a confidence level (CL) of 90%. The CL is defined as $1 - \alpha$, where $\alpha = 0.1$ is the critical p-value for H_0, yielding an upper limit on the signal parameter μ_s. This procedure is shown graphically in Figure 3.7, where the upper limit is set at the value of μ_s where it intersects the critical p-value of 0.1. The expected sensitivity of this procedure for a background only dataset can also be computed via the H_1 distribution, where we typically report the median as well as the 1- and 2-σ expected sensitivities via a dashed black line, and green and yellow bands, respectively. The corresponding values are highlighted by the blue points in this figure.

The upper limit on μ_s is computed for a range of WIMP masses to compute an upper limit curve. It can be converted to the upper limit on the WIMP-nucleon cross section via the 60 d $\times$ 5.5 t exposure, which is plotted in Figure 3.8. The limit was power constrained between the masses 19 GeV/c^2 and 26 GeV/c^2 by setting the reported limit to the critical discovery power threshold $\pi_{\text{crit}} = 0.32$ [99]. This constraint limits the claimed sensitivity due to a downward fluctuation in background events below the ER median for S1c between 3 and 10 phd, in accordance with the recommendation in [88]. LZ claims the world leading limit on spin independent WIMP-nucleon scattering cross-sections between 9 GeV/c^2 and 10 TeV/c^2.

There is also the possibility that WIMP-nucleon interactions are spin dependent. The cases considered in the dark matter direct detection community for limit setting are typically that a spin dependent interaction couples exclusively to neutrons or protons. The signal

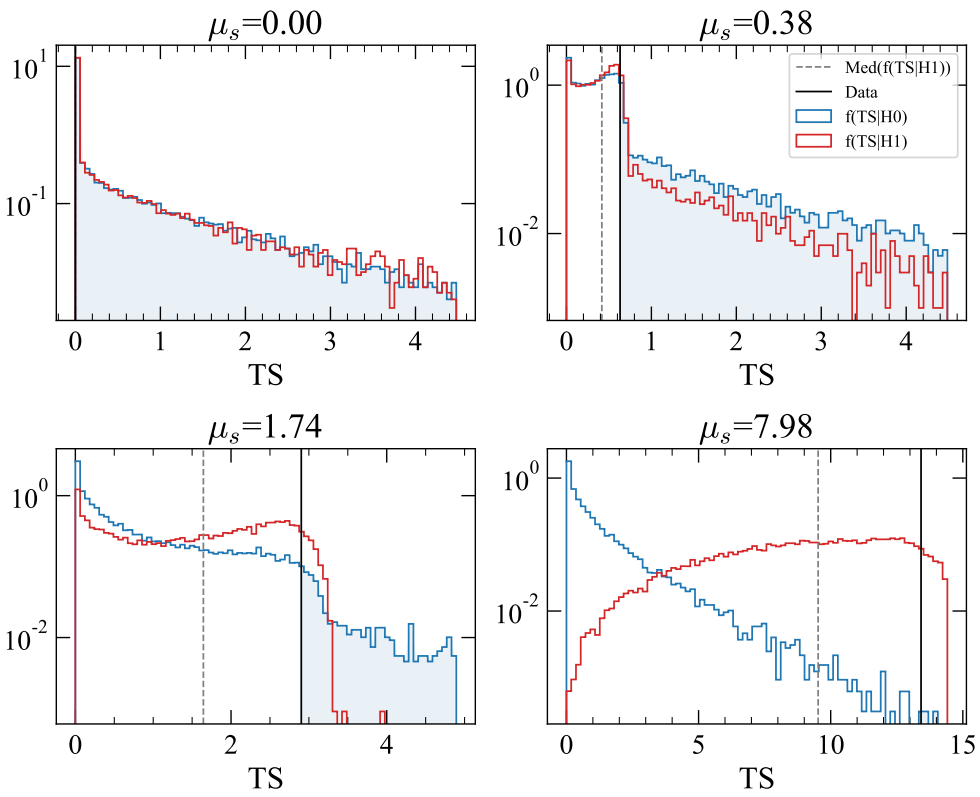

Figure 3.6: The test statistic distributions for selected values of the model parameter μ_s for a 30 GeV/c^2 WIMP. The null hypothesis H_0 distribution in blue is for the combined signal and background model. The alternative hypothesis H_1 distribution in red is the for the background only model. The value computed for the data is the vertical black line and the median of the H_1 distribution is the dashed grey line.

models for these interactions were calculated according to the structure factors from [31–33], where theoretical uncertainty bands were constructed for the signal models according to the minimum and maximum signal rate as a function of recoil energy for the three sources of spin-dependent interaction models. The associated uncertainty applies similarly to all xenon-based limits. The nominal signal model was calculated according to the mean structure function from [32], the direct continuation of previous methods [30] used to set xenon spin-dependent limits [101, 102]. The WIMP-neutron interaction arises from the unpaired neutrons in ^{129}Xe and ^{131}Xe, together accounting for about half of the natural abundance of xenon [95]. The spin-dependent WIMP-neutron cross section upper limit curve is shown in Figure 3.9, with a power constraint applied between 19 GeV/c^2 and 23 GeV/c^2. As in the spin-independent case, LZ claims the world-leading limits in this parameter space for the full range of tested WIMP masses between 9 GeV/c^2 and 10 TeV/c^2.

Xenon is also sensitive to WIMP-proton interactions, via the mixing of proton and neu-

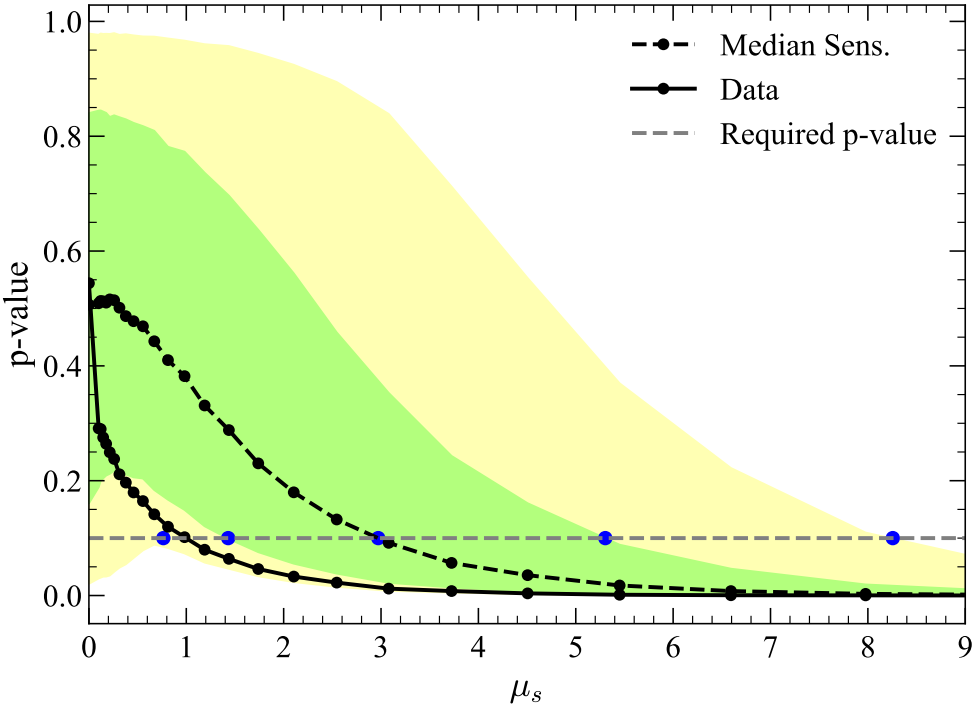

Figure 3.7: The calculated p-value as a function of the model parameter μ_s for a 30 GeV/c^2 WIMP. The dashed line is the median p-value from background only toys, and the green and yellow bands are 1- and 2-σ p-values from background only toys. The critical p-value is 0.1, indicated by the grey dashed lane, producing 90% confidence upper limits. The expected sensitivity intersection points are highlighted with blue points.

tron spin states in the unpaired neutron in ^{129}Xe and ^{131}Xe. The uncertainties associated with the form factor in this case are relatively larger than the neutron case. We show the limit on WIMP-proton interactions in Figure 3.10, where masses between 17 GeV/c^2 and 26 GeV/c^2 have been power constrained. In the parameter space of Figure 3.10, world-leading limits for most WIMP masses were set by the PICO-60 experiment, a bubble chamber with a 52 kg target of superheated C_3F_8 [104]. Nuclear recoils in the superheated target volume nucleate bubbles, which are imaged for three dimensional position reconstruction. Meanwhile, the efficiency of bubble nucleation due to electronic recoils is suppressed by a factor of approximately 3×10^{-9}, offering natural background discrimination. The sensitivity of PICO-60 to WIMP-proton recoils arises from the unpaired proton of ^{19}F, for which the calculation of the scattering rates has minimal uncertainty.

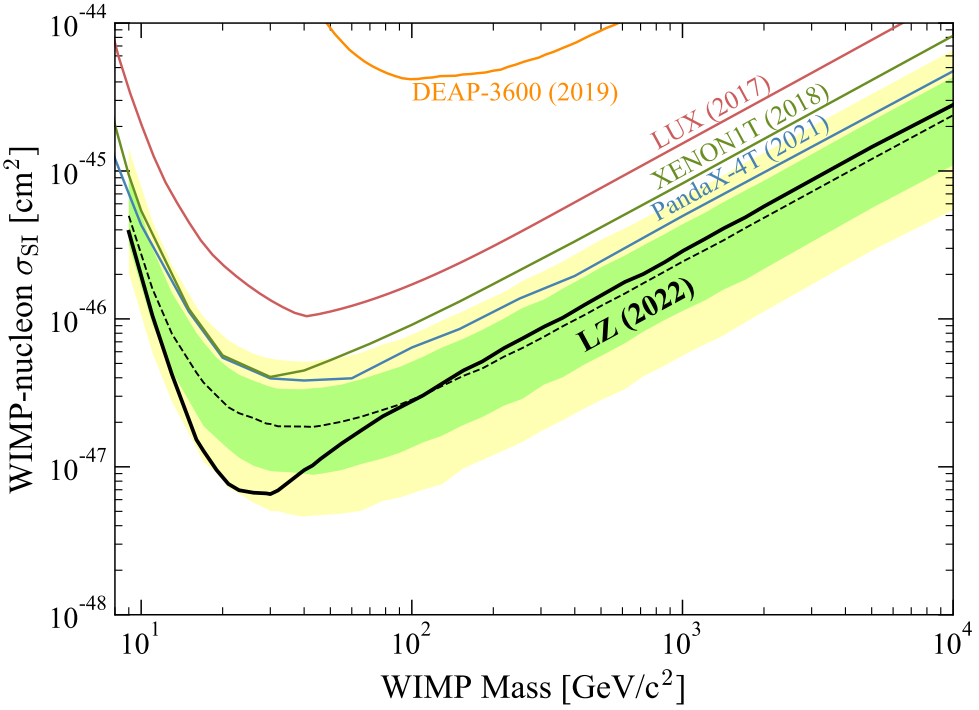

Figure 3.8: The black curve shows the 90% confidence limit for the spin-independent WIMP cross section. The expected median (dashed black), 1-σ (green band), and 2-σ (yellow band) sensitivities are also plotted, as well as limits from DEAP-3600 [45], LUX [100], XENON1T [42], and PandaX-4T [41]. Plot made by dissertation author and S. Haselschwardt.

3.5 Goodness-of-fit

The limits produced using the PLR method depend heavily on the accuracy of the underlying models and input parameters, both in the maximum likelihood fitting step and for generating the test statistic distributions used to calculate p-values. One method of testing how robust the limit results are to these model definitions is to vary them in some way and compare the results to the main limits presented here. A few such checks were performed, such as adopting the error band boundaries of the efficiency from Figure 3.2, using a three times higher rate of ^{37}Ar events in the background model, and removing the detector NR and accidentals backgrounds from the model definition. None of these changes had an effect on the resulting upper limit curve greater than 10% of the values shown here, indicating robustness to these kinds of modeling decisions.

Statistical tests for goodness-of-fit are challenging in two or more dimensions and for unbinned data-model comparisons [105]. Particularly, the maximum likelihood test statistic, $\mathcal{L}(\hat{\mu}_s, \hat{\boldsymbol{\theta}})$, is not suitable for goodness-of-fit testing for several reasons which can be illuminated under relatively simple example conditions [106]. For testing the goodness-of-fit of the SR1

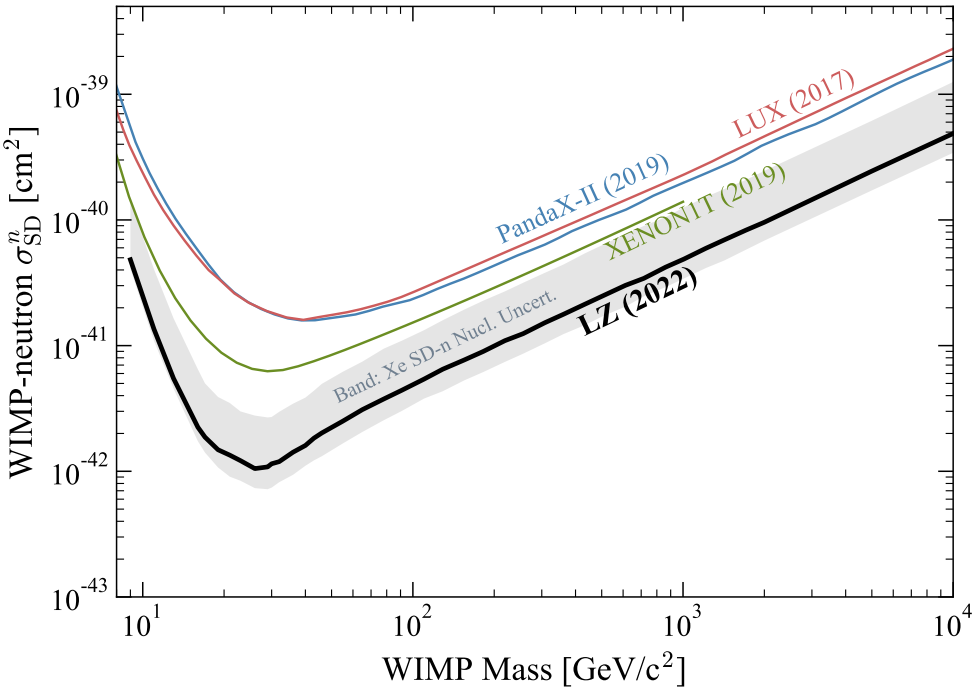

Figure 3.9: The black curve shows the 90% confidence limit for the spin-dependent WIMP-neutron cross section using the mean value of the nuclear structure factors from [32]. The range of the structure factors from [31–33] was propagated to the limit curve and shown in the grey band. Limits from LUX [101], PandaX-II [103], and XENON1T [102], to all of which the signal model uncertainty also applies, are also plotted. Plot made by dissertation author, S. Haselschwardt, and A. Manalaysay.

data to the models used in the PLR analysis, a one dimensional, binned χ^2 test in two different projected variable spaces was performed.

For each event and background component, the reconstructed energy was computed according Equation 2.5. Figure 3.11 shows the data and model comparison, where error bands show the systematic and statistical uncertainties associated with the model. Systematic uncertainties were calculated from the covariance matrix of the best fit model. Statistical uncertainties were added to each bin as the interval covering at least 68% of a Poission distribution with input parameters weighted according to the best fit model systematic errors. The combined errors were dominated by statistical errors for all bins. The model plotted here corresponds to the "Fit Result" column of Table 3.1.

Compatibility of the best fit background model to the data in the ROI was probed using a χ^2 test in reconstructed energy. The Poisson-likelihood χ^2 test statistic

$$\chi^2_\lambda = 2\sum_i y_i - n_i + n_i \ln\left(n_i/y_i\right), \tag{3.6}$$

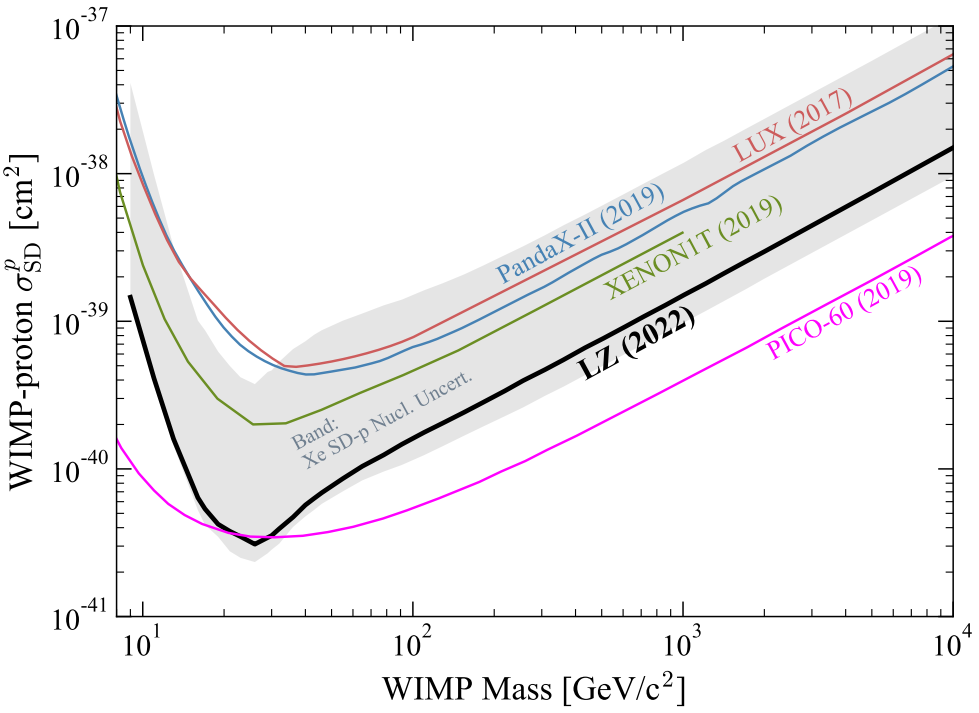

Figure 3.10: The black curve shows the 90% confidence limit for the spin-dependent WIMP-proton cross section using the mean value of the nuclear structure factors from [32]. The range of the structure factors from [31–33] was propagated to the limit curve and shown in the grey band. Also shown are limits from LUX [101], PandaX-II [103], and XENON1T [102], to all of which a similar structure factor uncertainty applies. The limit from PICO-60 [104] has minimal uncertainty due to nuclear structure. Plot made by dissertation author, S. Haselschwardt, and A. Manalaysay.

where n_i is the number of observed data points in the ith bin and y_i is the model prediction for the number of events in that bin, is a χ^2-distributed quantity that accounts for Poisson fluctuations in bin counts, rather than relying on assumptions of Gaussianity [107]. A distribution of χ^2_λ was computed using toy datasets sampled from the best fit model to estimate the p-value associated with the χ^2_λ computed for the SR1 dataset. The p-value was computed by directly counting the number of toys with χ^2_λ values greater than the SR1 dataset, yielding $p = 0.96$. It was confirmed that the toy dataset χ^2_λ values followed a χ^2 distribution, implying the calculation according to the functional form of the distribution would yield the same p-value results.

A similar procedure was repeated for a variable representing the distance of events from the electron recoil band median. The quantity $(\log_{10}(\mathrm{S2}c)$ - $\mu_{\mathrm{ER}})/\sigma_{\mathrm{ER}}$, where μ_{ER} is the median of the electron recoil band shown in Figure 2.8 and σ_{ER} is the Gaussian width of the ER band as a function of S1c, was computed for events and background components.

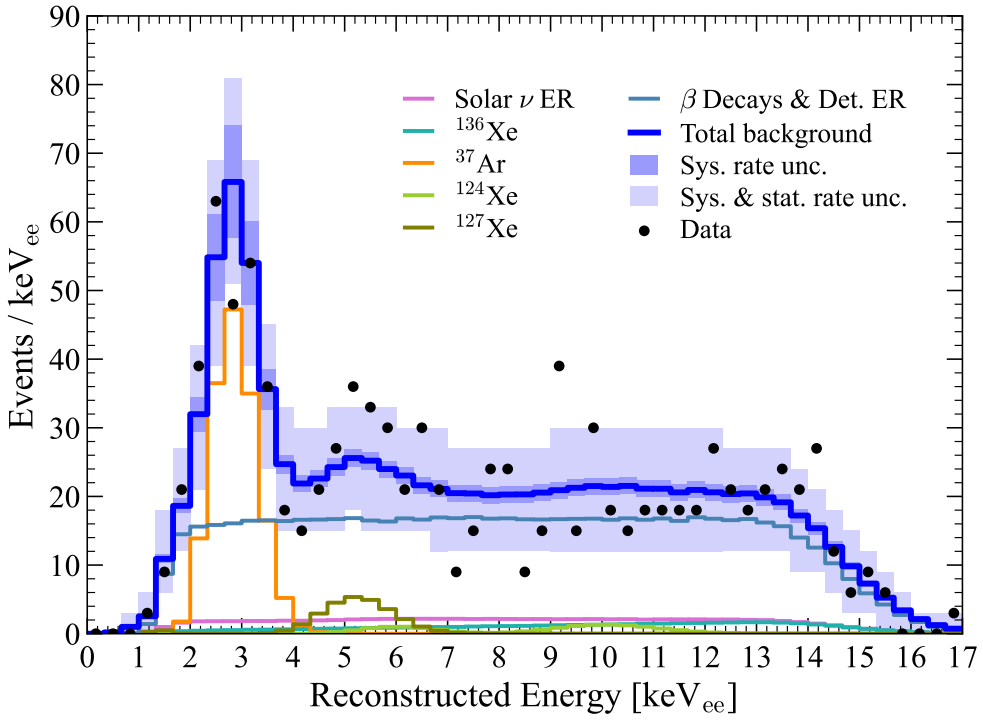

Figure 3.11: The reconstructed energy spectrum of the SR1 dataset (black) and best fit model (blue). The darker blue band corresponds to the model uncertainties, while the light blue band includes statistical uncertainties as well. ^{8}B neutrinos and accidentals were included in the background model but omitted from this plot.

The results are shown in Figure 3.12. The χ^2_λ p-value procedure was repeated for this projection and we found $p = 0.33$. The combined p-value results in this projection and the reconstructed energy provide no evidence for inconsistencies between the background model and the observed dataset.

3.6 Summary

The results in this chapter represent the first WIMP search using the LZ detector, yielding world-leading sensitivity to spin-independent WIMP-nucleon and spin-dependent WIMP-neutron interactions. The LZ detector will continue operations to expand the search for WIMP dark matter into an expected 1000 day exposure. Future analyses will also consider other kinds of dark matter and rare event searches [108, 109]. In the next chapter we describe an extension of the search for WIMP dark matter to lower masses than presented here using the SR1 dataset.

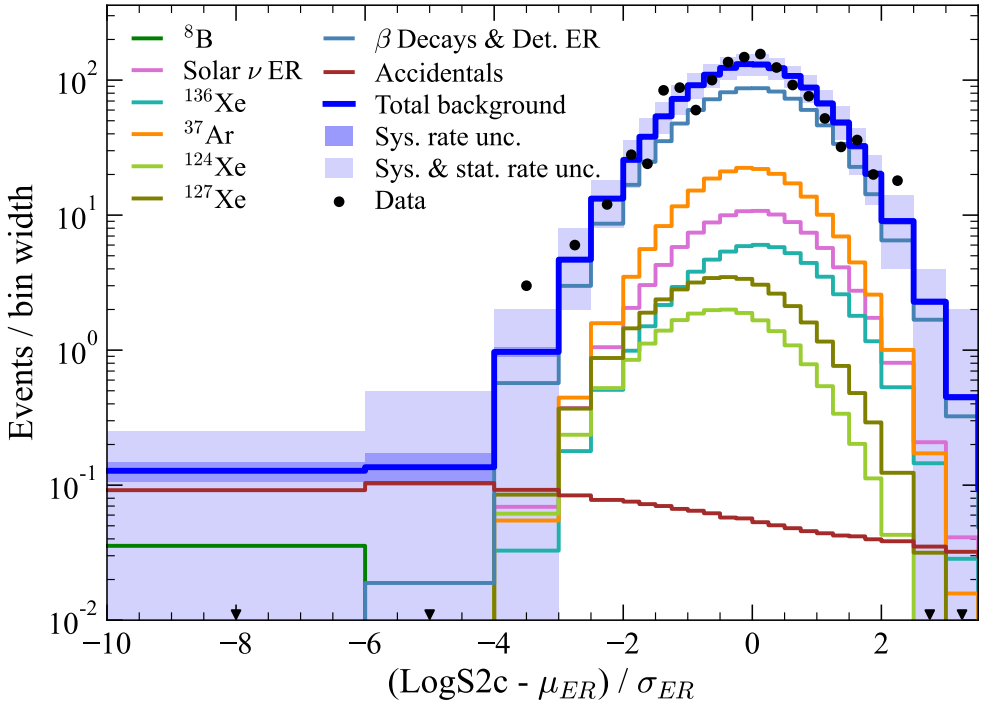

Figure 3.12: The SR1 dataset (black) and best fit model (blue) projected into $\log_{10}(\mathrm{S2}c)$, corrected for the distance from the median of the ER band as a function of S1c.

Chapter 4

A Sub-GeV Dark Matter Search in LZ via the Migdal Effect

The standard style of nuclear recoil WIMP search from Chapter 3 is just one of many analysis strategies employed by contemporary dark matter experiments. Another typical analysis that has emerged in recent years is the search of WIMP-induced electron recoil events via the Migdal effect [43, 47, 48, 72, 110]. This process describes the additional ionization of an electron in the process of an otherwise typical nuclear recoil. Distinct from the ionization electrons formed during the track formation of the recoiling xenon atom, the Migdal electron is ejected due to a nonzero probability of a transition to the ionized atomic state during the initial dark matter scattering process [111]. While this effect is rare compared to regular nuclear recoils, it is possible to generate keV-scale recoil electrons even for very low energy nuclear recoils, offering a mechanism to extend sensitivity to light dark matter which would otherwise produce only sub-threshold energy deposits in a detector target.

Direct observation of the Migdal effect is still unclaimed; several methods have been proposed [112–114]. The experimental excitement surrounding this dark matter search method, kicked off by the calculation of a signal model in [111], has also invited plenty of theoretical scrutiny and new developments for different kinds of targets [115–119]. However, in the absence of a direct observation, the precise rates and the detector response associated with this signal channel retain some uncertainty.

In this chapter we present a search for WIMP-induced Migdal events in the SR1 dataset, leveraging the same event selection and detector response work developed for the main SR1 WIMP search in Chapter 3. In addition, we present an idea of how theoretical developments of the Migdal effect in dielectric materials could be applied to verify the rates down to the lowest recoil energies in liquid xenon. The analysis and discussion in this chapter is primarily the work of the dissertation author.

4.1 The signal model

Previous Migdal limits on nuclear recoil dark matter scattering in xenon [43, 72, 110] used the signal model calculations presented in [111]. The differential recoil spectrum is shown to be

$$\frac{\mathrm{d}R}{\mathrm{d}E_R \mathrm{d}E_e \mathrm{d}v_{DM}} \simeq \frac{\mathrm{d}R_0}{\mathrm{d}E_R \mathrm{d}v_{DM}} \times \frac{1}{2\pi} \sum_{n,l} \frac{\mathrm{d}}{\mathrm{d}E_e} p^c_{q_e}(nl \to E_e), \tag{4.1}$$

where the first term in the product is the dark matter nuclear recoil spectrum (see Section 1.3). The second term contains the ionization probabilities for the different electron orbitals, $p^c_{q_e}(nl \to E_e)$, and encodes the spectrum of ejected electron energies E_e. These ionization probabilities were computed in [111] for an isolated xenon atom, where it is noted that the outer $n = 5$ shell may be affected by neighboring atoms in a liquid xenon detector. The terms associated with the different values of n are independent from another in Equation 4.1, so previous analysis do not include $n = 5$ as a conservative treatment of the signal. They also exclude $n = 1$ and $n = 2$ because the tight binding of these orbitals leads to a negligible contribution to the total spectrum.

Equation 4.1 is subject to kinematic constraints relating the atomic recoil energy E_R to the energy imparted onto the electron $E_e + E_{nl}$, where E_e is the energy of the ionized electron and E_{nl} is its binding energy. This relationship leads to the modified minimum dark matter velocity contributing to the total recoil rate as

$$v_{DM,\mathrm{min}} \simeq \frac{m_N E_R + \mu_N (E_e + E_{nl})}{\mu_N \sqrt{2 m_N E_R}}. \tag{4.2}$$

The maximum energy imparted into the electron ionization process is given by

$$(E_e + E_{nl})_{\mathrm{max}} = \frac{1}{2} \mu_N v^2_{DM} = \frac{m_N}{\mu_N} E_R. \tag{4.3}$$

This relation highlights the utility of the Migdal search strategy; the maximum energy of the electronic excitation extends past the endpoint of the elastic nuclear spectrum for a given dark matter velocity. Finally, we define the total electronic recoil energy

$$E_{EM} = E_e + E_{\mathrm{casc.}} \tag{4.4}$$

where $E_{\mathrm{casc.}}$ is additional ER energy from the cascade of de-excitation processes after inner-shell electrons are ionized. We treat E_{EM} as the single-site observable electron recoil energy.

In the absence of a direct observation of the Migdal effect, the signal response in the detector is not known. Following previous analyses [43, 110], we consider only the electron recoil component to construct the signal model, another conservative treatment which minimizes any additional discrimination power from the nuclear recoil component. The observable Migdal recoil spectrum in a liquid xenon detector is

$$\frac{\mathrm{d}R}{\mathrm{d}E_{\mathrm{det}} \mathrm{d}v_{DM}} \simeq \int \mathrm{d}E_R \mathrm{d}E_{EM} \delta(E_{\mathrm{det}} - q_{\mathrm{nr}} E_R - E_{EM}) \frac{\mathrm{d}R}{\mathrm{d}E_R \mathrm{d}E_{EM} \mathrm{d}v_{DM}}, \tag{4.5}$$

where E_{det} is the observed signal, $q_{\text{nr}} = 0.15$ is the nuclear recoil quenching factor, and we have made a small change of variables from E_e to E_{EM} for the rate in Equation 4.1. The signal model calculated for $n = 3\&4$ is shown in blue in Figure 4.1 for various WIMP masses, where the dark matter velocity profile parameters match the recommendations in [88]. The elastic recoil spectrum is also shown, demonstrating the shift to higher recoil energies enabled by the Migdal signal. Alternative calculations for free xenon atoms typically show good agreement with this signal model, particularly for the $n = 3$ and $n = 4$ states of interest [116, 119].

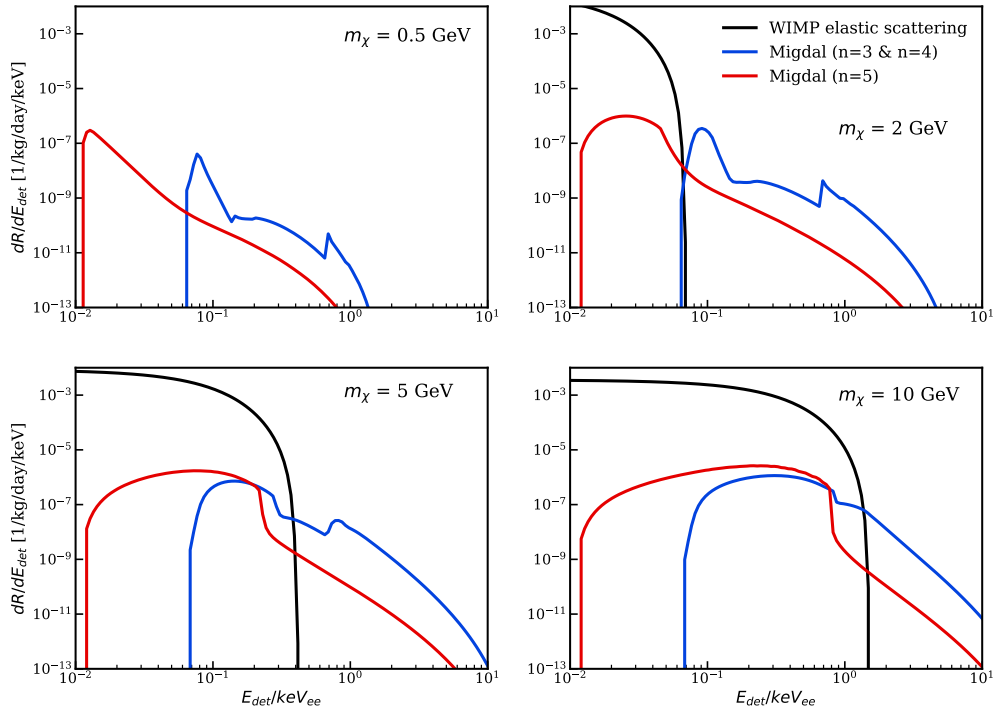

Figure 4.1: The signal spectra of dark matter-induced Migdal events used in the analysis in this chapter for several masses of dark matter. The elastic nuclear recoil spectrum is shown in black. The signal model using only the $n = 3$ & 4 shells is shown in blue and was used to set the limits presented here. The signal model from the outer $n = 5$ shell is in red.

The detector response model developed for the main SR1 WIMP search from Chapter 3 was applied to the signal models calculated from Equation 4.5. WIMP masses ranging from 0.3 GeV/c^2 to 9 GeV/c^2 were considered, where the upper bound was set by the lower bound of the main WIMP search. Two example signal models in the SR1 ROI are shown in Figure 4.1.

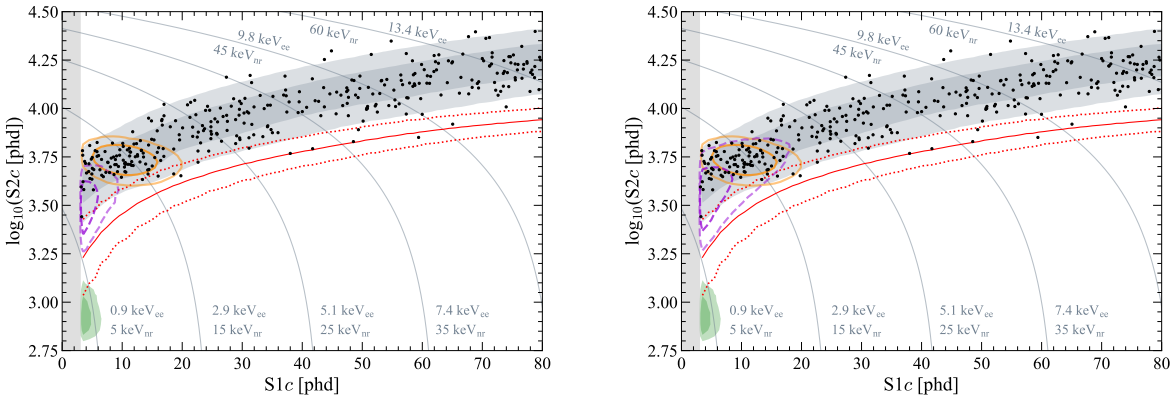

Figure 4.2: The SR1 dataset and models used for the WIMP search via Migdal effect signals. 68% and 95% contours of the background model are shown in grey. The green contour is the expected B8 neutrino coherent scattering region. ^{37}Ar events are are expected inside of the orange curves. The dashed purple lines correspond to the expected Migdal signal from a 1 GeV/c^2 WIMP (left) and a 5 GeV/c^2 WIMP (right). The solid and dashed red lines are the same nuclear recoil band from Figure 2.8. Also shown in grey is the minimum 3 phd cut applied to the data and models.

4.2 Incorporating time into the likelihood

Electronic recoil events from ^{37}Ar contamination in the liquid xenon were an expected background component in the SR1 data, but uncertainties on the expected rate were fairly large [90]. One possible method of constraining the ^{37}Ar background in this data is to incorporate its known half-life of 35 days. Adding a time variable to the SR1 likelihood was investigated in WIMP sensitivity studies before analysis of the SR1 data [120]. WIMP sensitivity was found to be robust to ^{37}Ar backgrounds for a wide range of possible activities due to discrimination between ER and NR signals, so ultimately the SR1 likelihood took the form of Equation 3.1.

ER signal searches are more likely to be limited by the ^{37}Ar background due to the lack of discrimination, particularly for monoenergetic signals near the 2.82 keV electron capture signal. Since both signal and ^{37}Ar are unconstrained in rate, the addition of the exponential time dependence of ^{37}Ar decays is critical in recovering some sensitivity to new physics signals which are expected to have a uniform time distribution. This argument is only weakly applicable to the Migdal signals in this chapter, which partially overlap the ^{37}Ar region as shown in Figure 4.2. Still, this analysis took advantage of the time-dependent PLR framework that was developed for a broader suite of ER signal searches. The formalism for these studies follows the aforementioned SR1 sensitivity studies [120].

We define the likelihood as

$$\begin{aligned}\mathcal{L}(\mu_s, \boldsymbol{\theta}) = \text{Poiss}(N_0|\mu_{\text{tot}}) \\ \times \frac{1}{\mu_{\text{tot}}} \prod_{i=1}^{N_0} \left(\mu_s f_s(\text{S1}c_i, \log_{10} \text{S2}c_i, t_i) + \sum_{b=1}^{9} \mu_b f_b(\text{S1}c_i, \log_{10} \text{S2}c_i, t_i) \right) \\ \times \prod_{b=1}^{9} g_b(\mu_b|\nu_b),\end{aligned} \tag{4.6}$$

where now the signal and background PDFs are the product of a time-dependent component $a(t)$ and the original signal-space PDFs $b(\text{S1}c, \log_{10} \text{S2}c)$:

$$f(\text{S1}c, \log_{10} \text{S2}c, t) = a(t) \times b(\text{S1}c, \log_{10} \text{S2}c). \tag{4.7}$$

The PDF $a(t)$, in turn, is a product of two separate sources of time dependence

$$a(t) = T_{\text{live}}(t) \times r(t), \tag{4.8}$$

where $T_{\text{live}}(t)$ is a histogram that encodes the detector live fraction over short time intervals and $r(t)$ encodes the time dependence of the rate of a background or signal component. $T_{\text{live}}(t)$ is the derivative of the orange dashed line in Figure 3.1. The function $r(t)$ is a constant for all of the model components except the two backgrounds with known exponential decay behavior, namely ^{37}Ar and ^{127}Xe. For these components,

$$r(t) = r_0 e^{-t/\tau} \tag{4.9}$$

where $\tau = 50.6$ days for ^{37}Ar and 52.4 days for ^{127}Xe and r_0 represents the activity of the background at the start of SR1.

Using this definition of the likelihood was tested on the SR1 WIMP search and yielded limit curves about 5% stronger than the ones reported in Chapter 3, consistent with sensitivity studies [120]. Additionally, bounds can be placed on the major β decay activities over the course of SR1 by measuring the activity in peaks outside of the ROI. These were observed to be mostly uniform, and using a data-driven $r(t)$ derived from these measurements did not yield significant modification to any WIMP limits.

The pre- and post-fit values of the SR1 data using the likelihood from Equation 4.6 to a 5 GeV/c^2 WIMP Migdal model are reported in Table 4.1. As in the SR1 WIMP search, the input constraints are generally stronger than those that can be derived from the dataset. The post-fit values and errors are largely unchanged for most components, indicating their time distribution is consistent with the uniform model implicitly applied in Chapter 3. The best fit value for ^{37}Ar is slightly different, but it remains well within the errors reported for the fit without time. The best fit number of WIMP Migdal signal counts was 0 for all tested masses between 0.3 and 9 GeV/c^2.

Table 4.1: The pre- and post-fit event counts and errors for a 5 GeV/c^2 WIMP Migdal model fit with the likelihood given by Equation 4.6. Input constraints were identical to the SR1 WIMP search model from Chapter 3. Post-fit values are nearly identical, with the exception of a slightly different best fit value of ^{37}Ar counts.

Source	Expected Events	Fit Result
β decays + Det. ER	215 ± 36	221 ± 16
ν ER	27.1 ± 1.6	27.2 ± 1.6
^{127}Xe	9.2 ± 0.8	9.3 ± 0.8
^{124}Xe	5.0 ± 1.4	5.2 ± 1.4
^{136}Xe	15.1 ± 2.4	15.2 ± 2.4
^{8}B CEνNS	0.14 ± 0.01	0.14 ± 0.01
Accidentals	1.2 ± 0.3	1.2 ± 0.3
^{37}Ar	[0, 288]	$53.8^{+9.4}_{-8.7}$
Detector neutrons	$0.0^{+0.2}$	$0.0^{+0.2}$
5 GeV/c^2 WIMP Migdal	–	$0.0^{+2.6}$
Total	–	$333^{+19.2}_{-18.3}$

4.3 Dark matter limits

Limits were placed on the spin-independent WIMP-nucleon cross section with the same PLR framework described in Section 3.4. These are shown in Figure 4.3, alongside a crowded field of limits from different experiments and search strategies. The limit from the SR1 dataset does not exclude any significant unprobed parameter space, but future analyses with a larger exposures have the potential to do so.

The dark matter recoil spectrum in Equation 4.1 does not have to correspond strictly to the spin-independent case; signal models for spin-dependent WIMP-neutron and WIMP-proton interactions were also computed and used to set limits. The spin-dependent WIMP-neutron cross section limit, shown in Figure 4.4 is world-leading between about 1 GeV/c^2 and 6 GeV/c^2. The spin-dependent WIMP-proton section is shown in Figure 3.10. The nuclear form factor uncertainties shown in Figure 3.9 and Figure 3.10 apply to these spin-dependent limits as well.

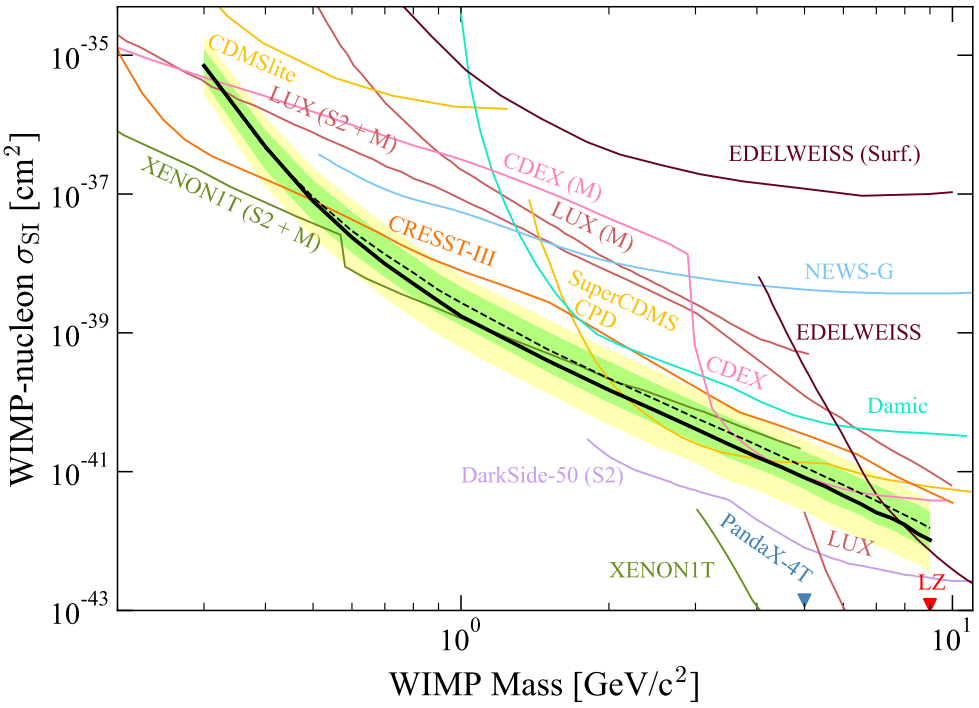

Figure 4.3: The black curve shows the 90% confidence limit for the spin-independent WIMP cross section probed via the Migdal effect. The expected median (dashed black), 1-σ (green band), and 2-σ (yellow band) sensitivities are also plotted, as well as limits from LUX ([100], Migdal [110], S2 only and Migdal [72]), XENON1T ([44], S2 only and Migdal [43]), DarkSide-50 [46], EDELWEISS ([121], surface run [47]), SuperCDMS CPD [38], Damic [39], NEWS-G [50], CRESST-III [37], CDMSLite [122], and CDEX [49]. Limits from PandaX-4T [41] and LZ (Chapter 3) are below the bottom boundary of the plot; the lowest mass at which they report limits is shown with a triangle for each.

4.4 Calculating event rates via the energy loss function

Since first Migdal signal model was presented for dark matter direct detection, it has been pointed out that neighboring atoms may have an influence on electron orbitals not accounted for in the free atom approximation used in the calculation [111]. This concern has been particularly examined for semiconductor materials, where electron behavior is strongly modified by in-medium effects [115, 117, 118, 125, 126].

In this section we leverage the DarkELF code for calculating dark matter Migdal scattering rates by treating xenon as a dielectric material [126]. DarkELF is formulated to treat isotropic materials under conditions relevant to dark matter-induced Migdal scatter-

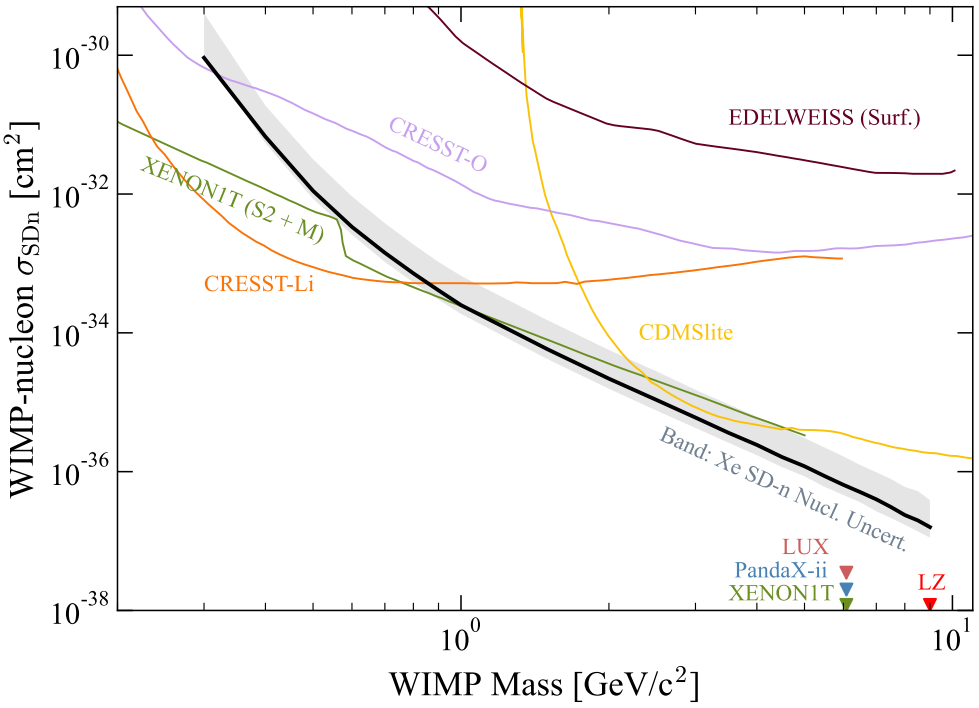

Figure 4.4: The black curve shows the 90% confidence limit for the spin-dependent WIMP-neutron cross section using the mean value of the nuclear structure factors from [32]. The range of the structure factors from [31–33] was propagated to the Migdal signal spectrum and the associated limit curves, shown in the grey band. Also shown are limits from EDELWEISS [47], CRESST (O [37], Li[123]), CDMSlite [122], XENON1T (S2-only with Migdal signal [43]). Limits from LUX [101], PandaX-II [103], XENON1T [102], and LZ (Chapter 3) are below the bottom boundary of the plot; the lowest mass at which they report limits is shown with a triangle for each.

ing. The form of the differential rate expression is similar in structure to Equation 4.1, with a quasielastic cross section term for dark matter nuclear recoils in a solid state target and an electron shaking probability term given by

$$\frac{\mathrm{d}P}{\mathrm{d}\omega} = \frac{4\alpha E_N}{3\pi^2\omega^4 m_N}\int \mathrm{d}k Z^2_{\mathrm{ion}}(k)k^2 \mathrm{Im}\left(\frac{-1}{\epsilon(\omega,\mathbf{k})}\right), \tag{4.10}$$

where $Z_{\mathrm{ion}}(k)$ is the effective charge of the nucleus and bound core electrons as a function of the electron momentum transfer and

$$\mathrm{Im}\left[\frac{-1}{\epsilon(\omega,\mathbf{k})}\right] \tag{4.11}$$

is the energy loss function (ELF).

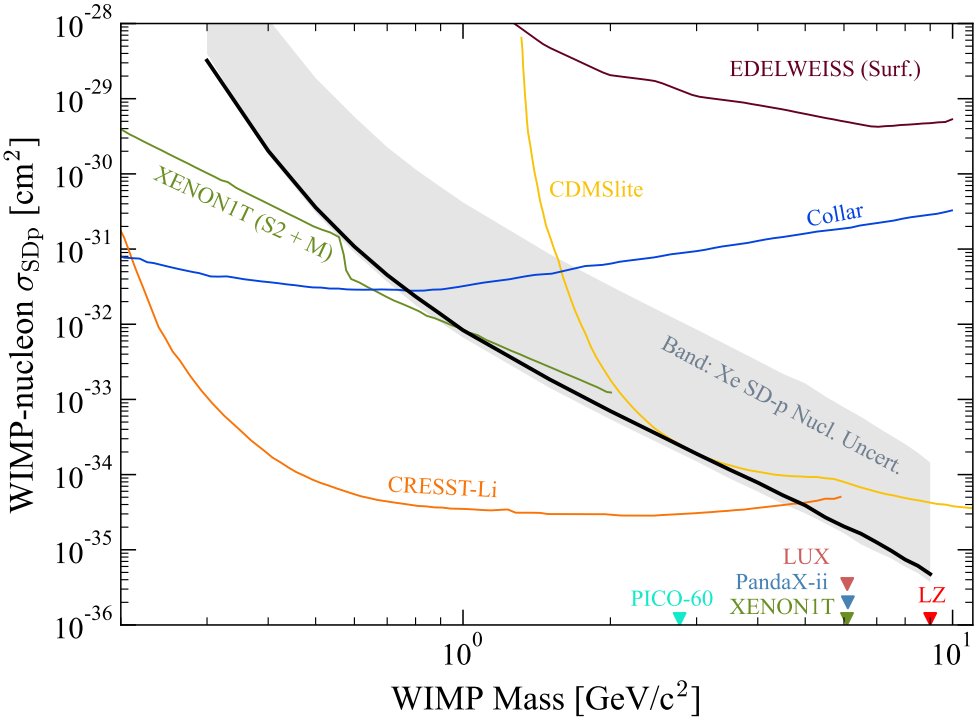

Figure 4.5: The black curve shows the 90% confidence limit for the spin-dependent WIMP-proton cross section using the mean value of the nuclear structure factors from [32]. The range of the structure factors from [31–33] was propagated to the Migdal signal spectrum and the associated limit curves, shown in the grey band. Also shown are limits from EDELWEISS [47], CRESST [123], CDMSlite [122], XENON1T (S2-only with Migdal signal [43]), and Collar [124]. Limits from LUX [101], PandaX-II [103], and XENON1T [102], PICO-60 [104], and LZ (Chapter 3) are below the bottom boundary of the plot; the lowest mass at which they report limits is shown with a triangle for each.

The ELF is related to the complex dielectric function dependent on both energy transfer ω and momentum transfer $\mathbf{k}$. Data for the complex dielectric function in the optical ($k = 0$) regime [127] was previously compiled and used for a search for lightly ionizing particles in LUX [128]. These datasets can be accessed in the CXRO online database [129]. We verified our optical data against the calculations in [128], which also notes the existence of an alternative set of optical data for xenon. We do not consider this alternative dataset in this work, but this disagreement should be considered as a possible source of uncertainty in the results presented here. The complex dielectric function $\epsilon(\omega) = \epsilon_1(\omega) + i\epsilon_2(\omega)$ respects the Kramers-Kronig relations

$$\epsilon_1(\omega) - 1 = \frac{2}{\pi}\mathcal{P}\int_0^\infty \frac{\omega'\epsilon_2(\omega')}{\omega'^2 - \omega^2}\mathrm{d}\omega' \tag{4.12}$$

and

$$\epsilon_2(\omega) = -\frac{2}{\pi}\mathcal{P}\int_0^\infty \frac{\omega'\epsilon_1(\omega')}{\omega'^2-\omega^2}\mathrm{d}\omega', \tag{4.13}$$

so it is in principle only necessary to obtain data for the real or the complex part of $\epsilon(\omega, \mathbf{k})$.[1] Furthermore, the ELF also obeys these relations with its real counterpart. The practical calculations underlying the following discussion often employed the Kramers-Kronig relations, and it was useful to check for the numerical stability of these transformations along the way.

To extrapolate the ELF to finite values of k, we employ a method of approximating it by a sum of oscillators and performing the extrapolation on that model. There are several versions of this calculation, with various levels of complexity taking different effects into account.[2] We use the Mermin-Levine-Louie function discussed in [131], which we briefly describe here.

As summarized by [126], the Lindhard model of the dielectric function is

$$\epsilon_L(\omega, k, \omega_P) = 1 + \frac{3\omega_P^2}{k^2 v_F^2}\lim_{\eta\to 0}\left[f\left(\frac{\omega+i\eta}{kv_F}, \frac{k}{2m_e v_F}\right)\right], \tag{4.14}$$

where

$$v_F = \left(\frac{3\pi\omega_P^2}{4\alpha m_e^2}\right)^{1/3},$$

$$f(u,z) = \frac{1}{2} + \frac{1}{8z}[g(z-u) + g(z+u)],$$

$$g(x) = (1-x^2)\log\left(\frac{1+x}{1-x}\right),$$

α is the fine structure constant, m_e is the electron mass, and ω_P is a plasma frequency parameter defining the model. The Mermin dielectric function is a modification of this model with an added damping parameter [133]

$$\epsilon_M(\omega, k, \omega_P, \Gamma) = 1 + \frac{(1+i\Gamma/\omega)(\epsilon_L(\omega+i\Gamma, q, \omega_P) - 1)}{1 + i\Gamma/\omega[\epsilon_L(\omega+i\Gamma, q, \omega_P) - 1]/[\epsilon_L(0, q, \omega_P) - 1]}. \tag{4.15}$$

Separately from Mermin, the Levine-Louie modification to the Lindhard dielectric function incorporates an approximation of the band gap by the replacement

$$\mathrm{Im}[\epsilon_{LL}(q, \omega, U)] = \begin{cases} \mathrm{Im}[\epsilon_L(q, \sqrt{\omega^2 - U^2})] & |\omega| \geq U, \\ 0 & |\omega| \leq U, \end{cases} \tag{4.16}$$

where U is a parameter related to—but not exactly equal to—the band gap [131, 134]. The Mermin-Levine-Louie (MLL) dielectric function is the combination of these modifications, replacing ϵ_L with ϵ_{LL} in the Mermin function of Equation 4.15.

[1] The Kramers-Kronig relations are satisfied independent of $\mathbf{k}$.

[2] There are summaries of the different models discussed in [126, 130–132] and in references therein.

The final model for the ELF is a sum of several oscillators with different weights A_i, ω_{Pi} and Γ_i parameters, and a common U parameter:

$$\mathrm{Im}\left[\frac{-1}{\epsilon(\omega,k)}\right] = \sum_i A_i \,\mathrm{Im}\left[\frac{-1}{\epsilon_{MLL}(\omega,k,\omega_{Pi},\Gamma_i,U)}\right]. \tag{4.17}$$

In addition to the Kramers-Kronig relations, this model should respect the sum rules

$$\sum_i A_i = 1 \tag{4.18}$$

and

$$\frac{1}{2\pi^2}\int_0^\omega \omega' \,\mathrm{Im}\left[\frac{-1}{\epsilon(\omega',k)}\right] \mathrm{d}\omega' = N, \tag{4.19}$$

where N is the number of electrons per unit volume with binding energy less than ω. We have fitted the optical data on hand up to $\omega = 200$ eV with the MLL oscillator model and approximated the core electron contributions using the method described in [132]. The model was fit to the ELF extracted from optical data using the Chapidif program, which allows user inputs for a number of oscillators and computes the resulting ELF and sum rules [135]. A three oscillator model was used to reproduce the main features of the ELF data with the parameters provided in Table 4.2. The computed N per unit cell for this model is $25.599 \sim 26$ electrons in the outer two orbitals. The optical ELF data and model defined by these parameters are shown in Figure 4.6. The corresponding complex dielectric function model and optical data, separated into real (ϵ_1) and complex (ϵ_2) components, are shown in Figure 4.7. Finally, the ELF fit to optical ($k = 0$) data is extrapolated to finite k using Chapidif. Figure 4.8 shows the extrapolated ELF, qualitatively comparable to similar extrapolations in silicon and germanium despite the relatively simple model [126].

Table 4.2: A three oscillator fit using the MLL dielectric function described in the text obtained with the Chapidif program [135].

A_i^{MLL} (eV)	ω_i^{MLL} (eV)	Γ_i (eV)	U_i (eV)
0.9618	11.2	9	16.59
0.0360	98.6	45.5	16.59
0.0016	64.9	8	16.59

The extrapolated ELF was converted back into an extrapolated dielectric function with the Kramers-Kronig relations and given as input to DarkELF, which was used to calculate the shaking probability from Equation 4.10. We replaced $Z_{\mathrm{ion}}(k)$ with the constant $Z_{\mathrm{ion}} = 8$ for the number of valence electrons in xenon, which should be a conservative treatment in the absence of a functional form for Z_{ion}. Extrapolating to high ω and $k > 12 - 15$ keV with

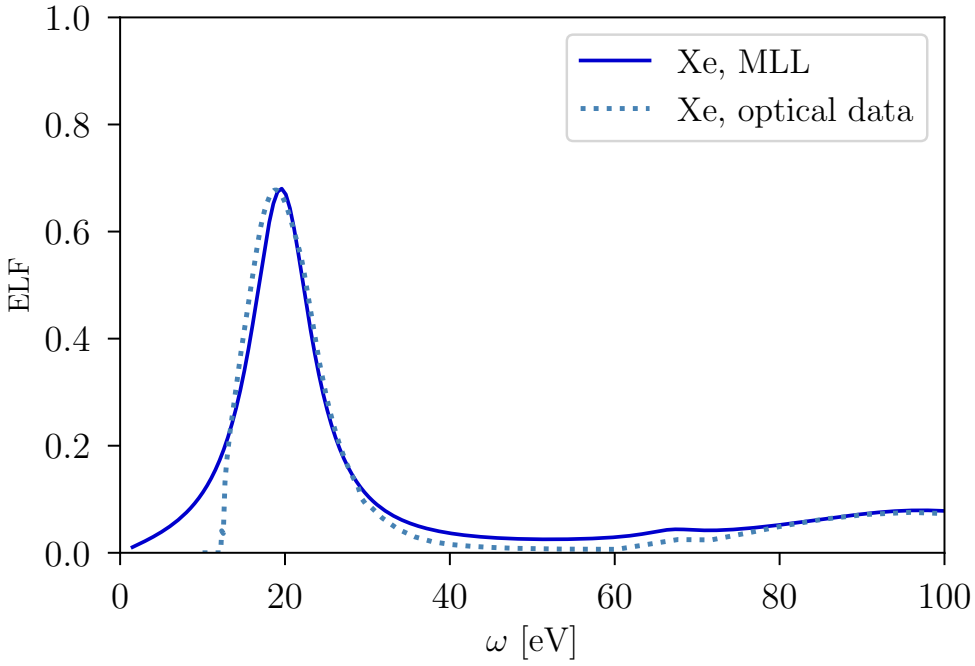

Figure 4.6: The xenon energy loss function in the optical limit (k = 0). The MLL oscillator model was fit to the compiled optical data in this form using the CHAPIDIF program [135]. Plot made with DarkELF [126].

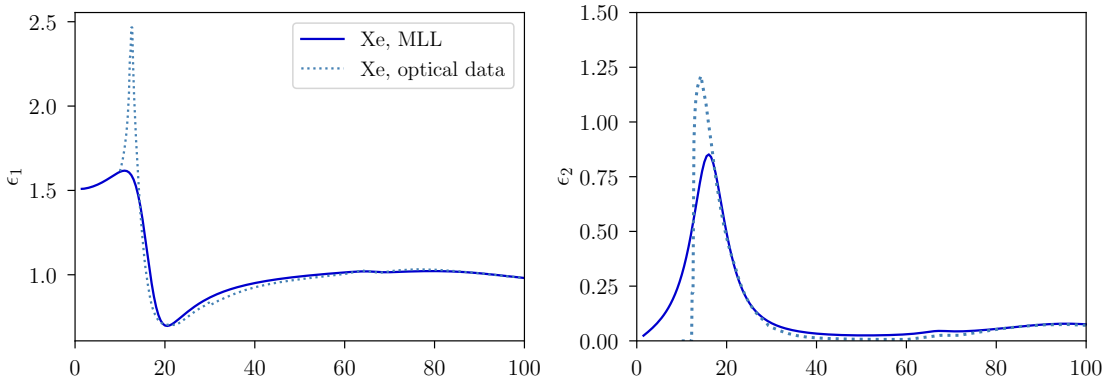

Figure 4.7: The dielectric function of xenon separated into its real part ϵ_1 (left) and imaginary part ϵ_2 (right). The dashed line is the data and solid line is the model corresponding to the fitted energy loss function. Plot made with DARKELF [126].

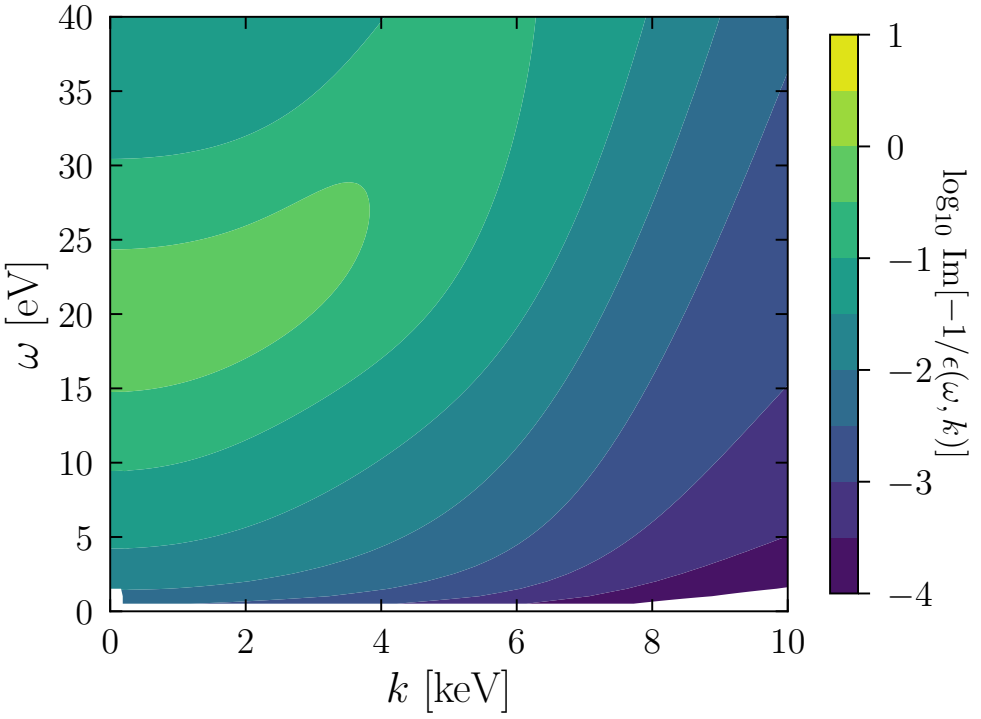

Figure 4.8: The extrapolated energy loss function corresponding to the fitted MLL oscillator model. Extrapolation was performed using the CHAPIDIF program [135]. Plot made with DARKELF [126].

the Mermin oscillator method was shown to be unstable compared to other methods [125, 126]. We therefore restrict our comparison to the 2–5e^- regime, which corresponds to about 20–50 eV in liquid xenon.

The shaking probability for a 100 eV nuclear recoil is shown in Figure 4.9. The band gap in liquid xenon is 9.3 eV [136], which is fairly close to the 10 eV cutoff seen in the free atom calculation [111]. On the other hand, the MLL model shows leakage below the $\sim$ 10 eV cutoff in the ELF optical data, so it is not surprising that the corresponding shaking probability extends past the band gap. It was previously observed that the Mermin oscillator method does not correctly follow the band gap in semiconductors and has a qualitatively similar rise in shaking probability at low energies [125, 126]. Compared to the results for semiconductors, the MLL shaking probability and free atom calculation show much better agreement.

Figure 4.10 is a comparison of the Migdal event rates for the ELF calculation and the free atom approximation. The $n = 3$ & 4 and $n = 5$ signal models for the free atom approximation are the same as those in Figure 4.1. Additionally, we show the distribution of simulated events comprising the signal model after the signal generation and event selection

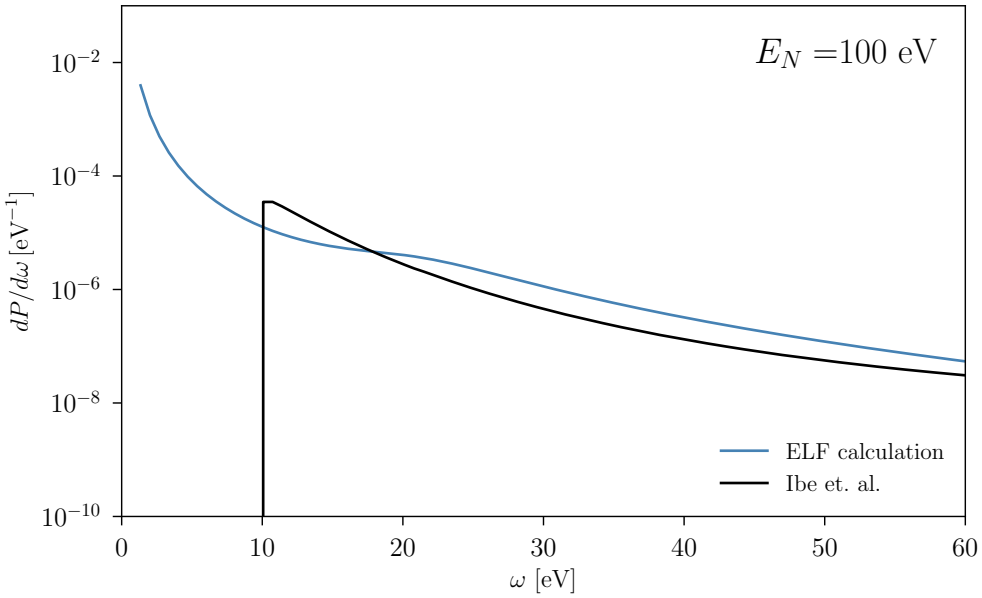

Figure 4.9: Electron shaking probability as a function of electron recoil energy for a 100 eV nuclear recoil via the DarkELF code [126]. The black curve is for the isolated atom calculation [111] and the blue curve uses a custom ELF for xenon.

efficiencies from Figure 3.2. The rate of events from the ELF calculation is shown in black, restricted to a maximum of 50 eV $\sim 5e^-$. This range of energy deposits is far from the regime relevant to the limits presented in this chapter, but future development of the ELF calculation could extend its range of validity to higher energies. Interestingly, the free atom approximation and the ELF calculation diverge near the band gap energy range of 10 eV, particularly in the higher WIMP mass case. The Mermin method is not expected to be a good approximation in this energy range [125, 126], but neither is the free atom approximation, motivating future theoretical and experimental development. This result from the ELF calculation should serve as a validation of the decision to exclude the $n = 5$ shell from the free atom approximation signal model.

There are several ways in which this calculation could be improved for xenon specifically. The ELF from the MLL model presented here is very simple and could be refined to fit the optical data better. It also needs validation in the finite k regime, as the extrapolation methods have been shown to break down within the energy and momentum range of interest for Migdal calculations [125, 126]. While the range of applicability remains narrow and at energies that are probably too low for practical use in a liquid xenon TPC, the preliminary results here warrant further consideration as an avenue for extending the Migdal signal model to lower energies in the analysis of dark matter detector data.

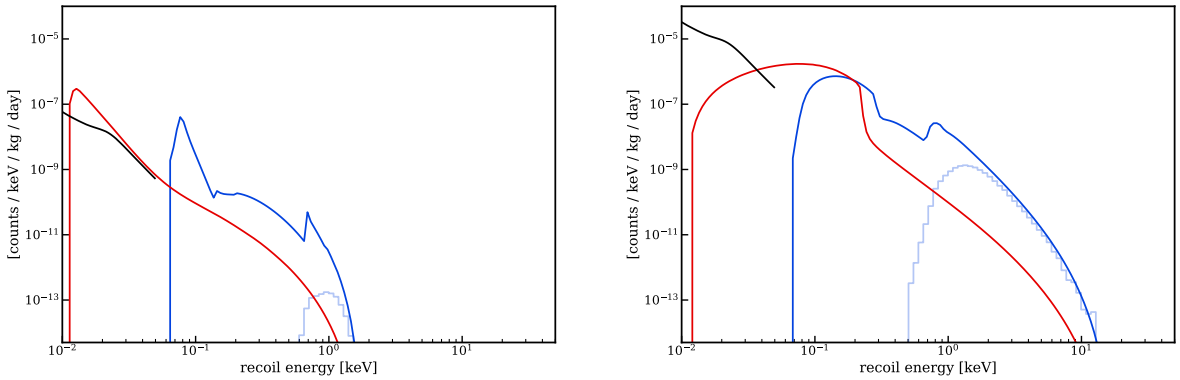

Figure 4.10: Comparison of the the predicted Migdal event rates with the isolated atom calculation [111] and the ELF calculation from DarkELF [126] for two WIMP masses: 0.5 GeV/c^2 (left) and 5 GeV/c^2 (right). The signal model used to set limits is the isolated atom calculation for the $n = 3$ & 4 shells is in blue. Events which survive to the final analysis according to the efficiency curve in Figure 3.2 (there in units of keV$_{\mathrm{nr}}$) yield the distribution in light blue. The rate estimate from the ELF calculation is shown in black, restricted to the range of 20–50 eV. These events are well below the S1-generating threshold. The signal model from the isolated atom $n = 5$ shell contribution is shown in red for comparison.

4.5 Future analyses

The Migdal effect has become a standard tool in the dark matter detection community, attracting theoretical and experimental attention in a wide range of detectors and detector media. The initial signal model provided by [111] has helped several experiments extend their reach to low mass WIMPs, including several analyses in liquid xenon TPCs. Inclusion of the $n = 5$ electron orbital in the signal model does not have meaningful impact on the limits presented in this chapter, increasing expected single scatter events only at the 1-2% level when considering the efficiency curve in Figure 3.2. However, the Migdal effect has previously been used in conjunction with liquid xenon TPC S2-only searches to dramatically lower the event detection threshold to 3.5 electrons [72] and 4.5 electrons [43]. In this application, the potential extra event rate provided by the $n = 5$ orbital would further enhance the reach to dark matter signals.

Convincing validation of the signal rate calculation down to the lowest recoil energies remains a hurdle in justifying inclusion of the $n = 5$ signals. The ELF-based approach presented in this chapter is one path forward, but further development in several facets of the calculation is needed for a robust result. Of course, experimental observation of the Migdal effect is another important step in solidifying this search methodology, although it is unlikely that the first measurements will definitively probe the lower energy electron emissions related the $n = 5$ signal. Validating and revising the signal model, both experimentally and theoretically, remains a project of interest moving forward for the whole community.

Chapter 5

Photoneutron Calibration of the LZ Experiment

In this chapter we describe the design, deployment, and analysis of a neutron calibration source for LZ based on the photonuclear process of neutron production. Calibration sources based on photoneutrons were introduced to the dark matter community as a method of calibrating low energy nuclear recoils [137] and have since been adopted by a wide range of experiments as a standard calibration tool [138–141]. An analysis of liquid xenon recoils using this kind of calibration source has thus far not been definitively demonstrated.

This chapter describes the LZ photoneutron source, simulations used to guide its design and the analysis of experimental data, and data collected from the first deployment of the source in November 2021. The design of the source described here represents several years of collaborative effort between the dissertation author, J. Lin, Q. Riffard, P. Sorensen, and D. McKinsey, was built on the prior work of K. O'Sullivan, and also incorporated feedback from the LZ collaboration at large. The analysis of the first deployment data described in this chapter was the work of the dissertation author, and a parallel analysis by M. Timalsina provided useful insights along the way. M. Timalsina also contributed to the preliminary characterization results referenced at the end of the chapter.

5.1 Photoneutron production

Photoneutron production for dark matter detector calibration is typically achieved using a beryllium target, inducing the reaction

$$\gamma + {}^{9}\mathrm{Be} \rightarrow n + {}^{8}\mathrm{Be}. \tag{5.1}$$

^{9}Be is the natural stable state of beryllium, so this reaction is practically achievable by putting a gamma ray producing source next to some material with natural beryllium in it. The initial energy of a photoneutron depends on the angle of its momentum vector relative

to the gamma that generated it according to

$$E_n(\theta) \approx \frac{M(E_\gamma + Q)}{M+m} + \frac{E_\gamma[(2Mm)(M+m)(E_\gamma+Q)]^{1/2}}{(M+m)^2}\cos\theta, \tag{5.2}$$

where E_γ is the gamma ray energy, $Q = -1664.54$ keV is the neutron separation energy for the ^{9}Be target nucleus, M is the mass of the recoiling ^{8}Be nucleus, and m is the neutron mass [142]. This approximate relation holds for the case that $E_\gamma \ll m = 931$ MeV, which is clearly satisfied for the the gamma energies of interest lying just above Q. Typically the cross section for this process is on the millibarn scale, so a normal source configuration yields a neutron for every 10,000 or so gamma rays passing through the target.

Good source candidates produce gamma rays with energy just above the photonuclear threshold without a significant intensity of higher energy transitions. A few sources considered for LZ are listed in Table 5.1. ^{88}Y is a particularly interesting calibration source for LZ because the 4.6 keV recoil endpoint is at a similar energy scale as that of coherent ^{8}B solar neutrino scattering in xenon. This coherent scattering signal is expected to limit sensitivity to GeV-scale WIMPs in LZ, but it is also an interesting and unobserved source of events in its own right [44]. Calibrating the detector and analysis efficiency at these energies is a critical step in extending LZ's sensitivity to low energy nuclear recoils from WIMPs and coherent neutrino scatters.

Table 5.1: A few gamma ray sources of interest for photoneutron production. These are the principal neutron energies of interest, but some of these sources produce additional gamma ray energies above the photoneutron production threshold at reduced rates. Details of ^{88}Y photoneutrons are discussed in this chapter, while ^{124}Sb is the subject of Chapter 9.

Isotope	Gamma ray energy [keV]	Neutron energy [keV]	Xenon recoil endpoint [keV]
^{88}Y	1836.1	152	4.6
^{205}Bi	1764.3	88.6	2.7
^{206}Bi	1718.7	48.1	1.4
^{124}Sb	1691.0	23.5	0.71

5.2 Source design

There are several practical complications to a photoneutron calibration. The principle concern is the relative inefficiency of generating neutrons; due to the large ratio of background gamma rays to photoneutrons leaving the beryllium target, a substantial amount of shielding is needed to reduce event rates in the detector. Dense shielding material is preferable for moderating gamma rays efficiently. In turn, the shielding affects the neutron spectrum by

smearing it to lower energies, so heavy nuclei are desirable to prevent large energy transfers in a neutron scatter. Since it satisfies both criteria, photoneutron calibration measurements have typically employed lead for shielding purposes [137–141].

The shielding material used in the LZ photoneutron source design is tungsten in the form of MT-185 alloy. Tungsten nuclei are not quite as heavy as lead, but sufficiently heavy that a single neutron scatter can transfer only up to about 2% of its energy. Tungsten is a particularly powerful gamma ray moderator due to its 18.55 g/cm^3 density, roughly 60% denser than lead, allowing for a more compact source shielding design. The MT-185 alloy used in the fabricatin of the LZ photoneutron source shielding consists of 97% tungsten, 2.1% nickel, and 0.9% iron, none of which pose significant concerns for enhanced neutron scattering for the energy range in Table 5.1. We will refer to the shielding material as tungsten for the rest of the chapter.

The shielding and source design is shown in Figure 5.1. It consists of a central stack of beryllium metal surrounding the gamma ray source inside of a cylindrical tungsten container called the inner source tube. The inner stack design assumes a cylindrical source pellet with a diameter of 4.7 mm and a height of 4.6 mm. ^{88}Y sources with these dimensions were purchased from the commercial supplier Eckert & Ziegler. There are additional tungsten disks inside of the inner source tube that allow for the addition or subtraction of beryllium material, as well as repositioning of the photoneutron-producing beryllium target. Early designs considered the use of BeO, a ceramic material, instead of beryllium metal for safety reasons; beryllium dust can induce beryllium sensitivity upon skin contact or inhalation. However, BeO poses similar safety risks, and it is less desirable for photoneutron production due to its lesser density and the presence of oxygen atoms that do not contribute to neutron production but reduce neutron energies via scattering. Instead, the beryllium disks were coated with a 24 μm layer of nickel to reduce the possibility of handling beryllium directly when assembling the source, which was performed in a manner that minimized both radiation and beryllium exposure to the person assembling the inner source tube.

The inner source tube is sealed inside of a larger conical shielding piece with a cylindrical base, called the source cone. Once inside this cone, a source with activity up to 3.7 MBq (100 μCi) is sufficiently shielded that there are minimal radiation exposure concerns from either gamma rays or neutrons for a person handling it. While the cone assembly is a bit cumbersome with a weight of 13.2 kg, the total shielding design amounts to about 120 kg. Two source cones and inner source tubes were manufactured, while only one larger shielding block was made for use and storage at the SURF facility. The multiple source cone system enables the replacement of gamma ray sources, to smoothly switch between different types of photoneutron sources and to replace sources with diminished activity. ^{88}Y has a half-life of 106.6 days, which is short enough that calibrations spaced a year or so apart will have drastically different activities if the source is not replaced. This is particularly true for the other sources under consideration: ^{124}Sb has a half-life of 60.2 days, while the half-lives of ^{205}Bi and ^{206}Bi are 14.9 and 6.2 days, respectively.

Figure 5.2 is a rendering of the deployment of the source for a calibration run of LZ. To minimize the distance between photoneutron production and the active TPC volume, the

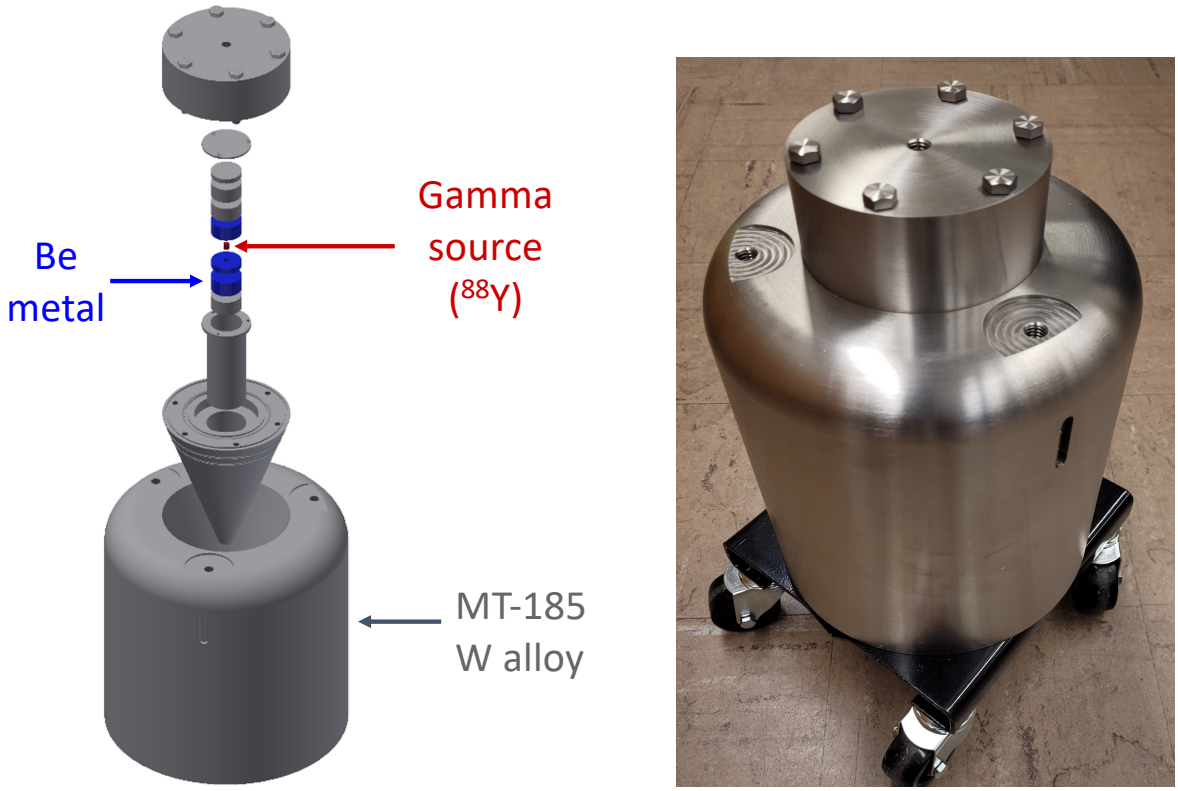

Figure 5.1: The left is a rendering of the photoneutron source showing the shielding volume and inner assembly. The inner can is a cylindrical volume filled with a stack containing the ^{88}Y source, beryllium metal disks, and tungsten disks. It is encapsulated in the source cone, which rests on top of the larger shield volume. The source cone can be removed from the water tank independently in case the larger shield cannot be retrieved after a deployment. The right is a photo of the assembled source. Rendering and photo by J. Lin.

source is placed into a recess on top of the outer cryostat vessel (OCV). The liquid scintillator acrylic tanks were designed with a cylindrical gap for the source, which is filled with a small acrylic cylinder filled with liquid scintillator called the photoneutron plug during normal operations. Since the entire detector system is housed inside of the water tank for additional shielding, the source must be lowered through the water into position with a crane. The large shield block and the cylindrical cone are separately rigged; in the unlikely scenario that the main shielding piece is stuck and cannot be retrieved, the active source can be removed separately by lifting out the cone. The cone assembly is water proof to prevent corrosion of the inner beryllium metal while deployed. The source is lowered through an access port at the top of the water tank. A special centering plate was fabricated to ensure that the source was lowered in the correct position to safely land in the OCV without damaging the acrylic tanks. Once in place, the water tank was re-sealed for the duration of the deployment so the

outer detector PMTs could be operated as part of the calibration.

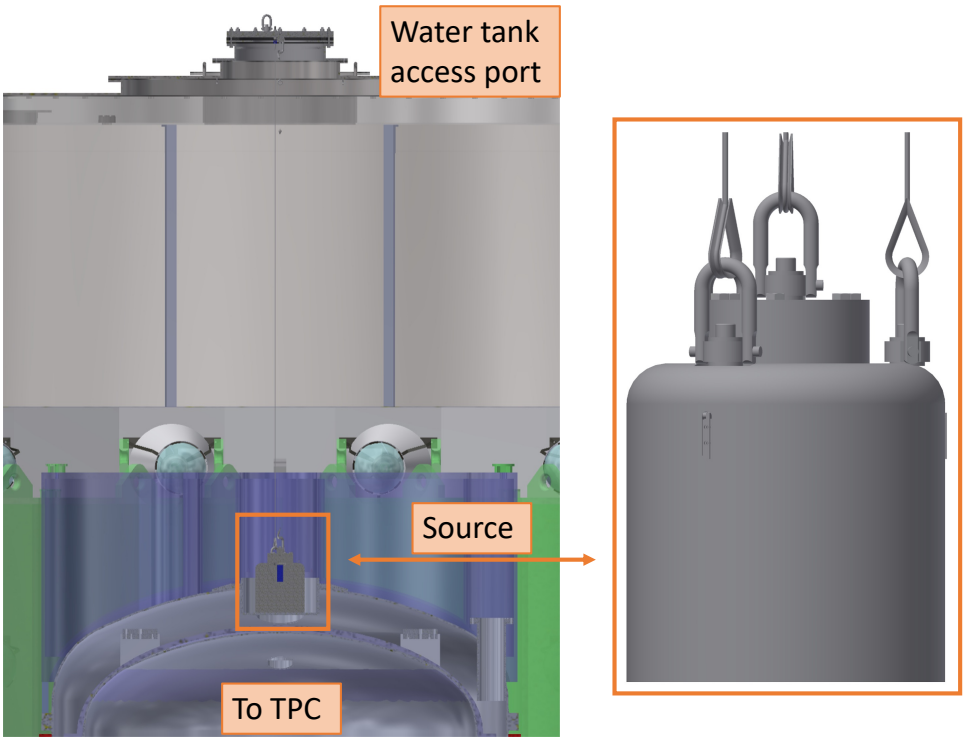

Figure 5.2: A rendering of the deployed photoneutron source. It is lowered through an access port on the water tank and rests on a recessed part of the outer titanium cryostat volume. The source is highlighted in an orange box. Also shown is a closeup of the source and rigging. Renderings by J. Lin.

5.3 Simulations

The final photoneutron source and shielding design was the product of many iterations of simulations, optimizing for the number of good single scatter neutron events, minimizing the total event rate in the detector, and accounting for existing constraints from the rest of the LZ detector systems like the size of the opening in the acrylic tanks and the weight tolerance of the OCV. Photoneutron and background gamma ray recoil spectra were simulated using LZ's simulation tool BACCARAT [65], built on GEANT4 [77–79]. Event recoil clustering and detector response was simulated using LZ software built on the NEST package [60]. Simulation results in this section use a detector response model fit to data taken under the detector conditions corresponding to the dataset in Section 5.4.

We have noted several times by now that photoneutron production is a fairly inefficient process. Accordingly, it is quite computationally inefficient to simulate all of the decays in

which no photoneutrons are produced when neutron recoils are the population of interest. In order to simulate only photoneutron events, we developed an algorithm to correctly sample their creation positions in the beryllium target and the energy-angle relationship from Equation 5.2. The steps in the algorithm are as follows:

1. A vector is generated in a random direction originating at the center of the gamma ray source volume. This vector corresponds to one of the photoneutron-generating gamma rays of interest (1836.1 keV in the case of ^{88}Y). We call this vector a virtual gamma ray, since it is not propagated in the simulation.

2. A point is sampled uniformly along the length of the vector, which is equal to the radius of the sphere encapsulating the beryllium target. There are one of two outcomes:

   a) The point is outside of the beryllium target volume. The virtual gamma ray did not generate a photoneutron, so we discard the vector and start over.

   b) The point is inside the beryllium target volume, so it is the location at which a photoneutron is generated.

3. A new vector is generated in a random direction originating at the neutron generation point. This is the momentum direction of the neutron. Its energy is assigned according to Equation 5.2 where the angle θ is the angle between the virtual gamma ray vector and the neutron momentum direction.

This algorithm is summarized graphically in Figure 5.3.

This population can be rescaled to the background gamma ray spectrum by weighting it according to the estimated neutron production probability. The 1836.1 keV transition has an intensity of 99.2%. At this gamma ray energy, the ENDF/B-VIII.0 photonuclear cross section has a value of 1.41 mb [29]. Alternative fits for the photonuclear cross section yield values 6% less [143] and 7% more [144]. Using the ENDF/B-VIII.0 value to estimate the equivalent interaction length in beryllium metal gives 116.4 m, notably much larger than the 1.27 cm scale of the beryllium target. The resulting neutron production probability for a ^{88}Y decay is 1.07×10^{-4}, or 1 neutron produced per 9,350 ^{88}Y decays. The neutron to gamma ray ratio from this source is smaller, because ^{88}Y typically releases more than one gamma ray per decay. Most of these are below the photonuclear production threshold, but there are two rare transitions above the threshold with sub-percent intensities. Because the photonuclear cross section is also significantly lower at those energies, we do not consider them further. In principle, high energy gammas can also originate from neutron captures or inelastic scatters, but these are relatively rare compared to the primary neutron-generating transition, since neutron production is already inefficient compared to the ^{88}Y decay rate.

^{88}Y decays are simulated directly with the built-in nuclear decay generator in GEANT4. The spectrum of electronic recoil backgrounds, from gamma rays directly from ^{88}Y decays and also from photoneutron captures or inelastic scatters, is shown in Figure 5.4. The blue histogram in this figure is a simulated dataset including both photoneutrons and ^{88}Y in the

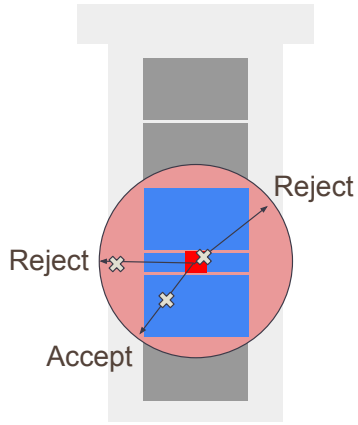

Figure 5.3: A diagram of the algorithm used for generating photoneutron position, initial energy, and momentum. First a vector is generated at the location of the ^{88}Y source (red) pointing in a spherically random direction. A point is selected randomly along the vector yielding one of two outcomes: 1. the point is inside the beryllium target volume (blue) and is accepted or 2. the point is outside of the beryllium target volume and is rejected, starting over with a new vector. If accepted, a neutron is generated at that point with initial momentum pointing in a spherically random direction and with energy specified by Equation 5.2.

appropriate ratio. The sharp edge at 1836.1 keV is effectively the maximum gamma ray energy from ^{88}Y decays, since the higher energy transitions are relatively rare. The long tail extending to higher recoil energies is due to gamma rays originating from photoneutron inelastic scatters or capture, shown by the red histogram from a neutron-only dataset scaled to the appropriate activity. There are two prominent peaks at the high energy end of this spectrum, both originating from neutron capture. The peak at 9.3 MeV is due to capture on ^{129}Xe in the natural xenon comprising the active TPC volume, making it an unavoidable feature of calibrations introducing a high flux of neutrons into the detector. The additional peak at 9 MeV is due to capture on ^{58}Ni found in various materials near the active xenon, including the tungsten alloy used as the shielding material for the photoneutron source. The total rate of events in the detector for a 1.14 MBq ^{88}Y source is 94 recoils per second.

We have previously noted that the presence of the heavy tungsten shielding moderates the neutron energies produced in the beryllium target. Additional materials between the photoneutron source and the liquid xenon target were minimized via deployment onto the OCV, but these may still contribute to addtional smearing of the neutron spectrum. Figure 5.5 shows the simulated energy spectrum of neutrons entering the liquid xenon target volume. While the spectrum is relatively flat—rather than monoenergetic—the kinematic endpoint of photoneutron production at 152 keV is still fairly well preserved.

The events of interest for the calibration analysis are single scatter neutron recoils. Fig-

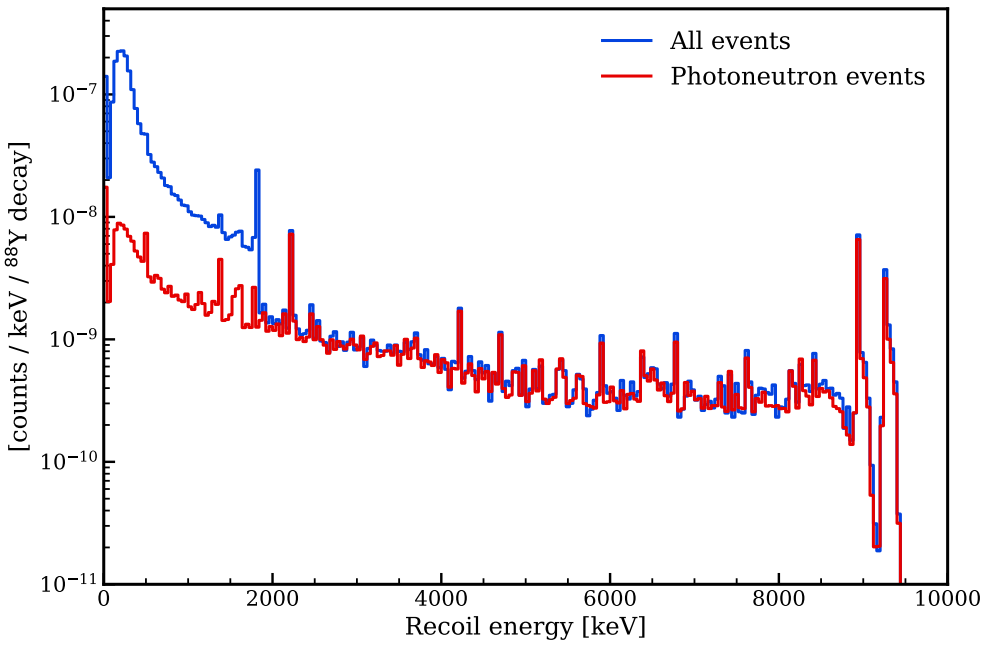

Figure 5.4: The simulated total recoil energy deposited in the liquid xenon target for events from the YBe photoneutron source. The blue histogram is the total spectrum due to both gamma rays directly from ^{88}Y decays and events initiated by photoneutron production. The red histogram corresponds to only those events starting with photoneutron production, showing that the high energy tail is the result of neutron inelastic scatters or capture in the detector materials. The total rate is dominated by gamma rays directly from ^{88}Y decay.

ure 5.6 shows event positions for these events as red points. It also shows the total event distribution for low energy single scatter events in blue. In this case, low energy events are defined by the region of interest (ROI) with S1c between 0 and 30 phd and log(S2c) between 2.5 and 4.5. These ranges correspond to maximum energies of 19 keV$_{\mathrm{nr}}$ and 4 keV$_{\mathrm{ee}}$. Due to the source position on top of the detector, most events are at the top of the TPC volume. Additionally, single scatter gammas tend to occur at the corner of the detector, while neutrons are more likely to to scatter towards the center of the detector. Therefore, we define the fiducial volume for the analysis with the narrow disk towards the top of the detector shown by the dashed black line. A larger radial extent for this volume would be helpful in collecting more neutron scattering statistics, but features in the first dataset described in Section 5.4 led to this definition.

A simulated dataset of 4 billion ^{88}Y decays was produced with the appropriate ratio of photoneutron production to show the population of single scatter events in the ROI in Figure 5.7. For a 1.14 MBq source, this corresponds to just under one hour of data. The neutron population is the group of events between a log(S2c) of 2.5 and 3.25, clearly separated from the electronic recoil band above. Once the fiducial volume selection from Figure 5.6

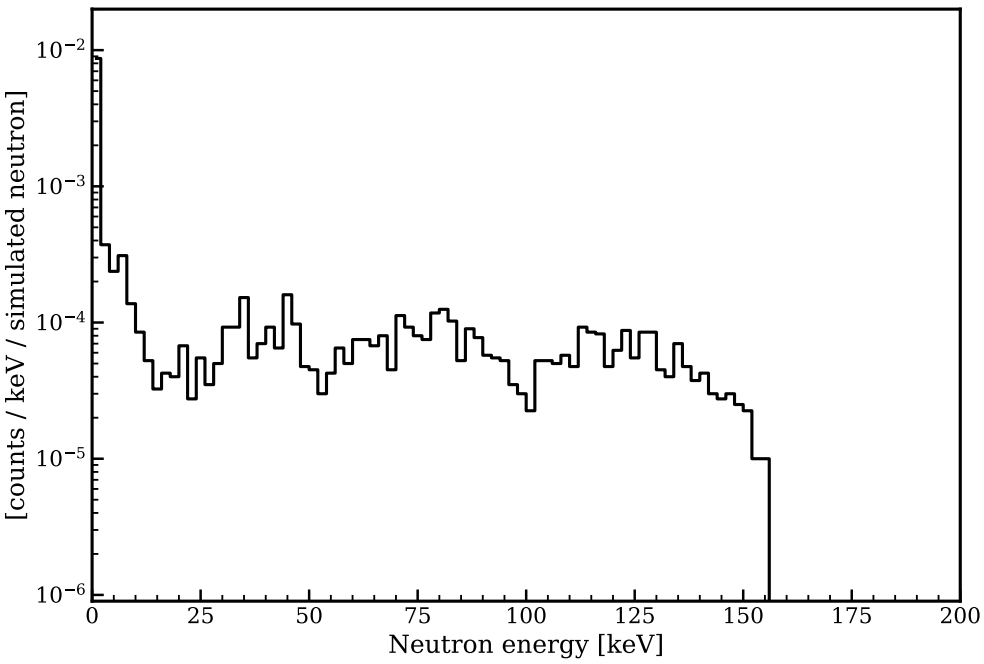

Figure 5.5: The simulated energy spectrum of neutrons entering the liquid xenon target volume. While the tungsten shield and other moderating materials smear the monoenergetic spectrum, it has a well-defined endpoint at 152 keV.

is included, 10 neutron events are the only remaining events. A full calibration run would amount to more than 1 hour of data acquisition, which might include some electronic recoils as well. This simulated dataset shows that the two populations are fairly distinct at the simulation level without invoking a significant number of event selection cuts. Of course, the reality of experimental physics is often more complicated.

Once the neutron single scatter events are identified and selected, we aim to reconstruct the their recoil energy endpoint at 4.6 keV. Figure 5.8 shows two versions of the neutron single scatter population in the fiducial volume. The black histogram takes full advantage of the simulation information, selecting only those events consisting of a single nuclear recoil in the liquid xenon target. In this population, we see a sloped spectrum ending sharply at 4.6 keV, as expected. The purple histogram takes into account detector response effects in identifying single scatter events, leading to a tail of events past the 4.6 keV endpoint of true single scatters. This misreconstruction effect is expected, and the slope of the distribution changes when it takes over from real single scatter events. The bulk of the recoils are still in the main population near the 4.6 keV endpoint. The efficiency for detecting events drops as a function of the recoil energy, explaining the divergence of the black and purple curves.

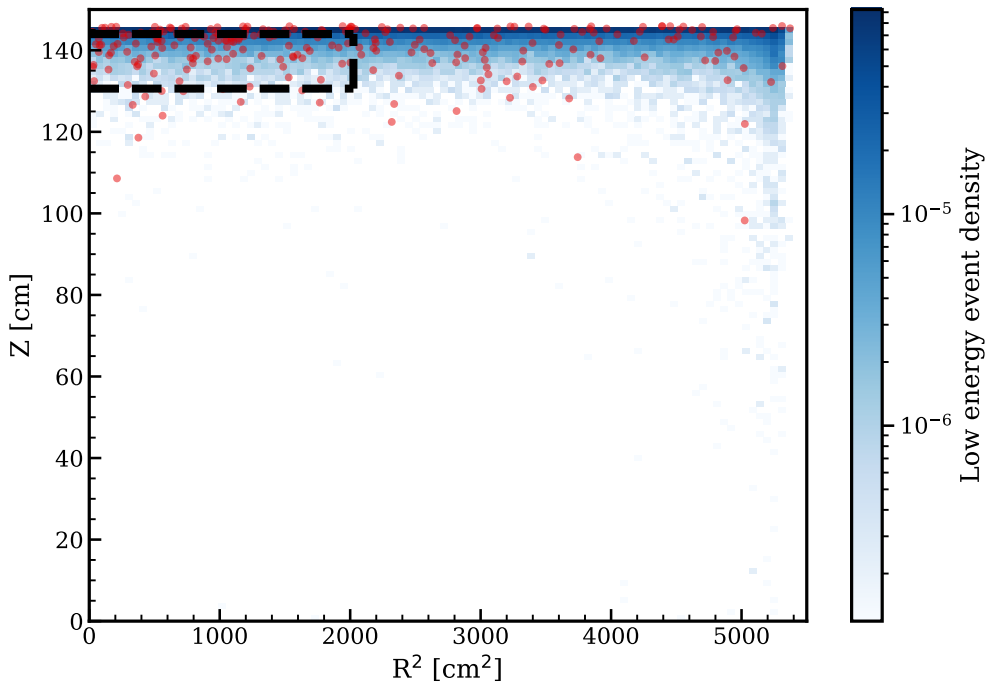

Figure 5.6: The blue histogram shows the simulated event position density for all low energy single scatter events, dominated by gamma ray backgrounds. The red points are a set of 250 neutron single scatter events to show the position distribution of an approximate calibration dataset. The fiducial volume for this analysis is in the dashed black, where the radial extent was chosen due to features in the collected dataset (see Figure 5.10).

5.4 First data run

The photoneutron source was deployed in LZ for 61.6 hours of data acquisition starting on November 15th, 2021. Figure 5.9 is a photograph of the source as it was lowered into position through the water tank access port. It was outfitted with a cover of PTFE for increased light collection efficiency in the outer detector during the deployment. During this early operation phase of LZ, settings for the grid voltages were different than those in the first WIMP search dataset from Chapter 3. A tuning of NEST parameters yielded the results in Table 5.2, although these predated the change to recombination skewness used in the WIMP search results. Ultimately the LZ operating parameters were revised before the first science run to improve the detector's stability and performance.

The ^{88}Y source activity during the time of deployment was 1.14 MBq, which was also the source activity used for the simulations presented in Section 5.3. The observed event rate was comparable to the predicted 94 counts per second, almost all of which are relatively high energy electron recoils. To reduce the number of events consisting purely of trailing electrons from these recoils, a data acquisition hold-off of 10-13 ms was implemented after

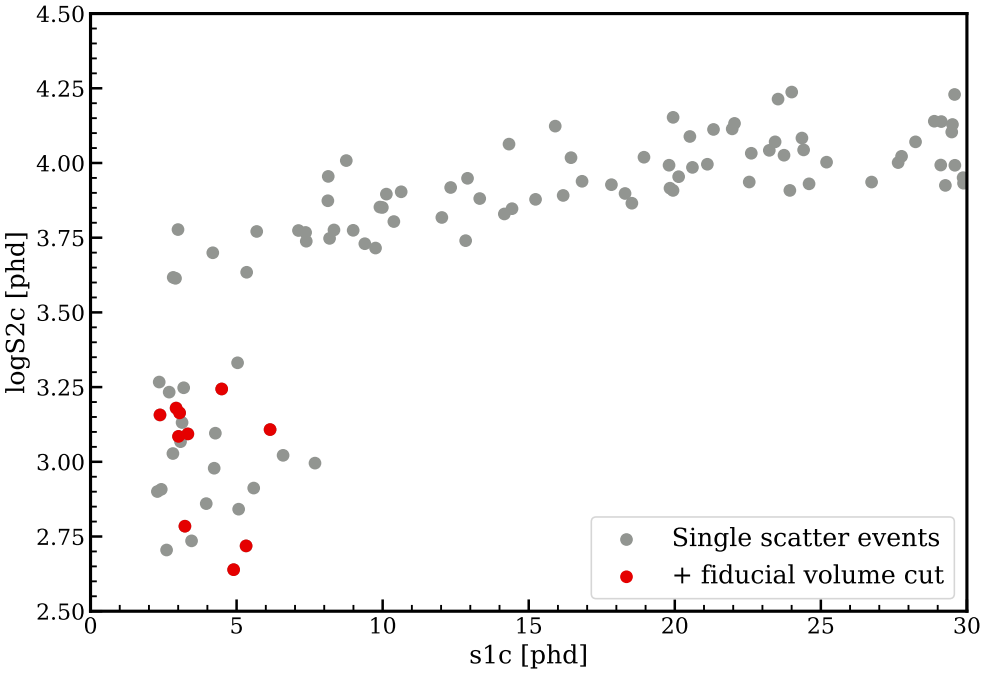

Figure 5.7: A simulated dataset including detector response, corresponding to about 1 hour of activity of a 1 MBq ^{88}Y source. All single scatter events are shown in grey and events within the fiducial volume defined for this analysis (see Figure 5.6) are in red. The photoneutron population, between 2.5 and 3.25 in log(S2c), is well separated from the electronic recoil band above. Single scatter electron recoils are also less likely to occur within the fiducial volume than neutron single scatter events.

Table 5.2: NEST tuning parameters corresponding to the LZ detector conditions during the photoneutron deployment. The top half of the table are inputs to NEST, and the bottom half are are additional parameters of interest derived from NEST.

Parameter	Value
g_1^{gas}	0.0800 phd/photon
g_1	0.1080 phd/photon
Effective gas extraction field	9.95 keV/cm
Single electron	64.1 phd
Extraction efficiency	90.8%
g_2	58.19 phd/electron

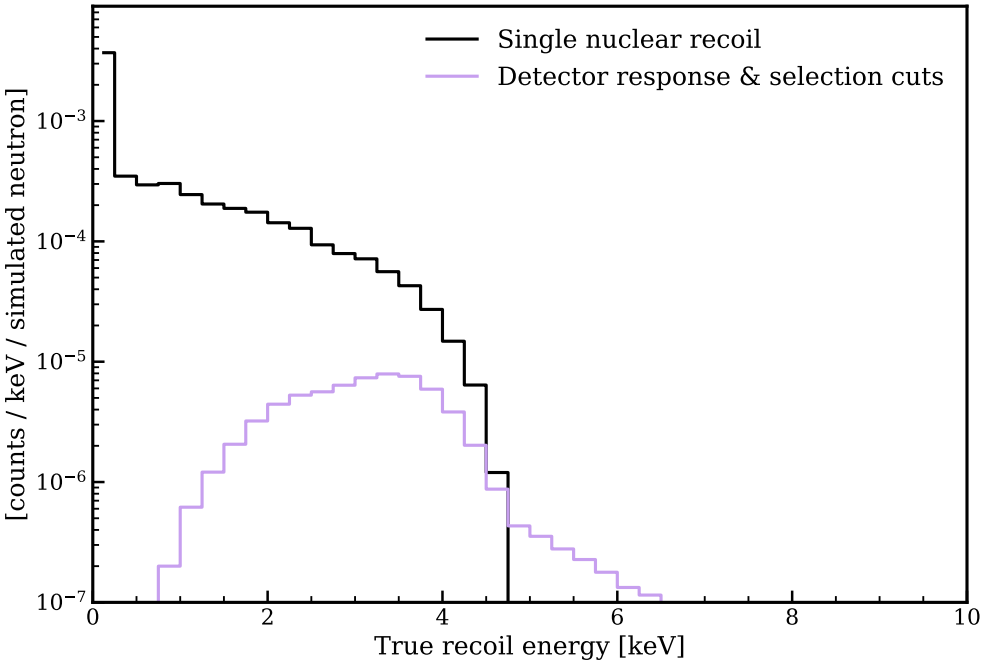

Figure 5.8: Simulated recoil spectra of single scatter neutron events in the liquid xenon target. The black histogram is only those events that scatter once in the simulation, and the recoil endpoint of 4.6 keV is clearly visible. The purple histogram includes scatter site clustering and simulated detector response in the single scatter definition, inducing a tail of higher energy events. Both histograms include only events in the fiducial volume defined for this analysis, shown in Figure 5.6.

each triggered event. This hold-off time accounted for the majority of the deployment time; the estimated livetime of the deployment was 32.8% of the 61.6 hours.

A total of 1.4×10^7 events were acquired during the deployment. Of these, 5.4×10^6 were classified as single scatter events and their positions are shown in Figure 5.10. The fiducial volume for the analysis is also shown. The radial extent of the fiducial volume was limited due in part to the presence of grid emission hotspots, visible in both position distribution plots.[1] The expected number of neutron recoil events from the purple histogram in Figure 5.8 corresponding to the 20.2 hour livetime is 146, hidden amongst the several million single scatters in Figure 5.10.

[1]There are some event clusters inside of the fiducial volume visible in the X-Y positions in the left plot. These are due to features in the light response map used to reconstruct event positions. They were later smoothed out for the first science run data, but the newest version of the event processing software was not applied to this dataset.

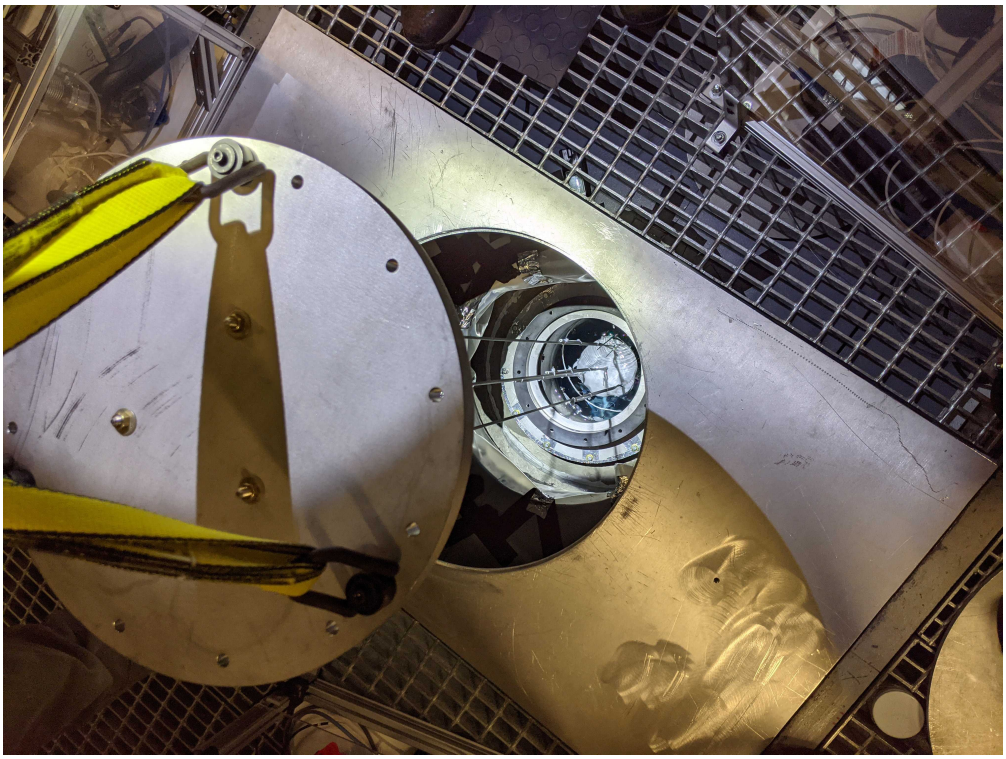

Figure 5.9: Photo from the first deployment of the LZ photoneutron source, taken as it was lowered through the water tank port into its position on top of the outer cryostat. The source was covered with a PTFE hood to increase light collection efficiency in the liquid scintillator veto detector.

5.5 Identifying neutron recoils

A number of data selection cuts were developed to reduce the collected data to the neutron recoil events of interest. Since much of this analysis work was performed before the main WIMP search analysis from Chapter 3 was fully developed, some of the general data quality cuts were not as refined, particularly for the different detector conditions under which this dataset was taken. Single scatter events were initially selected from the full dataset with some loose data quality requirements, including a muon event veto, a cut ensuring the data acquisition buffers were not overloaded while recording an event, and a cut requiring the S1 pulse not be dominated by a single channel—a common accidental coincidence topology. Additionally, the ROI was restricted to the ranges of S1c between 0 and 30 phd and log(S2c) between 2.0 and 4.5, and the previously discussed fiducial volume cut was also applied.

These initial skimming criteria were applied to the photoneutron dataset. The top left panel of Figure 5.11 shows the skimmed events and the expected region that neutron single scatters would appear in the purple contours. The expected signal bands for typical nuclear

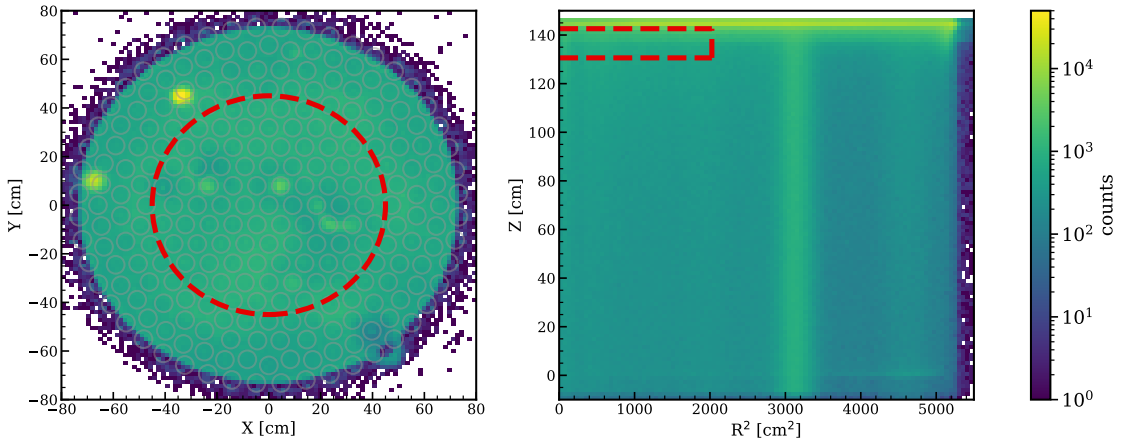

Figure 5.10: The full dataset of single scatter events recorded during the photoneutron source deployment. The fiducial volume was defined to exclude grid emission hot spots visible at around 9 o'clock and 11 o'clock in the left plot, corresponding to the increased event density at $R^2 = 3000$ and $R^2 = 4500$ in the right plot. Apparent hotspots inside of the fiducial volume are actually a result of the position reconstruction algorithm–these were resolved in later versions of data processing software, which were not applied to this dataset.

and electronic recoils are shown in red and blue, respectively, but these are not well-populated in this dataset for distinct reasons. In the nuclear recoil case, the photoneutron recoil energies are well below the typical energies accessible to the detector; the 4.6 keVnr recoil endpoint was roughly at the 50% detection efficiency point for these detector conditions.[2]. Due to these low recoil energies, the photoneutron single scatter events are expected appear somewhat below the red nuclear recoil band in the purple contours. The electronic recoil band is also relatively unpopulated, an expected result of the fiducialization as highlighted in Figure 5.7.

There are two major categories of events that do populate this plot, obscuring potential photoneutron single scatters. The first is a vertical band at small S1c resulting from accidental coincidences, where stray S1 pulses have been paired with stray S2 pulses. While large S2 pulses, with $\log_{10}(\text{S2}c)$ greater than ~ 3.5, are likely pulses directly associated with event interactions, these can be paired with a small stray S1 to form events in the upper half of the vertical band. Accidentals are an especially likely categorization in the presence of electron train events, where there is a steady stream of delayed electrons producing S2s after a large energy deposit. These persist despite the long hold-off time applied to the data acquisition system when collecting the data. These events are event more concerning in this context because they overlap directly with the photoneutron single scatter region of interest. In the absence of a dedicated electron train veto, a cut was developed to eliminate these events by comparing the size of the event S2 with the total amount of light in the event. Events with a large total area likely have many extra electron pulses in them, suggesting an

[2]The efficiency curve shown in Figure 3.2 is for slightly different detector conditions

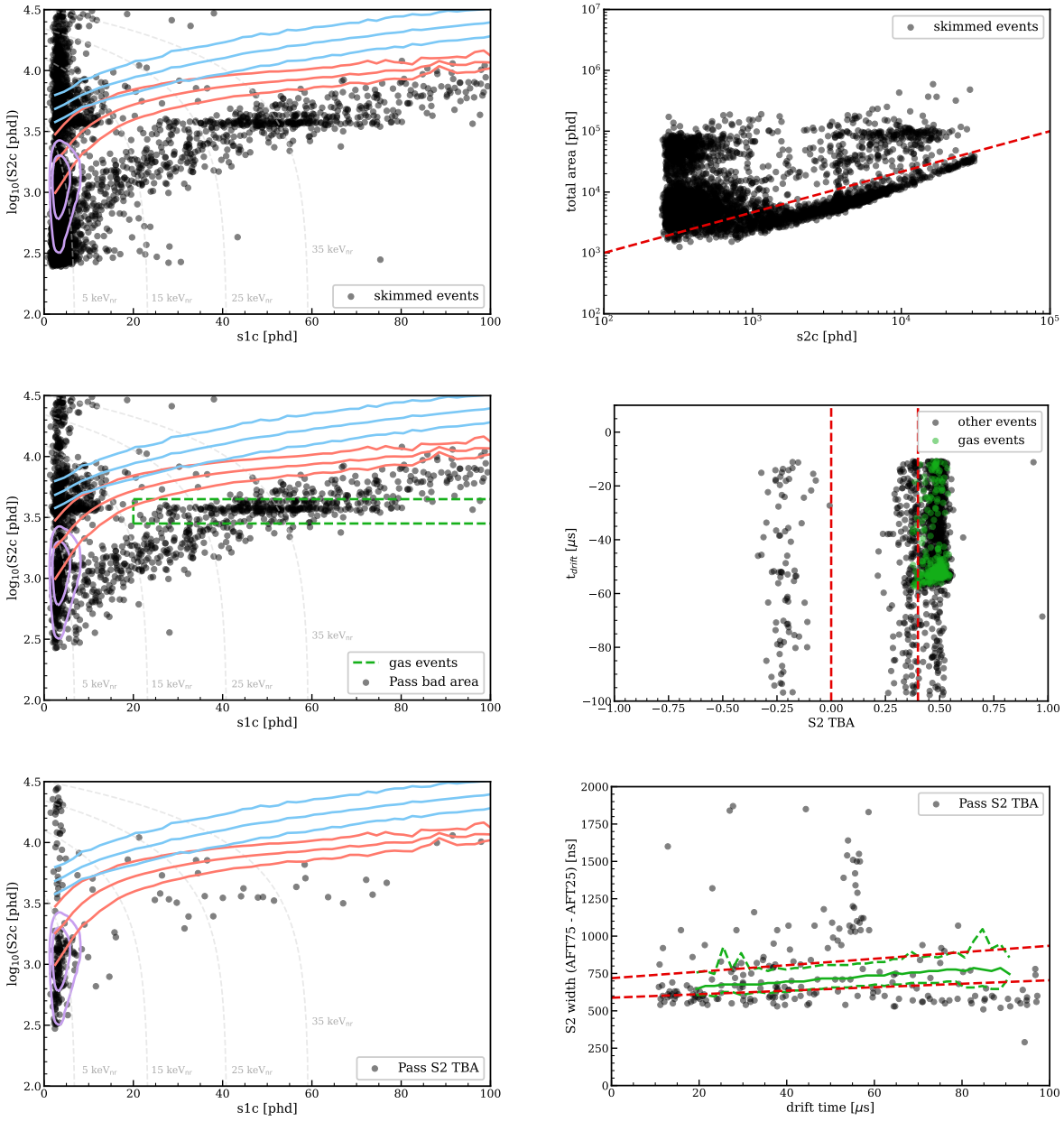

Figure 5.11: The progression of data selection cuts to arrive at the final set of candidate events in Figure 5.12. Events from Figure 5.10 are skimed according to the fiducial volume, a few basic data quality cuts, and the S1c and $\log_{10}$(S2c) ranges of the figures in the left column. Events in the left column correspond to those in the right column, and events surviving the cut in the right column are shown in the next row. More details on these cuts can be found in the text. Also shown in the left column are the 10-50-90% bands for typical electronic recoils in blue and typical nuclear recoils in red. The expected 1- and 2-σ contours for photoneutron single scatter events in the fiducial volume are shown in purple.

electron train. The separation of electron train events from good single scatters was defined as the red dashed line in the top right panel, where events below the line were accepted and events above were rejected.

The second population is a smeared band with an apparent peak at S2$c \sim 1000$, lying below the nuclear recoil band in red. These events are caused by scattering in the gas above the anode grid, giving them a distinct maximum drift time of 60 μs due to the electric field formed between the anode and PMT faces, and the temperature and pressure of the gas. They can also be seen at that drift time in Figure 3.3, but they were not a major concern for the WIMP search because they are outside of the fiducial volume for that analysis. Due to our interest in events closer to the liquid surface, they are a significant background in the dataset. These events can mainly be identified by a quantity called the S2 top-bottom asymmetry (TBA):

$$\text{S2 TBA} = \frac{\text{S2}_{\text{top}} - \text{S2}_{\text{bottom}}}{\text{S2}_{\text{top}} + \text{S2}_{\text{bottom}}}, \tag{5.3}$$

where top/bottom refer to the observed signal in the top and bottom PMTs, respectively. Events which scatter in the gas have an S2 TBA > 0.4, while liquid events lie below this value. S2 TBA for liquid events is also typically not negative, because the scintillation signal from extracted electrons is near the top array. The events with negative S2 TBA in the middle right panel of Figure 5.11 were caused by a separate, minor pathology in the pulse finding and classification algorithm and were also removed by this cut. We highlight the main population of gas scattering events in green, which are the events inside of the dashed green selection in the left middle panel. These events have the characteristic drift time < 60 μs and S2 TBA > 0.4.

A separate DD calibration dataset, collected under the same LZ detector conditions, was also skimmed using a set of standardized cuts for DD event positions, drift times, and S1 timing. The resulting sample from the DD dataset was assumed to be a fairly pure neutron sample and was used to asses the impact of the cuts developed for the photoneutron analysis, summarized in Table 5.3. The efficiencies estimated from the DD dataset serve as upper limits since it contains some of the same pathologies as the photoneutron dataset, albeit in significantly reduced quantities. An additional set of cuts was developed from this DD dataset, targeting the width of the S2 pulse as a function of drift time. The width of the S2 was defined using *area fraction time* (AFT) quantities, which represent the time at which the integrated area of a pulse is a given percentage of its total. The panel on the bottom right shows the AFT 75 - AFT 25 quantity for the photoneutron events passing the other cuts described so far. The green curves show the 5-50-95% contours for the same quantity in the DD dataset, and the red dashed lines are linear fits to the 5% and 95% contours, where events inside of the dashed lines were accepted. The S2 width is typically a nonlinear function of drift time, but the relatively short drift times under consideration in this analysis obscure the nonlinear shape. Multiple AFT-derived quantities provide better information about pulse shape than any single one in isolation, which was previously leveraged in combination with machine learning in LUX [72]. In this case, we defined three separate S2 width cuts based

on three pulse shape quantities: AFT 75 - AFT 25, AFT 50 - AFT 25 and AFT 10 - AFT 5.

Table 5.3: The effect of the cuts shown in Figure 5.11 on the photoneutron and DD datasets. Each row shows the cumulative effect, where the % column is the percentage of the initial skimmed events remaining after the cut in each row. The photoneutron scatter selection efficiency was estimated as 76% from the number of DD events surviving the cuts.

	Photoneutron		DD	
Skimmed events	4,253		11,519	
Cumulative effect of cuts	#	%	#	%
Bad area	1,647	39	10,980	95
S2 TBA	215	5	10,316	90
S2 Width	35	0.8	8,775	76

The 35 events remaining after these cuts are shown in Figure 5.12, demonstrating promising overlap with the signal region where photoneutron single scattering events are expected. We estimated the recoil energy of these events using an S2-only reconstructed energy, defined by $g_2 = 58.19$ phd/electron and $Q_y = 7.06$ electrons/keV$_{\mathrm{nr}}$, the NEST 2.2.3 average for 1–5 keV$_{\mathrm{nr}}$. The S2-only energy is more reliable in this case, because the S1 population is strongly biased by the detection efficiency for S1s of this size. The energy spectrum of the data is shown in Figure 5.13, and compared to the equivalent quantity from simulations in red. The simulation histogram was scaled by the appropriate livetime and the estimated selection efficiency from the DD dataset of 76%. We expect 112 single scatter events from the simulated spectrum, leaving a discrepancy of an approximate factor of 3 between data and simulation.

The final event selection looks very promising as a set of candidate photoneutron scattering events when compared with the simulation prediction of the same spectrum. However, it is hard to argue definitively that these events are not just a small set of background events surviving all of the selection cuts due to the extreme fraction of events cut away. The factor of 3 difference between simulations and the data is less concerning; there are some efficiencies that remain unquantified in this comparison. The pulse finder and event classifier was ultimately tuned for quieter detector conditions, both due to a change in the high voltage settings of the detector and the relatively lower event rates of background acquisitions. Therefore, the efficiency of detecting few-photon S1s is not well quantified under the conditions of this calibration, particularly because the high event rate during the calibration induced a steady stream of single photon backgrounds in the detector. The combination of this factor and the relatively high uncertainties of the light and charge yields for nuclear recoils in this energy range could account for the remaining factor of 3 difference in the two spectra. Despite the remaining ambiguity, this first deployment was a success in testing the capabilities of the LZ detector and ensuring the calibration design was practically achievable.

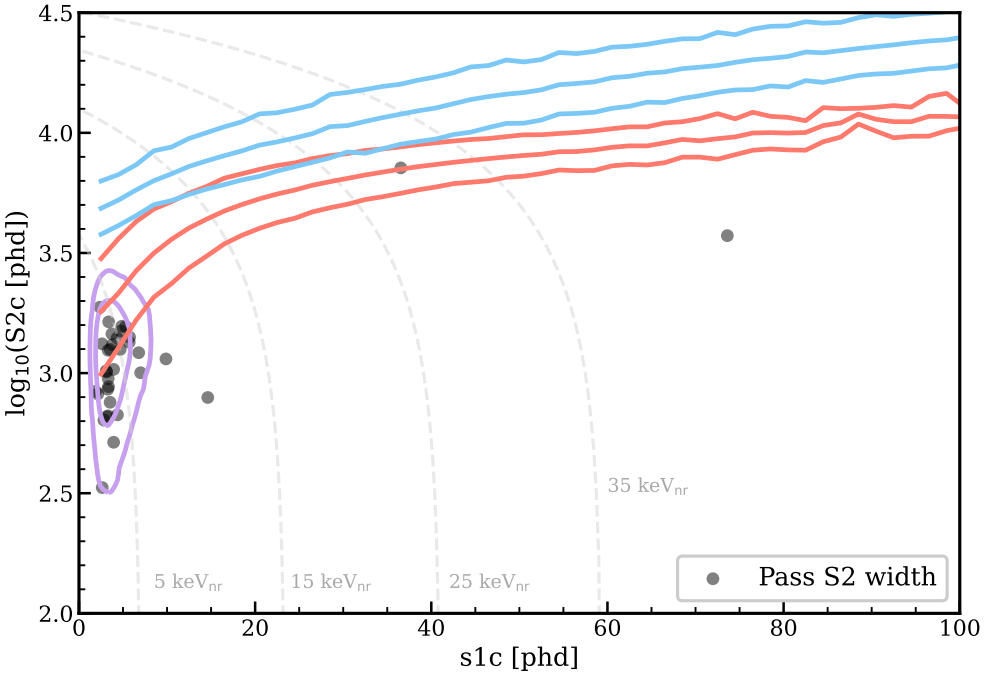

Figure 5.12: The final population of candidate events after the cuts shown in Figure 5.11. Also shown in the left column are the 10-50-90% bands for typical electronic recoils in blue and typical nuclear recoils in red. The expected 1- and 2-σ contours for photoneutron single scatter events in the fiducial volume are shown in purple.

5.6 Looking forward

There are several ways forward for the calibration approach described in this chapter. As was planned, future photoneutron calibrations of LZ will include more ^{88}Y runs, as well as datasets from ^{205}Bi, ^{206}Bi, and ^{124}Sb. Future deployments will also include the measurement of the gamma ray spectrum with the beryllium replaced by a magnesium target, which has a similar density to beryllium but does not produce photoneutrons for this gamma ray energy range. This photoneutron-less dataset will confirm the presence of photoneutrons rather than backgrounds passing selection cuts. An alternative low energy neutron source, based on reflecting DD neutrons using deuterium and hydrogen targets, provides a complementary calibration for similar nuclear recoil energies [145]. These methods have an entirely different set of systematic errors associated with their measurements, an invaluable cross-check in this difficult analysis regime.

The source described in this chapter was the subject of preliminary characterization studies at Lawrence Berkeley National Lab, using a ^{3}He proportional counter and polyethylene moderating layers to measure the neutron production and propagation through the shielding. These measurements yielded an estimated neutron production rate of 370 $\pm$ 9

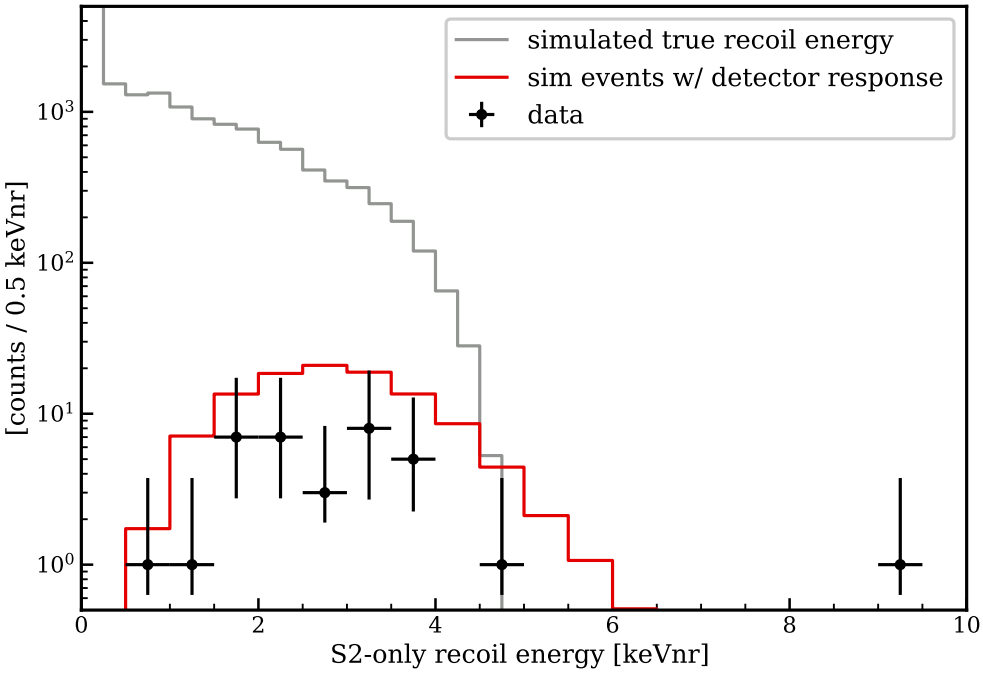

Figure 5.13: A comparison of the reconstructed energy of single scatter events passing the data selection cuts described in this section with simulated single scatter photoneutron events in the fiducial volume shown in Figure 5.6.

neutrons per second, comparable to the expected 343 neutrons per second estimated from the methods described in this chapter. A more extensive and detailed characterization analysis is planned, including making similar measurements in the underground SURF campus to reduce backgrounds.

Future analysis of photoneutron data will also benefit from the inclusion of outer detector signals, which were optimized to tag neutrons scattering in the TPC. This would serve as an alternative method of confirming events are neutron recoils rather than backgrounds. The next deployments will take advantage of a better understood LZ detector and improved analysis software, leaving future calibration runs poised for a successful identification of the photoneutron population and measurement of its recoil spectrum.

Chapter 6

The HeRALD Experiment

A dark matter physicist is exposed to countless acronyms describing experimental collaborations, detector technologies, readout technologies, signal topologies, groupings of all of these categories, and, of course, acronyms of the miscellaneous variety. Before we go further, we have to untangle the relationship of three such acronyms: TESSERACT, SPICE, and HeRALD.

TESSERACT, which stands for "Transition Edge Sensors with Sub-eV Resolution And Cryogenic Targets", is the name of a Department of Energy (DOE) project uniting different target materials for dark matter detection by via shared shielding, cryogenic, and readout platforms. As the name suggests, a large part of the TESSERACT research program revolves around transition edge sensors (TESs), which serve as the sensors to read out particle interactions in the different targets. Low threshold, large area calorimeters based on TES technology have been experimentally demonstrated [38, 146], already promising access to new parameter space in combination with the TESSERACT targets.

There are three different target materials currently included under the TESSERACT umbrella, which are sapphire (Al_2O_3), GaAs, and superfluid helium. Al_2O_3 and GaAs are both polar crystal materials, and together the experimental collaboration focusing on them is called the Sub-eV Polar Interactions Cryogenic Experiment (SPICE). The superfluid helium experiment is called the Helium Roton Apparatus for Light Dark Matter (HeRALD). Figure 6.1 is a schematic overview of the TESSERACT project, and Figure 6.2 shows how the targets are complimentary to one another in searching for dark matter in a variety of parameter spaces. Taken in its entirety, the TESSERACT experimental program has sensitivity to a large amount of yet-unprobed and theoretically interesting parameter space. Scientific results from this program are published under the joint SPICE/HeRALD collaboration.

Superfluid helium promises to be a particularly powerful probe of the nuclear recoil parameter space for dark matter masses below the typical GeV-scale WIMP. The rest of this chapter serves as an introduction to the HeRALD detector concept and the studies evaluating its sensitivity to produce the curves shown in the top left panel of Figure 6.2. An overview of the HeRALD detector and its nuclear recoil dark matter sensitivity was published in Physical Review D [148], to which the dissertation author contributed the gamma ray background

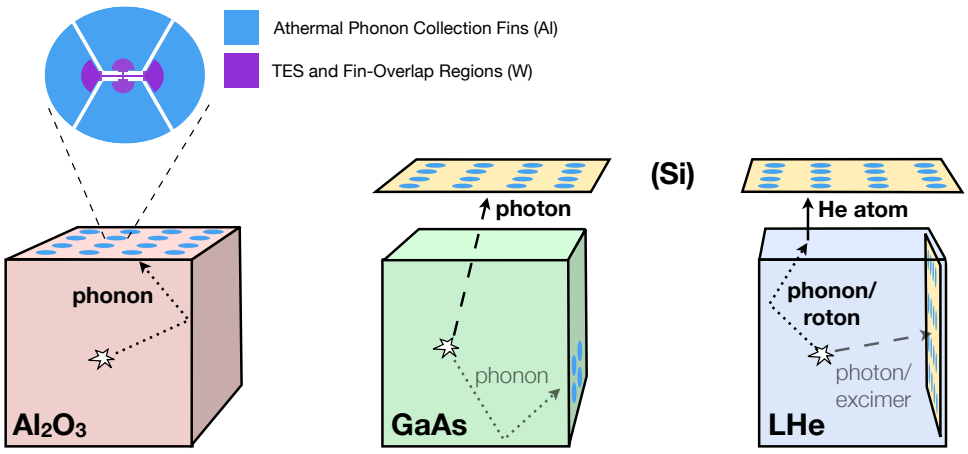

Figure 6.1: A visual overview of the TESSERACT dark matter detection project. The three target materials are complementary in dark matter sensitivity and significantly overlap in signal readout strategies. HeRALD is the name of the experiment using superfluid helium as the target material. Figure from [147].

estimates, as well as the signal modeling which will be described in more detail in the next chapter. We also summarize key results from the rest of the paper to set the context of the remaining chapters.

6.1 Detector design

Superfluid helium provides some basic advantages as a target material, particularly for light dark matter searches. Most immediately, helium is one of the lightest nuclei, allowing for better kinematic matching to light dark matter compared to other common detector materials. This matching means that the recoil energy endpoint for light dark matter masses is relatively higher compared to other target nuclei. Additionally, helium forms a superfluid down to zero K, allowing for a scalable target mass not susceptible to internal stress microfractures, identified as sources of spontaneous phonon bursts in cryogenic crystals [149].

The superfluid phase is beneficial for other reasons. A superfluid helium target boasts high radiopurity as contaminants freeze out at these temperatures and helium has no natural radioisotopes. It enables compatibility with calorimetric readout which requires temperatures in the 10s of mK. Scintillation signals and long-lived triplet excimers can be read out via calorimeters immersed in the superfluid target for a high fraction of geometric coverage. At these temperatures, quasiparticles are long-lived and propagate ballistically. The HeRALD design takes advantage of a unique process called quantum evaporation, where quasiparticles can eject individual helium atoms from the superfluid surface into the vacuum above. They eventually adsorb onto the surface of a calorimetric detector suspended in the vacuum and

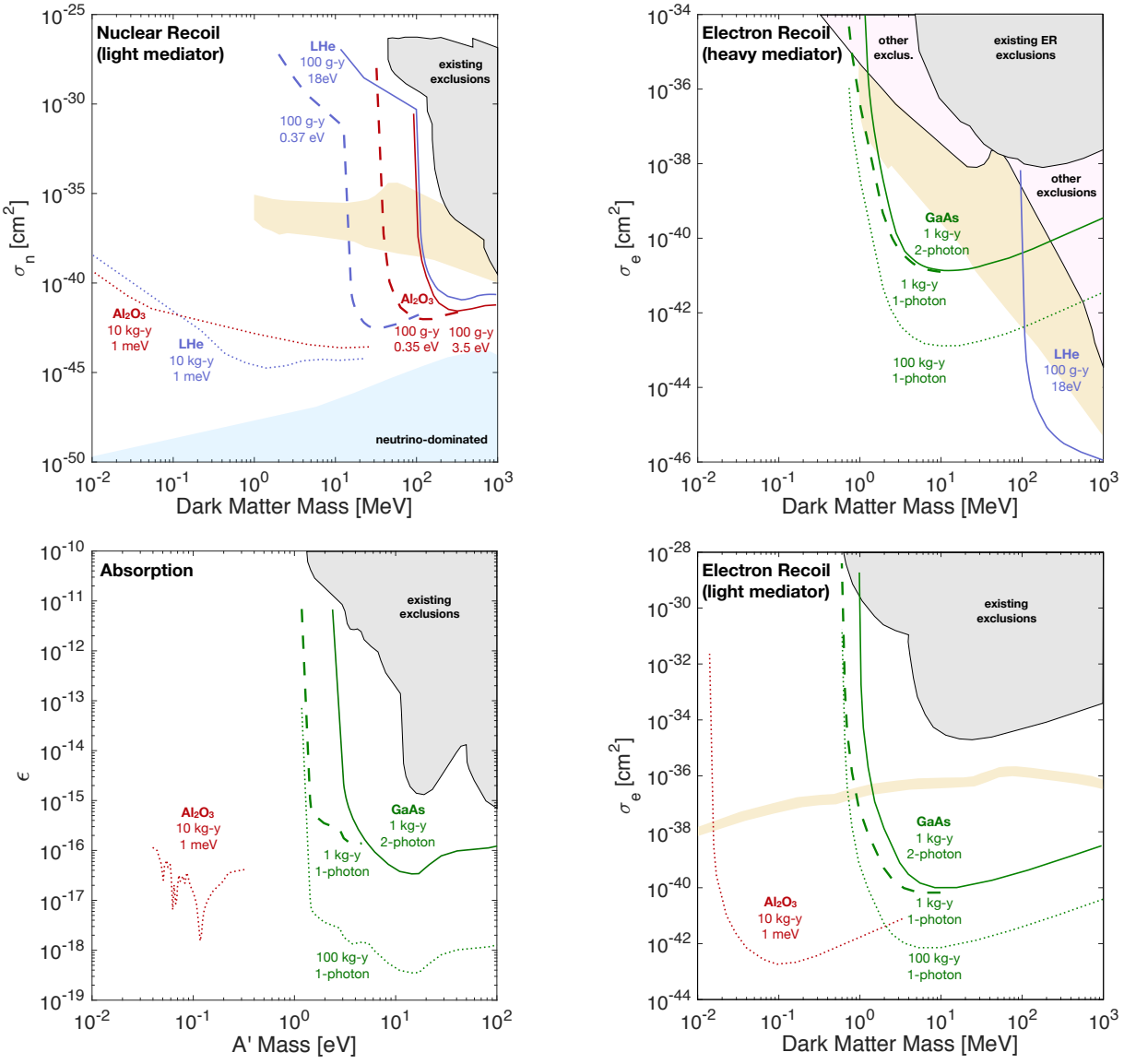

Figure 6.2: The projected sensitivities of the dark matter experiments under the TESSERACT umbrella. Solid lines assume already-demonstrated readout technology, dashed curves assume the baseline project goals for readout after further R&D, and dotted curves represent an absolute sensitivity for each technology. Grey and pink regions are already excluded by other experiments, and the light blue region is nuclear recoil parameter space dominated by neutrino interaction backgrounds. Orange regions represent theoretical regions of interest for dark matter models. Figure from [147].

release energy for readout. Coincidence signals from the quantum evaporation process are a potential avenue to vetoing stress events in the readout calorimeters.

There are, of course, some drawbacks relative to other target materials and detector designs as well. Due to its small number of nucleons, helium has a suppressed coherent enhancement factor in Equation 1.10 relative to other materials, leading to a reduced recoil rate for similar exposures. Additionally, the quasiparticle detection efficiency via quantum evaporation is relatively low, leading to a higher effective detection threshold for recoils in the helium target, despite the kinematic matching benefits described earlier.

HeRALD is based on a detector design proposed for solar neutrino studies called HERON [150, 151]. This design does not use any applied electric fields, but a liquid helium TPC dark matter experiment has also been proposed [152, 153]. The HeRALD design is summarized by Figure 6.3, and we will discuss the different signal channels and their detection in more detail in Section 6.2.

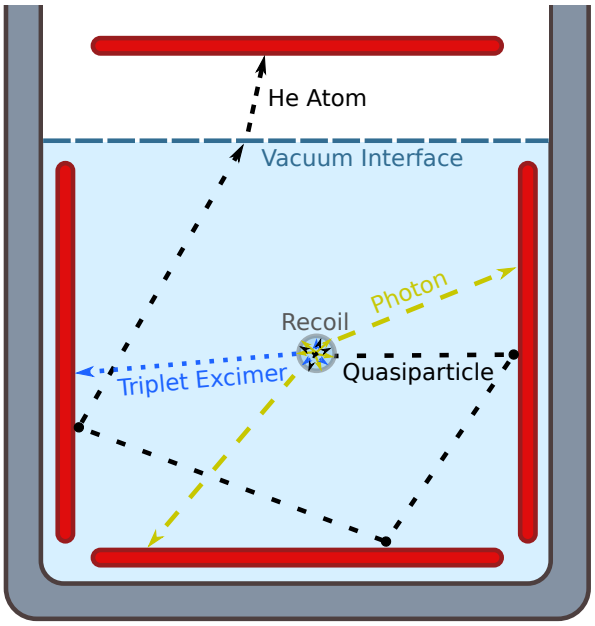

Figure 6.3: Simplified HeRALD detector signal readout scheme. Superfluid ^{4}He is blue, large-area calorimeters are red, and the passive containing vessel is grey. Quasiparticles are detected via quantum evaporation of helium atoms and other signals are detected with sensors immersed in the superfluid.

6.2 Signal channels

The precise partitioning of energy into different signal channels will be discussed in detail in the next chapter, but in this section we will give an overview of what those signal channels are

and how we detect them in the HeRALD detector concept. Unlike LZ, there is no applied electric field, so ionized atoms recombine and form neutral excited diatomic states called excimers. These may have some rotational energy, which is shed in the form of eV-scale IR photons. The $A^1\Sigma_u^+$ singlet state decays on the order of nanoseconds into 16 eV UV photons. All of these photons can be detected by the calorimeters in the HeRALD experiment with high efficiency, particularly since the design offers a high degree of geometric coverage. In subsequent steps leading to the sensitivity estimates, we assume a detection probability of 0.95 for photon signals.

The $a^3\Sigma_u^+$ triplet state also has a binding energy of about 16 eV, but it is unusual due to its 13 second half-life [154]. These states have been shown to travel at the meter per second scale [155], so they will traverse the length of the helium target and quench on the immersed calorimeters before decaying directly. The readout of this quenched energy in superfluid helium-immersed calorimeters has been experimentally demonstrated [156]. This signal, delayed from the prompt scintillation photons, will be visible in immersed calorimeters. In the absence of clear evidence of what happens to triplet excimers at the vacuum interface, we assume these are not detected and adopt a detection efficiency of 5/6, stemming from the cubic detector geometry shown in Figure 6.3.

Quasiparticle behavior in superfluid helium is largely defined by the dispersion relation, shown in the top panel of Figure 6.4. Unlike most other condensed materials, the dispersion relation has two local extrema, leading to a region of negative slope. The resulting shape divides helium quasiparticles into three categories: phonons and two kinds of rotons. The R- roton is the particle defined by region of negative slope in the dispersion relation, and the R+ roton takes over when the slope turns positive again. One consequence of the dispersion relation is a region of quasiparticle stability around the energy range defined by the local maximum and minimum, shown as the white region in Figure 6.4. Quasiparticles below this region have a finite lifetime defined by $\Lambda = A\epsilon^5$ where ϵ is the quasiparticle energy in K and $A = 7.12 \times 10^5$ s^{-1}, and those above the region of stability can also decay to two or more phonons or rotons [157].

While there exists a region of quasiparticle stability, the bottom panel of Figure 6.4 also indicates that the transmission of quasiparticles into solid materials is very unlikely, a feature also known as a high Kapitza resistance. This panel represents a simplified view, since these probabilities are also dependent on the angle of incidence. Detailed estimates of this angle dependence are provided in [148]. Evaporation of a helium atom at a vacuum interface is generally much more likely, motivating the HeRALD detector design. Measuring evaporated atoms with a suspended calorimeter turns out to be beneficial, rather than just a necessity, due to the release of binding energy when a helium atom adsorbs to the surface of the detector. This Van der Waals energy is typically about 10 meV [158], but could be up to 42.9 meV in theory [159]. Crucially, these energies are much larger than the single meV scale quasiparticles causing the evaporation, representing a significant gain in the detected signal.

Quasiparticles that do not transmit through the solid interface or evaporate a helium atom reflect, in principle. In this context, reflection includes conversion from one species

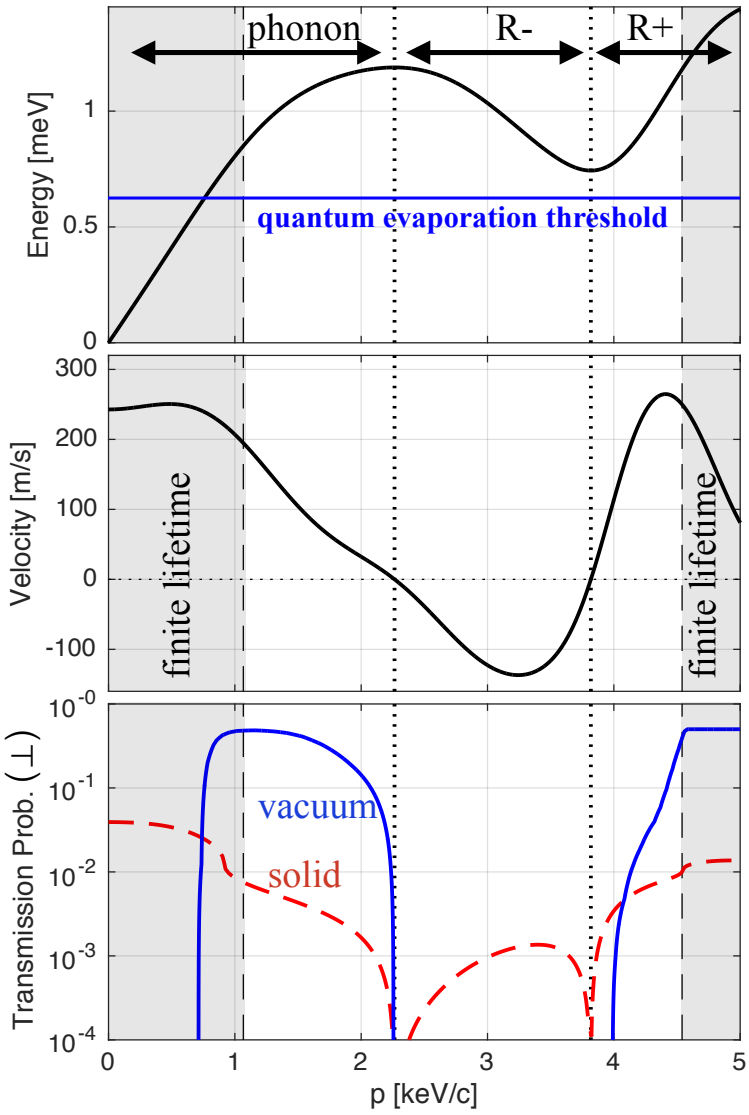

Figure 6.4: A summary the properties of superfluid ^{4}He quasiparticles. Top panel shows the dispersion relation of superfluid ^{4}He. Quasiparticles are classified into three categories; phonons and two kinds of rotons, defined by the slope of the dispersion relation. Equivalently, classification is by the sign of the quasiparticle velocity, shown in the middle panel. The bottom panel is the transmission probability into vacuum (blue) or a solid material (red) at normal incidence. The grey regions show the regions where decay into two lower energy quasiparticles is possible. Figure made by S. Hertel.

of phonon or roton to another. However, theoretical and experimental understanding of this reflection probability is very poor, and R&D from the HERON experiment observed a detection efficiency of about 5% of quasiparticle energy released in an event [160]. To bridge the gap between theoretical reflection and transmission probabilities, we performed a Monte Carlo simulation of quasiparticle propagation in a superfluid helium target. There are many details and points of discussion to be found in [148]; here we summarize the main results via Figures 6.5 and 6.6. In both figures, the probability of a phonon or roton down converting in a surface interaction to quasiparticles with energy below the evaporation threshold energy is varied, from the conservative 0.7 value yielding agreement with the observed fraction of 5%, to a number closer to the theoretical prediction of only 0.01. Figure 6.5 shows how the event length extends as quasiparticles reflect from more surfaces until eventually evaporating. Increasing the total evaporation fraction by improving the quasiparticle reflectance of calorimeters is one way to substantially lower the threshold of the experiment, and is a possible direction for future R&D. For the sensitivity studies described in this chapter, we remain conservative and use the observed detection fraction of 5% for the quasiparticle channel.

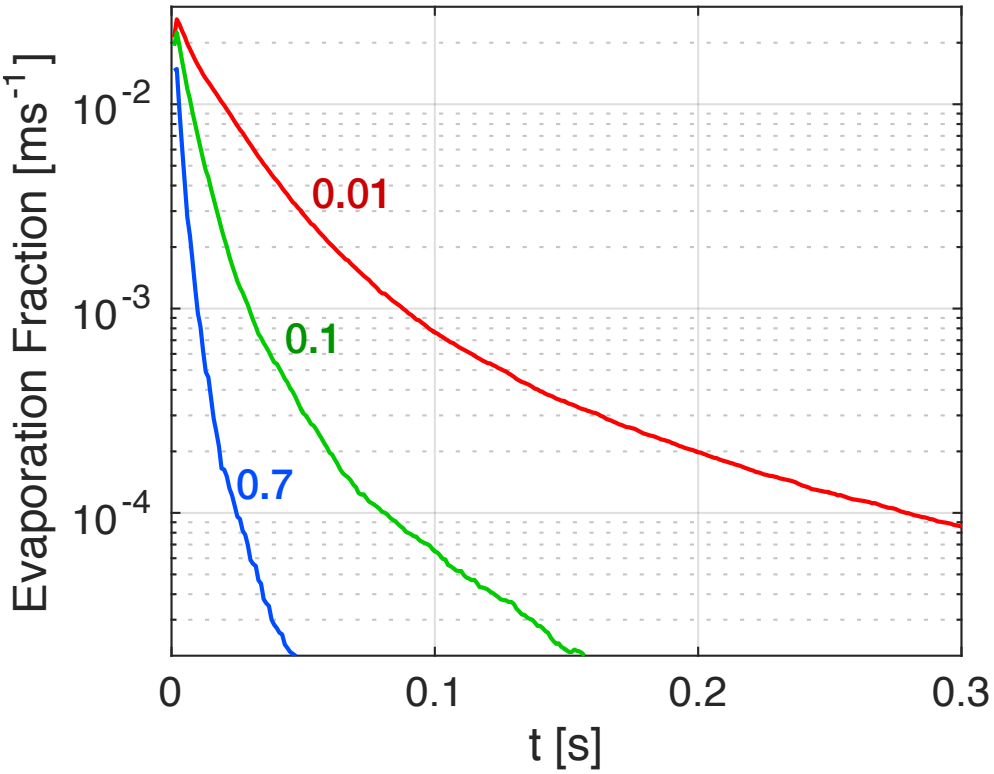

Figure 6.5: Simulation results for quasiparticle evaporation timescales, with varying solid interface quasiparticle loss probability. These results correspond to a 20 cm height, 20 cm diameter superfluid ^{4}He target. Figure made by S. Hertel.

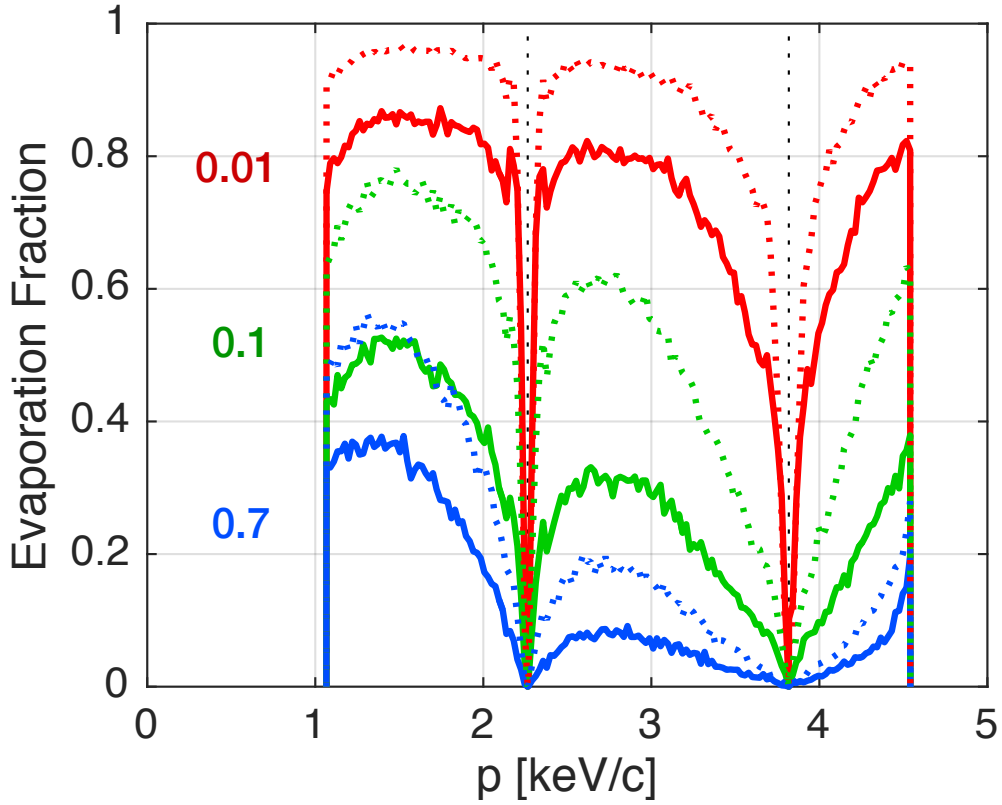

Figure 6.6: Simulation results for quasiparticle evaporation probabilities, with varying solid interface quasiparticle loss probability. Solid lines show results corresponding to a 20 cm height, 20 cm diameter superfluid ^{4}He target, while dashed lines correspond to a "pancake" geometry with 20 cm height and infinite radius. Figure made by S. Hertel.

An event depositing energy into the superfluid helium target will yield signals in the energy dependent ratios in the top panel of Figure 6.7, separated by nuclear and electronic recoils. This model is a projection and its construction is described in more detail in Chapter 7. For the sensitivity study, fluctuations were applied to these mean fractions by independently sampling Poisson distributions for the singlet, triplet and IR channels, and taking the remaining energy to be in the quasiparticle channel. Additional binomial fluctuations are applied via the detection efficiencies for each channel as we have listed them in this section, and the addition of a Gaussian noise with $\sigma_e = 0.5$ eV for each channel. The resulting signal bands are shown in the bottom panel of Figure 6.7, yielding clear separation at keV scales and above. These bands can be used to identify nuclear and electronic recoils, rejecting background events from dark matter candidates.

The energy of exciting a helium atom to the $n = 2$ state is 19.77 eV. Below this energy, there are no electronic excitations, so events are read out purely through the quasiparticle channel. At energies above this threshold, event reconstruction is driven mostly by photon

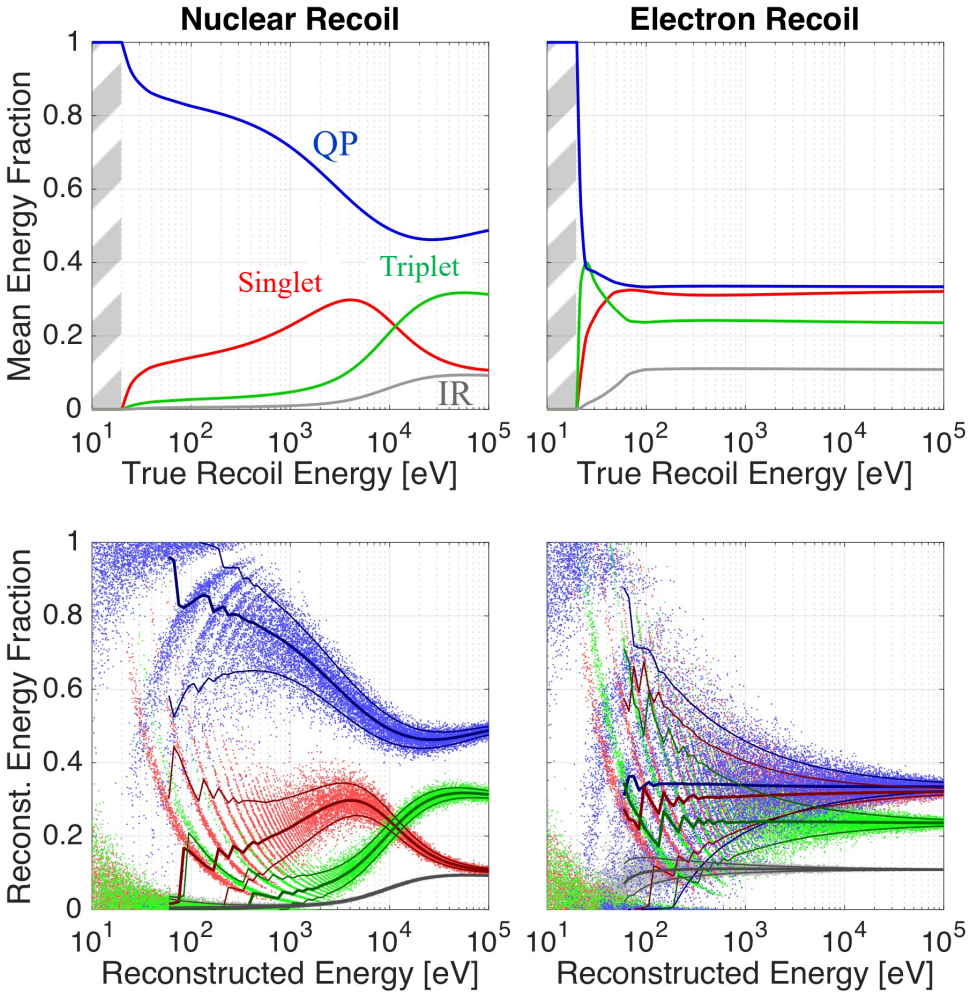

Figure 6.7: Signal channel energy partitioning for the HeRALD detector. The mean fraction of recoil energy going into the quasipartcle (QP, blue), singlet (red), triplet (green), and infrared (IR, grey) channels is shown in the top panels, for nuclear recoils (left) and electron recoils (right). The calculation of this energy partitioning model is described in detail in Chapter 7. The mean values in the top panels serve as inputs for Poisson fluctuations and binomial detection probabilities to model the detected signals in the bottom panels. The bottom panels also show the median and 10%-90% interval of the simulated distributions. Figure made by the dissertation author and S. Hertel.

signals, yielding two regimes of HeRALD: the quasiparticle-only regime and the electronic excitation regime. While extensive R&D on superfluid helium quasiparticle propagation and readout is critical to the future sensitivity of the HeRALD experiment, near-term goals require a good understanding of the energy partitioning presented in the top panel of Figure 6.7 as it is a key tool in rejecting some of the background events described in the next section.

6.3 Background modeling

Unlike most other experimental targets, helium has no natural radioactive isotopes, and due to the extremely cold temperature of the superfluid helium it is possible to purify almost all contaminants from the target itself. Still, the target is surrounded by other cryogenic and shielding materials, so radiogenic backgrounds will populate any dark matter search data.

In order to quantify the magnitude of radiogenic gamma backgrounds, GEANT4 simulations [77–79] were performed on a simplified detector with shielding geometry modeled on the proposed design of the SuperCDMS SNOLAB experiment [161]. The simulation geometry, depicted in Figure 6.8, consisted of a cube of ^{4}He in nested layers of copper surrounded by layers of high density polyethylene (HDPE), lead, and water, with thicknesses derived from the SuperCDMS SNOLAB design. Simulations were performed on geometries with 0.01 kg, 1 kg, 10 kg, and 100 kg active ^{4}He masses. We used a modified version of the SHIELDING physics list to account for atomic shell effects in Compton scattering and neglected any detector response effects in producing the electron recoil spectrum. Gamma rays produced in significant amounts in the ^{238}U, ^{232}Th, ^{40}K, ^{60}Co, and ^{137}Cs decay chains, assuming secular equilibrium where relevant, were generated uniformly and isotropically in each component of the simulation geometry assuming the same impurity concentrations as SuperCDMS SNOLAB [161].

Gamma rays can also coherently scatter in materials in the form of Rayleigh, nuclear Thomson, and Delbrück scattering, which become significant sources of nuclear recoils at low recoil energies [162]. The gamma ray coherent scattering cross section was computed as the coherent sum of Rayleigh scattering using nonrelativistic form factors [163], direct calculation for nuclear Thomson scattering, and interpolated amplitudes for Delbrück scattering [162, 164]. Structure effects from collective atomic interactions, which may significantly modify the total cross section at recoil energies below 100 meV, were not considered.

To calculate the associated spectrum, the simulated gamma ray flux into the detector was combined with the coherent sum of cross sections contributing to elastic gamma scattering, assuming only single scattering events. This single scatter approximation is valid down to gamma ray energies of about 1 keV, where the mean free path for this process is comparable to the meter-scale dimensions of largest target volume considered in the simulations. The maximum recoil energy at this gamma ray energy is only 50 meV, and the computed cross sections are dominated by shallow-angle scattering with even lower recoil energies. At more common nuclear decay gamma ray energies of a few hundered keV, the mean free path for coherent scattering in liquid helium is several hundred meters. The coherent scattering recoil

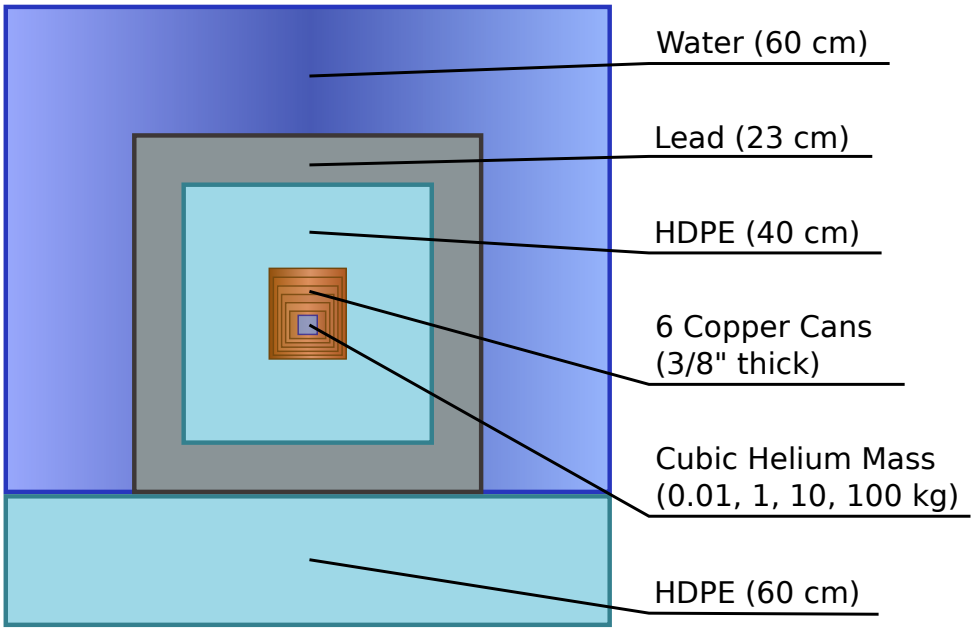

Figure 6.8: Simulation geometry used to estimate gamma ray backgrounds in a simplified HeRALD detector volume for several masses of the ^{4}He target. Each component was cylindrically symmetric except for the ^{4}He volume, which was cubic. The thicknesses of the shielding components were adapted from SuperCDMS [161]. The radial dimensions of the copper shells were set by the size of the central ^{4}He volumes.

spectrum was calculated according to

$$\frac{\mathrm{d}R}{\mathrm{d}E_r} = D \int \frac{\mathrm{d}N}{\mathrm{d}E_\gamma} \frac{\mathrm{d}\sigma}{\mathrm{d}E_r} \mathrm{d}E_\gamma, \tag{6.1}$$

where $\mathrm{d}R/\mathrm{d}E_r$ is the differential recoil rate, D is the number of ^{4}He atoms per unit mass, $\mathrm{d}N/\mathrm{d}E_\gamma$ is the gamma flux, and $\mathrm{d}\sigma/\mathrm{d}E_r$ is the differential cross section at a particular recoil energy. GEANT4 implementations of coherent gamma scattering–including contributions from Rayleigh, nuclear Thomson, and Delbrück scattering–have been developed [165, 166] allowing for the direct simulation of these processes, but they were not available while this work was conducted and published in [148].

While it may be possible to discriminate multiple and single scattering events by examining TES hit patterns, doing so does not substantially alter background rates for recoil energies of interest since the mean free path for Compton scattering in helium is also relatively long. In the analysis of simulated events, we do not consider discrimination between single and multiple scattering. The bottom panel of Figure 6.9 shows the gamma ray background rates for a 1 kg ^{4}He target, distinguishing between nuclear recoils from coherent scattering and electron recoils from Compton scattering. It also shows the power of electron

recoil discrimination at energies above the 19.77 eV binding energy of helium, simply using the ratio of observed atomic excitation (singlet, triplet, and IR) to observed quasiparticle energy from the bottom of panel of Figure 6.7.

Also shown in Figure 6.9 is the background due to coherent neutrino scattering from solar, atmospheric, and supernova neutrinos. It was treated using the methods described in [167]. We also considered environmental neutrons as a possible background source by simulating the detector geometry shown in Figure 6.8 in a volume with the inner dimensions of the Davis cavern at the Sanford Underground Research Facility (SURF) surrounded by 0.5 m of rock with the same composition and radioactive impurities assumed by LUX-ZEPLIN (LZ) studies [89]. The spectra of neutrons produced in the rock by spontaneous fission and (α, n) reactions from ^{232}Th and ^{238}U decays, as found by LZ simulations [89], were sampled to simulate a year-long exposure. Since no events were found to deposit energy in the helium volume, we conclude that neutron events are subdominant to other backgrounds in the energy window of interest, although neutron backgrounds must be studied more carefully with more detailed detector geometries in the future.

All of the backgrounds discussed so far are due to physical interactions in the detector that are not caused by dark matter. However, there is another class off events that may be considered more instrumental in nature. These are often harder to predict, but can be the limiting factor in experiments pushing to lower energy thresholds. While we do not consider these kinds of backgrounds directly in the sensitivity study in the next section, we present some arguments as to the qualitative benefits of the HeRALD detector design in mitigating such instrumental backgrounds.

A major background in many dark matter experiments is the degradation of the signal from high energy events due to poor signal collection. We note that these types of events usually occur at boundaries of sensitive detector volumes and passive materials, while the the helium target and the readout sensors are in direct contact and both signal-generating materials. There is perhaps a possibility for signal degradation in the helium between the vessel wall and calorimeter, but in this case, the signal will appear predominantly in that one calorimeter rather than spread out over multiple sensors. The availability of multiple signal channels and several sensitive detector readout channels can help in identifying and reconstructing events of this nature. Similarly, the detailed information spread over these different kinds of channels can be leveraged to distinguish between genuine recoils in the detector target from other types of events.

Finally, we consider the pileup in time of multiple events. In the most extreme case, for a 100 kg cubic helium volume with meter-scale side lengths, the integrated rate of background events from the simulations amounts to approximately 0.25 events per second. For comparison, the estimated quasiparticle fall time is about 20 ms, leading to about 0.5 seconds for the decay of an MeV-scale event to recover single-atom evaporation sensitivity. Similarly, assuming a triplet excimer velocity of about 2 m/s [155], we find a maximum of about 0.5 seconds for the signal to appear in the detector readout. We emphasize these are rough calculations for the largest detector volume considered, yielding a Poisson overlap probability of about 10%. The comparable estimate for the smaller targets to be implemented in the

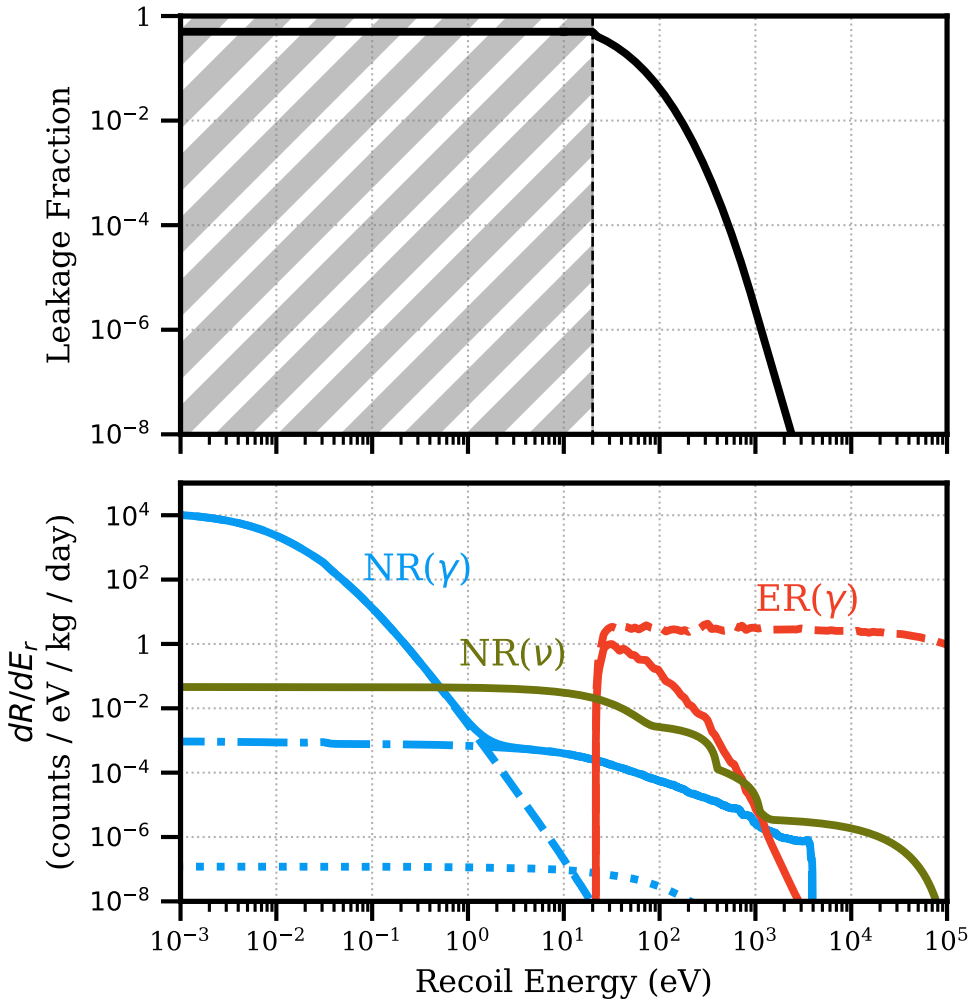

Figure 6.9: The top panel shows the electron recoil leakage fraction assuming 50% nuclear recoil acceptance, defined as the ratio of total observed atomic excitation (singlet, triplet, and IR) to observed quasiparticle excitation using the bottom panel of Figure 6.7. In the shaded region (below 19.77 eV), atomic excitation is impossible. In this region, there is no discrimination ability based on atomic excitation, but there are also no electron recoil backgrounds. The bottom panel shows the predicted recoil energy spectra contributing to electron recoil (ER) and nuclear recoil (NR) backgrounds assuming a 1 kg liquid ^{4}He detector mass. Total gamma ray ER backgrounds (dashed red line) were simulated directly and multiplied by the ER leakage fraction to obtain the post-discrimination ER backgrounds (red line). Gamma NR backgrounds (solid), including Rayleigh (dashed), nuclear Thomson (dash-dotted), and Delbrück (dotted) scattering, are in blue. Coherent elastic nuclear scattering of astrophysical neutrinos appears in green.

earlier generations of the experiment yield considerably smaller overlap estimates, so we do not consider this effect in our sensitivity projections.

6.4 Sensitivity projections

Sensitivity projections were estimated using a similar profile likelihood ratio (PLR) framework as described in Section 3.4. In this case, the signal and background PDFs were constructed as functions of only the deposited energy, and the event detection efficiency was taken to be 100% above the assumed energy threshold. The discrimination curve in the top panel of Figure 6.9 was applied to the Compton scattering backgrounds, at the cost of 50% acceptance in nuclear recoil signal and backgrounds above the ionization threshold of 19.77 eV. The resulting sensitivity projections are shown in Figure 6.10, overlaid on the same parameter space landscape of Figure 1.12, with the view extended to lower dark matter masses.

We consider four generations of the HeRALD experiment, starting with a 40 eV threshold based on technology that has already been demonstrated: calorimeters with 3.9 eV baseline noise [146], a 5% efficiency for turning recoil energy into evaporation signal [160], and a gain factor of 9 for helium adsorption on silicon [158]. As we have noted in this chapter, all three factors are subject to active research to push to lower thresholds.

We consider three additional generations with successively thresholds, also stepping up the exposure with each. As the detector threshold is lowered below the excitation threshold of 19.77 eV, coherent scattering of solar neutrinos becomes the dominating background, creating the first bump in the limit curves just below 1 GeV dark matter mass. The intermediate generation sensitivities have been extended to lower masses by including an additional PLR study looking for dark matter-induced bremsstrahlung emission [168]–a strategy similar to the Migdal effect search described in Chapter 4. When the cross section for dark matter interaction is large enough, detectors deep underground can be shielded from dark matter scattering by the overburden of the Earth [36]. We show the sensitivity limit to large cross sections assuming a 1478 meter overburden, although we also showed comparable curves for a 100 m overburden in [148], which reduce the gap to previously probed parameter space.

The ultimate threshold for the technology of the detector is about 1 meV due to the energy required to evaporate a single helium atom. Searches for dark matter masses at about 50 MeV and below are dominated by coherent gamma ray scattering, leading to the second bump in the sensitivity curve. With such a low threshold, it becomes worthwhile to search for events consisting of off-shell phonon production, where the additional degrees of freedom from the simultaneous production of two phonons extend the amount of energy that can be deposited in the detector by light dark matter [169]. The two-phonon curve shown in Figure 6.10 has been rescaled from [169] to correspond to a 100 kilogram year exposure.

Dark matter electron scattering was also considered. The sensitivity projection is shown in the top right of Figure 6.2, but more details and a plot focused on superfluid helium can be found in [148].

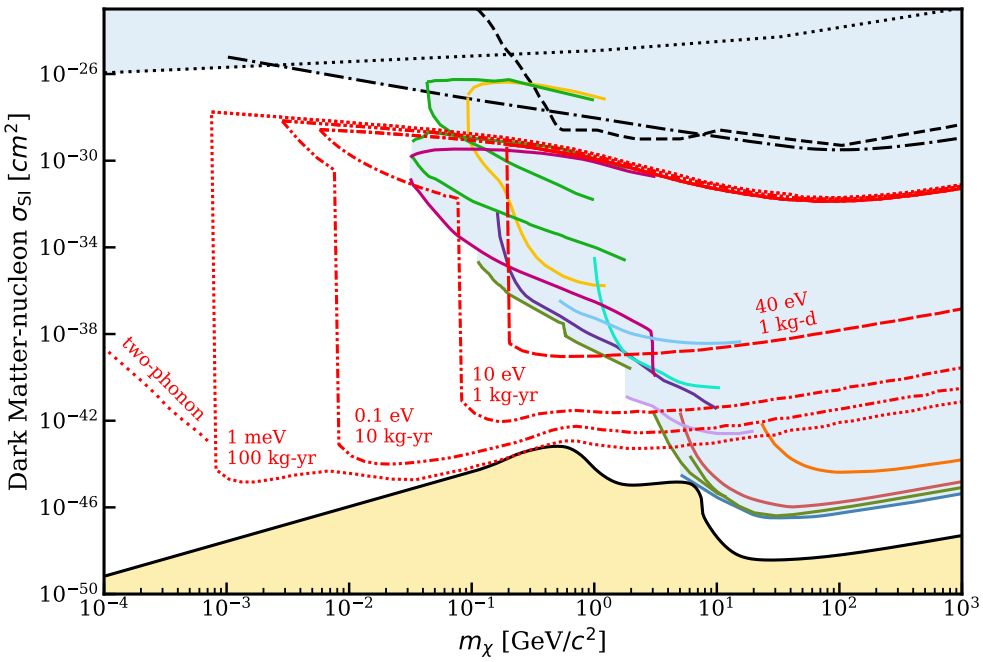

Figure 6.10: Projected 90% confidence sensitivity curves of several generations of the HeRALD detector concept, using the background model described in Section 6.3. The four curves are labeled with threshold and exposure assumptions. Additional considerations are sensitivity extensions to lower masses via searches for bremsstrahlung photon emission [168] and exclusion regions extending to a maximum cross section due an assumed 1478 m overburden [36]. Single atom evaporation ultimately limits the threshold to 1 meV. The sensitivity can also be extended by searching for off-shell phonon scattering [169]; here the estimated sensitivity curve has been re-scaled to a 100 kg-yr exposure. Other features of this plot are the same as those labelled in Figure 1.12.

A large portion of these sensitivity projections rely only on the quasiparticle signal. In this regime, below the excitation threshold of 19.77 eV, modeling the formation and propagation of quasiparticles is crucial. There are large theoretical and experimental uncertainties, motivating future studies. However, in the near term, more important to the sensitivity is the signal modeling in the top panels of 6.7. The detection, reconstruction, and background identification of events scattering in the helium target rely on these projections, which have not been validated to the low energies of interest, particularly for nuclear recoils. We devote the remaining chapters of this thesis to discussions of the signal model in detail, measurements probing that model, and development of a neutron source for future measurements at lower recoil energies.

Chapter 7

Modeling Signals in Superfluid Helium

We gave a brief summary of the different signal channels that can be read out in a superfluid helium target in Section 6.2. Figure 6.7 presented a model of the partitioning for the fraction of recoil energy in each of those channels for nuclear and electronic recoils. In this chapter, we describe that model in more detail.

The cross section calculations in section 7.2 mostly follow the methodology published by T. Ito and G. Seidel [170]. Similar calculations, with some differences in the underlying cross section data, were also presented in work by W. Guo and D. McKinsey [171]. Methods for turning cross section data into full predictions for energy partitioning were previously presented by G. Seidel [172, 173].

The material in this chapter is pulled from the dissertation author's contributions to two publications, where a) the signal modeling was crucial to estimating the sensitivity of the HeRALD experiment to dark matter [148] and b) the signal model was directly compared to experimental data from neutron scattering on superfluid helium [174]. Since this comparison included an analysis of afterpulsing in the data, we also discuss the extension of this model to predict delayed scintillation by R. Smith based on the work of King and Voltz [175].

7.1 Signal channels

The four signal channels available for readout in the HeRALD detector concept are UV photons, triplet excimers, IR photons, and quasiparticles via quantum evaporation of helium atoms. Figure 7.1 shows an abstracted flow chart of how recoil energy from particle interactions ends up in these four channels. The primary products of a recoil are ionized atoms and their liberated electrons, excited diatomic molecules called excimers, and heat in the form atomic motion. In HeRALD there is no applied electric field, so ionized atoms recombine on short timescales, yielding additional excimers and heat. Excimers may have additional energy above the ground state energy of around 16 eV, which is radiated away in eV-scale

IR emissions. As we have previously discussed in Section 6.2, singlets decay very quickly on nanosecond timescales, while triplets have a much longer 13 s half life [154]. Excimers can also de-excite nonradiatively via the Penning process,

$$\begin{aligned} \mathrm{He}_2^* + \mathrm{He}_2^* &\rightarrow 3\mathrm{He}(1^1S) + \mathrm{He}^+ + \mathrm{e}^- \\ \mathrm{He}_2^* + \mathrm{He}_2^* &\rightarrow 2\mathrm{He}(1^1S) + \mathrm{He}_2^+ + \mathrm{e}^- \end{aligned} \tag{7.1}$$

where energy is released in the form of heat and the free ion and electron recombine to form a new excimer [170].

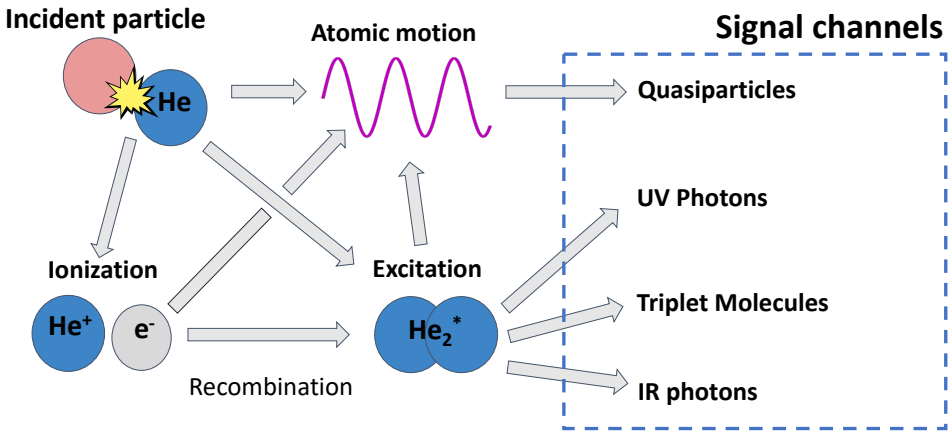

Figure 7.1: A general schematic of the de-excitation pathway of energy deposited in a particle interaction in a helium detector target.

Energy for particle interactions may also end up in topological defects called quantum vortices. The fraction of energy appearing this channel should be very small compared to the processes shown in Figure 7.1 [176]. We also note that there is no evidence for their formation via the Kibble-Zurek mechanism in superfluid ^{4}He [177, 178], so we do not consider them further in the model presented in this chapter.

The ratio of energies following the different pathways in Figure 7.1 is different for nuclear and electronic recoils, owing to different recoil track densities and cross sections for ionizing and exciting helium atoms. The resulting difference in energy collected in the various signal channels allows for the discrimination between event types as demonstrated in Figure 6.7. To build up to the model shown in Figure 7.1, we first consider the ratio of ionizations to singlet and triplet excitations we expect from a particle recoil via the well-studied and extensive scattering cross sections available for helium.

7.2 Building on cross section data

The cross sections for an electron ionizing the recoiling helium atom or exciting it to the lowest singlet or triplet state are theoretically and experimentally known [179] and plotted in Figure 7.2. In the case of a gamma ray scatter, we consider the primary recoiling electron from the interaction and proceed with a generalized electronic recoil case. Our aim for the rest of this section is to construct estimates for ionization and excitation cross sections in the nuclear recoil case.

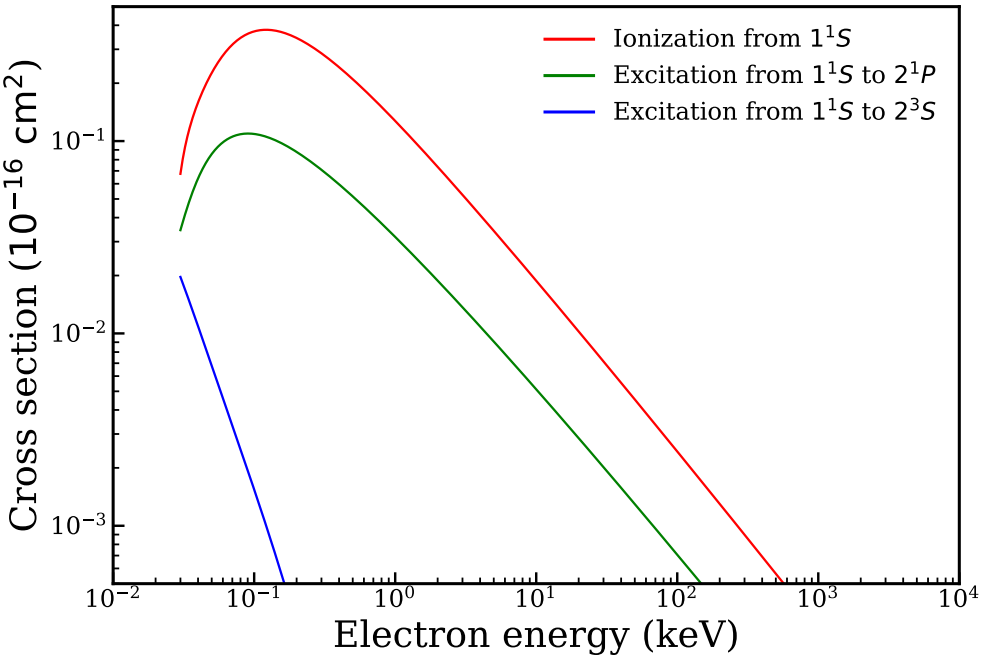

Figure 7.2: Electron impact cross sections for ionization and excitation of helium atoms. Figure reproduced from [173] with original data from [179].

7.2.1 Helium charge states

A nuclear recoil from a neutron or dark matter particle transfers energy to a single helium atom which goes on to interact with other helium atoms in the medium. Recoiling helium atoms can occupy three charge states, with different He-He scattering cross sections for each state. The equilibrium charge state fraction as a function of the helium projectile energy is shown in Figure 7.3. Helium atoms arrive at these equilibrium charge states extremely quickly over the formation of the recoil track [171]. Therefore, we do not consider the initial charge state of a recoiling helium atom but rather the equilibrium values at its recoil energy.

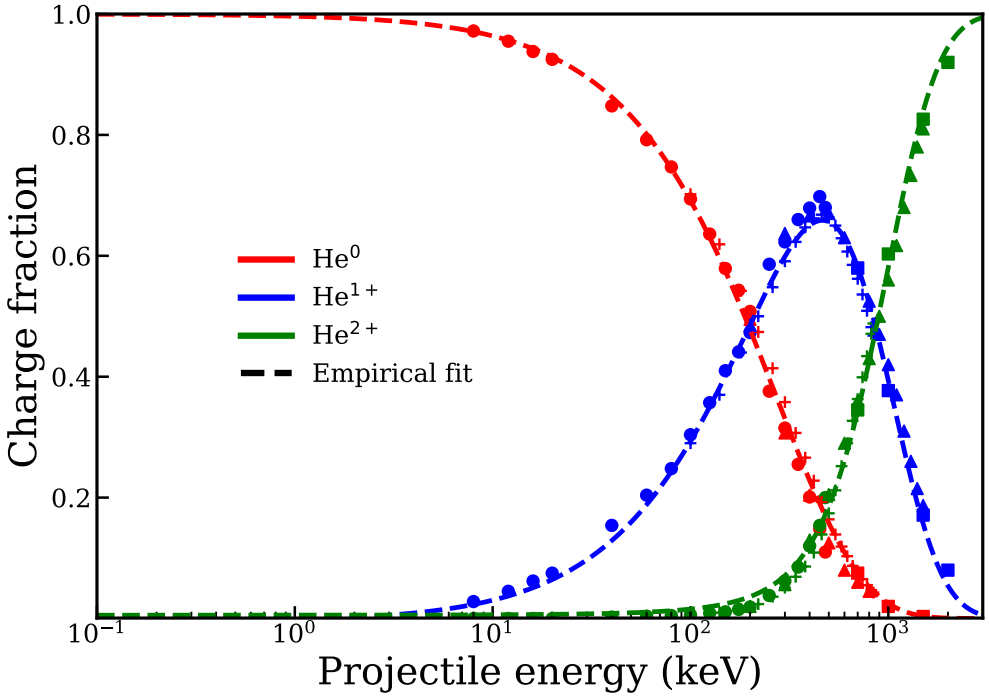

Figure 7.3: The fraction of helium atoms in a particular charge state as a function of kinetic energy. Experimental data plotted with markers: circles [180], crosses [181], triangles [182], squares [183]. Lines are empirical fits to the data. Figure reproduced from [170] with new empirical fits.

7.2.2 Atomic cross sections

Experimental He-He scattering cross sections are widely available for the different charge states of helium projectiles. These describe the process of ionization or excitation of helium target atoms by the projectile helium atom. Figure 7.4 shows the ionization cross sections for the three charge states from various datasets spread over different energy ranges [184–194]. As in [171], we fit the cross sections with polynomials in log-log space

$$\log(\sigma) = \sum_i C_i \log(E)^i, \tag{7.2}$$

using third order polynomials in all three cases and extrapolating where necessary. We compare to the fits presented in [170], which included most, but not all, of the same datasets. We omit one dataset shown in unfilled green triangles in the top panel [189], because it does not match well with the trends shown in other data.

Effective ionization cross sections, computed as the product of the charge fractions of Figure 7.3 and the ionization cross sections in Figure 7.4, are shown in Figure 7.5. These represent the ionization cross sections applicable to a recoiling helium atom of a particular

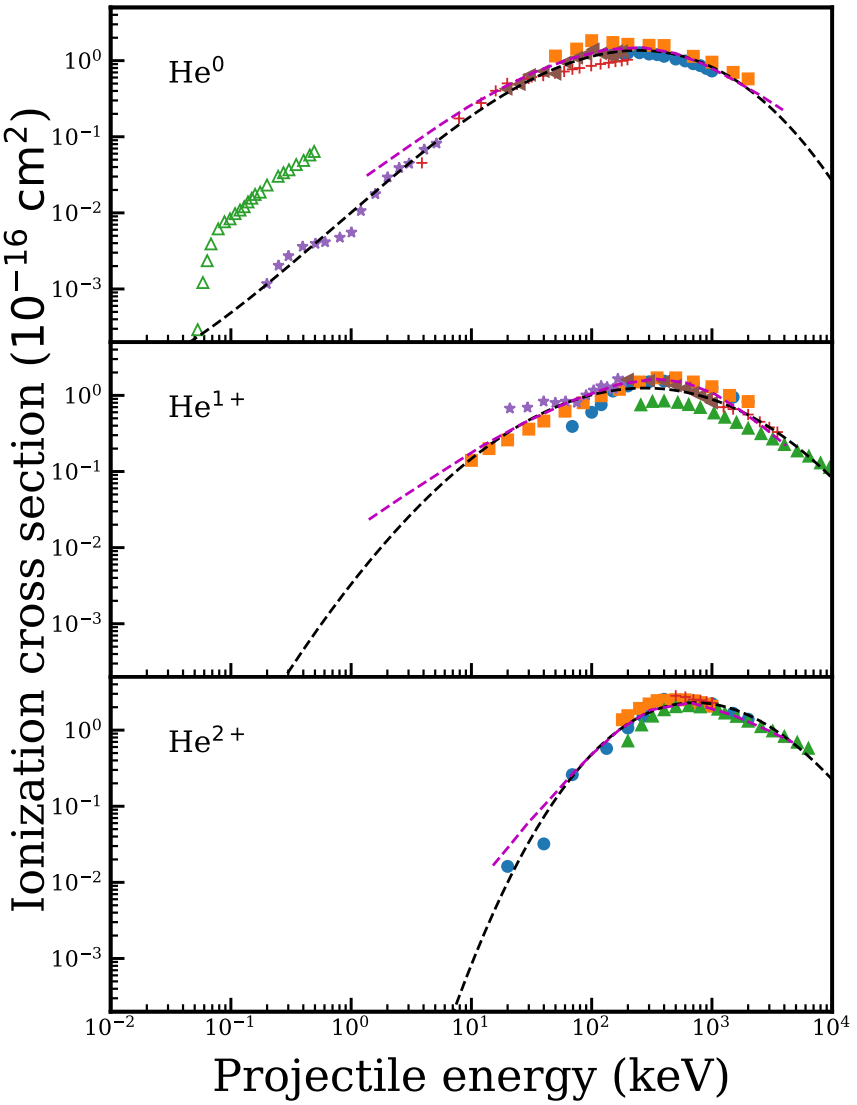

Figure 7.4: Collection of experimental data for ionization cross sections for helium atoms in different charge states. Empirical fits to data used in this work are dashed black curves. Also shown are the empirical fits to a subset of this data from [170] as dashed magenta curves. Top panel: blue circles [184], orange squares [185], red crosses [186], purple stars [187], brown triangles [188]; green triangles [189] not included in empirical fit. Middle panel: blue circles [190], orange squares [191], green triangles [192], red crosses [193], purple stars [188], brown triangles [194]. Bottom panel: blue circles [190], orange squares [184], green triangles [192], red crosses [194]. Reproduced from [170] with additional datasets and new empirical fits.

energy, due to the equilibrium charge states at each energy. Since the effective cross section is ultimately the quantity of interest, differences between the polynomial extrapolations in black and the extrapolations in magenta from [170] in Figure 7.5 are largely irrelevant except in two cases. The extrapolation to lower energies for neutral helium atoms in the top panel is the dominant contribution to the effective cross section. However, we note that data extends down to 200 eV [187] and that the polynomial fit follows this data well until that point. The high energy extrapolation for the He^{2+} state is also significant in the model, where data extends to about 6 MeV [192]. The extrapolation from the polynomial fit could possibly be improved in this case based on trends in the MeV-scale data, but our interests generally lie at lower recoil energies.

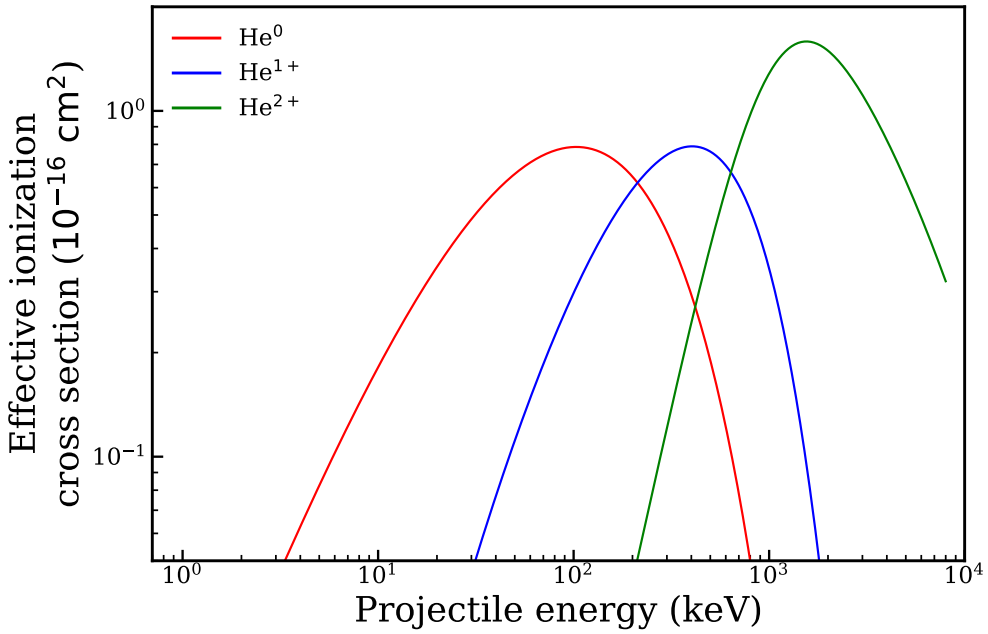

Figure 7.5: The effective ionization cross sections for helium atoms of each charge state recoiling on helium atoms. Computed by taking the product of the dashed curves from Figure 7.3 and the dashed black curves in each panel of Figure 7.4. Reproduced from [170] with new empirical fits.

Constructing similar effective cross sections for the case of atomic excitations is more difficult due to the available experimental data. Figure 7.6 shows experimental data from the datasets [195–200] compiled in [170], which describe the excitation from the ground state to the lowest lying excited state, which is a singlet state. Neutral helium data were fit with a fourth-order polynomial and singly-ionized data were fit with a sixth-order polynomial function. In the case of He^{2+}, the only available data concerns simultaneous excitation and charge exchange, and we include theoretical values from the same source [200]. In the absence of a good polynomial fit to the available He^{2+} values, a cubic spline function was

used for fitting and extrapolation instead. We find the effective cross sections for excitation to singlets, shown in Figure 7.7, by taking the product of the fitted curves with the charge fractions from Figure 7.3, and multiplying by a factor of 1.4 to account for higher energy states as estimated by [170]. This modification means that Figure 7.7 represents the total effective excitation cross section, rather than just the lowest energy transition shown in Figure 7.6.

Electrons from ionized helium atoms, called secondary electrons, can produce further ionizations and excitations, modifying the effective cross sections in Figures 7.5 and 7.7. To estimate the effect of secondary electrons on these effective cross sections, we follow a similar procedure as described in [170], by first computing the secondary electron energy spectrum with the semiempirical expression from [201]. We find the average secondary electron energy above the ionization energy of 19.77 eV and count the average number of ionizations by dividing by the helium electron W value of 43 eV. We take the ratio of excited helium atoms to ionized ones to be 0.45 [170]. Finally we add to each of the cross sections the ionization cross section times the estimated number of secondary electrons, scaling by their estimated contribution to either ionization or excitation. The effective ionization and excitation cross sections after the consideration of secondary electron effects are shown in solid black in Figure 7.8, and again compared to the equivalent curves presented in [170] (ionization in dashed red and excitation in dashed blue). The addition of the secondary electron contributions reduces the magnitude of excitation cross section extrapolation differences between this work and [170].

The ultimate quantity of interest for the energy partition calculation is the ratio of effective ionization cross section to effective excitation cross section. The fraction of the total effective cross section in ionizations is shown in Figure 7.8. The differences in the effective cross sections between our model and the curves from [170] do not result in a large modification to this ratio once secondary electrons are taken into account. This is particularly true in the recoil energy range of 53.2 to 1090 $\mathrm{keV_{nr}}$, the range of the experimental data described in Chapter 8.

7.3 Predicting energy partitioning

The energy partitioning represents the fraction of recoil energy in each of the signal channels in the box in Figure 7.1. We compute these fractions by assigning characteristic energies to the different de-excitation pathways represented by the arrows leading from one population to the next. We follow [173] for these characteristic energies; Figure 7.10 provides intuition for many of the values. Singlet and triplet excimers were each assigned average energies 16 eV. Since excimers arise from both the ionization channel via recombination and direct excitation, the IR channel was assigned 4 eV for each ionization atom and 2 eV for each excited-state atom to account for decaying higher energy states. The quasiparticle channel is assigned 2 eV for each dimer formed and 4 eV for dissociation of ground state helium atoms after excimers decay. Secondary electrons with energy below the 19.77 eV excitation threshold

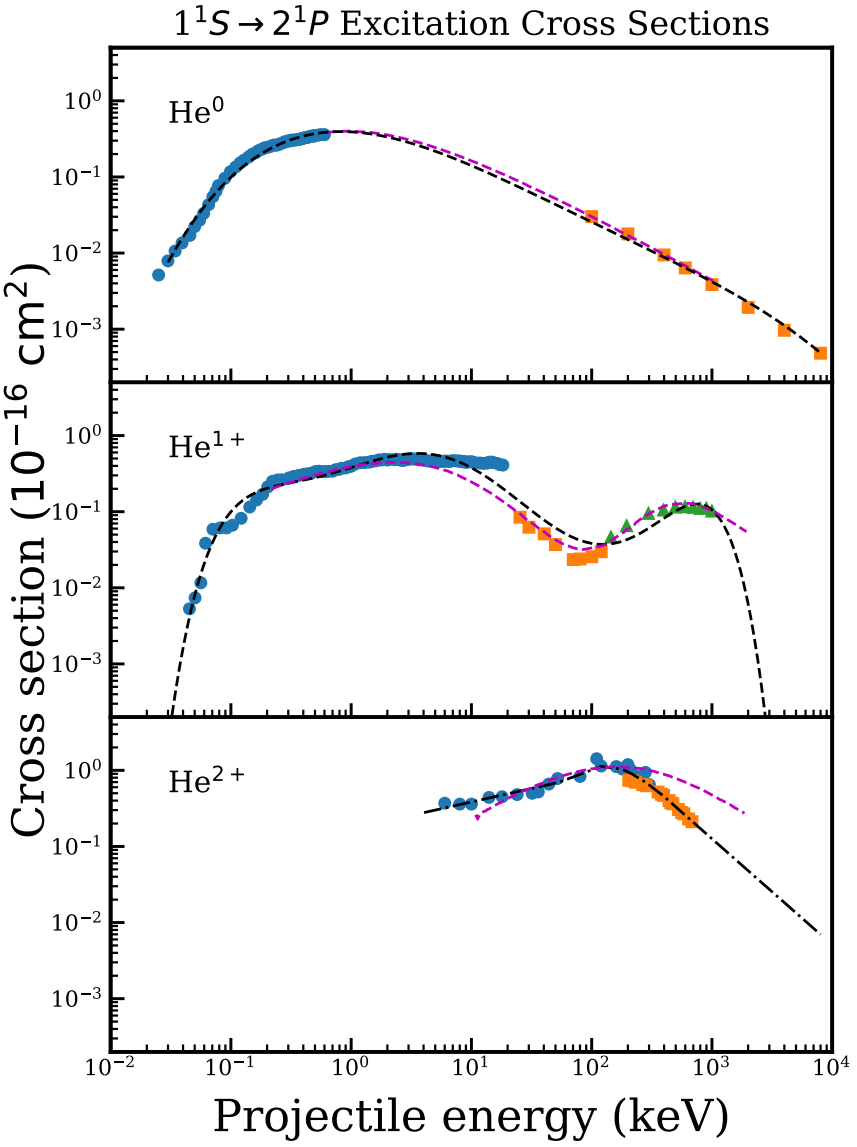

Figure 7.6: Collection of theoretical predictions and experimental data for the direct excitation of ground state helium atoms by helium atom projectiles in different charge states. Empirical fits to data used in this work are dashed black curves. Also shown are the empirical fits from [170] as dashed magenta curves. Top panel: blue circles [195] scaled as in [170], orange squares are theory values from [196]. Middle panel: blue circles [197], orange squares [198], green triangles [199]. Bottom panel: blue circles are experimental data from [200] and orange squares are theoretical values from [200], which describes simultaneous excitation and charge exchange. Reproduced from [170] with new empirical fits.

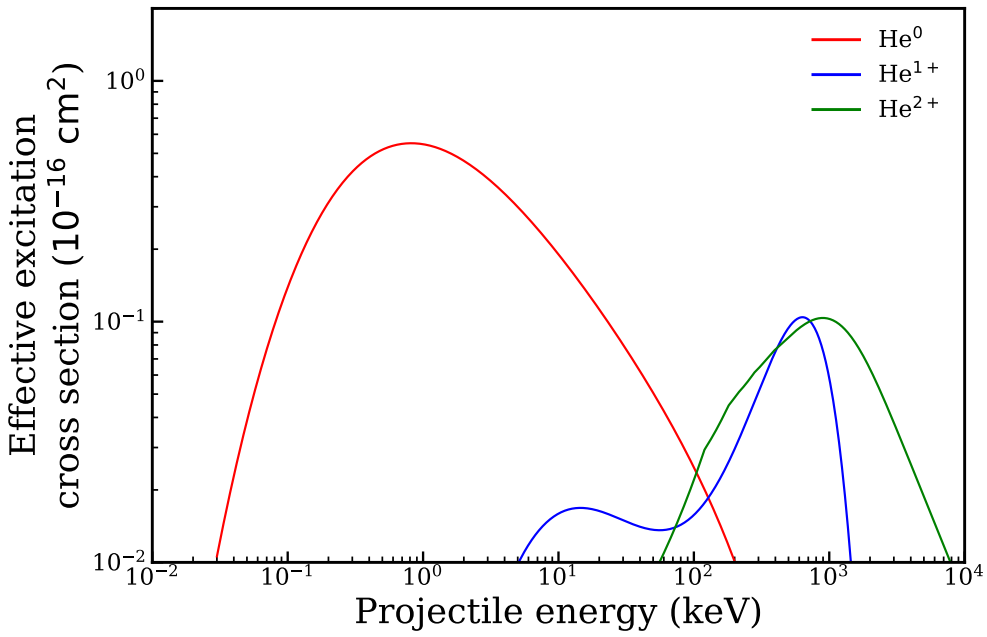

Figure 7.7: The effective excitation cross sections for helium atoms of each charge state recoiling on helium atoms. Computed by taking the product of the dashed black curves from Figure 7.3 and the dashed curves in each panel of Figure 7.6, and multiplying by a factor of 1.4 to account for higher energy states as in [170]. Note the He^{2+} curve is for the process of simultaneous excitation and charge exchange, due to the absence of other experimental data.

energy lose their energy as an additional contribution to the quasiparticle population. We assign 8 eV as the average contribution to the quasiparticle channel from these subthreshold secondary electrons, consistent with [170]. These assigned characteristic energies were the same for both electronic and nuclear recoils.

7.3.1 Electronic recoil partitioning

For the partitioning fractions in the electron recoil case, we estimate the ratio of ionizations, singlet excitations, and triplet excitations by the ratio of the cross sections from Figure 7.2. For ionized atoms, we assume geminate recombination yielding a fraction of 50% singlet excimers due to the low track densities associated with electron recoils. The resulting energy partitioning for electron recoils is shown in Figure 7.11. The model prediction is relatively flat with recoil energy over a wide range, which we probe experimentally in Chapter 8. The electron cross sections extend all the way to the exciation threshold of 19.77 eV, below which we assume all recoil energy appears in the detector as quasiparticles. In the right panel of

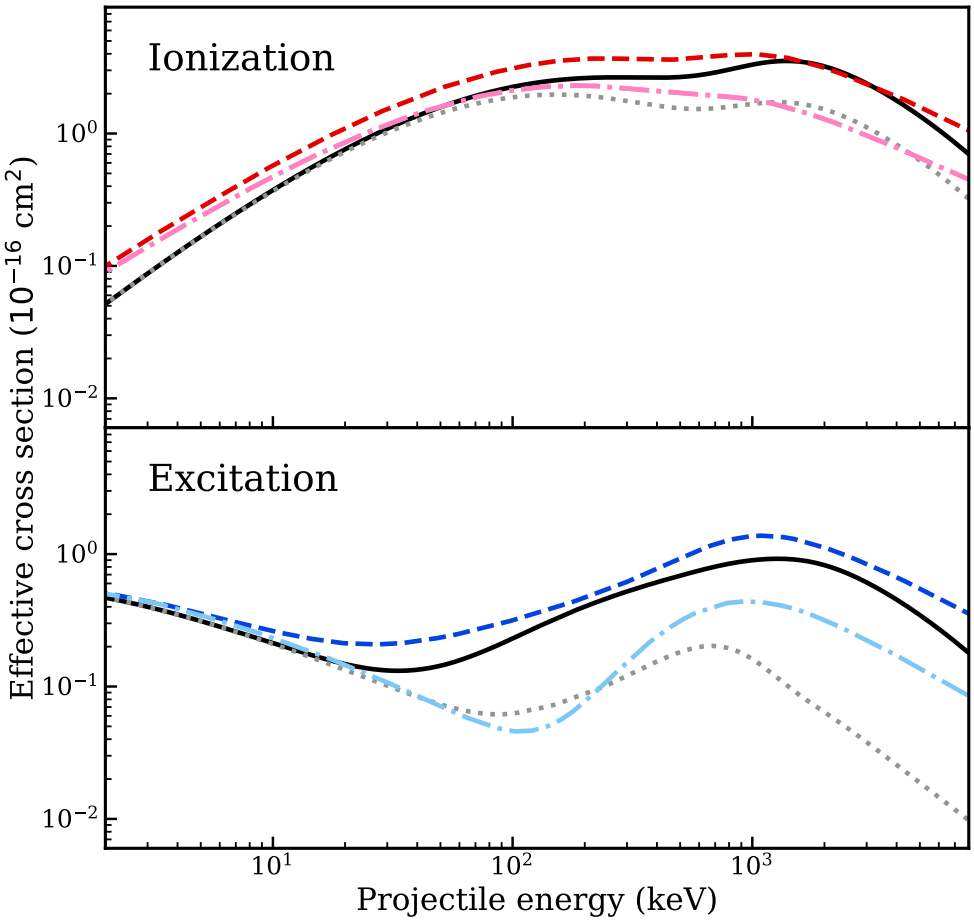

Figure 7.8: Effective ionization and excitation cross sections used to compute the energy partitioning of nuclear recoils in superfluid helium. For the model compared to data in Chapter 8, we use the curves for ionization with secondary electrons and excitations with secondary electrons (solid black in both panels). We also compare ionizations without secondary electrons and excitations without secondary electrons (dotted gray in both panels) to show the effect of secondary electrons in the model. The cross sections used in this work are compared to [170], from which the curves shown in Figure 7 are plotted here: ionization without secondary electrons (dash-dotted pink), ionization with secondary electrons (dashed red), excitation without secondary electrons (dash-dotted light blue), excitation with secondary electrons (dashed blue).

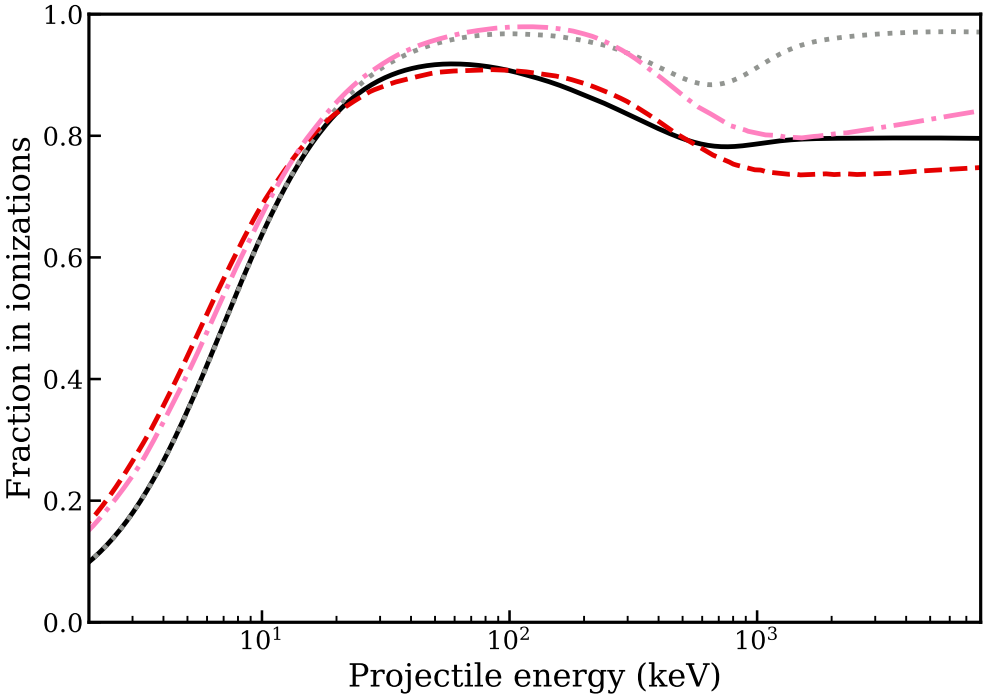

Figure 7.9: The fraction of effective cross section associated with ionization in the sum of ionization and excitation cross sections. The curve from this work (solid black) is computed from the solid black curves in Figure 7.8, which include the effects of secondary electrons in the effective cross sections. For comparison, we also show curves computed without the effect of secondary electrons (dotted gray), and curves from [170] without secondary electrons (dash-dotted pink) and with secondary electrons (dashed red).

Figure 6.7, we smoothly extrapolated the electronic excitation curves to 0 at this threshold.[1]

7.3.2 Nuclear recoil partitioning

In the case of nuclear recoils, we first assume an overall partitioning between energy deposited by nuclear stopping ν and deposited by electronic stopping (via ionizations and excitations) η, as

$$E = \nu + \eta. \tag{7.3}$$

Following the Lindhard model [202], the nuclear portion of this partitioning is given by

$$\nu(\epsilon) = \frac{\epsilon}{1 + kg}, \tag{7.4}$$

[1]There were minor revisions to aspects of the signal model after this plot was published, including to the characteristic energies. The ones used in Figure 6.7 were detailed in [148].

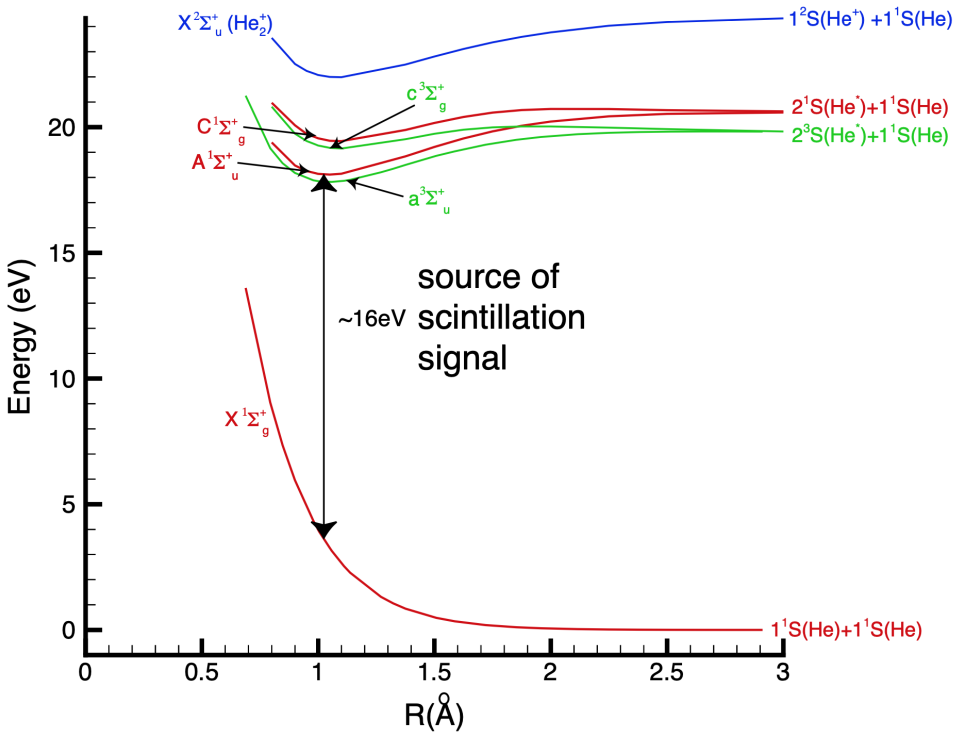

Figure 7.10: The potential energy of helium excimer states and the He-He interatomic energy as a function of atomic distance. Figure copied from [176].

where $\epsilon = 11.5E/Z^{7/3}$ is a reduced energy (with E in keV and Z the atomic number), $k = 0.133\ Z^{2/3}A^{-1/2}$ (with A being the atomic mass) and g is well approximated by $g = 3\epsilon^{0.15} + 0.7\epsilon^{0.6} + \epsilon$ [203]. The relative fraction of energy appearing in each Lindhard channel, shown in Figure 7.12, is the ratio of ν to η. We assume the fraction of energy deposited in the ^{4}He through nuclear stopping will be efficiently converted to quasiparticle excitations.

Within the electronic partitioning fraction, energy will appear as ionization and excitation with the energy-dependent ratio from Figure 7.9. Ionization results in a 1:3 ratio of singlet to triplet excitation after recombination, since the electron and ion spins should be uncorrelated in the dense recoil track environment. In the case of direct excitation, the estimated singlet:triplet excitation ratio is 0.86:0.14 [170].

In tracks of high excimer density, excimer-excimer interactions can result in Penning quenching. We estimate the scale of this effect following again a model presented in [170], in which the density of excited atoms, n, at a recoil site is given by the differential equation

$$\frac{\mathrm{d}n}{\mathrm{d}t} = -\gamma n^2 - \frac{rn}{\tau}, \tag{7.5}$$

where γ is a bimolecular rate taken to be the same for all species, $r = 0.4$ is determined

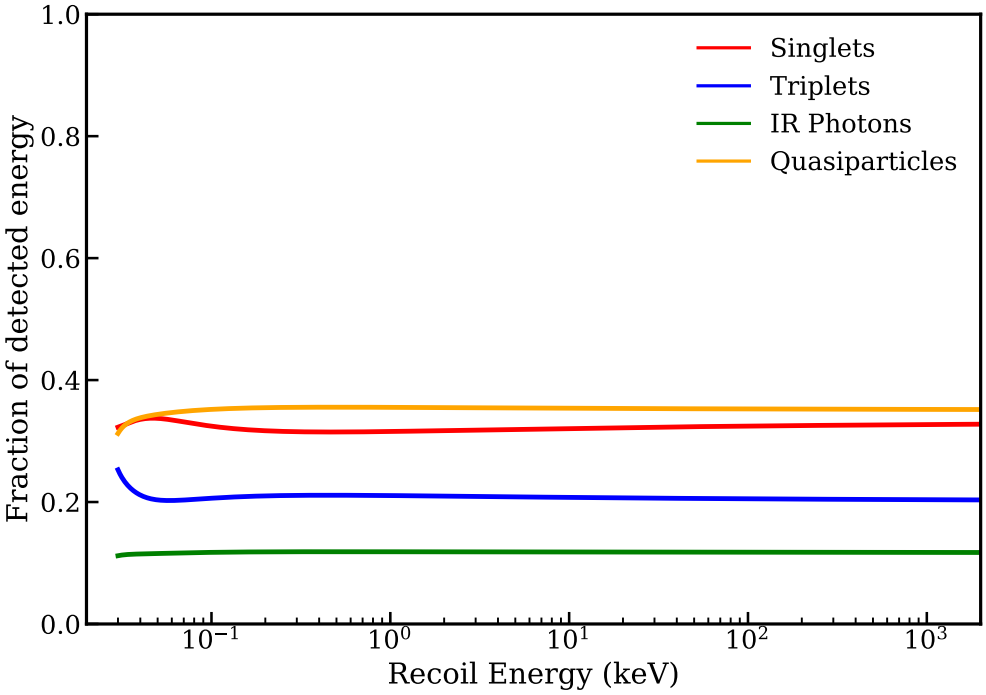

Figure 7.11: Electron recoil energy partitioning into observable signal channels.

by the fraction of singlet excitations, and τ is the singlet lifetime. The Penning quenching factor

$$f = \frac{1}{n_0}\int_0^\infty \frac{rn}{\tau}\mathrm{d}t = \frac{\ln(1+\xi)}{\xi}, \tag{7.6}$$

with $\xi = n_0\gamma\tau/r$, is the fraction of excimers that decay radiatively, while the rest of the energy is quenched and appears in the quasiparticle channel. This parameter has been estimated as $f = 0.5$ with calorimetric measurements of 5.5 MeV α particles [170, 204, 205]. Using the linear track density calculations from [170], a rough estimate of the bimolecular rate is $\gamma = 13$ cm^{-1} s^{-1}. We adopt the same parameters for the quenching model applied to the energy partitioning in this work.

The resulting energy partitioning for nuclear recoils is shown in Figure 7.13. Below ~10 keV, the region most interesting for a dark matter detector like HeRALD, singlet excitation dominates the electronic stopping. The fraction of energy appearing in quasiparticle modes also steadily increases toward lower energies in this region. Helium cross section data for ionization extend down to about 200 eV, below which we extrapolate the value as shown in the top panel of Figure 7.4. The relevant excitation cross section data extend down to the excitation threshold near 20 eV. As in the electronic recoil case, we assume the sub 20 eV response is solely quasiparticles, so we enforce a condition at the electronic channels are 0 at this threshold.

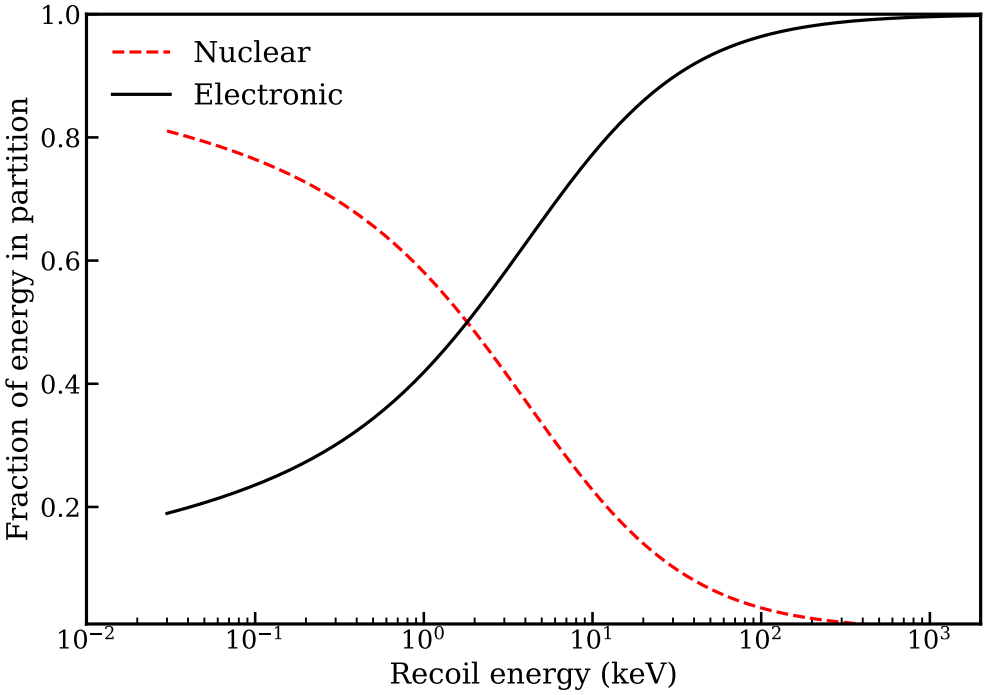

Figure 7.12: The Lindhard partitioning of nuclear recoil energy into nuclear motion (dashed red) and electronic excitation and ionization (black) [202], computed according to the approximation presented in [203].

Compared to electron recoil case, we expect less energy in singlet scintillation signal, as is the case in other noble elements. The model does predict a peak in scintillation yield between 1 and 10 keV, an interesting feature for experimental verification of the calculations. The quenching model applied to Figure 7.13 assumes relatively long timescales due to the readout times of the HeRALD detector design, on scales up to several hundred milliseconds. However, the experiment described in Chapter 8 measured 32 μs event windows, giving a window into time scales relevant to the Penning quenching process. For comparison to that data, we predict the delayed scintillation yields using the unquenched energy partition fractions as input.

7.4 Delayed scintillation

The Penning process between two triplet molecules can yield a singlet excimer from the recombination of the electron ion pair on the right hand side of Equation 7.1. This can occur on relatively long time scales due to the 13 s half life of the triplet state [154]. A model of the scintillation time dependence associated with Penning quenching of triplets in

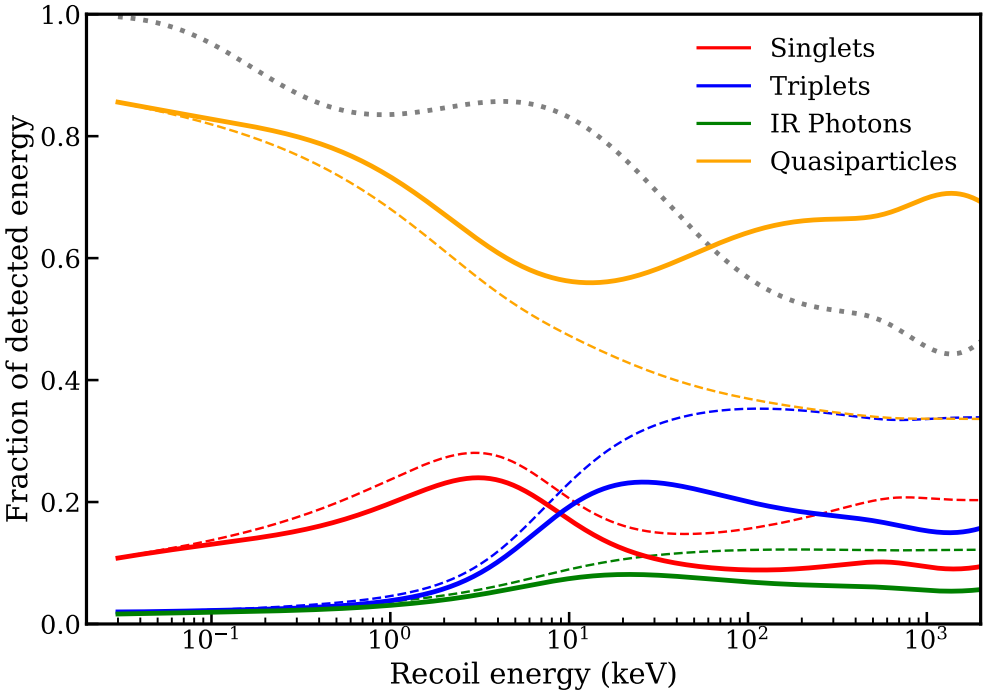

Figure 7.13: Nuclear recoil energy partitioning into observable signal channels. Dashed curves are those before the effects of Penning quenching are taken into account. The fraction of quanta surviving after the Penning quenching process is shown by the dotted grey line. For singlets, triplets, and IR photons, the product of the dashed lines and the dotted grey line yield the final prediction for the partitioning in each channel, shown by the solid lines. Quenched energy is assumed to convert to quasiparticles.

a cylindrical track is presented in [175] as

$$I'(t) = \frac{k_f k_{tt} \tau_s}{2\chi_{tt} t_{tt}} \frac{N_T(0)}{[1 + \frac{t_d}{2t_{tt}} \ln(1 + \frac{t}{t_d})]^2 (1 + \frac{t}{t_d})}, \tag{7.7}$$

where the initial number of triplets in the track, $N_T(0)$, is given by the dashed blue line in Figure 7.13. τ_s, the nanosecond scale singlet lifetime, is exactly cancelled by $k_f = \tau_s^{-1}$, since each singlet decay yields a photon. Triplets interact with one another on a timescale given by $t_{tt} = \pi r_0^2 L / \chi_{tt} N_T(0)$. We estimate the track radius $r_0 = 20$ nm and the track length L with the stopping power from ASTAR [206], and we use the experimentally measured value of the annihilation constant, $\chi_{tt} = 4 \times 10^{-10}$ cm^{3}s^{-1} [207]. Triplet interactions are balanced by diffusion away from the recoil track with timescale $t_d = r_0^2 / 4D_T$, where experimentally $D_T = 4.2 \times 10^{-4}$ cm^{2}s^{-1} at 2.0 K [208], yielding $t_d = 3$ ns.

There were several sources of uncertainty considered in the application of this delayed scintillation model. Uncertainties on the experimentally measured parameters χ_{tt} and D_T

were included, as was their temperature dependence in the range of 1.6 K to 2.0 K. While these temperatures are significantly warmer than the mK-scale envisioned in the HeRALD design, they correspond to the temperature of the superfluid helium target in the experiment described in Chapter 8. Uncertainties were dominated by the parameter $k_{tt} = f\chi_{tt}$, where f is the fraction of triplet-triplet interactions yielding singlets which decay. The central value was obtained by assuming geminate recombination yielding singlets 50% of the time. However, we also considered the uncorrelated case based on the number of states, which yields three times as many triplets as singlets and gives $f = 0.2$. If a singlet is produced in every recombination, $f = 0.5$.

Figure 7.14 summarizes the steps in constructing the model that we compare to the experimental data in Chapter 8. We use the quenching model discussed in the previous section for the prompt scintillation fraction, yielding the solid green line. We apply the triplet-triplet interaction model from this section to the triplet population, yielding the solid magenta curve. This curve is a prediction specific to the event windows of the superfluid helium experiment in Chapter 8, obtained by integrating Equation 7.7 from 640 ns for the delayed scintillation to be clearly visible in the events to the end of the event acquisitions at 32 μs. There are several sources of uncertainty in the delayed scintillation model, yielding a band to quantify the range of predictions.

7.5 Summary and ideas for the future

In this chapter, we outlined the steps to arrive at a semiempirical model predicting the energy partitioning of particle recoils in superfluid helium into several signal channels. This model yields different predictions for the partitioning in the case of nuclear and electronic recoils, giving rise to strong discrimination power in the HeRALD detector concept from Chapter 6. While there are many sources of experimental data used as input for the model in this chapter, they are all removed in some way from the low energy nuclear recoil region of interest for a dark matter detector, either by representing more fundamental quantities like scattering cross sections or by representing scintillation yield measurements at higher energies. Direct experimental measurement of the predictions output by the model in this chapter are the best test for validating the sensitivity projections for the HeRALD detector from Chapter 6.

Once such experimental measurements are made, there is room for further refining the modeling of microscopic physics important to generating measurable signals in superfluid helium. New measurements of the parameters in the quenching model and delayed scintillation model would provide direct feedback into the predictions offered here. Additionally, the cross sections used analytically here could be developed into a Monte Carlo simulation to better estimate the number of quanta produced in particle recoils and the characteristic energy assignments for the different de-excitation pathways. There are many directions opened up by new experimental data to use as feedback for this modeling work, although (spoiler alert!) the work presented here already agrees remarkably well with dedicated measurements

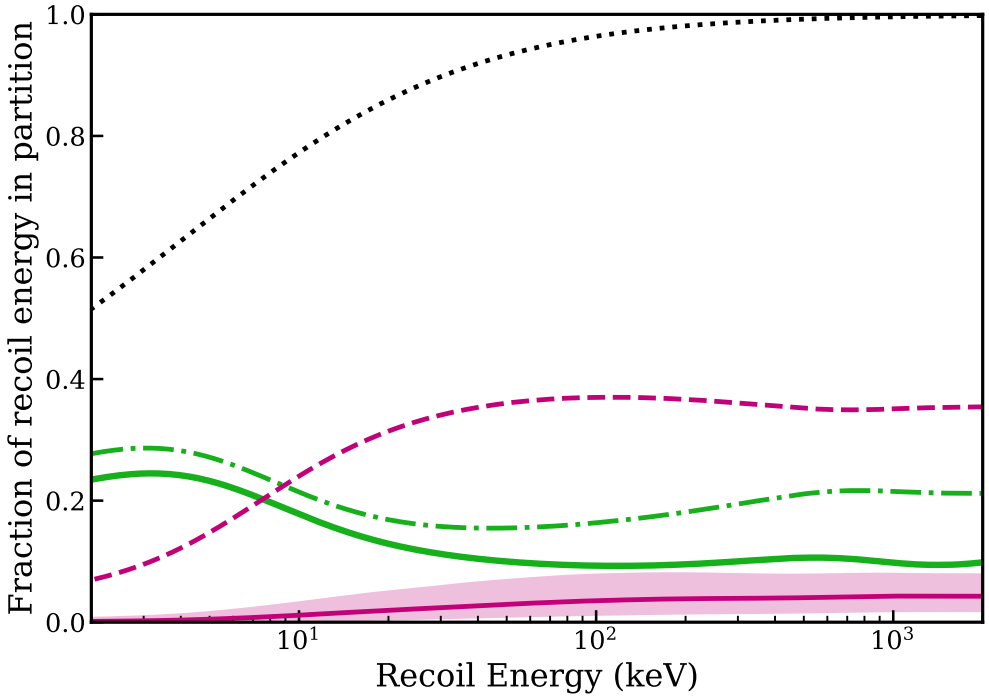

Figure 7.14: Nuclear recoil energy partitioning in the vein of Figure 7.13, with an additional curve showing an estimate for the fraction of energy observed in delayed scintillation photons. Triplets which are ionized by the Penning process and recombine into singlets produce visible scintillation (solid magenta), with the associated error band in the estimate described in the text. The estimate plotted here is specific to the event window length for the experiment described in Chapter 8. The dotted black line represents the fraction of recoil energy in electronic stopping according to the Lindhard model of the stopping power, equivalent to the black line in Figure 7.12. The electronic stopping energy is partially partitioned into singlets (dash-dotted green) and triplets (dashed magenta). Due to Penning quenching, only some singlets produce visible scintillation (solid green).

of neutron scattering in the 50 keV to 1 MeV recoil energy range.

Chapter 8

Measurement of the Scintillation Yield in ^{4}He

In this chapter we discuss two experiments to measure the scintillation yield of particle interactions in helium for nuclear and electronic recoils. Direct measurements of the signal channels described in chapter 7 do not exist to the low recoil energies of interest for dark matter detection experiments, particularly for the NR case that is crucial for excluding dark matter signals in experimental data. The experiments described in this chapter aim to test the scintillation component of the models developed in Chapter 7 by measuring the yield of scintillation signal as a function of energy deposited in a helium target.

First we describe the general experimental design that unites the two experiments. Then we discuss a neutron scattering experiment performed on a commercial high pressure helium gas detector, which was published in the Journal of Instrumentation [209]. The dissertation author was the primary author of this publication and was responsible for most aspects of the experiment, including the data acquisition, simulations, and analysis work. The rest of the chapter discusses a second experiment on a superfluid helium target which was published in Physical Review D [174]. The apparatus was chiefly designed and operated by J. Lin, with the dissertation author contributing to assembly and operations during data-taking. The main scintillation yield analysis was conducted by the dissertation author. It incorporated simulation work from L. Yuan and B. Suerfu, and it also built on pulse finding and single photoelectron calibration work by R. Smith. We include discussion of the complementary delayed scintillation analysis, also the work of R. Smith, as it is a crucial component of comparing the experimental data to the model presented in Chapter 7.

The papers were published as efforts of the HeRALD and SPICE/HeRALD collaborations, respectively.

8.1 Experimental design

Both experiments described in this chapter were designed around classical scattering kinematics. A helium atom recoiling from an elastic neutron scatter has energy

$$E_r = \frac{2m_n E_n}{(m_n + m_{\mathrm{He}})^2}\left[m_n \sin^2(\theta) + m_{\mathrm{He}} - \cos(\theta)\sqrt{m_{\mathrm{He}}^2 - m_n^2 \sin^2(\theta)}\right], \tag{8.1}$$

where m_n is the mass of the neutron, E_n is the initial energy of the neutron, m_{He} is the mass of the helium atom, and θ is the scattering angle of the neutron in the lab frame relative to its initial direction. For a monoenergetic neutron source, the recoil energy and recoil angle in equation 8.1 are fixed to one another. Thus, the aim of both experiments is to tag neutrons which scatter in a helium target using a second detector with a known position, defining the recoil angle precisely. The measured scintillation signal of tagged neutron scatter events therefore corresponds to a known recoil energy for a given configuration of the tagging detector. An example of the experimental layout is shown via the simulation geometry of the second experiment, described in sections 8.3-8.5, in figure 8.1.

A similar scheme can yield measurements of the ER scintillation yield via Compton scattering of gamma rays. Compton scattering kinematics can be written concisely as an expression of the energy of the outgoing gamma ray:

$$E'_\gamma = \frac{E_\gamma}{1 + (E_\gamma/m_e c^2)(1 - \cos\,\theta)}, \tag{8.2}$$

where E_γ is the ingoing energy, m_e is the mass of the electron, c is the speed of light, and θ is the lab frame scattering angle. As in the neutron case, a monoenergetic gamma ray source fixes the equation to a relation between the energy transfer in the interaction and the scattering angle of the photon. While we could not apply this method to the first experiment—described in section 8.2—for reasons specific to the instrumentation of the helium target, we did successfully measure Compton scattering in superfluid helium in the second experiment.

There are several practical considerations to optimize this experimental approach. Equation 8.1 holds true for a single elastic scatter, so the target helium mass should be small enough that neutrons predominantly scatter once before leaving the target. An additional motivation for a smaller target mass is to reduce the uncertainty on the scattering angle, lessening uncertainty on the corresponding recoil energy. Reducing the angular uncertainty can also be achieved by moving the target and tagging detectors further apart, decreasing their cross sectional area in the scattering geometry.[1] Similarly, angular uncertainty due to the initial direction of the scattering particle can be lowered by moving the source away from the helium target. These distances cannot be arbitrarily large, since the experiment

[1]Technically, this geometric spread in recoil energies should be accounted for in the Monte Carlo simulations used in the analysis, but the ease of interpreting the data is greatly increased with a clear single scattering peak corresponding to as small of a spread in energies as feasible.

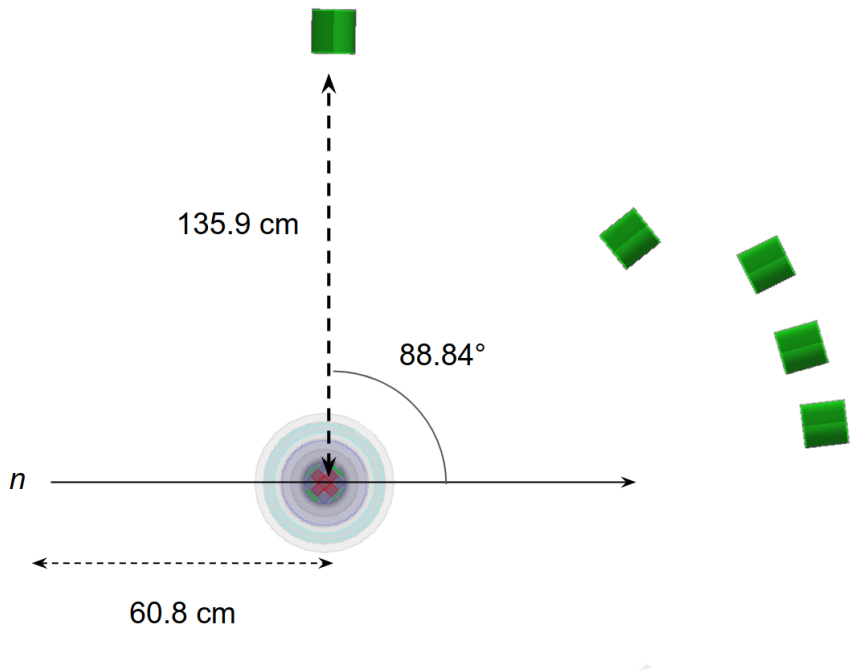

Figure 8.1: Rendering of the simulation setup for neutron scattering showing the strategy of the measurement described in this chapter. Monoenergetic neutrons from the DD neutron source, located at the lower left corner 60.8 cm away from the liquid helium target, scatter into far-side detectors at fixed angles, depositing known energy into the helium target. Figure made by B. Suerfu.

should be conduced in a reasonable amount of time, and the uncertainty in the scattering angle from measuring the physical positions of the source, target, and tagging detector will dominate at some distance anyway.

8.2 Results from a commercial high pressure helium gas detector

The first experiment we discuss in this chapter used an off-the-shelf commercial high-pressure helium gas detector as the target for neutron scattering. Recent work has shown ^{4}He gas can be used as a detection medium for fast neutrons, due to its properties as a scintillator and a barn-scale cross section for the elastic scattering of MeV-scale neutrons [210, 211]. It has previously been experimentally shown that the scintillation response of helium gas to neutron recoils is fairly linear down to 380 keV [212] and more recently to about 240 keV [213]. This response linearity is consistent with the modeled behavior in this energy region

shown in Figure 7.13, with the caveat that the modeled quenching effect from dashed to solid lines in this figure is for superfluid helium densities rather than gas.

8.2.1 The Arktis fast neutron detector

Arktis Radiation Detectors, Ltd. has produced a commercial product based on a detector volume consisting of ^{4}He gas instrumented with light collection sensors to detect scintillation from particle recoils in the gas. The first versions of the detectors were instrumented with photomultiplier tubes (PMTs) on both ends of the cylindrical vessel [210]. Pulse shape discrimination based on the prompt light fraction can distinguish between neutron interactions and electron recoils from environmental gamma-rays and charged particles [214, 215]. More importantly, the detector is naturally less sensitive to gamma-rays because the recoiling electron will likely travel far enough to deposit some of its energy into the detector wall instead of the scintillating gas [210]. Thus, the main discrimination strategy in the modern iteration of the detector is simply to compare the size of the pulse and discard events below a threshold as electron recoil backgrounds [215, 216]. For neutron recoils, on the other hand, the detector has been used to extract spectral information about neutron sources [213, 217, 218].

The newer iteration of the Arktis S-670 fast neutron detector is instrumented with silicon photomultipliers (SiPMs) [219, 220]. The active one liter volume consists 180 bar of ^{4}He gas in an approximately 1 meter long stainless steel tube with 4 millimeter thick walls. There are three equally-sized, optically isolated segments, each containing four channels corresponding to a SiPM pair for a total of 24 SiPMs in the detector. Each channel can be read out through an analog board with amplification and shaping electronics provided by Arktis.

8.2.2 Neutron scattering configuration

We performed the experiment with the SiPM-instrumented Arktis detector and a St. Gobain BC-501A organic liquid scintillator detector with PMT readout and a 5 inch diameter and 5 inch height active volume. The neutrons were produced by a Thermo Fisher Scientific MP 320 deuterium-deuterium (DD) neutron generator yielding 2.8 MeV neutrons in the forward direction [221]. A schematic top-down diagram of the experimental geometry is shown in Figure 8.2, where the long axis of the detector was oriented along the direction of the neutron flux and all three components were positioned at the same distance from the floor.

We studied five scattering angles ranging from 20-60 degrees, corresponding to 83-626 keV in mean recoil energy as shown in Table 8.1. Monte Carlo (MC) simulations were performed with GEANT4 10.2 [77–79] using the QGSP_BIC_HP physics list. In the simulation, the DD generator output was approximated as 2.8 MeV neutrons distributed isotropically from the source plane. The DD generator neutrons in reality had a small dependence in energy and flux with the angle they left the target plane [221], but these variations were negligible due to the small solid angle subtended by the Arktis detector volume when placed 1 m away from the DD source plane as in our experiment. Simulated events that deposited energy

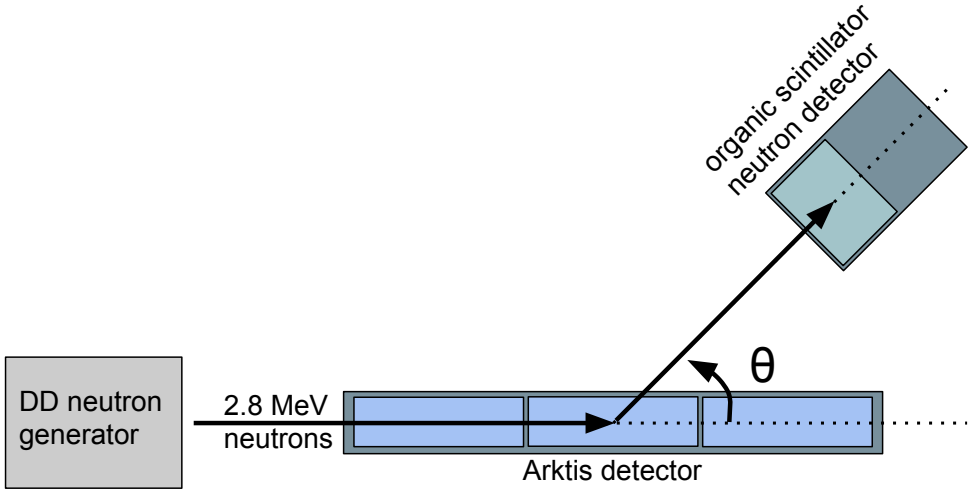

Figure 8.2: The scattering geometry for measuring the nuclear recoil scintillation linearity of the high pressure helium gas in the Arktis detector. The detectors were positioned about 1 m apart for each configuration; this figure is not drawn to scale.

in both the middle cell of the Arktis detector and the organic scintillator had their recoil energies and deposit times recorded. The expected time of flight between the Arktis and organic scintillator detectors in our configurations was between 44 and 49 ns, depending on the energy of the scattered neutron. Neutrons which scattered more than once in the Arktis detector or other materials, and therefore did not deposit the energy given by Equation 8.1, contributed about 10% of events in the single scattering signal region in the simulation.

Table 8.1: The measured scattering angles and the corresponding energy of single-scattering neutrons given by Equation 8.1, as well as the 1σ spread in angles from the finite sizes of detector elements and the corresponding 1σ spread in energies.

θ [deg.]	σ_θ [deg.]	E_r [keV]	σ_{E_r} [keV]
20	3	83	22
25	3	129	27
30	3	182	32
45	4	384	52
60	4	626	58

Since the detectors have finite physical size, there is a spread in scattering angles and therefore recoil energies represented in each geometric configuration, even when only considering single scatter events. To estimate the size of this effect, we selected single scattering

events from the MC simulations for each experimental geometry and fit a Gaussian to their spread in energy. We report the 1σ spread in energy and scattering angle in Table 8.1. Since each cell of the Arktis detector has slightly different optical properties [220], we restricted ourselves to using the middle cell of the Arktis detector.

Pulses were read out of the Arktis and organic scintillator detectors into a NIM module trigger system. A Phillips Scientific NIM Model 710 discriminator was used to determine when two or more of the four channels in the middle segment of the Arktis detector had pulses cross the threshold value within a 50 ns window. This two-fold coincidence requirement eliminated many electron recoil backgrounds, which are less likely to produce pulses in two or more channels at once [220]. The event was recorded if the Arktis pulse coincidence occurred within 150 ns of a pulse in the organic scintillator module. An extended coincidence window was selected to allow for a time of flight cut in the analysis of the data. When triggered, all detector channels were digitized and recorded by a CAEN V1720 digitizer with a 4 ns sampling rate. A typical neutron-like event with pulses from both detectors is shown in Figure 8.3.

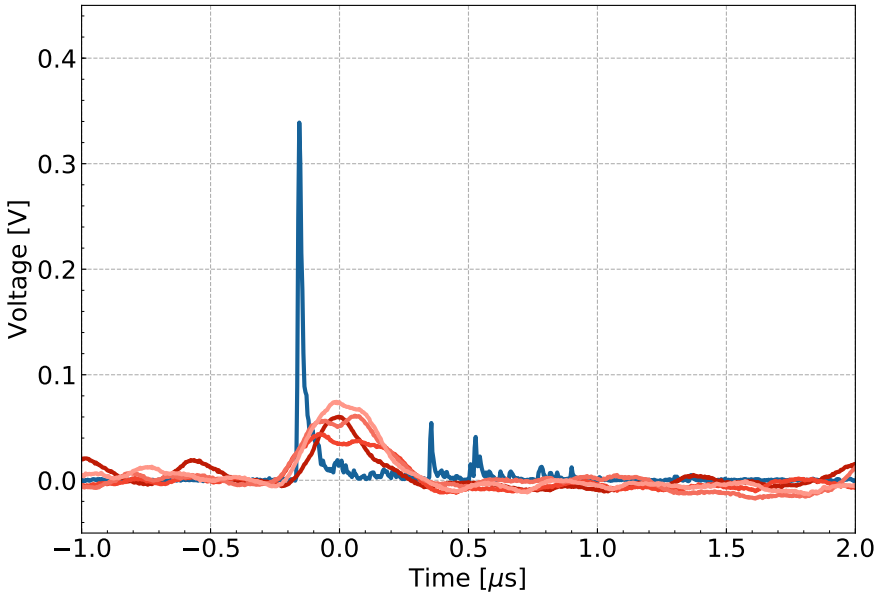

Figure 8.3: A sample event with pulses from the four channels of the Arktis detector in shades of red and the amplified PMT output of the organic scintillator detector in blue. Negative time corresponds to samples preceding the trigger. The y-axis is the relative voltage recorded by the digitizer after baseline subtraction has been performed on the five detector channels.

8.2.3 Trigger Efficiency Measurement

The trigger efficiency for detecting two or more pulses in the Arktis detector, shown in Figure 8.4, was measured with a modified experimental geometry and modified triggering approach. The Arktis detector was moved closer to the DD generator source plane, and we triggered the digitizer on the source pulse of the DD generator running at 2 kHz with a 5% duty cycle. For each DD generator pulse, we recorded the four Arktis channels and the trigger logic signal arising from two coincident Arktis pulses as in the main triggering scheme. The efficiency was determined by the fraction of events of a given pulse size, defined as the total area of the waveforms across all four Arktis channels, coincident with an Arktis trigger logic signal.

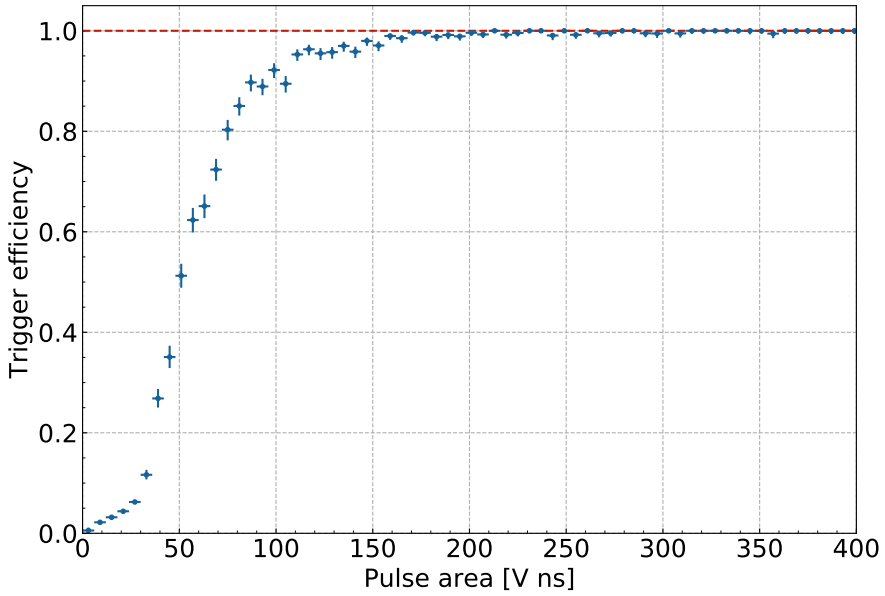

Figure 8.4: Hardware trigger efficiency as a function of pulse area in the Arktis detector. Experimental trigger efficiency values are applied to the MC spectra when fitting to the Arktis detector data.

8.2.4 Time Resolution Measurement

We used a ^{22}Na gamma-ray source to trigger the two detectors in coincidence to measure the time resolution of the setup. While gamma rays have a reduced probability of triggering the Arktis detector, direct exposure to a gamma ray source still provided a reasonable event rate. The detectors were positioned with the ^{22}Na source in the middle since ^{22}Na decays produce

back-to-back 511 keV gamma rays from positron annihilation; the distance of each detector from the ^{22}Na source was selected so the solid angle they subtended ensured that any gamma ray pair which triggered the Arktis detector could also trigger the organic scintillator detector [222]. Pulse times were calculated by using the time of the first sample greater than 25% of the pulse maximum, and for the Arktis detector we used the earliest pulse time in the four channels. We took the difference in the nominal pulse times for each of the two detectors and fit a Gaussian to the distribution of differences to find a mean offset and standard deviation. We measured the standard deviation in differences, corresponding to the time resolution for our setup, to be $\sigma_t = 34$ ns. We applied this time resolution to the event selection of the simulated events via Gaussian smearing to match the analysis of the experimental data.

8.2.5 Data Selection

The St. Gobain BC-501A organic scintillator used to tag scattered neutrons has strong pulse shape discrimination between nuclear recoils and electron recoils. These event types form two distinct bands in pulse height versus pulse area, so we select neutron events by accepting only events in the lower band. The two bands are shown in the top left panel of Figure 8.13, which shows data from the other experiment described in this chapter collected with the same detector module as the one used in this experiment.

There is a minimum area cut below which two bands overlap with each other. This cut eliminates about 90% of the recorded events, serving as the main method to prevent accidental coincidences from entering the analysis. Gamma rays can originate from the DD generator directly, from neutron capture in materials in and around the experiment, or simply from environmental backgrounds. Additionally, some good neutron events are outside of the acceptance region because the recoil energy in the organic scintillator detector was not enough to allow for good pulse shape discrimination.

We also apply a time of flight cut to the data and each corresponding set of MC events, for which the time of flight has been smeared according to the measured time resolution. This cut helps eliminate events that are accidental coincidences and neutrons which scatter multiple times in the Arktis detector and surrounding components. Since the time resolution is comparable to the time of flight of the scattered neutrons, we select events that are $+3/-1$ σ_t around the expected time of flight of neutrons at each scattering angle. The asymmetry in the acceptance window was chosen to eliminate trailing multiple scattering neutrons from the dataset while accounting for time resolution.

Combined, the cuts result in an acceptance of 1-5% of the total recorded events for the five datasets. The results from these cuts are consistent with our expectation of events caused by baseline fluctuations in the Arktis detector, since the smallest acceptance fraction came from lowest-energy recoil dataset, where the neutron event pulses have the lowest trigger efficiency.

8.2.6 Fitting Procedure

After the data selection cuts, we fit the MC spectra to each scattering dataset independently. We assume that the energy resolution is Gaussian and that it scales as the square root of the recoil energy times a constant factor, A, which has units $\sqrt{\text{keV}}$, to account for light production and detection efficiency in the detector, as we did not simulate these processes directly. We also take the MC output energy to the digitizer units with a scale factor C with units V ns / keV. It is this factor C that serves as our measurement of the response linearity, since it should have a consistent value across a range of recoil energies given a linearly responding target material.

The MC events were smeared in energy and scaled to the digitizer units according to the Gaussian probability distribution

$$p(x) = \frac{1}{\sqrt{2\pi C^2 A^2 E}} \exp\left[\frac{-(x - CE)^2}{2C^2 A^2 E}\right], \tag{8.3}$$

where x is the simulated detector response in V ns and E is the energy of the MC event in keV, and we use χ^2 minimization to find the best values of the parameters A and C.

The smeared MC events were binned in pulse area, and an experimental measure of the hardware trigger efficiency, shown in Figure 8.4, was applied to the spectrum. The resulting MC spectra were compared to corresponding experimental datasets by computing

$$\chi^2 = \sum_{i=1}^{N} \frac{(n_i - \nu_i)^2}{\nu_i}, \tag{8.4}$$

where n_i is the number of experimental events and ν_i is the number of simulated events in the ith bin. The fitting region was first selected by hand to approximate the single-scattering signal region. The MC spectrum in the fitting region was normalized to the experimental spectrum before computing χ^2. This fitting procedure, from MC smearing through computing χ^2, was repeated for a range of energy resolution factors, A, and MC scale factors, C in a two dimensional scan of the parameters. The best fit parameters for each dataset were those corresponding to the minimum χ^2 value.

After this first pass parameter scan, a smeared MC distribution was produced using the best fit A and C. A Gaussian was fit to the distribution of single-scattering neutrons without the application of the trigger efficiency. The fitting region was redefined as $\pm 3\sigma$ of the fit Gaussian around its mean to minimize bias in selecting the fitting region. It was also bounded from below with the same minimum value of 30 V ns for each scattering angle to exclude an extraneous population of low-area events, which can be seen in Figure 8.5. These events are likely noise triggers or electron recoils in the Arktis detector accidentally coincident with neutron events in the organic scintillator detector, since they are fairly consistent in number throughout the datasets and the total population of these events is much larger before the time of flight cut. For the new fit region, MC smearing and computing χ^2 was repeated for the same range of parameters, and the reported best fit parameters A and C were those found after this second pass.

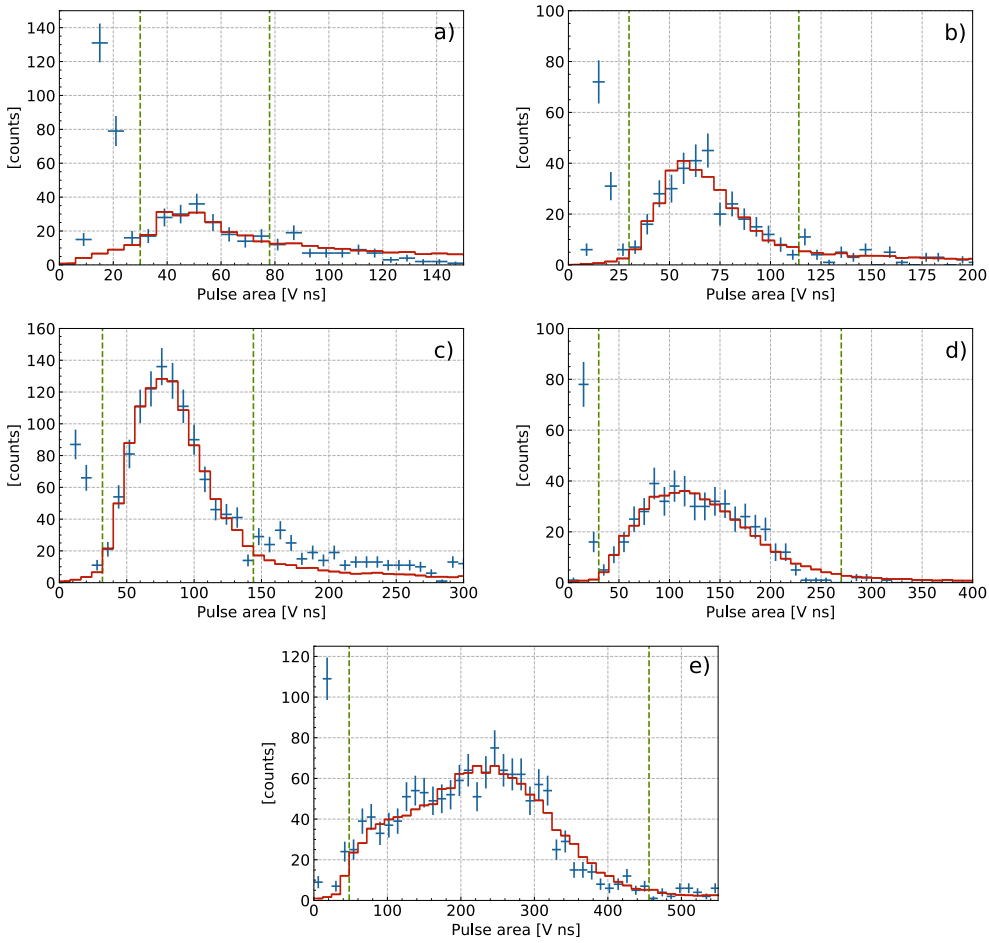

Figure 8.5: Plots of the experimental data (blue) and fitted Monte Carlo spectra (red) for all five scattering angles. The fit region is between the vertical green dashed lines. The scattering angle (energy) is **a)** 20° (83 keV) **b)** 25° (129 keV) **c)** 30° (182 keV) **d)** 45° (384 keV) and **e)** 60° (626 keV).

8.2.7 Error Analysis

There were several effects considered for estimating the errors in the reported best fit values. Statistical error was obtained directly from the χ^2 fits. To estimate the systematic errors, we evaluated the effect on the best fit parameters when changing the pulse timing parameters, data selection cuts, and MC geometry in the analysis procedure above. For each systematic error fit, the energy resolution factor was capped at $A = 13\ \sqrt{\text{keV}}$, roughly twice the average energy resolution factor found in the main analysis fits. This restriction was imposed so that the energy resolution factor A did not diverge too far from the values found at high recoil energy, which yielded more consistent results. The systematic error associated with each variation was taken as the difference between the best fit value in the original analysis and after the modification was applied.

We used 10% and 50% of the maximum value as alternate values for the pulse timing threshold, to gauge the effect of the pulse timing cut. We also used the second pulse time of the Arktis detector instead of the first to evaluate whether there was a systematic effect from stray pulses. The organic scintillator detector pulse shape discrimination minimum area cut was modified by ±50% to study the impact of the band separation. The accepted time of flight region was expanded to $+4/-4\ \sigma_t$ and contracted to $+2/-0\ \sigma_t$. To better understand the effect of the fit region, the number of deviations of the single-scatter peak that defined the fit region were decreased to $\pm 2\sigma$ and increased to $\pm 4\sigma$.

We determined an uncertainty of 0.5 cm in the measured positions of the two detectors to evaluate systematic errors associated with uncertainties in the detector positions used in the MC geometry. We propagated these errors into errors in the neutron scattering angle and distance between the detectors and generated MC events according to the modified angle and distance for a total of four additional MC datasets for each scattering angle.

The individual systematic errors were ultimately combined in quadrature for a total systematic error estimate for each scattering angle. Then, the systematic and statistical errors were combined in quadrature for an estimate of the total error in the best fit parameters. The combined total errors from this analysis, which are uniformly dominated by the systematic errors, can be seen in Figure 8.6 and Table 8.2.

8.2.8 Discussion

The best fit MC scale factors have been plotted in Figure 8.6, along with a horizontal line showing their mean. If the scintillation response of the detector is linear, the same MC scale factor, C, should provide the best fit across the range of recoil energies. In addition to the scintillation behavior of the helium gas itself, nonlinearities in the response could be introduced by the onboard readout electronics of the Arktis detector and possible non-homogeneity in the light collection efficiency of the detector. While we attempted to model the light production physics and the light collection efficiency of the detector using simple Gaussian smearing proportional to the square root of the recoil energy, it is possible that a more detailed simulation of the optical processes in the detector could yield better fits to

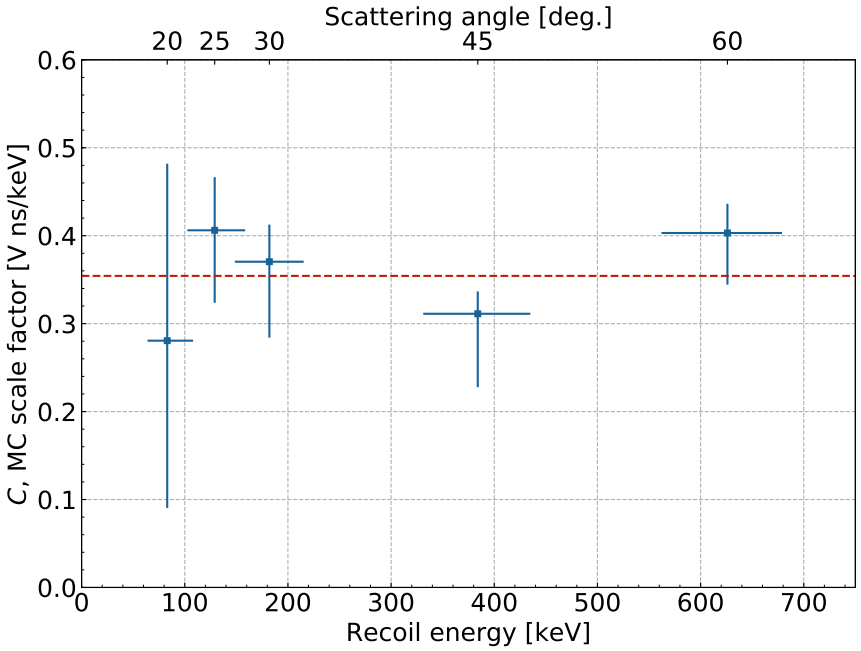

Figure 8.6: Best fit MC scale factor, C, for each scattering angle, shown in terms of the corresponding neutron recoil energy in the Arktis detector calculated in Equation 8.1. Best fit scale factors are shown in blue, and the mean value of all the data points is the dashed red line. The horizontal error bars correspond to the spread in angles/energies given in Table 8.1. The vertical error bars are from the combination of statistical and systematic uncertainties and are reported in Table 8.2.

the data. Still, each scattering angle was fit to a reasonable χ^2 per degree of freedom and the best fit values of C deviated at most 21% from the mean of 0.35 V ns/keV.

At the lowest energies, we do not resolve the fitted parameters well because the effects of the energy resolution and scaling factor compete with the effects of the threshold efficiency. This analysis does not provide much traction on the energy resolution factor, which is large most likely due to a combination of the light collection efficiency of the detector and the onboard shaping electronics used for signal amplification. For applications such as this experiment, where detailed energy resolution and signal timing information are preferred, the earlier generation of Arktis fast neutron detectors instrumented with PMTs may be advantageous. Still, the off-the-shelf detector used in this experiment was a valuable initial test of the signal modelling for helium scintillation described in Chapter 7.

Table 8.2: Best fit values of the energy resolution factor, A, and MC scale factor, C, and their errors for each scattering angle θ corresponding to a recoil energy E_r. Errors are quadratic sum of the 1σ statistical errors from the χ^2 fit and systematic errors found as reported in the text. The χ^2 results and number of degrees of freedom for each fit are also reported.

θ [deg.]	E_r [keV]	A [$\sqrt{\text{keV}}$]	C [V ns/keV]	χ^2 / DoF
20	83	$6.4^{+9.7}_{-6.0}$	$0.28^{+0.20}_{-0.19}$	2.044 / 5
25	129	$3.6^{+1.3}_{-0.8}$	$0.41^{+0.06}_{-0.08}$	10.18 / 11
30	182	$5.4^{+4.5}_{-1.1}$	$0.37^{+0.04}_{-0.09}$	10.71 / 11
45	384	$8.4^{+5.8}_{-1.7}$	$0.31^{+0.03}_{-0.08}$	22.89 / 21
60	626	$6.9^{+3.8}_{-2.2}$	$0.40^{+0.03}_{-0.06}$	49.12 / 32

8.3 Description of superfluid helium apparatus

Since our ultimate interest is in characterizing superfluid helium as a target material, we now turn our attention to an experiment with a target designed explicitly for this measurement approach. First we describe the hardware, with subsequent sections covering the data analysis and results of the experiment. Figure 8.7 shows a labelled photo of the various components arranged in the lab.

8.3.1 Target instrumentation and cryogenics

The active superfluid ^{4}He target of was defined by a 16 cm^3 cube formed by the faces of six Hamamatsu R8520-06-MOD photomultiplier tubes (PMTs) as shown in Figure 8.8. The entire PMT array was immersed in the superfluid helium to maximize the light collection efficiency of scintillation in the target cube. In front of each PMT window was was a 1 mm thick fused quartz sheet with a 0.3 mg/cm^2 layer of tetraphenyl butadiene (TPB) [223, 224], used to shift the 80 nm wavelength prompt scintillation light of ^{4}He to 430 nm, which can better penetrate the PMT windows.

Since the PMTs were submerged in superfluid helium, a special PMT biasing and readout scheme was implemented. It was based on previous work for running similar PMTs at milli-Kelvin temperatures in vacuum [225], leveraging Cockroft-Walton generators (CWG) for turning low voltage AC input to high voltage DC output. CWGs dissipate a minimal amount of heat, particularly compared to resistive voltage dividers, which is a critical design parameter of operating cryogenic electronics. Additionally, the target instrumentation design

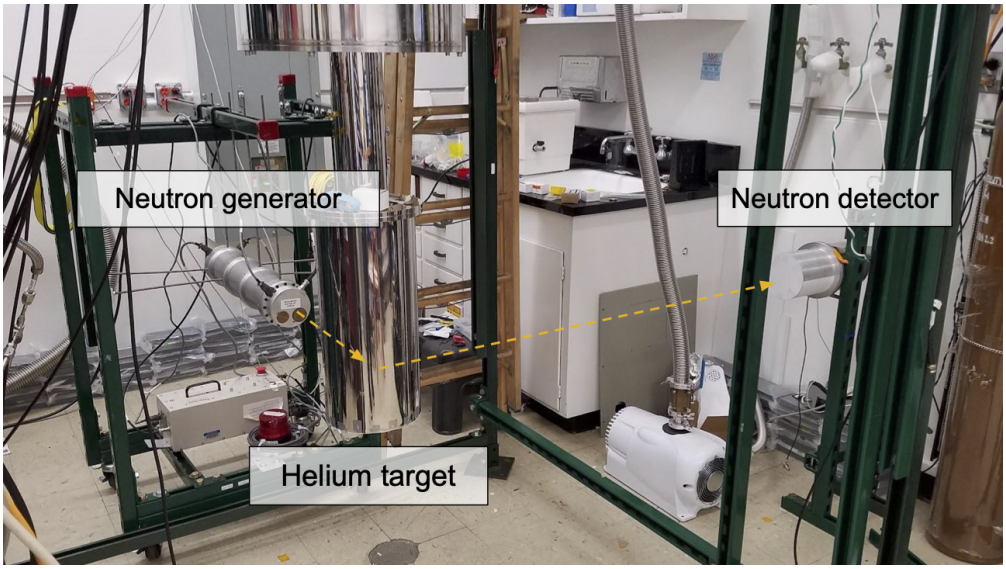

Figure 8.7: A photo of the experimental setup. Labelled are the DD neutron generator, the cell containing the helium target, and the neutron tagging detector. Arrows trace the approximate neutron scattering path.

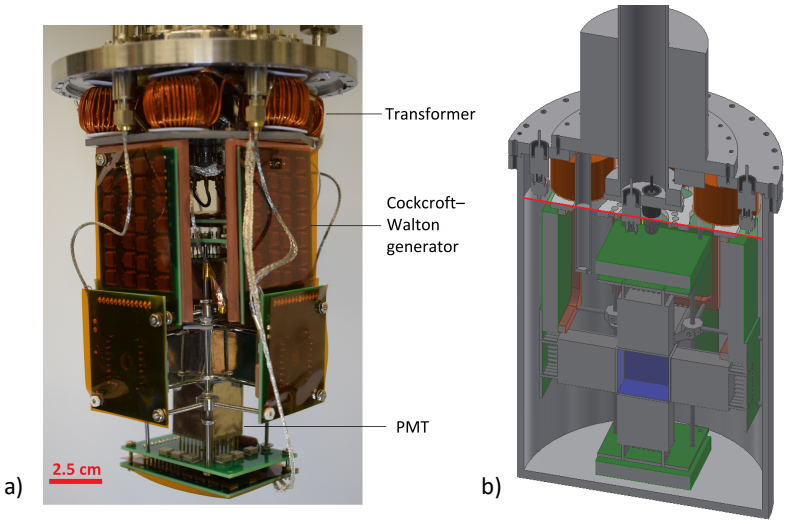

Figure 8.8: a) Photograph of the detector used for the experiment described in this chapter. b) CAD model of the detector. The TPB wavelength shifter is shown in blue, defining the active volume of the detector. The measured ^{4}He liquid-gas interface at 1.75 K is indicated by a red line, near the top of the green printed circuit boards. Figure adapted from [174]; both panels originally made by J. Lin.

did not require any cryogenic high voltage feedthroughs. The PMT gains were monitored using trailing single photoelectron pulses in the datasets–for more details refer to Section 8.4.2.

The helium target, PMTs, and electronics were mounted inside a Janis Cryogenics pumped ^{4}He cryostat with a 1 K pot. The helium target was condensed using purified ^{4}He, with impurities <200 ppb, while the cooling ^{4}He was kept separate. Typically PMTs are very sensitive to helium permeation through the glass into the vacuum space even in regular atmospheric conditions, let alone in contact with pure liquid helium. However, the permeability drops exponentially with temperature [226], so a special cool down procedure was employed to submerge the PMTs without damaging them. First the sample space was cooled to 77 K using liquid nitrogen and filled with helium gas. Then it was flushed with high purity helium gas and the cryostat was cooled to 4.2 K, where helium condenses to liquid. At this stage, the sample space was filled with liquid helium through a 4.2 K cold trap and further cooled through the superfluid helium transition to 1.75 K. In this configuration, the sample space valve was shut and data were taken over the course of 50 days in December 2019 and January 2020. Temperatures were stable to within 0.1 K over the course of the run.

8.3.2 Radioactive sources and data taking configuration

As in the experiment described in Section 8.2, NR data were collected using the 2.8 MeV neutrons from a Thermo Scientific MP 320 deuterium-deuterium (DD) fusion neutron generator. The same 12.7 cm diameter, 12.7 cm thick cylindrical BC-501A liquid scintillator (LS) detector with PMT readout was used to tag neutrons recoiling in the helium detector at a specific angles.

ER data were obtained using a 270 kBq ^{137}Cs source, which emits gamma rays of 661.7 keV. Two cylindrical 5.1 cm diameter, 5.1 cm thick NaI detectors with PMT readout were used as far side detectors to tag gamma rays which Compton scattered in the helium target at specific angles.

Improving on the experiment described in Section 8.2, laser tools were used to measure the positions and orientation of the radioactive sources and the detectors, with an estimated position uncertainty of 1 mm.

8.3.3 Data acquisition and trigger efficiency

The signals from the helium detector and far side detector PMTs (LS and NaI) were amplified and fed into a discriminator. The triggering logic was very similar to the one described in Section 8.2.2; for both DD and ^{137}Cs data, the trigger was satisfied with two-fold coincidence within a window of 150 ns among the helium detector PMTs. For DD data, an extra coincidence between the LHe detector and the LS detector signal was required, also within a window of 150 ns. The comparatively slower event rate in the ^{137}Cs data taking runs allowed for a more inclusive triggering scheme at the hardware level.

Each triggered event was recorded with a CAEN V1720 digitizer with 250 MHz sampling frequency and consisted of samples amounting to 1 μs pre-trigger and 31.7 μs post-trigger length. All six helium detector channels and the tagging detector channels were saved for each trigger. Summed outputs of the helium detector PMTs are shown for two typical events in Fig. 8.9.

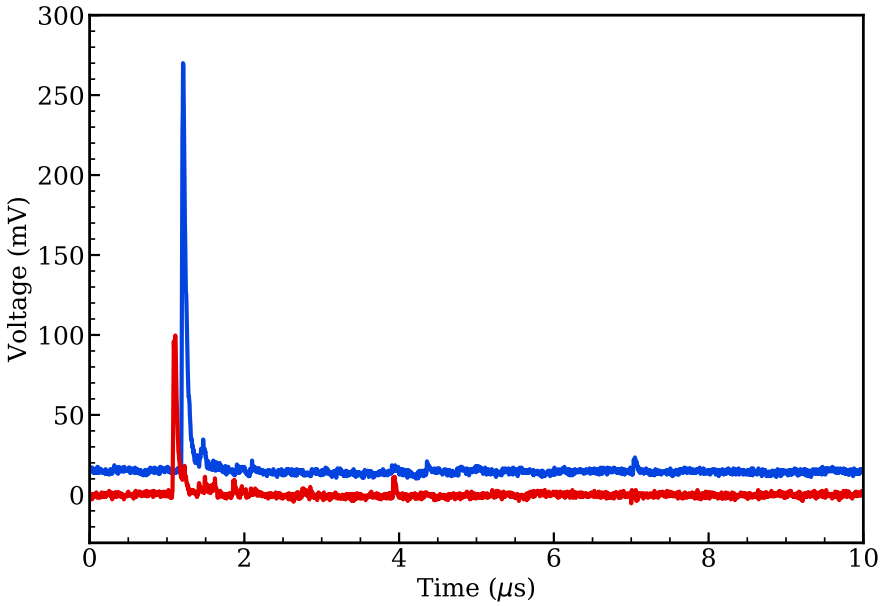

Figure 8.9: The summed output of the helium detector PMT channels from two sample events passing the analysis cuts. The ER event (blue), offset by +15 mV, was selected from the dataset corresponding to a recoil energy of 154 keV$_{ee}$ and the NR event (red) to 142 keV$_{nr}$. Both events contain small single photoelectron (SPE) pulses following the large prompt pulse.

As in Section 8.2.4, the timing for the helium detector PMTs and the far side detector PMTs was synchronized by the back-to-back 511-keV gamma rays from a ^{22}Na source. In this experiment, we were also able to use the same ^{22}Na source to measure the trigger efficiency for the helium detector channels. In this trigger efficiency study, the NaI detector signal was used to trigger the data acquisition, and the signals of the helium detector PMTs and the output from the discriminator channel linked to the helium detector PMTs were recorded.

Our software analysis chain required the pulse finder to identify pulses in at least two helium channels as a data quality control. We calculated the combined pulse area from the PMTs normalized to the individual PMT gain (see Sec. 8.4.2), and calculated the combined efficiency of triggering the discriminator and passing the analysis-level coincidence require-

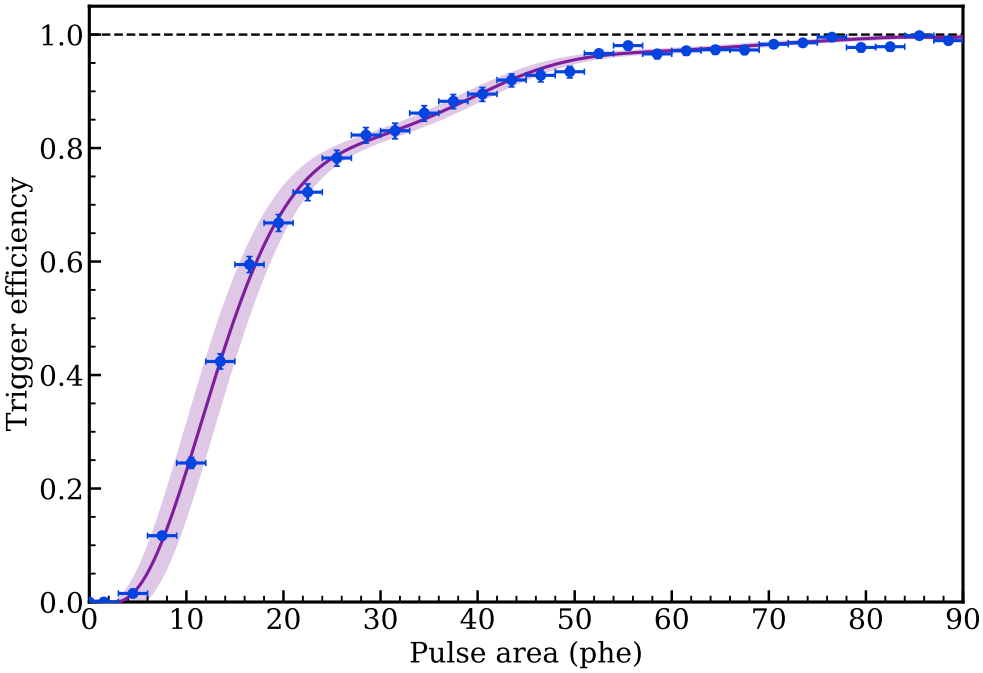

Figure 8.10: The measured trigger efficiency from the combined effects of hardware triggering and software event selection as a function of signal size. A histogram of dedicated trigger efficiency data (blue) was interpolated with an 11th degree polynomial fit (purple), shown with the 1-σ confidence band, which was derived using the horizontal and vertical error bars treated as 1-σ errors.

ment as a function of pulse area. This trigger efficiency as a function of normalized pulse area is shown in Fig. 8.10. The measured trigger efficiency was low up to fairly large signal sizes, which we attributed to the fairly low PMT signal gain and an unstable baseline prone to low frequency fluctuations, affecting the discriminator behavior. However, most of the datasets in this study have pulse areas larger than those with low trigger efficiency, with the exception being the 53.2 keV$_{\mathrm{nr}}$ dataset.

8.4 Analysis of superfluid helium data

This section discusses the steps taken to analyze the data obtained during this experiment. In this discussion, a single dataset refers to the events corresponding to one recoil type (ER or NR) scattering into a particular recoil angle. Thus, we have a total of 13 datasets for consideration: 6 ER and 7 NR, spanning 36.3-185 keV$_{\mathrm{ee}}$ and 53.2-1090 keV$_{\mathrm{nr}}$. Each dataset can consist of events collected in non-contiguous periods of time, so we refer to these distinct collection periods as data taking runs.

We performed two related analyses on the scintillation behavior of the superfluid helium target. The first analysis was largely similar to the one discussed in Section 8.2, where we considered the total scintillation signal in the helium target for the events in each dataset and attempted to extract a scaling factor taking the simulated energy deposit to the observed signal size. We discuss the steps and decisions of this analysis in detail, as many of them were refined in this analysis relative to the version in Section 8.2, even if the broad strokes were the same. Additionally, we examined the delayed scintillation behavior of the events in each dataset as an additional lever for testing the modeling presented in Section 7.

8.4.1 Monte Carlo simulations

The experimental setup was simulated with GEANT4 [77–79] version 10.5 using the reference SHIELDING physics list. An example run geometry is shown in Figure 8.1. Multiple far side backing detectors corresponding to different scattering angles were placed in a single simulation run to increase computational efficiency. When neutrons or gamma rays scattered between different far side detectors, only the first interaction was used in the subsequent analysis. During the processing, electronic recoil and nuclear recoil energies were tracked separately so that the correct signal scale could be applied in the analysis, in case a simulated event consisted of both types of interactions. However, the helium nucleus does not undergo inelastic scatters with neutrons, making mixed NR/ER events fairly rare in the simulations.

The angle-energy relation of the DD generator neutron production was modeled as a 4th order polynomial in the simulation according to [221]. The ^{137}Cs source was implemented as isotropic 661.7-keV gamma rays originating from the Mylar/Kapton source packaging (Eckert & Ziegler Type M).

8.4.2 SPE size calibration

We previously introduced the delayed scintillation component from helium deexcitation in Chapter 7. Experimentally, we also see an elevated rate of single photoelectron (SPE) pulses trailing a prompt pulse in the helium. Some SPEs are visible in both events in Figure 8.9. While the subject of its own analysis, the delayed component was also used for one of the first steps in analyzing the total signal size, as a calibration for the total number of photons seen by the PMTs in each event.

To determine the SPE size, pulses were selected that arrived more than 476 ns after the nominal trigger time. The areas of selected pulses in each data taking run were histogrammed and fit to a Gaussian. An example fit is shown in Fig. 8.11. Delayed scintillation was a particularly valuable SPE source since it was observable in each data taking run, allowing changes in gain to be monitored over the course of the experiment. Each data taking run was calibrated based on the SPE sizes observed in that same set of events. A subset of the SPE sizes were checked against in-situ LED calibrations which yielded similar results.

The pulse finder removed pulses below a fixed area to avoid identifying noise as pulses. Inefficiency in finding SPEs was estimated as the fraction of the Gaussian fit to the SPE

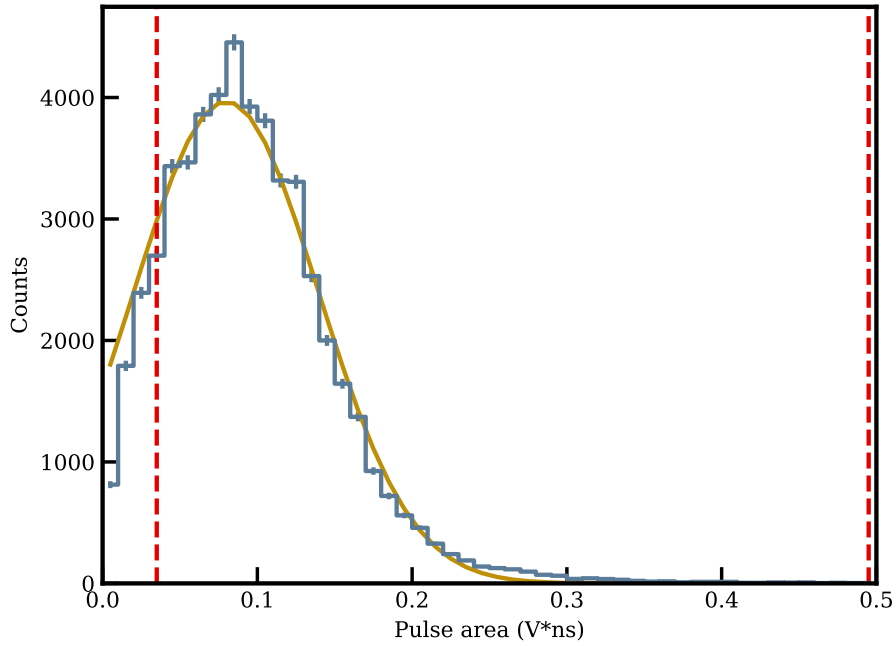

Figure 8.11: Example spectrum of delayed scintillation pulses used to calibrate SPE size for a single dataset. The observed spectrum (blue) is fit to a Gaussian (yellow-orange) between the dashed red lines. Below the lower dashed line, a noise pedestal is visible in a minority (∼15%) of datasets. Figure made by R. Smith.

area distribution that fell below this threshold. Across all of the PMT channels and datasets included in the analysis, the average SPE finding efficiency was 72%.

Of the six PMTs in the helium detector, calibration confirmed four to be usable in most data taking runs after the detector was cooled down. One channel appeared disconnected, while another demonstrated poor gain such that SPEs were not readily distinguished from noise. There were two ER datasets, about 7% of the total ER data taking time, in which a single additional PMT was dropped from the analysis due to the fitted SPE size falling close to the baseline noise.

8.4.3 Data selection cuts

The scintillation signal size for individual events in each dataset was determined using the SPE size calibration described in the previous section. The trailing pulse area in the event acquisition was corrected by the SPE finding efficiency for that dataset and then added to the prompt area for a total scintillation signal size in the event.

As in the analysis in Section 8.2, the datasets were reduced by a series of cuts based on pulse timing and the far side detector response. The main backgrounds for this type of analysis are multiple scatter events and events formed by accidental coincidences in the helium and tagging detector volumes, both of which lead to events with recoil energies and/or scattering angles not corresponding to those in Equations 8.1 and 8.2. Therefore, the cuts were designed to reject these types of events, while maximizing the acceptance of good single scatter events. We also discuss the effect of varying these cuts on the best fit values found in the analysis, to provide an estimate of the systematic error associated with each cut.

Monte Carlo (MC) simulation spectra, with the same event selection applied, were fitted to each dataset independently by floating a mean signal scaling parameter, a parameter for the energy resolution of the liquid helium response, and an overall scale factor of the distribution.

ER data selection cuts

The NaI tagging detectors in the ER configurations provided information about timing and recoil energy of events scattering in them. Each detector was calibrated independently for both timing and energy resolution.

Timing cut—As mentioned in Section 8.3.3, we synchronized the helium detector and tagging detector timing with the back-to-back gamma rays from ^{22}Na decays. For each tagging detector, we fit a Gaussian to the distribution of pulse time differences between that detector and the helium detector to calibrate the time resolution of the experimental configuration. We found a resolution of 4 ns (sigma) for both NaI detectors, comparable to the 1-2 ns it takes the scattered gamma ray to travel between the liquid helium and NaI volumes in the Compton scattering data taking configurations.

For the timing cut in the Compton scattering analysis, we used a relatively wide coincidence window of $\pm$20 ns since we found that a tighter definition had no strong effects when used in conjunction with the NaI energy deposit cut described below. The same timing cut was applied to the MC spectra after applying Gaussian smearing with the measured 4 ns resolution. We estimated the systematic uncertainty associated with this cut by rerunning the analysis with modified values of $\pm$16 ns and $\pm$24 ns and found variations at 1% or less for all datasets except 98.9 keVee, which had a 5% variation in the best fit value.

NaI energy deposition cut—Gamma rays which Compton scatter once in the helium target have an outgoing energy described by 8.2, ranging from 476 to 625 keV for the recoil energies in this study. NaI detector scintillation can be used to reconstruct the deposited energy to a high degree of accuracy, providing an additional data selection cut by looking for events which match the expected remaining gamma ray energy in the NaI detector.

We used the decay gamma rays from ^{22}Na, ^{57}Co, ^{133}Ba, and ^{137}Cs to calibrate the NaI detector response from 122 to 1275 keV. First, the mean response at each gamma ray energy was found by fitting a Gaussian to the photoabsorption peak. Then, we used a linear fit to determine the detector response as a function of energy. Similarly, the behavior of the

energy resolution was estimated by fitting a function of the form

$$\sigma_r(E) = c_1 E + c_2 E^{1/2} + c_3, \tag{8.5}$$

to the standard deviations obtained from the Gaussian fits, where the c_i are fit coefficients for each term. Our measured single standard deviation resolution for gamma ray energies in the range expected of E'_γ was 3%-4%.

For each dataset in the analysis, events were cut according to the signal response in the NaI detector. Events were accepted if the response in the NaI detector was within $E'_\gamma \pm 5\sigma_r(E'_\gamma)$. The effect of the cut is demonstrated in the bottom panel of Fig. 8.12, where the orange population consists of events with only the timing cut described above and the blue spectrum represents those also passing the NaI energy cut. While this cut removes some events in the single scatter peak visible in the liquid helium signal spectrum, selecting events consistent with an energy deposit of E'_γ in the NaI boosted the ratio of events in the liquid helium single scatter peak relative to its side bands. The NaI energy deposit cut was replicated in the MC events by applying the measured energy resolutions of the two tagging detectors. The distinct calibrations of the two tagging detectors were weighted according to the number of events collected with each detector in a given dataset. The systematic uncertainty resulting from this cut definition was estimated by rerunning the analysis with $\pm 4\sigma_r$ and $\pm 6\sigma_r$ as the selection window, resulting in variations at the 0.5-3% level.

NR data selection cuts

NR datasets were reduced using pulse shape discrimination and timing cuts enabled by the LS tagging detector.

Pulse shape discrimination cut—The BC-501A LS pulse shape can be used to discriminate recoil types by considering the maximum pulse height and total pulse area in the event. An example of the pulse shape discrimination (PSD) cut for the 561 $\mathrm{keV_{nr}}$ dataset is shown in the left panel of Fig. 8.13; electronic recoils form a clear upper band and nuclear recoils form the lower band. Events from the lower band within the orange lines were tagged as neutron scatters in the liquid scintillator. We applied a minimum area cut of 5 V ns because the two bands merge at low area, reducing the discrimination power. A maximum height cut was used to eliminate events saturating the digitizing electronics. Since the PSD bands were clearly separated for large area events, the systematic uncertainty estimate for this cut was to vary the minimum area to 2.5 V ns and 10 V ns which resulted in at most 1%-level variation in the final signal scaling parameter values.

The effect of the PSD cut is shown in the top right panel of Fig. 8.13, which shows spectra of the time-of-flight, defined as the event time in the LS minus the event time in the liquid helium. All of the events in the dataset are shown in the black spectrum, while events tagged as neutrons by the PSD cut are plotted in orange. A prompt peak near a time-of-flight of 0 ns from gamma scatters is clearly visible in the events before the application of the PSD cut, and a peak in the tagged neutron events is apparent around the expected time-of-flight for the experimental configuration.

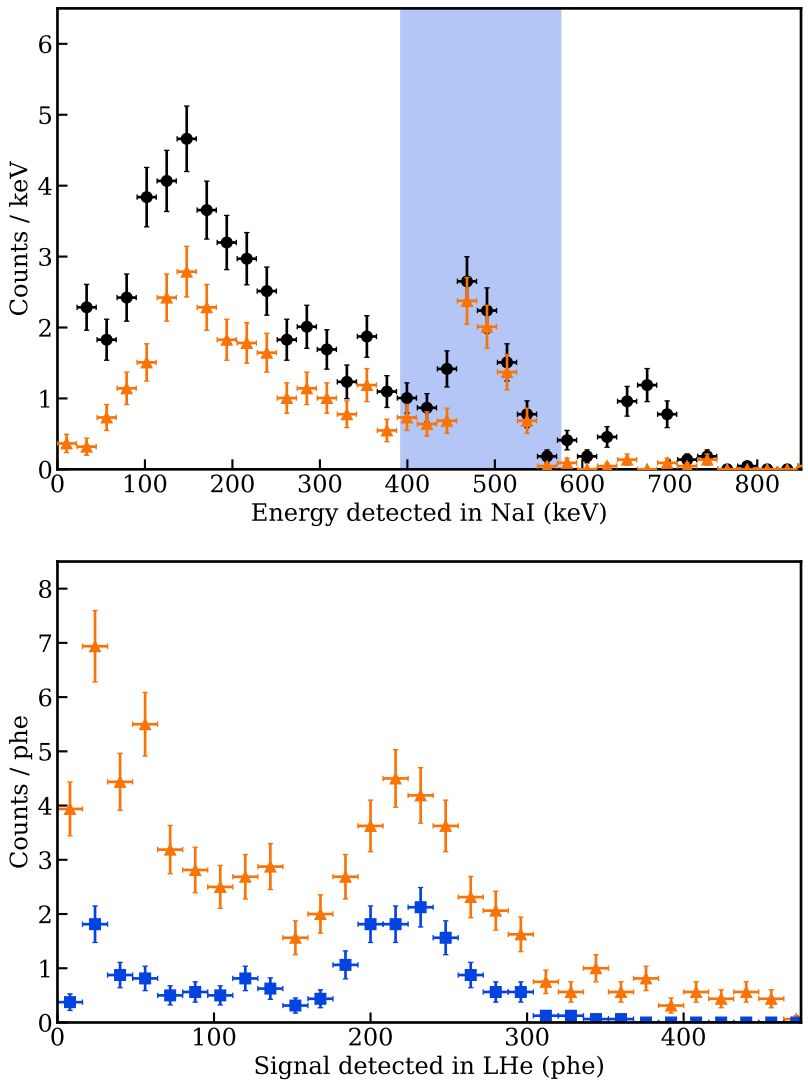

Figure 8.12: The 185 keV$_{ee}$ dataset as an example of the NaI cut applied to all of the Compton scattering datasets. The response in the NaI detector (top) was used to select events more likely to match the energy E'_γ expected from Eq. (8.2). All events before cuts are shown in the black circles, where the photoabsorption peak for 661.7 keV ^{137}Cs gamma rays is a visible feature. It mostly vanishes as a result of the timing cut after which the orange triangle events remain. Still present in the orange spectrum is a photoabsorption peak corresponding to $E'_\gamma = 476$ keV. Events which fall inside of the blue band are accepted for the analysis (the definition of the band is described in the text). The effect of the NaI energy cut on the helium scintillation spectrum (bottom), where the orange triangle events correspond to those in the top panel and the blue square events are those which also pass the NaI energy cut, is a more prominent peak attributed to single scatter events.

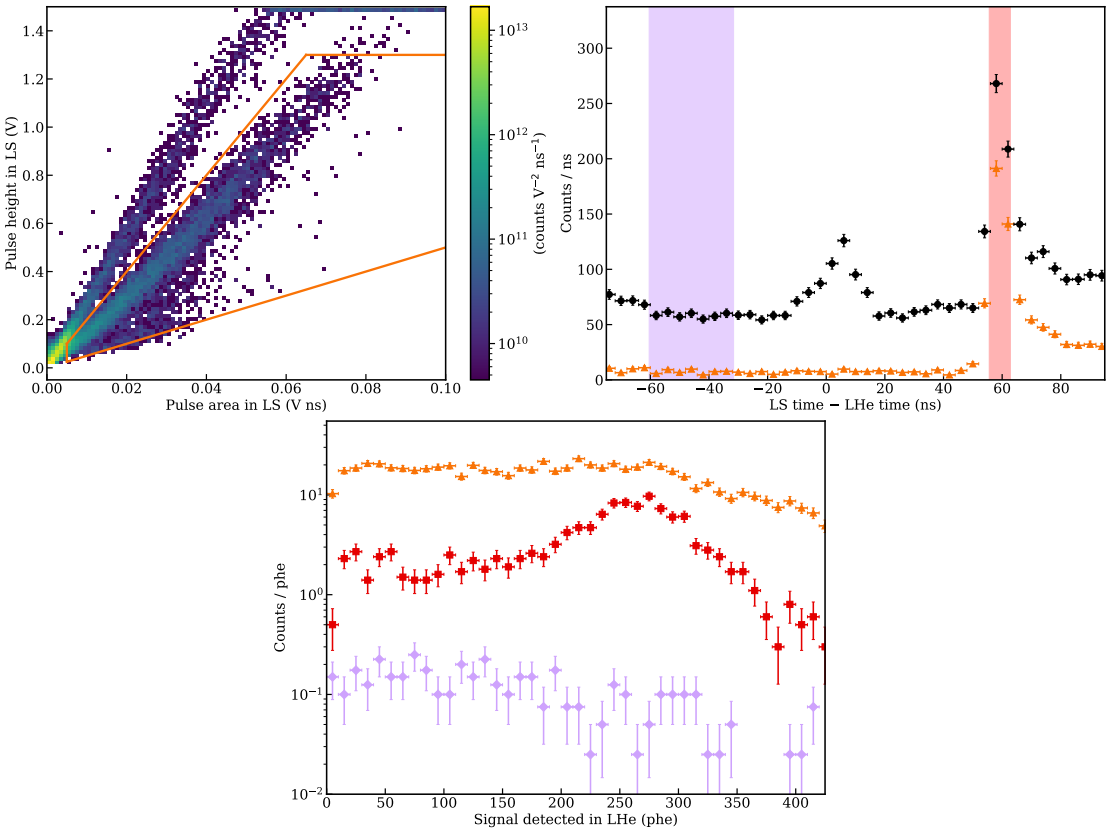

Figure 8.13: The 561 keV$_{\mathrm{nr}}$ dataset as an example of the cuts applied to the nuclear recoil datasets. (Top left) Pulse shape discrimination (PSD) of the liquid scintillator (LS) tagging detector. The upper band comes from electronic recoil events and the lower band from nuclear recoils. Events from the lower band inside of the orange lines are accepted and tagged as neutrons. (Top right) The effect of this cut on the event distributions in time-of-flight, defined as the liquid scintillator time minus the event time in the liquid helium. The spectrum marked by black circles consists of all events before cuts, while events plotted in orange triangles are those tagged as neutron scatters by the PSD cut. The prompt peak in the total event spectrum is consistent with scatters produced by gammas rather than neutrons as it disappears on application of the PSD cut. The peak in neutron events first arriving about 53 ns later corresponds to neutrons scattering once in the liquid helium, while the longer tail comes from multiple scatter events. Events in the red band are accepted as single scatter neutron events. We estimated the random coincidence backgrounds with the neutron scatters in the purple band. (Bottom middle) Liquid helium scintillation spectrum of neutron-tagged events shown as orange triangles in the right panel. Events passing the time-of-flight cut are shown as red squares. The accidental coincidence event spectrum was rescaled according to the size of the time-of-flight acceptance window and plotted as purple diamonds.

As with other cuts, this cut was replicated in the MC events. However, the effect of this cut on the MC events was minuscule because the majority of the events in the electronic recoil band of the LS discrimination plot were from accidental coincidences with background gammas, which were not simulated.

Time-of-flight cut—The time it takes a neutron to travel between the liquid helium volume and the tagging detector is well-determined by its energy, so an additional constraint on good single scatter events is that the time measured between events in the LHe target and the LS tagging detector corresponds to the remaining neutron energy predicted by Equation 8.1.

The time resolution of the setup with the LS tagging detector was measured with a ^{22}Na source in the same way as for the NaI detectors, resulting in a time resolution of σ_t = 2.4 ns. The middle panel of Fig. 8.13 shows a tagged neutron peak consistent with the expected 53 ns time-of-flight for single scatter neutrons in this experimental geometry. A time-of-flight cut was used to select these single scatter events and reject neutrons scattering multiple times before reaching the tagging detector, which do not necessarily deposit the energy described by Eq. (8.1). Events within -1/+2σ_t around the peak in the spectrum were accepted, where the bounds were optimized by examining the time-of-flight behavior in MC events and also by maximizing the liquid helium scintillation peaks relative to their side bands in experimental data. As with other cuts in the analysis, we modified these bounds to -2/+2σ_t and -1/+3σ_t as a systematic uncertainty estimate and found variations between 1-2%.

The time-of-flight acceptance region is the red band in the middle panel of Fig. 8.13, and the events that pass both cuts are shown in red in the right panel. The red distribution reveals a well-defined scintillation signal size peak associated with single scatters in the LHe. There is a flat distribution of nuclear recoil events in the time-of-flight spectrum arising from accidental coincidences in the two detector volumes. The contribution of such events to the signal region was estimated from the purple region in the middle panel of Fig. 8.13, scaled to the width of the time-of-flight acceptance window. This scaled spectrum is shown in purple in the right panel of Fig. 8.13, where it is clearly subdominant to the main signal events in red.

8.4.4 Fitting procedure

MC events were first converted from units of energy to signal size in number of photons. The number of photons S was determined by

$$S = Y_{xx} E_{xx}, \tag{8.6}$$

where Y_{xx} are the signal scaling parameters with units phe/keV and E_{xx} are the simulated deposit energies of each type in units of keV.

Next, the MC events were weighted according to the selection cuts and smeared using a Gaussian energy resolution function

$$f(x, S, A) = \frac{1}{\sqrt{2\pi A^2 S}} \exp\left[\frac{-(x-S)^2}{2A^2 S}\right], \tag{8.7}$$

where x is the smeared signal in phe, S is the signal from the MC event given by Equation (8.6), and A is a resolution factor with units $\sqrt{\text{phe}}$. The fitted trigger efficiency curve from Fig. 8.10 was applied to the smeared spectrum by integrating the function over each bin in the smeared spectrum and rescaling the bin by the result. It is possible, though unlikely, for DD neutron events to induce ERs in the liquid helium target through inelastic scatters and neutron capture on materials around the target. After the time of flight selection, fewer than 0.1% of MC neutron events had an ER energy component. Thus, we neglected the ER energy component in our treatment of the NR MC.

The smeared MC spectra were each separately fit to histograms of the experimental data passing selection cuts with three floating parameters: $Y_{ER/NR}$, A, and a third parameter determining the overall height of the MC spectrum. Fitting was performed by minimizing the χ^2 test statistic from Equation 8.4, just as in the analysis from Section 8.2.

The fit region was determined iteratively, first by hand selecting the boundaries and finding the best fit parameters. Then, those parameters were used to smear the distribution of the single scatter events of interest in the MC, and the iterated fit region was defined as $\pm 2\sigma$ about the mean of a Gaussian fit to those events. The final signal scaling parameter results were those resulting from rerunning the fitting procedure using the iterated fit region.

Table 8.3 lists the six fitted ER and seven fitted NR signal scaling parameters, along with statistical errors from the fits and systematic uncertainties estimated as described below. Figures 8.14 and 8.15 show histograms of the detected scintillation response in the helium target and the corresponding best fit MC spectra for the ER and NR datasets, respectively.

Within each dataset fit, the application of the energy resolution assumed the resolution scales with the square root of the signal size. However, the resolution factor was allowed to float across the dataset fits to make fewer assumptions about the underlying physics of the signal generation. Still, the best-fit values of the resolution factor were self-consistent across all of the datasets. Fixing the resolution factor to the mean value obtained from these fits and re-fitting the data did not yield significant differences in the final values of the signal scaling parameters or degrade the overall goodness of fit of the results.

An excess of events at small signal size for datasets corresponding to larger recoil energies was present in both the ER and NR data. One possible explanation might be varying light collection efficiency over the liquid helium target volume, but we did not find any evidence that such regions exist in the data. Most events in the final datasets were composed of roughly equal fractions of photons seen in each PMT. It is also unlikely to be the result of degraded recoil tracks, since the recoil track length in 1.75 K liquid helium for 1 MeV recoil alphas is about 40 μm and for 200 keV recoil electrons about 3 mm [206]. This explanation is especially unlikely to account for the excess in the NR data, where the effect is most

Table 8.3: Fitting results for the ER and NR datasets. Uncertainties for the recoil angles and energies were computed using the effect of position error uncertainties from the target helium volume and the tagging detector on the mean recoil energy. Uncertainties in the signal scaling parameter, Y, are separated into systematic uncertainty (consisting of the effects from the data selection cuts, the uncertainty due to the trigger efficiency, the recoil energy uncertainty, and the statistical uncertainty from the SPE size fits) and statistical uncertainty from the χ^2 minimization fitting. We also report the fitted resolution parameter A and its combined statistical and systematic uncertainty. Finally, we report the minimized χ^2 and number of degrees of freedom for each of the datasets.

	θ (degree)	E_r (keV)	Y (phe/keV)	δY_{sys}	δY_{stat}	A ($\sqrt{\text{phe}}$)	χ^2/n.d.f.
ER	17.2 ± 0.4	36.3 ± 1.5	1.43	$^{+0.10}_{-0.09}$	$^{+0.11}_{-0.09}$	$2.40^{+0.83}_{-0.67}$	6.1 / 7
	20.3 ± 0.4	49.2 ± 1.8	1.08	$^{+0.05}_{-0.05}$	$^{+0.05}_{-0.05}$	$1.56^{+0.66}_{-0.53}$	16.8 / 14
	28.9 ± 0.4	91.7 ± 2.2	1.44	$^{+0.06}_{-0.08}$	$^{+0.09}_{-0.08}$	$2.46^{+1.24}_{-0.65}$	10.2 / 7
	30.2 ± 0.4	98.9 ± 2.3	1.15	$^{+0.08}_{-0.08}$	$^{+0.05}_{-0.05}$	$2.39^{+0.94}_{-0.51}$	15.5 / 7
	40.0 ± 0.4	154.0 ± 2.3	1.33	$^{+0.08}_{-0.04}$	$^{+0.05}_{-0.05}$	$3.57^{+0.93}_{-0.75}$	7.9 / 11
	45.6 ± 0.4	185.0 ± 2.4	1.27	$^{+0.04}_{-0.04}$	$^{+0.03}_{-0.03}$	$1.74^{+0.43}_{-0.45}$	8.3 / 7
NR	15.9 ± 0.2	53.2 ± 1.1	0.48	$^{+0.02}_{-0.05}$	$^{+0.03}_{-0.03}$	$2.00^{+0.65}_{-0.17}$	20.1 / 23
	20.7 ± 0.2	89.4 ± 1.4	0.45	$^{+0.01}_{-0.01}$	$^{+0.02}_{-0.01}$	$2.09^{+0.29}_{-0.39}$	35.0 / 27
	26.3 ± 0.2	142.0 ± 1.7	0.50	$^{+0.01}_{-0.01}$	$^{+0.01}_{-0.01}$	$2.06^{+0.44}_{-0.20}$	25.0 / 17
	31.9 ± 0.2	207.0 ± 2.1	0.47	$^{+0.01}_{-0.01}$	$^{+0.01}_{-0.01}$	$2.44^{+0.25}_{-0.20}$	39.7 / 24
	38.6 ± 0.2	294.0 ± 2.4	0.52	$^{+0.01}_{-0.02}$	$^{+0.01}_{-0.01}$	$2.66^{+0.30}_{-0.43}$	21.9 / 26
	55.8 ± 0.2	561.0 ± 2.8	0.47	$^{+0.01}_{-0.01}$	$^{+0.01}_{-0.01}$	$2.22^{+0.41}_{-0.20}$	12.2 / 14
	87.6 ± 0.2	1090.0 ± 2.6	0.45	$^{+0.02}_{-0.01}$	$^{+0.01}_{-0.01}$	$2.82^{+0.64}_{-0.53}$	10.3 / 10

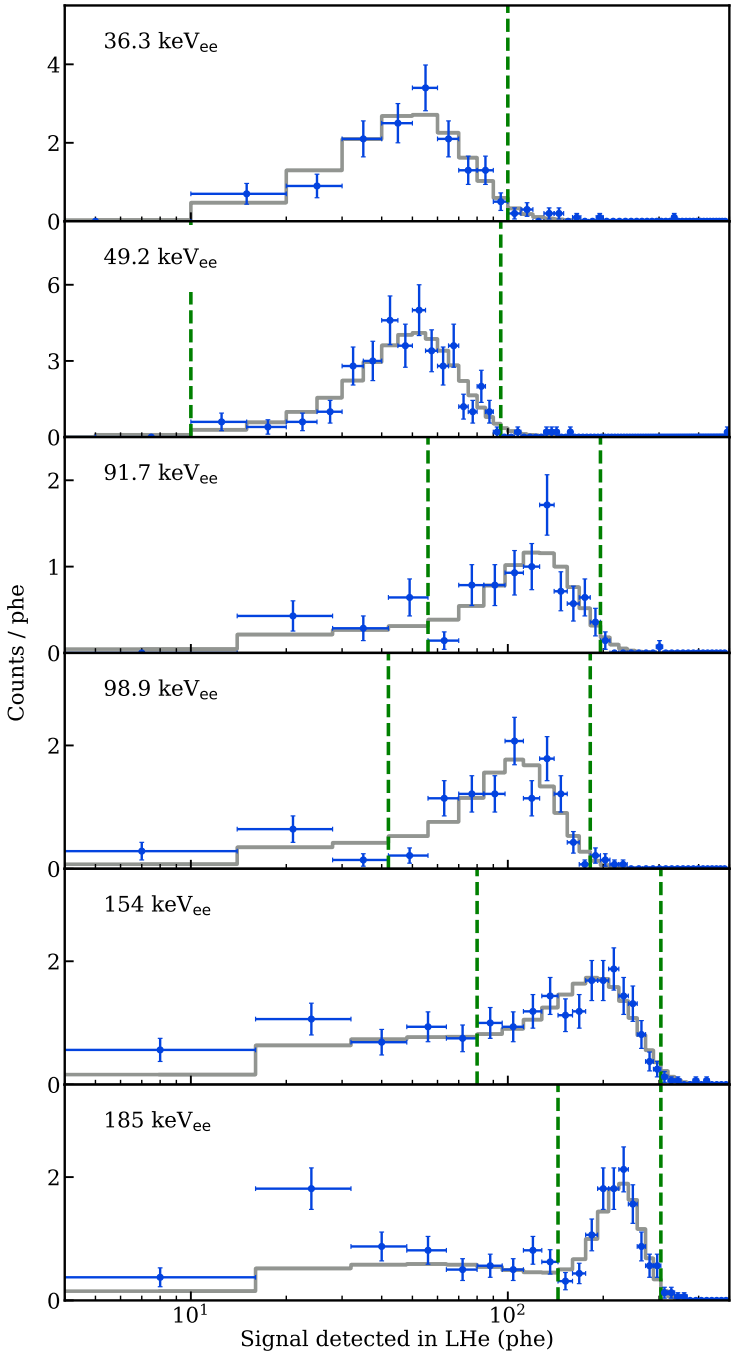

Figure 8.14: Histograms of experimental data (blue) and fitted MC (gray) for each Compton scattering recoil energy. The x-axis showing the signal size in the liquid helium is the same for each panel. The fit region for each fit is between the vertical green dashed lines.

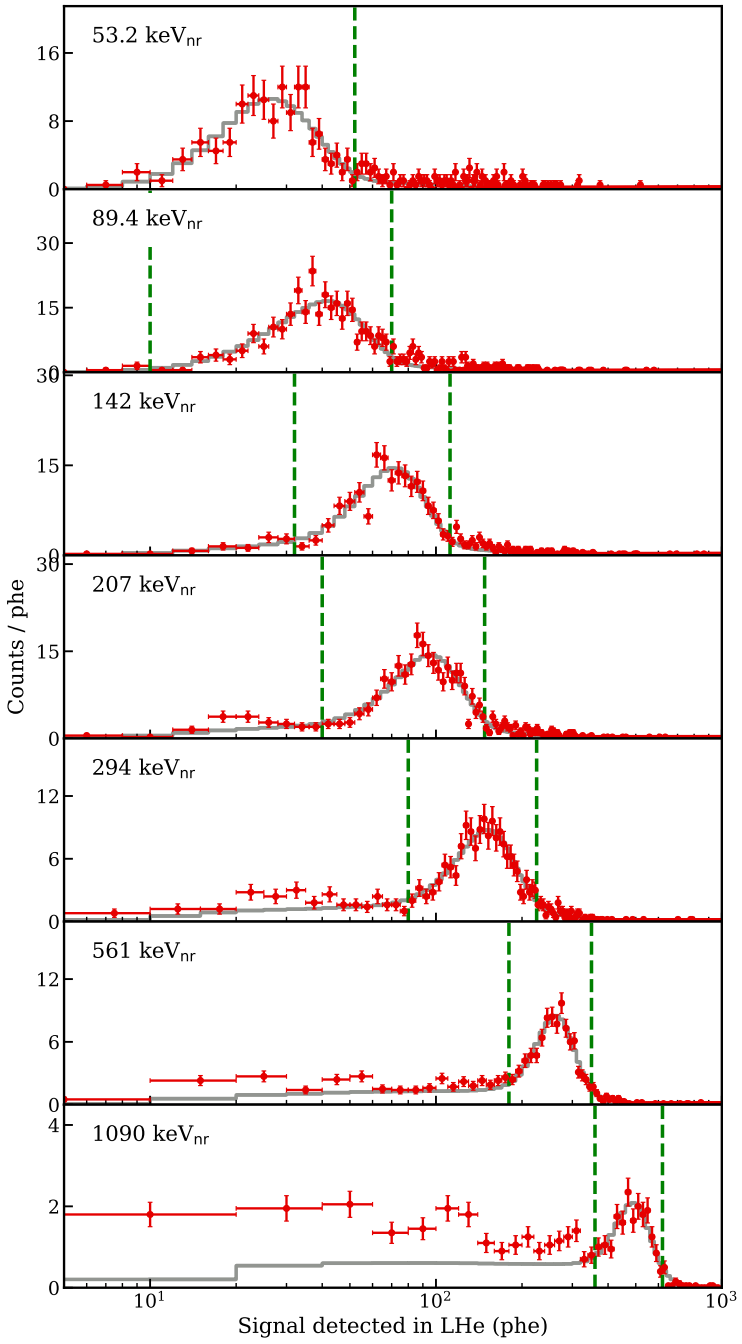

Figure 8.15: Histograms of experimental data (red) and fitted MC (gray) for each DD neutron scattering recoil energy. The x-axis showing the signal size in the liquid helium is the same for each panel. The fit region for each fit is between the vertical green dashed lines, and the lower bound for the 53.2 keV$_{nr}$ fit extends to a signal size of 0 phe.

apparent. Ultimately, the definition of the fit region around the single scatter peak excluded these low energy excesses from the fits.

8.4.5 Systematic uncertainties

Systematic uncertainties associated with the data selection cuts were estimated by varying those cuts and rerunning the fit for each dataset, as previously discussed in the descriptions of the cuts. The systematic uncertainty associated with each cut was estimated as the difference between the best fit value from the main analysis and the fit with the varied cut parameters. These cut-based systematic uncertainties each contributed at the percent level for all of the datasets in the analysis.

The systematic uncertainties due to the fit region definition and the application of threshold efficiency curve were also estimated in this way. The helium signal fit region for each dataset was varied from $\pm 2\sigma$ of the Gaussian fit on the MC single scatter distribution to $\pm 1.5\sigma$ and $\pm 2.5\sigma$. As with the cut-based systematic uncertainties, the fit region definition contributed at the 1-2% level for all of the datasets, except for a 4% difference in the 154 keVee dataset. Likewise, the threshold efficiency curve was replaced by the lower and upper 1-σ bounds shown in Fig. 8.10. The effect of this change was negligible for almost all of the datasets, since the fit regions generally excluded the signal sizes for which the threshold curve strongly varied. However, the systematic uncertainty for the 53.2 $\mathrm{keV_{nr}}$ fit, the smallest signal size across all of the datasets, was dominated by the uncertainty in the threshold efficiency curve with the best fit value varying -8% and +3% for the lower and upper threshold efficiency variations.

Uncertainties on the positions of the target and tagging detectors also contributed some uncertainty to the energies probed by each dataset. We estimated the size of this effect with a toy Monte Carlo approach by varying the positions of the detectors according to the 1 mm position uncertainty and calculating the nominal recoil energy for the modified configurations. A Gaussian was fit to the distribution of nominal recoil energies to translate the effect of the position uncertainty to an uncertainty in the recoil energy assigned to each dataset. This error is listed in Table 8.3 and folded into the systematic uncertainties on the measured signal scaling parameter values. This uncertainty in the recoil energy is distinct from the range of recoil energies sampled by the experimental geometry due to the finite sizes of the detector elements, which is accounted for by the simulation geometry in GEANT4. It is also distinct from the definition of the horizontal error bars in the analysis in Section 8.2, which included the finite sizes of the detector elements.

The uncertainty due to the SPE size calibration was estimated using the statistical error from the SPE fits for individual PMTs in each data taking run. Since the datasets consisted of events from multiple data taking runs, the signal size uncertainty for each dataset was estimated as the average of the SPE size uncertainties weighted according to the number of events from each data taking run in the dataset. This uncertainty contributed at the 2%-3% level for the NR datasets. It contributed a higher 3%-5% uncertainty in the signal scaling parameter of the ER datasets due to fewer SPE statistics for these acquisitions.

As described in Section 8.4.2, the effect of the SPE finding efficiency was corrected for in the total signal size associated with each event. The uncertainty in this efficiency was determined from the Gaussian fit parameters of the SPE area distribution, and propagated to the uncertainty in the total signal size for each dataset. The uncertainty associated with this correction was comparable to other systematic errors described in this section at 1%-5% in the best fit signal scaling parameter.

8.4.6 Delayed scintillation

In the modeling work presented in Chapter 7, we discussed expectations for the time dependence of helium scintillation and used the data collected in this experiment as a point of comparison. In our analysis we found evidence for both exponential and t^{-1} components in the delayed scintillation.

Events in this analysis were selected using the same selection cuts described in Section 8.4.3. The delayed components of these events consisted of well separated SPE pulses such that those that can be seen in Figure 8.9. We have previously discussed the SPE finding efficiency, which is a particularly important systematic error in this analysis. To mitigate it, we restricted the analysis to pulses found in a single PMT channel that demonstrated the highest gain and therefore a higher SPE efficiency.

For each dataset, the pulse times across all events were combined into a single histogram. The histogram was fit to the model

$$n_{phe}(t) = Ae^{-\lambda t} + Bt^{-1} \tag{8.8}$$

for times above 640 ns, where $t = 0$ was defined as the time of the prompt pulse, and the free parameters in the fits were the amplitudes A of the exponential component and B of the t^{-1} component, as well as the decay rate λ of the exponential component. The fits can be seen for ER datasets in Figure 8.16 and for NR datasets in Figure 8.17. We found that both components were critical for fitting the data. Goodness-of-fit from the χ^2 values and residuals from the fits did not suggest any clear modification to the time dependence for improved modeling. We expect a scintillation component due to triplet decay with a lifetime of 13 s, much longer than the 32 μs event window. However, any constant contribution to the rate was found to be negligible, also indicating that PMT dark rate was not a significant background in the study. Analysis of smaller timescales was not pursued due to the duration of the prompt pulses which triggered the events.

Finally, we found the fraction of scintillation in the prompt and two delayed components by integrating the terms in Equation (8.8) from 640 ns to 32 μs and assigning the remainder to the prompt scintillation. Along with statistical error, we considered two sources of systematic error. We varied the fit window lower bound to 400 ns and 1.6 μs, and we propagated the uncertainty from the SPE finding efficiency to uncertainty in the scintillation fractions. We found statistical uncertainty to be the dominant source of error bars in this analysis.

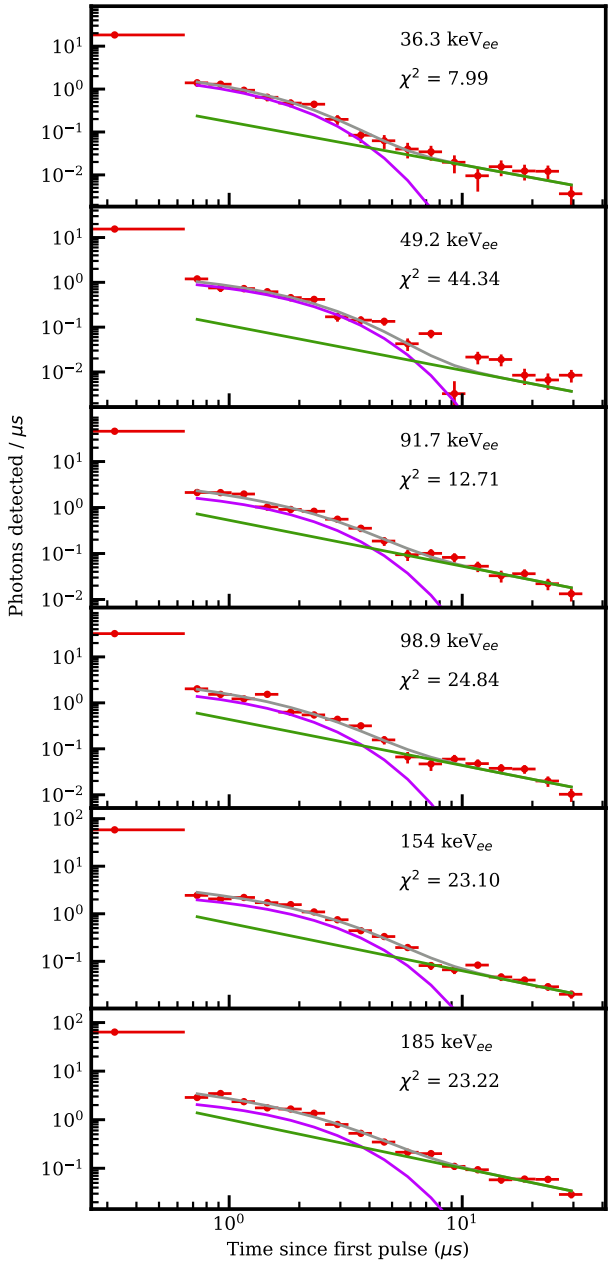

Figure 8.16: ER delayed scintillation fits of exponential (purple) and 1/t (green) components to data (red). The total model is the sum of the two fitted components (gray). The χ^2 value is shown for each fit; for each fit there are 14 degrees of freedom. Figure made by R. Smith.

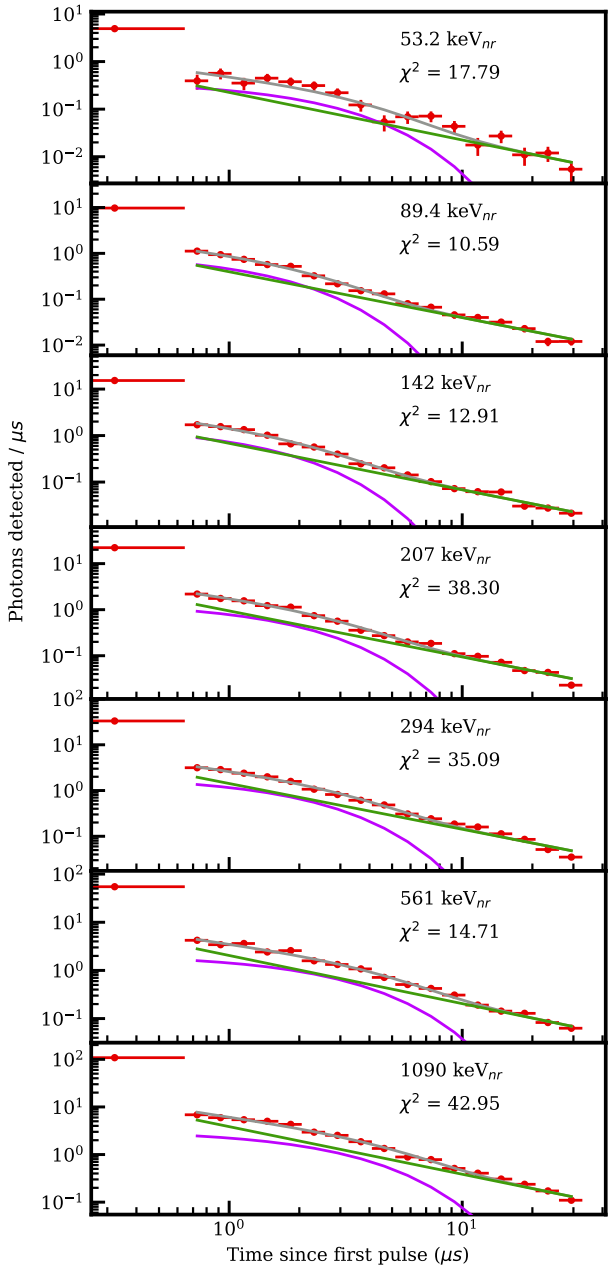

Figure 8.17: NR delayed scintillation fits of exponential (purple) and 1/t (green) components to data (red). The total model is the sum of the two fitted components (gray). The χ^2 value is shown for each fit; for each fit there are 14 degrees of freedom. Figure made by R. Smith.

8.5 Superfluid helium results

In this section we compare the results of the analyses to the modeling work from Chapter 7.

8.5.1 Total light yield

The ER signal size values from Table 8.3 are plotted in Figure 8.18 along with their mean value, 1.25±0.03 phe/keV. We see no evidence of deviation from linearity in the ER response of our data.

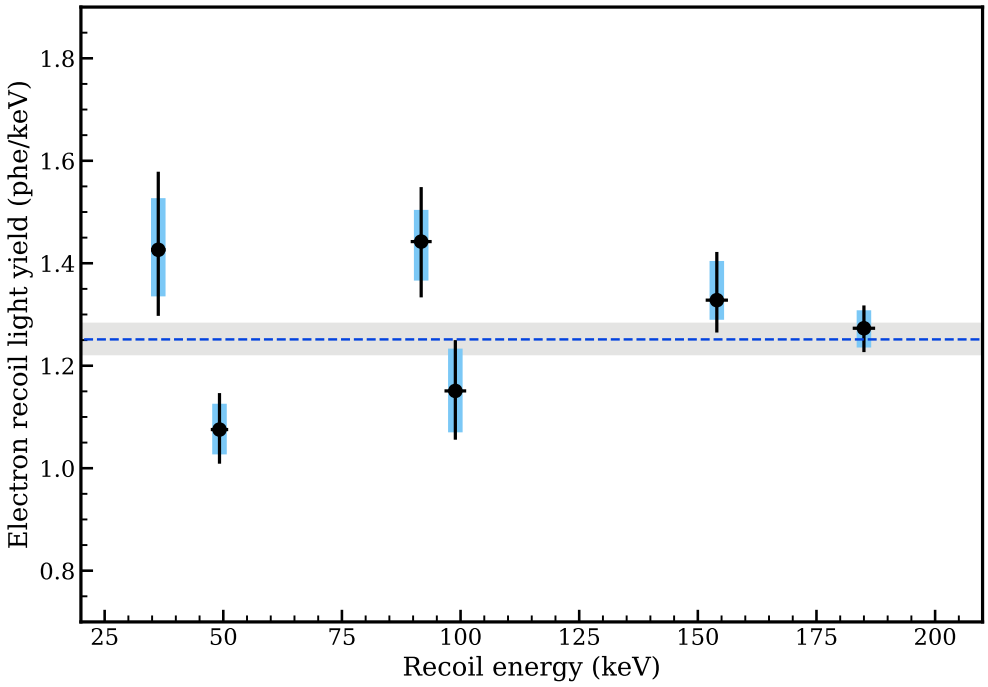

Figure 8.18: The measured ER signal sizes for the datasets shown in Figure 8.14 (points) and weighted mean ER signal size (blue dashed line). The vertical extent of the blue bands represents the systematic uncertainty associated with the measurement, and the black line is the total error from summing the systematic and statistical errors in quadrature. Table 8.3 lists these errors for each dataset. Horizontal black lines are the error on the recoil energy associated with the dataset also listed in Table 8.3; these are hidden by the markers for several points. The gray band represents the error on the weighted mean ER signal size.

The NR signal size values were divided by the mean ER signal size and plotted in Figure 8.19. Since the data were taken with the same target volume, this division should account for any geometric effects on the light yield and facilitate comparison to the model presented in Chapter 7. The model prediction for the relative light yield is also plotted in Figure 8.19 as the solid purple line. This model prediction curve is the sum of the prompt scintillation curve

from singlet decays (the solid green line in Figure 7.14) and the delayed scintillation model for our event window length (the solid magenta line in Figure 7.14). The ER fraction of recoil energy in scintillation is flat across the energy range of the measurements and predicted to be 0.32.

The level of agreement between the data and model prediction is quite encouraging, given that no fitting was performed in their comparison. The predicted fraction of energy in delayed scintillation accounts for about 25% of the model estimate for the solid curve, bringing it closer in apparent agreement with the measured data than the direct estimate of scintillation from singlets only. We do note that the error band on the model is estimated purely from the delayed scintillation model and not the main energy partitioning calculation, for which no errors were estimated.

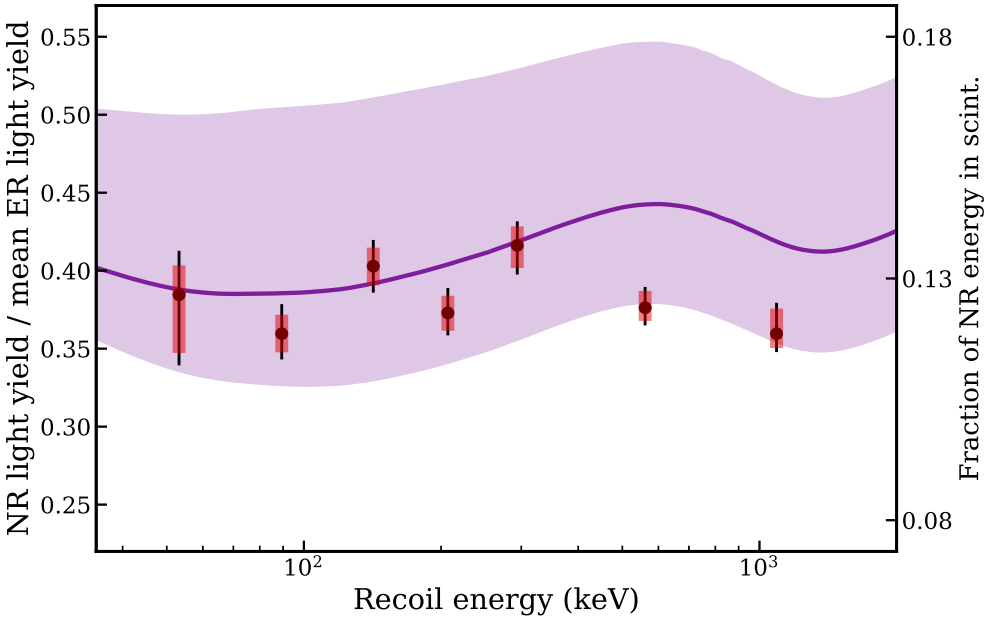

Figure 8.19: The relative light yields measured in this experiment, computed as the NR signal size parameters in Table 8.3 divided by the average ER signal size shown in Figure 8.18. As in Figure 8.18, the red bars represent systematic uncertainties and the thin black lines the total error associated with the measurement at each energy. On this scale, all horizontal error bars are hidden by the markers; they are listed in Table 8.3. The experimental results are compared to the predicted behavior from the semiempirical model (purple) described in Chapter 7, computed here as the sum of the singlet and triplet contribution to the scintillation signal. The right y-axis on this plot represents the fraction of NR energy recovered as scintillation assuming the ER light yield predicted by the model.

8.5.2 Delayed components

We show the partitioning results from the delayed scintillation analysis in Figures 8.20 and 8.21. There are a few noteworthy features in the data and how they compare to the model predictions plotted alongside them. The model prediction for the prompt fraction is in gray and the green curve is the prediction of scintillation from triplets via the Penning process, corresponding to the magenta curve in Figure 7.14. We do not have a corresponding model curve for the exponential term in the analysis, since its origin is unknown.

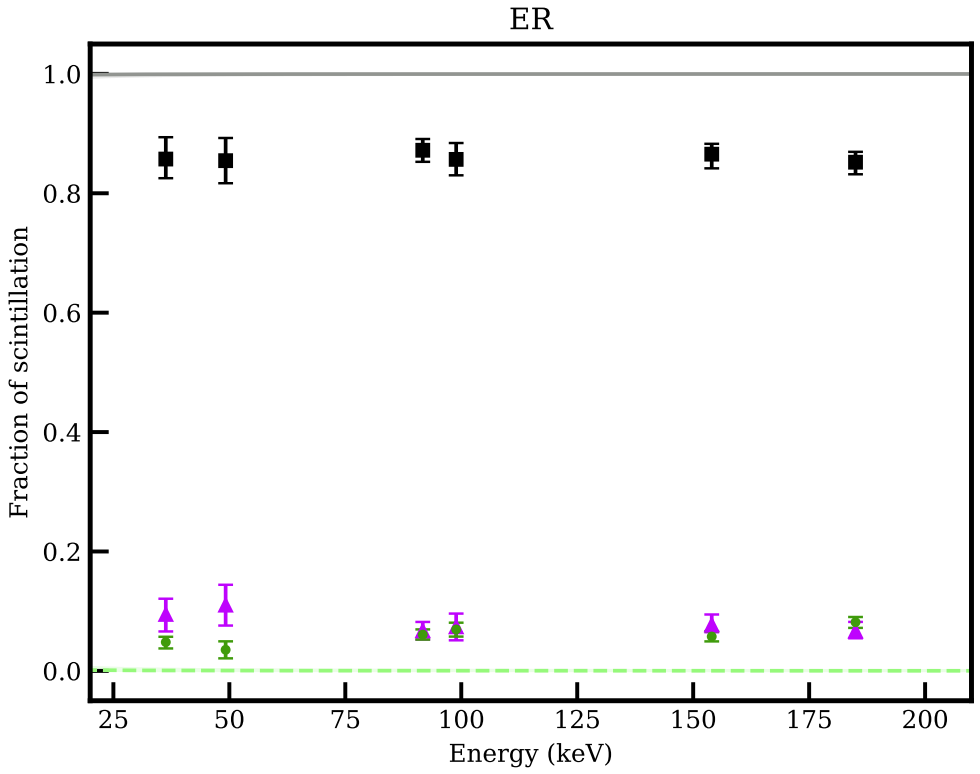

Figure 8.20: Fraction of ER scintillation light in the prompt (<640 ns, black square), exponential (purple triangle), and 1/t (green circle) components. Lines are the fraction of total scintillation predicted from singlets (solid gray) and triplets (dashed green); the error bands associated with the predictions are smaller than the width of the plotted lines. Figure made by R. Smith.

In both the model and the data, the prompt component is fairly uniform across recoil energies and a larger fraction for ERs relative to NRs. Equation 7.7 reduces to t^{-1} behavior in the limits

$$t \gg t_d \quad \text{and} \quad \frac{t_d ln(1+\frac{t}{t_d})}{2t_{tt}} \ll 1. \tag{8.9}$$

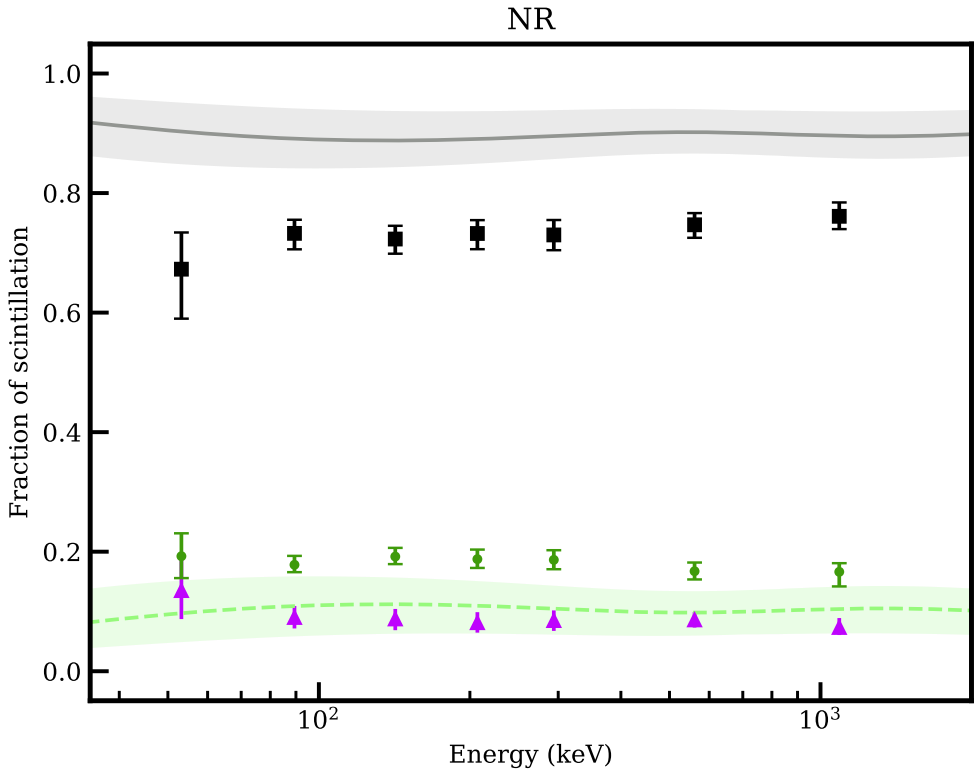

Figure 8.21: Fraction of NR scintillation light in the prompt (<640 ns, black square), exponential (purple triangle), and 1/t (green circle) components. Bands with central lines are the fraction of total scintillation from singlets (gray, solid central line) and triplets (green, dashed central line), by taking the fraction of each in the sum of the corresponding solid curves in Figure 7.14. Figure from [174] made by R. Smith.

We previous estimated $t_d = 3$ ns, much shorter than the μs timescales in this experiment. The second approximation approaches 1 at the end of the event windows, with more violation of the approximation as the nuclear recoil energy increases. Fits were repeated for the functional form of Equation 7.7 with the parameters from Section 7.4 and did not alter the results significantly. Thus, we associate the t^{-1} component with triplet-triplet interactions. We do not expect significant Penning quenching in the electronic recoil case due to the lower density of the track environment, and find a larger t^{-1} component in the nuclear recoil case.

The exponential term was previously observed in data and hypothesized to originate from reactions between metastable He(2^1S) and ground state helium atoms [227]. Interestingly, the fitted fraction in the exponential term is about the same for all of the datasets, and adding this term to the prompt fraction brings the data closer to the model prediction, lending some evidence towards this hypothesis. Since this explanation places the exponential term as part of the dimerization process, it would be covered by the singlet fraction in the partitioning

model. We did observe variation of the lifetime of the exponential term with NR energy. While the best fit value was approximately 1.4 μs for all of the ER datasets, it varied from 1.6 μs to 2.5 μs with increasing NR energy.

Again, we turn to the the density of the recoil track environment for a possible explanation. We hypothesize that the that the excited state responsible for the exponential term undergoes the same quenching as the singlet and triplet excimers in the model. We can estimate the timescale t_q at which quenching no longer occurs due to triplet-triplet annihilation and diffusion by

$$t_q = \frac{\chi_{tt}\tau_{exp}n_T(0)r_0^2}{D_T}, \tag{8.10}$$

where we use the triplet-triplet annihilation constant $\chi_{tt} = 4 \times 10^{-10}$ cm^{3}s^{-1}, $\tau_{exp} = 1.4$ μs, an initial cylindrical track with radius $r_0 = 20$ nm, and a triplet diffusion constant of $D_T \approx 7 \times 10^{-4}$ cm^2/s. The initial triplet concentration, $n_T(0)$, comes from the model assuming the same cylindrical track dimensions and varies with recoil energy. At the lowest NR energy we find $n_T(0) = 1.7 \times 10^{17}$/cm^3 which yields $t_q = 600$ ns. Notably, this is a shorter timeframe than the fit region for the delayed scintillation analysis, and suggests that the quenching timescale decays away before affecting the fitted exponential lifetime. However, for the highest recoil energy we find $n_T(0) = 5.2 \times 10^{17}$/cm^3 so $t_q = 1.8$ μs, which does impact the fit region but decays away relatively quickly relative to the total event lengths in our data. Qualitatively, this would push the fitted lifetime of the exponential term to a larger value, offering a possible explanation for our results. Additionally, the track density decreases again above about 1 MeV, meaning that the lower lifetime values found with higher energy alpha sources remain plausible in this density-dependent explanation.

Finally, we note that a complication in this analysis arises from the potential time dependence of TPB emissions. Delayed emission from photoionized TPB molecules has previously been suggested as the source of the t^{-1} component [228]. However, both the exponential and t^{-1} differed between helium gas and liquid helium in [227], suggesting helium itself was significant in the delayed scintillation process. Our model does not project any t^{-1} component in the ER scintillation, yet both terms are clearly present in the ER data. Therefore, we can not completely rule out TPB as a contributing factor to the delayed scintillation.

8.6 Future measurements

For a first comparison of lower energy nuclear recoil data to the model we developed in Chapter 7, we find extremely encouraging agreement. In our analysis of both total and delayed scintillation, we found ways to probe several aspects of the signal partitioning in this energy range and found no extreme disagreements. However, there are minor sources of tension that inspire future experimental measurements and corresponding sources of feedback for modeling.

In the probed energy range of 53-1090 keV$_{\rm nr}$, we found that the total scintillation model fit the data extremely well. This energy range only partially overlaps the true range of

interest for a dark matter experiment like HeRALD, and future measurements of the scintillation yield will focus on lower recoil energies. In Figure 7.13, we also project a rise in singlet fraction at energies just below the range probed by this experiment, a highly appealing feature for further testing the validity of the model. We expect a comparable feature in the delayed scintillation t^{-1} component. In fact, both the NR and ER model project a substantial increase of this component down to about 10 keV. A next iteration of the superfluid experiment is already planned, aiming to boost the total light collection efficiency by successfully cooling down with all six PMTs operational. Additionally, we plan to push to lower recoil energies by using a monoenergetic source of lower energy neutrons, the design of which is described in the next chapter. We have also developed a new tagging detector for keV-scale neutrons for use in the next iterations of neutron scattering experiments [229].

We also note that these measurements were taken at a single temperature of 1.75 K, while future dark matter detection schemes anticipate operating temperatures in the tens of mK [148]. The quenching time in Equation 8.10 is strongly temperature dependent via the diffusion coefficient D_T [208], already implicating temperature as an important variable for interpreting our data and extrapolating to the regime of interest for a dark matter experiment.

Finally, we return to the discussion of TPB in this experiment. The use of PMTs disfavors measuring the helium scintillation directly, due to its 80 nm scintillation wavelength lying outside of the typical range of sensitivity. However, the calorimeters planned for HeRALD do not have the same limitations and are sensitive to a much wider range of photon energies in principle. Running a neutron scattering measurement such as the ones described in this chapter using calorimeters instead of PMTs would help untangle the role of TPB in the delayed scintillation analysis and perhaps also probe the infrared channel discussed in Chapter 7.

Chapter 9

Design of a Portable Photoneutron Source with Iron Filter

We ended Chapter 8 by motivating future neutron scattering experiments targeting lower recoil energies. One step towards these lower recoil energies is to perform the same kind of scattering experiment with lower energy neutrons.

Sb^{124}-Be photoneutron sources are becoming a standard tool to calibrate dark matter experiments at low recoil energies [138, 140, 141]. Advantages of this calibration strategy include the portability of the sources and the production of 24 keV neutrons, with the energy well known due to kinematic considerations. However, they come with several drawbacks as well. Neutron production is typically subdominant to gamma rays passing through the beryllium target to the order of three or four orders of magnitude. The associated large gamma ray rate is typically reduced with dense shielding materials like lead or tungsten, at the cost of smearing the neutron spectrum towards lower energies. While the endpoint recoil energy of a single scatter is still well-defined, the additional material typically complicates simulations accompanying the calibration analysis, introducing systematic errors from neutron transport cross sections. A more detailed overview of photoneutron sources was presented in Chapter 5.

Another demonstrated method of obtaining 24 keV neutrons is the use of an iron filter in a reactor neutron beam [140, 230, 231]. This method takes advantage of a narrow dip in the neutron scattering cross section of natural iron, filtering out neutrons at nearby energies while acting like a window for those around 24 keV. The minimum in the cross section is at 24.5 keV, where the mean free path of a neutron in natural iron is 29.4 cm. In a high flux, broadband neutron source at a reactor, other materials can be used to scatter away neutrons at energies further away from the iron cross section notch to shape a monoenergetic beam at 24 keV. The major disadvantage of this approach is its lack of portability, requiring assembly of neutron scattering experiments at the reactor site.

These two neutron source concepts have never been used in conjunction, despite the coincidental overlap at around 24 keV. Figure 9.1 shows the energy range of Sb^{124}-Be photoneutrons and the mean free path of neutrons in natural iron, where it can be seen that

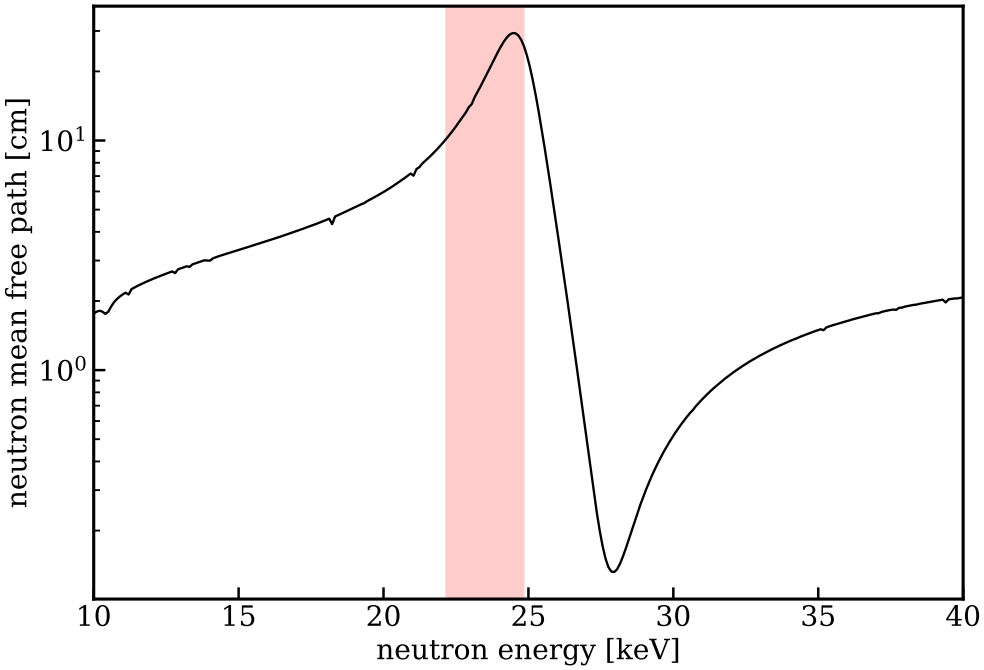

Figure 9.1: The red band is the neutron energy range generated by ^{124}Sb-^{9}Be photoneutron source and the black line is the neutron mean free path in natural iron. The neutrons generated by the Sb-Be source coincide with the crest in the neutron mean free path in iron. The neutron interaction cross section data, and thus mean free path, are from the ENDF/B-VIII.0 database [29].

these features coincide quite well. Although it is not as effective as denser materials such as lead or tungsten, iron can also be used as a gamma ray shielding material. We have designed a portable neutron source based on the combination of Sb^{124}-Be photoneutron production and iron neutron filtering that avoids the neutron energy smearing typically associated with photoneutron calibration sources.

The final source design was the product of many simulation iterations, with the intent of optimizing the performance of the source for detector calibrations, keeping it relatively portable, and considering its safety implications. The dissertation author performed these simulations to refine the source design that was ultimately fabricated by J. Lin.

9.1 Source design

Figure 9.2 shows a detailed model of a source design combining Sb^{124}-Be photoneutron production with an iron filter. The beryllium metal target for photoneutron production is placed inside of a cylindrical 99.9% iron container, with an additional cylinder made of

99.98% iron enclosing the source and serving as the main filtering volume. The total length of the iron is 20.32 cm, or about one mean free path for 23.5 keV neutrons. From Equation 5.2, Sb^{124}-Be photoneutrons range from 22.2 to 24.8 keV. A high activity antimony source, on the order of 1 GBq, ensures a high rate of neutron production.

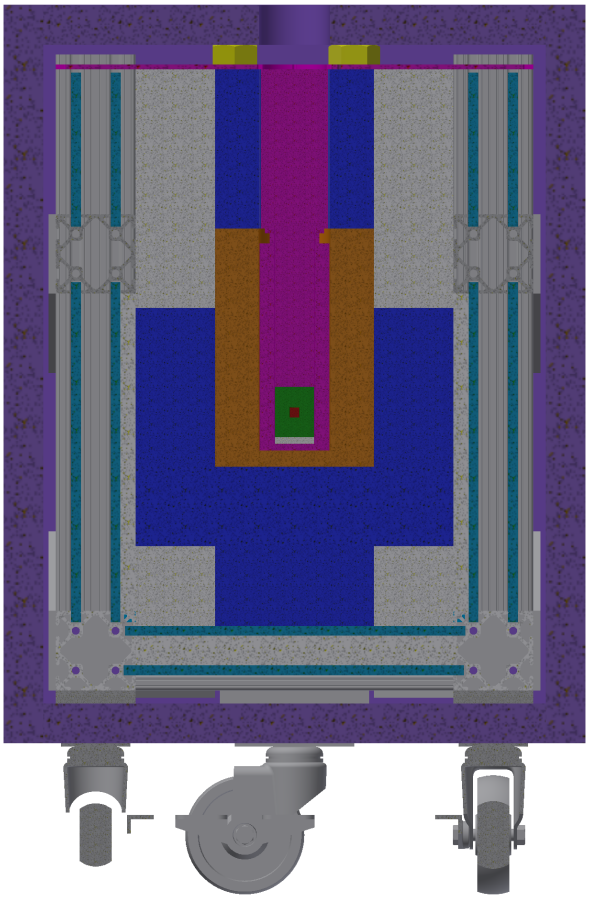

Figure 9.2: A CAD model cross section for the Sb-Be photoneutron source. The red square in the center indicates the activated Sb pellet. The green volume surrounding it is the beryllium metal target for photoneutron production, which is contained inside of an iron cylinder in magenta. The brown shape containing the lower part of the iron filter is tungsten, with further lead shielding in blue. Aluminum volumes are in grey, and the enclosing borated polyethylene is in purple. Figure made by J. Lin.

Unshielded gamma rays are a background in photoneutron calibrations, particularly for a source of such high activity. In this context the concern is twofold, where gamma backgrounds are undesirable in a calibration setting, but the level of radiation is also plausibly a safety concern. To reduce the rate of gammas impinging on a potential detector target and to make the source safer for use, there is ample shielding material surrounding the iron filter.

The filter is nested inside of a machined tungsten holder, and there are further lead bricks layered around it and a machined lead volume enclosing the downstream portion of the iron filter.

Photoneutron production is isotropic, and as was critical for the design of the photoneutron source in Chapter 5, dense gamma ray shielding materials still allow neutrons to pass somewhat effectively. To reduce the number of fast and thermal neutrons in the calibration environment, the source was enclosed with a 1-inch thick layer of 5% borated polyethylene, a common neutron shielding and absorbing material. This neutron shielding layer was not a part of the safety design of the source and added purely for calibration performance.

Finally, some comments on the portability of this source design. Of course, it is quite heavy, weighing in at about 450 pounds. However, it is possible to wheel the source around, and it can be maneuvered in the process of a calibration experiment using a crane. It was designed to comply with Department of Transportation radioactive material shipping guidelines. The source can be commercially shipped via a 55 gallon drum Type A shipping container. It is significantly more portable than an equivalent energy reactor source, valuable for applications to lab-based neutron scattering experiments and even *in situ* calibrations of existing particle detectors.

9.2 Simulated spectra

The source geometry was simulated with GEANT4 [77–79] version 10.5 using the SHIELDING physics list. Figure 9.3 shows the simulation source geometry corresponding to the CAD model in Figure 9.2. While most of the volumes were implemented exactly, the outer aluminum T-slot was instead modeled as a solid volume with density equivalent to the volume-averaged aluminum density in the T-slot geometry, and the wheels were omitted completely.

Photoneutron generation was implemented using the same strategy as described in Section 5.3. The neutrons of interest are produced from the Sb^{124} 1690.98 keV gamma ray line, which has an intensity of 47.79% [232]. For this gamma ray energy, the ENDF/B-VIII.0 photonuclear cross section [29] is in good agreement with the fits from Robinson [143] and Arnold *et al.* [144] with a value of 1.41 mb. We estimate the 24 keV neutron production rate to be 0.00010 neutrons per Sb^{124} decay for the beryllium metal target used in this source. This rate corresponds to one neutron produced per 4700 gamma rays from the 1690.98 keV transition.

The low energy neutron spectrum exiting the opening in the borated polyethylene volume at the end of the iron filter is shown in Figure 9.4. The flux of neutrons with energy >1 keV is 6.2 neutrons per cm^2 per second assuming a 1 GBq Sb^{124} source. 40% of this flux lies in the peak between 20 and 25 keV, indicating a fairly pure beam of low energy neutrons leaving the filter. The filter face has a radius of 4.9 cm^2, yielding a 20-25 keV neutron emission rate of 12 neutrons per second. This rate is directly proportional to the activity of the Sb^{124}

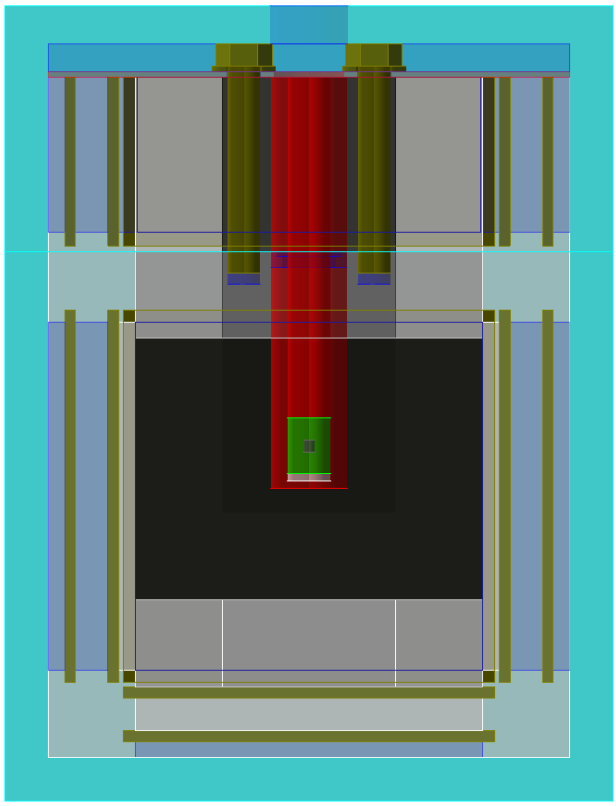

Figure 9.3: The GEANT4 geometry for the source simulations. The small grey square in the center indicates the activated Sb pellet. The green volume surrounding it is the beryllium metal target for photoneutron production, which is contained inside of an iron cylinder in red. The dark grey shape containing the lower part of the iron filter is tungsten, with further lead shielding in black. Aluminum volumes are in grey, and the enclosing borated polyethylene is in cyan.

source, so it is possible to increase the neutron emission rate further, up to a factor of about 5 for the safety parameters defined for this source design.

Sb^{124} has an additional transition that should be considered in the context of photoneutron production, with an energy of 2090.945 keV and an intensity of 5.51% [232]. Again referencing Equation 5.2, this transition yields 379 keV neutrons with a spread in energy of ± 7 keV. For the purposes of a monoenergetic, low energy neutron calibration, this neutron population represents a background. However, its production is subdominant not only because of the smaller branching fraction in Sb^{124}. At this gamma ray energy, the photonuclear cross section is reduced to 0.41 mb according to ENDF/B-VIII.0, and the Robinson [143] and Arnold *et al.* [144] values are even smaller at 0.26 and 0.25 mb, respectively. Considering the ENDF/B-VIII.0 value as a conservative estimate on the contamination of higher energy neutrons, we estimate that the 379 keV population accounts for about 3% of

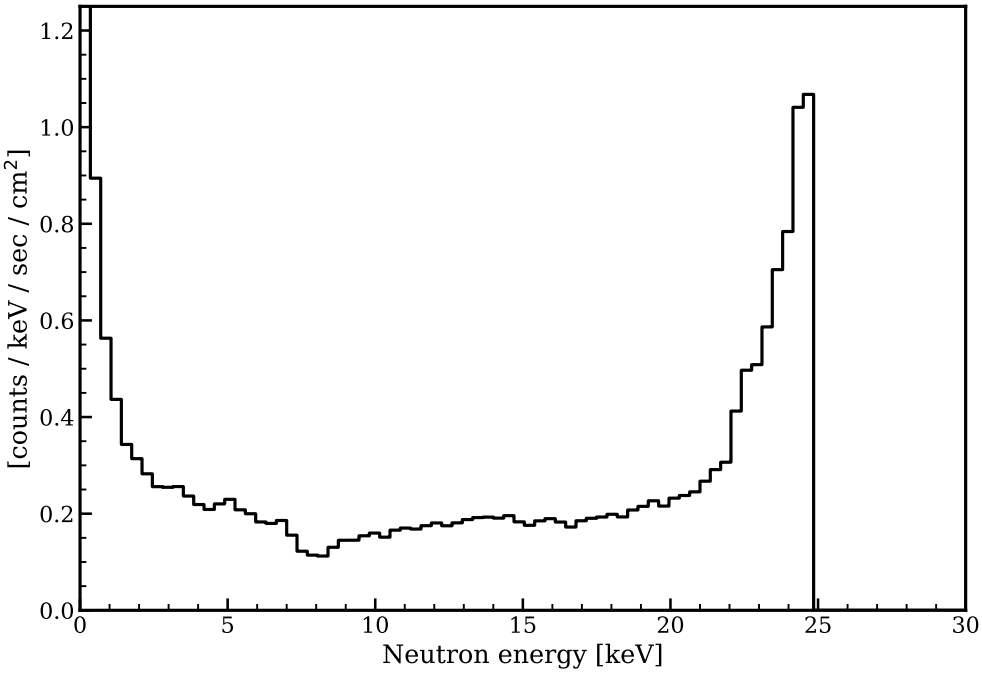

Figure 9.4: The neutron flux leaving the front source opening. Shown here is the spectrum associated with only the 24 keV neutrons most commonly produced in Sb^{124} decays.

the total photoneutron production in the source. There are some other transitions above the photonuclear threshold in Sb^{124} decays, but their sub-percent level intensities are small enough that we do not consider them further.

An extended neutron spectrum including the 379 keV neutron population is shown in Figure 9.5. Although the iron cross section for neutron scattering is lowest at 25 keV, there are other anti-resonances leading to regular dips in the cross section between 25 and 400 keV. The 379 keV neutron population extends the spectrum to include neutrons above the 25 keV energy of interest. Neutrons above 25 keV represent 5% of the total neutron flux leaving the front face of the iron filter, so we conclude they would remain mostly subdominant in a neutron scattering experiment.

In a neutron scattering experiment, such as those described in Chapter 8, gamma rays are an additional source of background. As previously discussed, dense shielding material such as tungsten and lead reduces the number of gamma rays propagating into the experimental environment. In principle, neutrons can inelastically scatter and capture on these materials to produce extra gamma rays. Figure 9.6 shows that these secondary gammas originating from photoneutrons are subdominant to those gammas originating directly from Sb^{124} decays. This also restricts the majority of the spectrum to energies below 3 MeV, with a small tail extending up to about 10 MeV.

The total flux leaving the front face of the source amounts to 108 gamma rays per cm^2 per

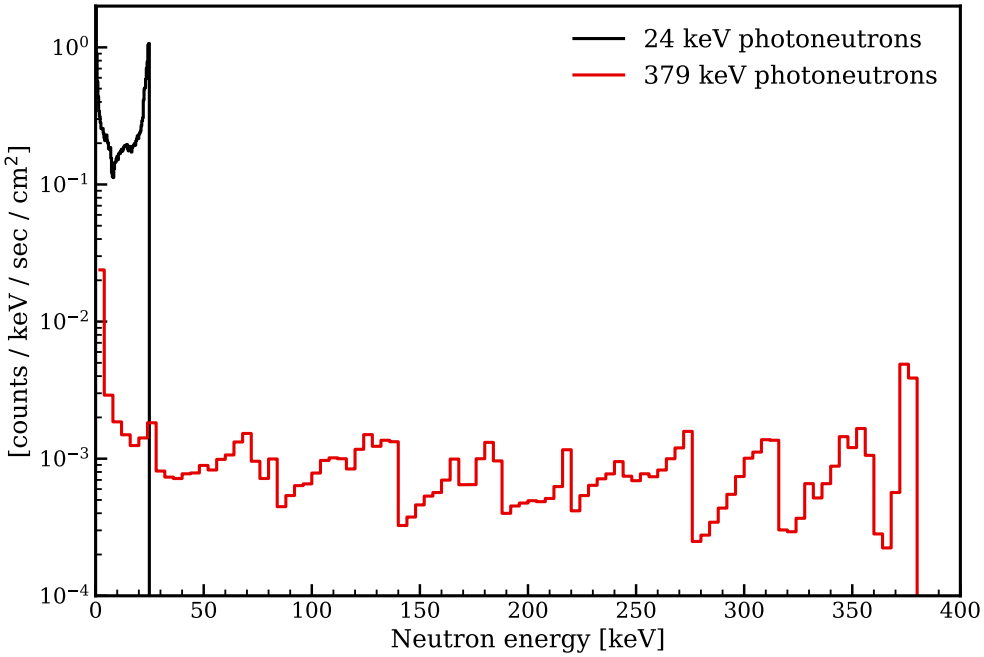

Figure 9.5: The neutron flux leaving the front source opening for the two major neutron energies produced in photoneutron interactions for Sb^{124} decay gammas. The higher energy neutrons, shown in red, are subdominant to the 24 keV population, in black, accounting for 6% of the neutron flux leaving the iron filter front.

second thanks to the dense shielding material in the line of sight between the Sb^{124} source and most of the front face. Since iron is not as dense as lead or tungsten, it is not as effective at shielding gamma rays, so, as a result, the flux at the end of the iron filter is about 2.5 times larger than the flux averaged over the whole front face. The main consideration for a calibration is keeping the total gamma ray emission rate low enough for a reasonable event rate in a target detector. In this regard, the total forward emission of 140,000 gamma rays per second, of which 3,800 leave the iron filter face, is relatively quiet.

For comparison, the back face emission rate is about three times larger than the front face. We also show the the average flux from the side of the source as a function of the distance from the source bottom in Figure 9.7, dividing out the source perimeter of 142 cm. The source position can be seen from the peak rate at 20 cm, but the distribution of gamma radiation also shows variations of only a factor of a few over the height of the source. The total gamma ray rate leaving the sides of the source amounts to 2 million per second, a radiation exposure risk comparable to other commonly used laboratory sources, particularly when averaged over the relatively large surface of the source. The neutron rate is very subdominant, and poses no extra safety concerns.

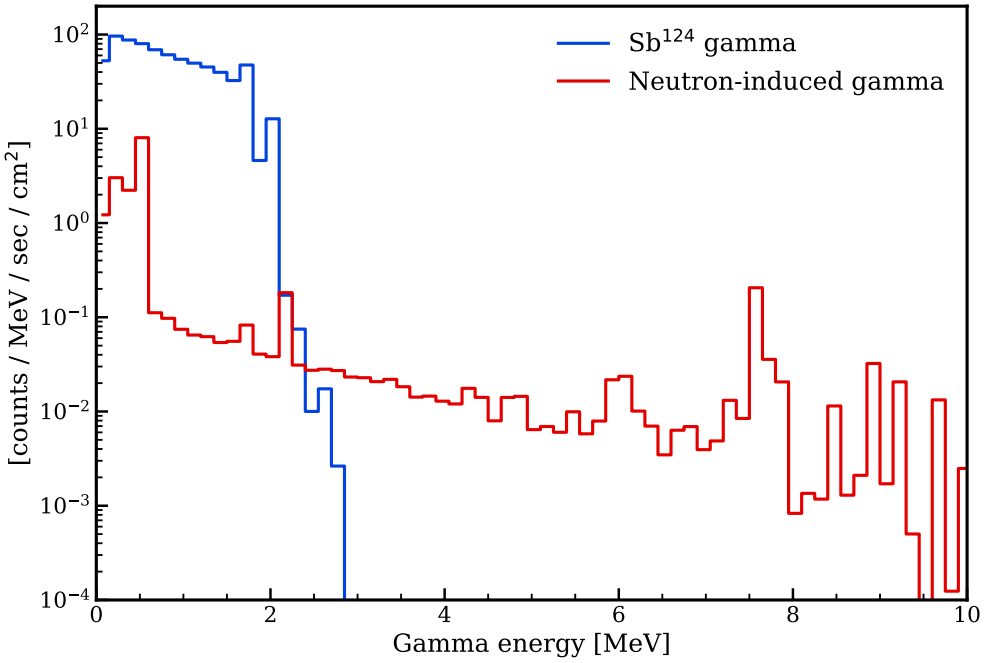

Figure 9.6: The gamma flux leaving the front face of the source. The spectrum is dominated by gamma rays originating from Sb^{124} decays, in blue. The spectrum in red is those gamma rays which originated from photoneutron capture or inelastic scattering off source materials. The rate in the red spectrum is about 2% of the total, but it does extend to higher energies.

9.3 Assembly and ongoing characterization

Figure 9.8 shows photos of the assembled photoneutron iron filter source, with and without the borated polyethylene outer layer. The Sb^{124} source was created via neutron activation of a metallic antimony pellet in a TRIGA reactor at the McLellan Nuclear Research Facility at UC Davis. It was irradiated long enough to produce a GBq-scale source. Sb^{124} has a half-life of 60.2 days, so the source was held in the reactor water pool away from neutron irradiation to let other unstable isotopes such as Sb^{122}, which has a 2.7 day half-life, to decay away. While the half life of Sb^{125} is even longer at 2.76 years, its decays do not produce gamma rays above the Be photoneutron production threshold of 1664.54 keV [233]. Assembly of the Sb^{124} source into the the beryllium metal target, iron filter container, and larger shielding construct was handled by reactor personnel due to its high activity. The entire assembly was commercially shipped to UC Berkeley for ongoing characterization studies, focused on validating the simulation results presented in this chapter.

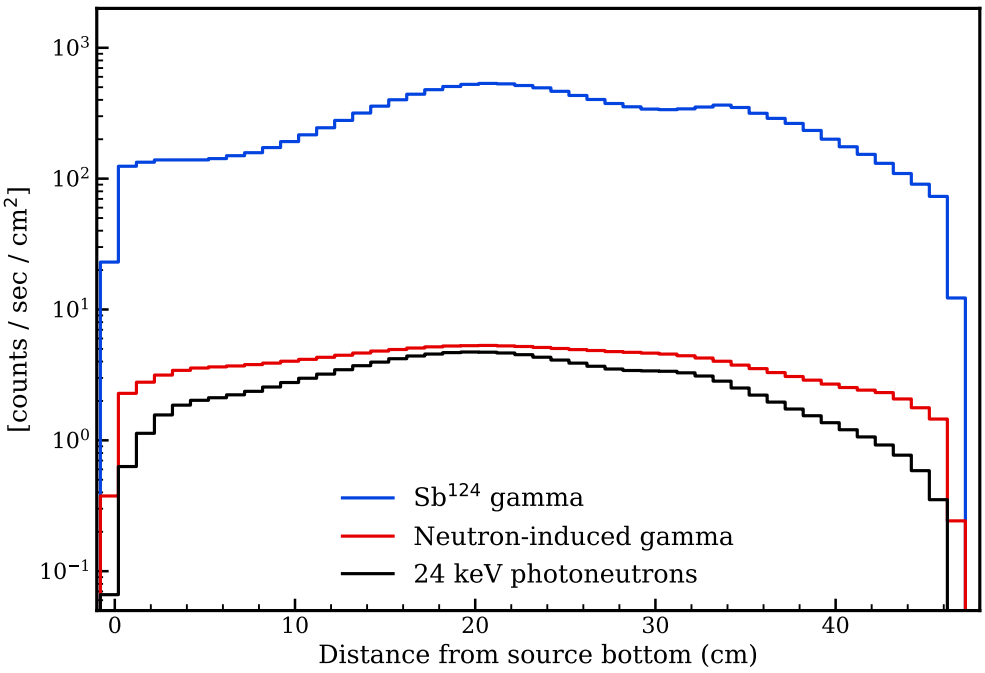

Figure 9.7: The flux of particles leaving the sides of the source geometry, as a function of the position from the bottom of the source. The dominant rate is from Sb^{124} decay gamma rays in blue, with additional contributions from gamma rays originating from photoneutron capture or inelastic scattering off source materials in red and photoneutrons in black. The flux is averaged over the perimeter of the source at each height.

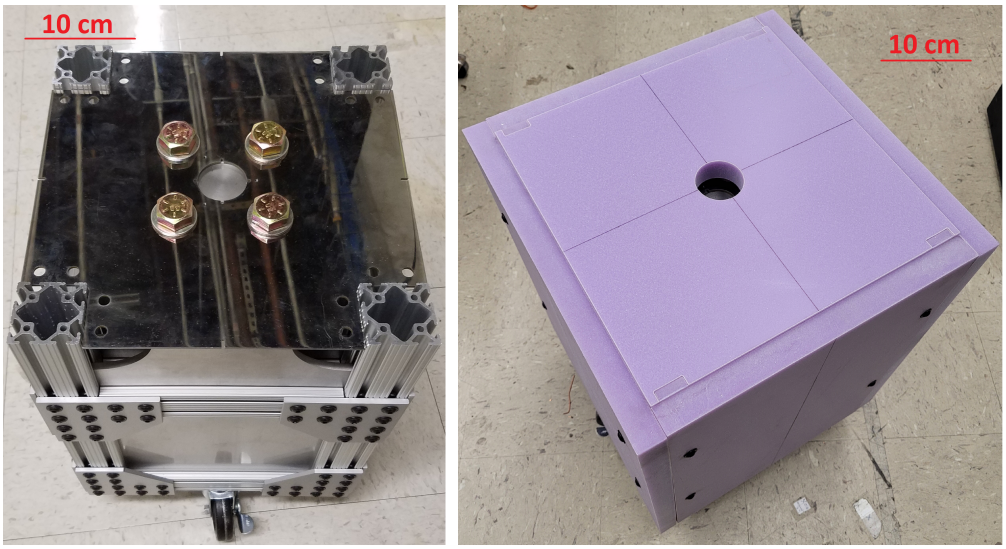

Figure 9.8: Photos of the Sb-Be photoneutron source assembly. Left, source assembly before installing the borated PE panels. Right, source assembly with the borated PE panels installed. Figure made by J. Lin.

Chapter 10

Conclusions

The field of direct detection is livelier than ever, spurred on by the ever-elusive particle identity of dark matter. While copious evidence for dark matter exists on the large scales of the universe, our attempts to detect its interactions conclusively have so far come up short. Still, a lot of progress has been made in developing detector technology to rule out dark matter candidates, some of which was described in this thesis. While the WIMP is not dead, a wider field of plausible dark matter candidates has opened up, motivating scientists to push detector concepts to their limits in probing for possible signals.

Liquid xenon time projection chambers are the dominant technology in the traditional WIMP mass range of 10s of GeV/c^2. We have presented on the main WIMP search from the first data taken with LZ, putting the strongest constraints on the spin independent WIMP-nucleon and spin dependent WIMP-neutron cross sections in the range of 9 GeV/c^2 to 10 TeV/c^2. The main competitors for LZ, XENONnT and PandaX-4T, are detectors built on equivalent technology, and the newest generation of an even larger xenon TPC is already under consideration [234]. Liquid xenon TPCs can also contribute meaningfully to the low mass regime, previously demonstrated by LUX and XENON1T. We have presented extensions of the SR1 analysis to masses between 0.3 and 9 GeV/c^2 by leveraging the Migdal effect. While not world-leading, this analysis paves the way for future parameter space exclusion with more data, the use of the Migdal effect in combination with an S2-only analysis, and/or the discussed use of an alternative method for calculating the signal model reliably to lower energy recoils. The final LZ chapter showed the design and first dataset from the LZ photoneutron source, another tool crucial for extending LZ's sensitivty to low mass WIMPs and nuclear recoil signals from ^{8}B solar neutrinos. Valuable lessons were learned from this first dataset, paving the way for future results measuring the LZ detector efficiency for low energy nuclear recoils and further measurements of the xenon yields themselves.

The second half of this thesis switched to the discussion of an entirely different detector concept based on superfluid helium, transition edge sensors, and quantum evaporation. While a less conventional design than the storied TPC, the HeRALD detector design promises extensive reach to low mass nuclear recoil dark matter, with current sensor technology already able to probe new parameter space in principle. Crucial to this statement is the

signal modeling associated with helium recoils, for which we presented a method to estimate the energy appearing in all four signal channels probed by the HeRALD design. We also presented measurements of the scintillation components of this model, with a particularly detailed analysis of scintillation signals from a superfluid helium target subjected to both nuclear and electronic recoils. A very encouraging level of agreement was found between the data and the model, which was developed without the input of any comparable experimental data. Future measurements will probe lower recoil energies and develop understanding of other aspects of the HeRALD design as part of the TESSERACT program. Photoneutrons made a triumphant return, this time in the form of a design leveraging the additional concept of neutron filtering. We showed the promise of this neutron source design, which is the active subject of experimental validation.

As with any scientific endeavor, the work presented here revealed many open avenues for future work. While dark matter was not discovered in my time working on LZ or HeRALD, the field has made an immense amount of progress and currently sits on the edge of an exciting new generation of experiments. What they will turn up is a thrilling prospect.

Bibliography

[1] Giorgio Arcadi et al. "The waning of the WIMP? A review of models, searches, and constraints". In: *The European Physics Journal C* 78.203 (Mar. 2018). DOI: 10.1140/epjc/s10052-018-5662-y. arXiv: 1703.07364 [hep-ph].

[2] Gianfranco Bertone and Dan Hooper. "History of dark matter". In: *Reviews of Modern Physics* 90.4 (Oct. 2018). ISSN: 1539-0756. DOI: 10.1103/revmodphys.90.045002. arXiv: 1605.04909 [astro-ph.CO]. URL: http://dx.doi.org/10.1103/RevModPhys.90.045002.

[3] Leaenne D. Duffy and Karl van Bibber. "Axions as dark matter particles". In: *New Journal of Physics* 11.105008 (Oct. 2009). DOI: 10.1088/1367-2630/11/10/105008. arXiv: 0904.3346 [hep-ph].

[4] Francesca Chadha-Day, John Ellis, and David J. E. Marsh. "Axion Dark Matter: What is it and Why Now?" In: *Science Advances* 8.8 (Feb. 2022). DOI: 10.1126/sciadv.abj3618. arXiv: 2105.01406 [hep-ph].

[5] Marco Battaglieri et al. "US Cosmic Visions: New Ideas in Dark Matter 2017: Community Report". In: (July 2017). arXiv: 1707.04591 [hep-ph].

[6] Rocky Kolb et al. "Basic Research Needs for Dark Matter Small Projects New Initiatives". In: (Oct. 2018). URL: https://www.osti.gov/servlets/purl/1659757.

[7] Rouven Essig et al. "Snowmass2021 Cosmic Frontier: The landscape of low-threshold dark matter direct detection in the next decade". In: (Mar. 2022). arXiv: 2203.08297 [hep-ph].

[8] D. S. Akerib et al. "Snowmass2021 Cosmic Frontier Dark Matter Direct Detection to the Neutrino Fog". In: (2022). arXiv: 2203.08084 [hep-ex].

[9] Simon D. M. White, Marc Davis, and Carlos S. Frenk. "The size of clusters in a neutrino-dominated universe". In: *Monthly Notices of the Royal Astronomical Society* 209.1 (July 1984), 27P–31P. DOI: 10.1093/mnras/209.1.27P.

[10] Y. Akrami et al. "Planck 2018 results. I. Overview and the cosmological legacy of Planck". In: *Astronomy and Astrophysics* 641.A1 (Sept. 2020). DOI: 10.1051/0004-6361/201833880. arXiv: 1807.06205 [astro-ph.CO].

[11] P. A. Zyla et al. "Review of Particle Physics". In: *Progress of Theoretical and Experimental Physics* 2020.083C01 (Aug. 2020). DOI: 10.1093/ptep/ptaa104.

[12] N. Aghanim et al. "Planck 2018 results VI. Cosmological parameters". In: *Astronomy and Astrophysics* 641.A6 (Sept. 2020). DOI: 10.1051/0004-6361/201833910. arXiv: 1807.06209 [astro-ph.CO].

[13] Wayne Hu. "Lecture Notes on CMB Theory: From Nucleosynthesis to Recombination". In: (Feb. 2008). arXiv: 0802.3688 [astro-ph].

[14] Wayne Hu and Scott Dodelson. "Cosmic Microwave Background Anisotropies". In: *Annual Review of Astronomy and Astrophysics* 40.1 (Sept. 2002), pp. 171–216. DOI: 10.1146/annurev.astro.40.060401.093926. arXiv: astro-ph/0110414.

[15] Douglas Clowe et al. "A direct empirical proof of the existence of dark matter". In: *The Astrophysical Journal* 648 (Aug. 2006), pp. L109–L113. DOI: 10.1086/508162. arXiv: astro-ph/0608407.

[16] F. Zwicky. "On the Masses of Nebulae and of Clusters of Nebulae". In: *The Astrophysical Journal* 86.3 (Oct. 1937), pp. 217–246. DOI: 10.1086/143864.

[17] David Harvey et al. "The nongravitational interactions of dark matter in colliding galaxy clusters". In: *Science* 347.6229 (Mar. 2015), pp. 1462–1465. DOI: 10.1126/science.1261381. arXiv: 1503.07675 [astro-ph.CO].

[18] Vera C. Rubin, W. Kent Ford, and Norbert Thonnard. "Extended Rotation Curves of High-Luminosity Spiral Galaxies. IV. Systematic Dynamical Properties, Sa → Sc". In: *The Astrophysical Journal* 225 (Nov. 1978), pp. L107–L111. DOI: 10.1086/182804.

[19] Lawrence J. Hall et al. "Freeze-in production of FIMP dark matter". In: *Journal of High Energy Physics* 2010.3 (Mar. 2010). DOI: 10.1007/jhep03(2010)080. arXiv: 0911.1120 [hep-ph].

[20] Gerard Jungman, Marc Kamionkowski, and Kim Griest. "Supersymmetric dark matter". In: *Physics Reports* 267.5-6 (Mar. 1996), pp. 195–373. DOI: 10.1016/0370-1573(95)00058-5.

[21] Benjamin W. Lee and Steven Weinberg. "Cosmological Lower Bound on Heavy-Neutrino Masses". In: *Physical Review Letters* 39.4 (July 1977), pp. 165–168. DOI: 10.1103/PhysRevLett.39.165.

[22] Nicolás Bernal et al. "The dawn of FIMP Dark Matter: A review of models and constraints". In: *International Journal of Modern Physics A* 32.27 (Sept. 2017), p. 1730023. ISSN: 1793-656X. DOI: 10.1142/s0217751x1730023x. arXiv: 1706.07442 [hep-ph].

[23] Yonit Hochberg et al. "Mechanism for Thermal Relic Dark Matter of Strongly Interacting Massive Particles". In: *Physics Letters* 113.171301 (Oct. 2014). DOI: 10.1103/PhysRevLett.113.171301. arXiv: 1402.5143 [hep-ph].

[24] Yonit Hochberg et al. In: *Physical Review Letters* 115.2 (July 2015). DOI: 10.1103/physrevlett.115.021301. arXiv: 1411.3727 [hep-ph].

[25] Kathryn M. Zurek. "Asymmetric Dark Matter: Theories, signatures, and constraints". In: *Physics Reports* 537.3 (Apr. 2014), pp. 91–121.

[26] J. D. Lewin and P. F. Smith. "Review of mathematics, numerical factors, and corrections for dark matter experiments based on elastic nuclear recoil". In: *Astroparticle Physics* 6.1 (June 1996), pp. 87–112. DOI: 10.1016/S0927-6505(96)00047-3.

[27] R. W. Schnee. "Introduction to dark matter experiments". In: *Physics of the Large and the Small* (2011), pp. 775–829. DOI: 10.1142/9789814327183_0014. arXiv: 1101.5205 [astro-ph.CO].

[28] Teresa Marrodán Undagoitia and Ludwig Rauch. "Dark matter direct-detection experiments". In: *Journal of Physics G: Nuclear and Particle Physics* 43.013001 (Dec. 2016). DOI: 10.1088/0954-3899/43/1/013001. arXiv: 1509.08767 [physics.ins-det].

[29] D.A. Brown et al. "ENDF/B-VIII.0: The 8th Major Release of the Nuclear Reaction Data Library with CIELO-project Cross Sections, New Standards and Thermal Scattering Data". In: *Nuclear Data Sheets* 148 (Feb. 2018), pp. 1–142. DOI: 10.1016/j.nds.2018.02.001.

[30] P. Klos et al. "Large-scale nuclear structure calculations for spin-dependent WIMP scattering with chiral effective field theory currents". In: *Physical Review D* 88.083516 (Oct. 2013). DOI: 10.1103/physrevd.88.083516. arXiv: 1304.7684 [nucl-th].

[31] P. Pirinen, J. Kotila, and J. Suhonen. "Spin-dependent WIMP-nucleus scattering off ^{125}Te, ^{129}Xe, and ^{131}Xe in the microscopic interacting boson-fermion model". In: *Nuclear Physics A* 992.121624 (Dec. 2019). DOI: 10.1016/j.nuclphysa.2019.121624.

[32] Martin Hoferichter, Javier Menéndez, and Achim Schwenk. "Coherent elastic neutrino-nucleus scattering: EFT analysis and nuclear responses". In: *Physical Review D* 102.7 (Oct. 2020). DOI: 10.1103/physrevd.102.074018. arXiv: 2007.08529 [hep-ph].

[33] B. S. Hu et al. "Ab initio structure factors for spin-dependent dark matter direct detection". In: *Physical Review Letters* 128.7 (Feb. 2022). DOI: 10.1103/physrevlett.128.072502. arXiv: 2109.00193 [nucl-th].

[34] G. Adhikari et al. "Strong constraints from COSINE-100 on the DAMA dark matter results using the same sodium iodide target". In: *Science* 7.46 (Nov. 2021). DOI: 10.1126/sciadv.abk2699. arXiv: 2104.03537 [hep-ex].

[35] Ciaran A. J. O'Hare. "New Definition of the Neutrino Floor for Direct Dark Matter Searches". In: *Physical Review Letters* 127.25 (Dec. 2021). DOI: 10.1103/physrevlett.127.251802. arXiv: 2109.03116 [hep-ph].

[36] Timon Emken, Chris Kouvaris, and Ian M. Shoemaker. "Terrestrial effects on dark matter-electron scattering experiments". In: *Physical Review D* 96.015018 (July 2017). DOI: 10.1103/physrevd.96.015018. arXiv: 1702.07750 [hep-ph].

[37] "First results from the CRESST-III low-mass dark matter program". In: *Physical Review D* 100.102002 (Mar. 2019). DOI: 10.1103/PhysRevD.100.102002. arXiv: 1904.00498 [astro-ph.CO].

[38] I. Alkhatib et al. "Light Dark Matter Search with a High-Resolution Athermal Phonon Detector Operated Above Ground". In: *Physical Review Letters* 127.061801 (Aug. 2021). DOI: 10.1103/PhysRevLett.127.061801. arXiv: 2007.14289 [hep-ex].

[39] A. Aguilar-Arevalo et al. "Results on Low-Mass Weakly Interacting Massive Particles from an 11 kg d Target Exposure of DAMIC at SNOLAB". In: *Physical Review Letters* 125.241803 (Dec. 2020). DOI: 10.1103/PhysRevLett.125.241803. arXiv: 2007.15622 [astro-ph.CO].

[40] D. Akimov et al. "Observation of coherent elastic neutrino-nucleus scattering". In: *Science* 357.6356 (Aug. 2017), pp. 1123–1126. DOI: 10.1126/science.aao0990. arXiv: 1708.01294 [nucl-ex].

[41] Yue Meng et al. "Dark Matter Search results from the PandaX-4T Comissioning Run". In: *Physical Review Letters* 127.261802 (Dec. 2021). DOI: 10.1103/PhysRevLett.127.261802. arXiv: 2107.13438 [hep-ex].

[42] E. Aprile et al. "Dark Matter Search Results from a One Ton-Year Exposure of XENON1T". In: *Physical Review Letters* 121.11 (Sept. 2018). DOI: 10.1103/physrevlett.121.111302. arXiv: 1805.12562 [astro-ph.CO].

[43] E. Aprile et al. "Search for Light Dark Matter Interactions Enhanced by the Migdal Effect or Bremsstrahlung in XENON1T". In: *Physical Review Letters* 123.24 (Dec. 2019). DOI: 10.1103/physrevlett.123.241803. arXiv: 1907.12771 [hep-ex].

[44] E. Aprile et al. "Search for coherent elastic scattering of solar ^{8}B neutrinos in the XENON1T dark matter experiment". In: *Physical Review Letters* 126.091301 (Dec. 2021). DOI: 10.1103/PhysRevLett.126.091301. arXiv: 2012.02846 [hep-ex].

[45] R. Ajaj et al. "Search for dark matter with a 231-day exposure of liquid argon using DEAP-3600 at SNOLAB". In: *Physical Review D* 100.022004 (Feb. 2019). DOI: 10.1103/PhysRevD.100.022004. arXiv: 1902.04048.

[46] P. Agnes et al. "Low-Mass Dark Matter Search with the DarkSide-50 Experiment". In: *Physical Review Letters* 121.8 (Aug. 2018). ISSN: 1079-7114. DOI: 10.1103/physrevlett.121.081307. arXiv: 1802.06994 [astro-ph.HE].

[47] E. Armengaud et al. "Searching for low-mass dark matter particles with a massive Ge bolometer operated above-ground". In: *Physical Review D* 99.082003 (Apr. 2019). DOI: 10.1103/PhysRevD.99.082003. arXiv: 1901.03588 [astro-ph.GA].

[48] E. Armengaud et al. "Search for sub-GeV Dark Matter via Migdal effect with an EDELWEISS germanium detector with NbSi TES sensors". In: *Physical Review D* 106.062004 (Mar. 2022). DOI: 10.1103/PhysRevD.106.062004. arXiv: 2203.03993 [astro-ph.GA].

[49] Z. Z. Liu et al. "Studies of the Earth shielding effect to direct dark matter searches at the China Jinping Underground Laboratory". In: *Physical Review D* 105.5 (Mar. 2022). DOI: 10.1103/physrevd.105.052005. arXiv: 2111.11243 [hep-ex].

[50] Q. Arnaud et al. "First results from the NEWS-G direct dark matter search experiment at the LSM". In: *Astroparticle Physics* 97 (Oct. 2017), pp. 54–62. DOI: 10.1016/j.astropartphys.2017.10.009. arXiv: 1706.04934 [astro-ph.IM].

[51] Vera Gluscevic and Kimberly K. Boddy. "Constraints on scattering of keV-TeV dark matter with protons in the early Universe". In: *Physical Review Letters* 121.081301 (Aug. 2018). DOI: 10.1103/PhysRevLett.121.081301. arXiv: 1712.07133 [astro-ph.CO].

[52] Kimberly K. Boddy and Vera Gluscevic. "First Cosmological Constraint on the Effective Theory of Dark Matter-Proton Interactions". In: *Physical Review D* 98.083510 (Oct. 2018). DOI: 10.1103/PhysRevD.98.083510. arXiv: 1801.08609 [astro-ph.CO].

[53] Amit Bhoonah et al. "Calorimetric Dark Matter Detection with Galactic Center Gas Clouds". In: *Physical Review Letters* 131.131101 (Sept. 2018). DOI: 10.1103/PhysRevLett.121.131101. arXiv: 1806.06857 [hep-ph].

[54] Adrienne L. Erickcek et al. "Constraints on the Interactions between Dark Matter and Baryons from the X-ray Quantum Calorimetry Experiment". In: *Physical Review D* 76.042007 (Aug. 2007). DOI: 10.1103/PhysRevD.76.042007. arXiv: 0704.0794 [astro-ph].

[55] J. Aalbers et al. "First Dark Matter Search Results from the LUX-ZEPLIN (LZ) Experiment". In: (Oct. 2022). arXiv: 2207.03764 [hep-ex].

[56] V. N. Solovov et al. "Position Reconstruction in a Dual Phase Xenon Scintillation Detector". In: *IEEE Transactions on Nuclear Science* 59.6 (Dec. 2012), pp. 3286–3293. DOI: 10.1109/TNS.2012.2221742. arXiv: 1112.1481 [physics.ins-det].

[57] B. J. Mount et al. "The LUX-ZEPLIN (LZ) Technical Design Report". In: (Mar. 2017). arXiv: 1703.09144 [physics.ins-det].

[58] D. S. Akerib et al. "Position reconstruction in LUX". In: *Journal of Instrumentation* 13 (Feb. 2018). DOI: 10.1088/1748-0221/13/02/P02001. arXiv: 1710.02752 [physics.ins-det].

[59] M. Szydagis et al. "NEST: a comprehensive model for scintillation yield in liquid xenon". In: *Journal of Instrumentation* 6.10 (Oct. 2011). DOI: 10.1088/1748-0221/6/10/p10002. arXiv: 1106.1613 [physics.ins-det].

[60] M. Szydagis et al. *Noble Element Simulation Technique*. Sept. 2022. DOI: 10.5281/zenodo.7061832.

[61] M. Szydagis et al. "A Review of Basic Energy Reconstruction Techniques in Liquid Xenon and Argon Detectors for Dark Matter and Neutrino Physics Using NEST". In: *Instruments* 5.13 (Mar. 2021). DOI: 10.3390/instruments5010013. arXiv: 2102.10209 [hep-ex].

[62] Carl Eric Dahl. "The Physics of Background Discrimination in Liquid Xenon, and First Results from XENON10 in the Hunt for WIMP Dark Matter". PhD thesis. Princeton University, Sept. 2009.

[63] Laura Baudis, Patricia Sanchez-Lucas, and Kevin Thieme. "A measurement of the mean electronic excitation energy of liquid xenon". In: *The European Physical Journal C* 81.1060 (Dec. 2021). DOI: 10.1140/epjc/s10052-021-09834-x. arXiv: 2109.07151 [physics.ins-det].

[64] G. Anton et al. "Measurement of the scintillation and ionization response of liquid xenon at MeV energies in the EXO-200 experiment". In: *Physical Review C* 101.6 (June 2020). DOI: 10.1103/physrevc.101.065501. arXiv: 1908.04128 [physics.ins-det].

[65] D. S. Akerib et al. "Simulations of Events for the LUX-ZEPLIN (LZ) Dark Matter Experiment". In: *Astroparticle Physics* 125.102480 (Feb. 2021). DOI: 10.1016/j.astropartphys.2020.102480. arXiv: 2001.09363 [physics.ins-det].

[66] D. S. Akerib et al. "The LUX-ZEPLIN (LZ) Experiment". In: *Nuclear Instruments and Methods in Physics Research Section A: Accelerators, Spectrometers, Detectors and Associated Equipment* 953.163047 (Feb. 2020). DOI: 10.1016/j.nima.2019.163047. arXiv: 1910.09124 [physics.ins-det].

[67] S.J. Haselschwardt et al. "A liquid scintillation detector for radioassay of gadolinium-loaded liquid scintillator for the LZ Outer Detector". In: *Nuclear Instruments and Methods in Physics Research Section A: Accelerators, Spectrometers, Detectors and Associated Equipment* 937 (Sept. 2019), pp. 148–163. DOI: 10.1016/j.nima.2019.05.055. arXiv: 1808.05595 [physics.ins-det].

[68] R. Linehan et al. "Design and production of the high voltage electrode grids and electron extraction region for the LZ dual-phase xenon time projection chamber". In: *Nuclear Instruments and Methods in Physics Research Section A: Accelerators, Spectrometers, Detectors and Associated Equipment* 1031.165955 (May 2022). DOI: 10.1016/j.nima.2021.165955. arXiv: 2106.06622 [physics.ins-det].

[69] C.H. Faham et al. "Measurements of wavelength-dependent double photoelectron emission from single photons in VUV-sensitive photomultiplier tubes". In: *Journal of Instrumentation* 10.09 (Sept. 2015), P09010–P09010. DOI: 10.1088/1748-0221/10/09/p09010. arXiv: 1506.08748 [physics.ins-det].

[70] B. López Paredes et al. "Response of photomultiplier tubes to xenon scintillation light". In: *Astroparticle Physics* 102 (Nov. 2018), pp. 56–66. DOI: 10.1016/j.astropartphys.2018.04.006. arXiv: 1801.01597 [physics.ins-det].

[71] D. S. Akerib et al. "Investigation of background electron emission in the LUX detector". In: *Physical Review D* 102.092004 (Apr. 2020). DOI: 10.1103/PhysRevD.102.092004. arXiv: 2004.07791 [physics.ins-det].

[72] D. S. Akerib et al. "Improving sensitivity to low-mass dark matter in LUX using a novel electrode background mitigation technique". In: *Physical Review D* 104.1 (July 2021). DOI: 10.1103/physrevd.104.012011. arXiv: 2011.09602 [hep-ex].

[73] D. S. Akerib et al. "^{83m}Kr calibration of the 2013 LUX dark matter search". In: *Physical Review D* 96.112009 (Dec. 2017). DOI: 10.1103/PhysRevD.96.112009. arXiv: 1708.02566 [physics.ins-det].

[74] D. S. Akerib et al. "Tritium calibration of the LUX dark matter experiment". In: *Physical Review D* 93.7 (Apr. 2016). DOI: 10.1103/physrevd.93.072009. arXiv: 1512.03133 [physics.ins-det].

[75] D. S. Akerib et al. "Low-energy (0.7-74 keV) nuclear recoil calibration of the LUX dark matter experiment using D-D neutron scattering kinematics". In: (Oct. 2016). arXiv: 1608.05381 [physics.ins-det].

[76] D. S. Akerib et al. "Calibration, event reconstruction, data analysis, and limit calculation for the LUX dark matter experiment". In: *Physical Review D* 97.10 (May 2018). ISSN: 2470-0029. DOI: 10.1103/physrevd.97.102008. arXiv: 1712.05696 [physics.ins-det].

[77] S. Agostinelli et al. "Geant4—a simulation toolkit". In: *Nuclear Instruments and Methods in Physics Research Section A: Accelerators, Spectrometers, Detectors and Associated Equipment* 506.3 (July 2003), pp. 250–303. DOI: 10.1016/s0168-9002(03)01368-8.

[78] J. Allison et al. "Geant4 Developments and Applications". In: *IEEE Transactions on Nuclear Science* 53.1 (Feb. 2006), pp. 270–278. DOI: 10.1109/TNS.2006.869826.

[79] J. Allison et al. "Recent developments in GEANT4". In: *Nuclear Instruments and Methods in Physics Research Section A: Accelerators, Spectrometers, Detectors and Associated Equipment* 835 (Nov. 2016), pp. 186–225. DOI: 10.1016/j.nima.2016.06.125.

[80] D. S. Akerib et al. "Discrimination of electronic recoils from nuclear recoils in two-phase xenon time projection chambers". In: *Physical Review D* 102.112002 (Dec. 2020). DOI: 10.1103/PhysRevD.102.112002. arXiv: 2004.06304 [physics.ins-det].

[81] D. S. Akerib et al. "Projected WIMP sensitivity of the LUX-ZEPLIN (LZ) dark matter experiment". In: *Physical Review D* 101.052002 (Jan. 2020). DOI: 10.1103/PhysRevD.101.052002. arXiv: 1802.06039 [astro-ph.IM].

[82] D. S. Akerib et al. "Chromatographic separation of radioactive noble gases from xenon". In: *Astroparticle Physics* 97 (Jan. 2018), pp. 80–87. DOI: 10.1016/j.astropartphys.2017.10.014. arXiv: 1605.03844 [physics.ins-det].

[83] E. H. Miller et al. "Constraining radon backgrounds in LZ". In: *AIP Conference Proceedings* 1921.050003 (Jan. 2018). DOI: 10.1063/1.5018996. arXiv: 1708.08533 [physics.ins-det].

[84] D.S. Akerib et al. "The LUX-ZEPLIN (LZ) radioactivity and cleanliness control programs". In: *The European Physical Journal C* 80.1044 (Nov. 2020). DOI: 10.1140/epjc/s10052-020-8420-x. arXiv: 2006.02506 [physics.ins-det].

[85] J. Aalbers et al. "Background Determination for the LUX-ZEPLIN (LZ) Dark Matter Experiment". In: (Nov. 2022). arXiv: 2211.17120 [hep-ex].

[86] D.S. Akerib et al. "Measurement of the Gamma Ray Background in the Davis Cavern at the Sanford Underground Research Facility". In: *Astroparticle Physics* 116.102391 (Mar. 2020). DOI: 10.1016/j.astropartphys.2019.102391. arXiv: 1904.02112 [physics.ins-det].

[87] E. Aprile et al. "Observation of two-neutrino double electron capture in ^{124}Xe with XENON1T". In: *Nature* 568 (Apr. 2019), pp. 532–535. DOI: 10.1038/s41586-019-1124-4. arXiv: 1904.11002 [nucl-ex].

[88] D. Baxter et al. "Recommended conventions for reporting results from direct dark matter searches". In: *European Physics Journal C* 81.907 (May 2021). DOI: 10.1140/epjc/s10052-021-09655-y. arXiv: 2105.00599 [hep-ex].

[89] David Woodward. "Simulations of cosmic muons and backgrounds radiations for muon tomography and underground experiments". PhD thesis. University of Sheffield, Mar. 2018. URL: https://etheses.whiterose.ac.uk/19916/.

[90] J. Aalbers et al. "Cosmogenic production of ^{37}Ar in the context of the LUX-ZEPLIN experiment". In: *Physical Review D* 105.8 (Apr. 2022). DOI: 10.1103/physrevd.105.082004. arXiv: 2201.02858 [hep-ex].

[91] M. Agostini et al. "Simultaneous precision spectroscopy of *pp*, ^{7}Be, and *pep* solar neutrinos with Borexino Phase-II". In: *Physical Review D* 100.8 (Oct. 2019). DOI: 10.1103/physrevd.100.082004. arXiv: 1707.09279 [hep-ex].

[92] B. Aharmim et al. "Combined analysis of all three phases of solar neutrino data from the Sudbury Neutrino Observatory". In: *Physical Review C* 88.2 (Aug. 2013). DOI: 10.1103/physrevc.88.025501. arXiv: 1109.0763 [nucl-ex].

[93] Núria Vinyoles et al. "A New Generation of Standard Solar Models". In: *The Astrophysical Journal* 835.2 (Jan. 2017), p. 202. DOI: 10.3847/1538-4357/835/2/202. arXiv: 1611.09867 [astro-ph.SR].

[94] J. B. Albert et al. "Improved measurement of the $2\nu\beta\beta$ half-life of ^{136}Xe with the EXO-200 detector". In: *Physical Review C* 89.1 (Jan. 2014). DOI: 10.1103/physrevc.89.015502. arXiv: 1306.6106 [nucl-ex].

[95] John R. de Laeter et al. "Atomic weights of the elements. Review 2000 (IUPAC Technical Report)". In: *Pure and Applied Chemistry* 75.6 (2003), pp. 683–800. DOI: 10.1351/pac200375060683.

[96] D. S. Akerib et al. "Ultralow energy calibration of LUX detector using ^{127}Xe electron capture". In: *Physical Review D* 96.11 (Dec. 2017). DOI: 10.1103/physrevd.96.112011. arXiv: 1709.00800 [physics.ins-det].

[97] Wolfgang A. Rolke, Angel M. López, and Jan Conrad. "Limits and confidence intervals in the presence of nuisance parameters". In: *Nuclear Instruments and Methods in Physics Research Section A: Accelerators, Spectrometers, Detectors and Associated Equipment* 551.2-3 (Oct. 2005), pp. 493–503. DOI: 10.1016/j.nima.2005.05.068. arXiv: physics.data-an/0403059.

[98] Glen Cowan et al. "Asymptotic formulae for likelihood-based tests of new physics". In: *The European Physical Journal C* 71.2 (Feb. 2011). ISSN: 1434-6052. DOI: 10.1140/epjc/s10052-011-1554-0. arXiv: 1007.1727 [physics.data-an].

[99] Glen Cowan et al. "Power-Constrained Limits". In: (May 2011). arXiv: 1105.3166 [physics.data-an].

[100] D. S. Akerib et al. "Results from a Search for Dark Matter in the Complete LUX Exposure". In: *Physical Review Letters* 118.021303 (Jan. 2017). DOI: 10.1103/physrevlett.118.021303. arXiv: 1608.07648 [astro-ph.CO].

[101] D. S. Akerib et al. "Limits on Spin-Dependent WIMP-Nucleon Cross Section Obtained from the Complete LUX Exposure". In: *Physical Review Letters* 118.251302 (June 2017). DOI: 10.1103/physrevlett.118.251302. arXiv: 1705.03380 [astro-ph.CO].

[102] E. Aprile et al. "Constraining the Spin-Dependent WIMP-Nucleon Cross Sections with XENON1T". In: *Physical Review Letters* 122.141301 (Apr. 2019). DOI: 10.1103/physrevlett.122.141301. arXiv: 1902.03234 [astro-ph.CO].

[103] Jingkai Xia et al. "PandaX-II Constraints on Spin-Dependent WIMP-Nucleon Effective Interactions". In: *Physics Letters B* 792 (May 2019), pp. 193–198. DOI: 10.1016/j.physletb.2019.02.043. arXiv: 1807.01936 [hep-ex].

[104] C. Amole et al. "Dark Matter Search Results from the Complete Exposure of the PICO-60 C_3F_8 Bubble Chamber". In: *Physical Review D* 100.022001 (July 2019). DOI: 10.1103/physrevd.100.022001. arXiv: 1902.04031.

[105] Mike Williams. "How good are your fits? Unbinned multivariate goodness-of-fit tests in high energy physics". In: *Journal of Instrumentation* 5.P09004 (Sept. 2010). DOI: 10.1088/1748-0221/5/09/P09004. arXiv: 1006.3019 [hep-ex].

[106] Joel Heinrich. "Pitfalls of Goodness-of-Fit from Likelihood". In: (Oct. 2003). arXiv: physics.data-an/0310167.

[107] Steve Baker and Robert D. Cousins. "Clarification of the use of chi-square and likelihood functions in fits to histograms". In: *Nuclear Instruments and Methods in Physics Research* 221.2 (Apr. 1984), pp. 437–442. DOI: 10.1016/0167-5087(84)90016-4.

[108] D. S. Akerib et al. "Projected sensitivity of the LUX-ZEPLIN experiment to the $0\nu\beta\beta$ decay of ^{136}Xe". In: *Physical Review C* 102.014602 (July 2020). DOI: 10.1103/physrevc.102.014602. arXiv: 2104.13374 [physics.ins-det].

[109] D. S. Akerib et al. "Projected sensitivities of the LUX-ZEPLIN experiment to new physics via low-energy electron recoils". In: *Physical Review D* 104.9 (Nov. 2021). DOI: 10.1103/physrevd.104.092009. arXiv: 2102.11740 [hep-ex].

[110] D. S. Akerib et al. "Results of a Search for Sub-GeV Dark Matter Using 2013 LUX Data". In: *Physical Review Letters* 122.13 (Apr. 2019). DOI: 10.1103/physrevlett.122.131301. arXiv: 1904.08979 [astro-ph.IM].

[111] Masahiro Ibe et al. "Migdal Effect in Dark Matter Direct Detection Experiments". In: *Journal of High Energy Physics* 03.194 (Mar. 2018). DOI: 10.1007/JHEP03(2018)194. arXiv: 1707.07258 [hep-ph].

[112] Kiseki D. Nakamura et al. "Detection capability of Migdal effect for argon and xenon nuclei with position sensitive gaseous detectors". In: (Sept. 2020). arXiv: 2009.05939 [physics.ins-det].

[113] Nicole F. Bell et al. "Observing the Migdal effect from nuclear recoils of neutral particles with liquid xenon and argon detectors". In: *Physical Review D* 105.096015 (Apr. 2022). DOI: 10.1103/PhysRevD.105.096015. arXiv: 2112.08514 [hep-ph].

[114] H. M. Araújo et al. "The MIGDAL experiment: Measuring a rare atomic process to aid the search for dark matter". In: (Sept. 2022). arXiv: 2207.08284 [hep-ex].

[115] Rouven Essig et al. "On the relation between Migdal effect and dark matter-electron scattering in atoms and semiconductors". In: *Physical Review Letters* 124.021801 (Jan. 2020). DOI: 10.1103/PhysRevLett.124.021801. arXiv: 1908.10881 [hep-ph].

[116] C.-P. Liu et al. "Model-independent determination of the Migdal effect via photoabsorption". In: *Physical Review D* 102.121303 (July 2020). DOI: 10.1103/PhysRevD.102.121303. arXiv: 2007.10965 [hep-ph].

[117] Simon Knapen, Jonathan Kozaczuk, and Tongyan Lin. "The Migdal effect in semiconductors". In: *Physical Review Letters* 127.081805 (Nov. 2020). DOI: 10.1103/PhysRevLett.127.081805. arXiv: 2011.09496 [hep-ph].

[118] Yonit Hochberg et al. "Determining Dark-Matter–Electron Scattering Rates from the Dielectric Function". In: *Physical Review Letters* 127.15 (Oct. 2021). DOI: 10.1103/physrevlett.127.151802. arXiv: 2101.08263 [hep-ph].

[119] Peter Cox et al. "Precise predictions and new insights for atomic ionisation from the Migdal effect". In: (Aug. 2022). arXiv: 2208.12222 [hep-ph].

[120] Scott Haselschwardt and Jonathan Nikoleyczik. "Time-Dependent PLR Study for SR1 WIMP Search". In: *LZ Analysis Note* LZDB000068 (Oct. 2021).

[121] E. Armengaud et al. "Constraints on low-mass WIMPs from the EDELWEISS-III dark matter search". In: *Journal of Cosmology and Astroparticle Physics* 2016.019 (May 2016). DOI: 10.1088/1475-7516/2016/05/019. arXiv: 1603.05120 [astro-ph.CO].

[122] R. Agnese et al. "Search for low-mass dark matter with CDMSlite using a profile likelihood fit". In: *Physical Review D* 99.6 (Mar. 2019). DOI: 10.1103/physrevd.99.062001. arXiv: 1808.09098 [astro-ph.CO].

[123] G. Angloher et al. "Probing spin-dependent dark matter interactions with ^{6}Li". In: *The European Physical Journal C* 82.207 (Mar. 2022). DOI: 10.1140/epjc/s10052-022-10140-3. arXiv: 2201.03863 [physics.ins-det].

[124] J. I. Collar. "Search for a nonrelativistic component in the spectrum of cosmic rays at Earth". In: *Physical Review D* 98.2 (July 2018). DOI: 10.1103/physrevd.98.023005. arXiv: 1805.02646 [astro-ph.CO].

[125] Simon Knapen, Jonathan Kozaczuk, and Tongyan Lin. "Dark matter-electron scattering in dielectrics". In: *Physical Review D* 104.015031 (July 2021). DOI: 10.1103/PhysRevD.104.015031. arXiv: 2101.08275 [hep-ph].

[126] Simon Knapen, Jonathan Kozaczuk, and Tongyan Lin. "Python package for dark matter scattering in dielectric targets". In: *Physical Review D* 105.015014 (Jan. 2022). DOI: 10.1103/PhysRevD.105.015014. arXiv: 2104.12786 [hep-ph].

[127] B. L. Henke, E. M. Gullikson, and J. C. Davis. "X-Ray Interactions: Photoabsorption, Scattering, Transmission, and Reflection at $E = 50 - 30,000$ eV, $Z = 1 - 92$". In: *Atomic Data and Nuclear Data Tables* 54.2 (July 1993), pp. 181–342. DOI: 10.1006/adnd.1993.1013.

[128] Katayun Kamdin. "A Search for Lightly Ionizing Particles in the LUX Detector and Research and Development For Future Liquid Xenon Time Projection Chambers". PhD thesis. University of California, Berkeley, Dec. 2018. URL: https://escholarship.org/uc/item/9ck617mz.

[129] *CXRO X-Ray Database*. URL: https://henke.lbl.gov/optical_constants/.

[130] Maarten Vos and Pedro L. Grande. "Extracting the dielectric function from high-energy REELS measurements". In: *Surface and Interface Analysis* 49.9 (Mar. 2017), pp. 809–821. DOI: 10.1002/sia.6227.

[131] Maarten Vos and Pedro L. Grande. "Simple model dielectric functions for insulators". In: *Journal of Physics and Chemistry of Solids* 104 (May 2017), pp. 192–197. DOI: 10.1016/j.jpcs.2016.12.015.

[132] Maarten Vos and Pedro L. Grande. "Modelling the contribution of semi-core electrons to the dielectric function". In: *Journal of Physics and Chemistry of Solids* 124 (Sept. 2019), pp. 242–249. DOI: 10.1016/j.jpcs.2018.09.020.

[133] N. D. Mermin. "Lindhard Dielectric Function in the Relaxation-Time Approximation". In: *Physical Review B* 1.5 (Mar. 1970), pp. 2362–2363. DOI: 10.1103/PhysRevB.1.2362.

[134] Zachary H. Levine and Steven G. Louie. "New model dielectric function and exchange-correlation potential for semiconductors and insulators". In: *Physical Review B* 25.10 (May 1982), pp. 6310–6316. DOI: 10.1103/PhysRevB.25.6310.

[135] Maarten Vos and Pedro Grande. CHAPIDIF *code*. To be published.

[136] I. T. Steinberger and U. Asaf. "Band-Structure Parameters of Solid and Liquid Xenon". In: *Physical Review B* 8.2 (1973), pp. 914–918. DOI: 10.1103/PhysRevB.8.914.

[137] J. I. Collar. "Applications of an ^{88}Y / Be Photoneutron Calibration Source to Dark Matter and Neutrino Experiments". In: *Physical Review Letters* 110.21 (May 2013). ISSN: 1079-7114. DOI: 10.1103/physrevlett.110.211101. arXiv: 1303.2686 [physics.ins-det].

[138] A. E. Chavarria et al. "Measurement of the ionization produced by sub-keV silicon nuclear recoils in a CCD dark matter detector". In: *Physical Review D* 94.8 (Oct. 2016). DOI: 10.1103/PhysRevD.94.082007. arXiv: 1608.00957 [astro-ph.IM].

[139] B. J. Scholz et al. "Measurement of the low-energy quenching factor in germanium using an ^{88}Y/Be photoneutron source". In: *Physical Review D* 94.12 (Dec. 2016). ISSN: 2470-0029. DOI: 10.1103/physrevd.94.122003. arXiv: 1608.03588 [physics.ins-det].

[140] J. I. Collar, A. R. L. Kavner, and C. M. Lewis. "Germanium response to sub-keV nuclear recoils: a multipronged experimental characterization". In: *Physical Review D* 103.122003 (June 2021). DOI: 10.1103/PhysRevD.103.122003. arXiv: 2102.10089 [nucl-ex].

[141] M. F. Albakry et al. "Ionization yield measurement in a germanium CDMSlite detector using photo-neutron sources". In: *Physical Review D* 105.12 (June 2022). DOI: 10.1103/physrevd.105.122002. arXiv: 2202.07043 [physics.ins-det].

[142] Glenn F. Knoll. *Radiation Detection and Measurement*. Ed. by Robin Factor. Third. John Wiley & Sons, Inc., 2000.

[143] Alan E. Robinson. "Reanalysis of radioisotope measurements of the ^{9}Be$(\gamma, n)^{8}$Be cross section". In: *Physical Review C* 94.2 (Aug. 2016). ISSN: 2469-9993. DOI: 10.1103/physrevc.94.024613. arXiv: 1602.05911 [nucl-ex].

[144] C. W. Arnold et al. "Cross-section measurement of ^{9}Be$(\gamma, n)^{8}$Be and implications for $\alpha + \alpha + n \rightarrow {}^{9}$Be in the r process". In: *Physical Review C* 85.4 (Apr. 2012). DOI: 10.1103/physrevc.85.044605. arXiv: 1112.1148 [nucl-ex].

[145] Will Taylor. *Low-energy Monoenergetic Neutron Production with a DD-Neutron Source for sub-keV Nuclear Recoil Calibrations in the LUX and LZ Experiments*. CPAD Instrumentation Frontier Workshop. Mar. 2021. URL: https://indico.fnal.gov/event/46746/contributions/210532/.

[146] C. W. Fink et al. "Performance of a Large Area Photon Detector For Rare Event Search Applications". In: *Applied Physics Letters* 118.022601 (Sept. 2020). DOI: 10.1063/5.0032372. arXiv: 2009.14302 [physics.ins-det].

[147] C. Chang et al. *Snowmass2021 - Letter of Interest: The TESSERACT Dark Matter Project*. 2020. URL: https://www.snowmass21.org/docs/files/summaries/CF/SNOWMASS21-CF1_CF2-IF1_IF8-120.pdf.

[148] S. A. Hertel et al. "Direct detection of sub-GeV dark matter using a superfluid ^{4}He target". In: *Physical Review D* 100.9 (Nov. 2019). DOI: 10.1103/physrevd.100.092007. arXiv: 1810.06283 [physics.ins-det].

[149] Robin Anthony-Petersen et al. "A Stress Induced Source of Phonon Bursts and Quasiparticle Poisoning". In: (Aug. 2022). arXiv: 2208.02790 [physics.ins-det].

[150] R. E. Lanou, H. J. Maris, and G. M. Seidel. "Detection of Solar Neutrinos in Superfluid Helium". In: *Physical Review Letters* 58.23 (June 1987), pp. 2498–2501. DOI: 10.1103/PhysRevLett.58.2498.

[151] Y. H. Huang et al. "Potential for precision measurement of solar neutrino luminosity by HERON". In: *Astroparticle Physics* 30.1 (Aug. 2008), pp. 1–11. ISSN: 0927-6505. DOI: 10.1016/j.astropartphys.2008.06.003. arXiv: 0711.4095 [astro-ph].

[152] Junhui Liao et al. "A low-mass dark matter project, ALETHEIA: A Liquid hElium Time projection cHambEr In dArk matter". In: (Mar. 2021). arXiv: 2103.02161 [astro-ph.IM].

[153] Yuanning Gao Junhui Liao et al. "ALETHEIA: Hunting for Low-mass Dark Matter with Liquid Helium TPCs". In: (2022). arXiv: 2209.02320 [astro-ph.IM].

[154] D. N. McKinsey et al. "Radiative decay of the metastable $He_2(a^3\Sigma_u^+)$ molecule in liquid helium". In: *Physical Review A* 59.1 (Jan. 1999), pp. 200–204. DOI: 10.1103/PhysRevA.59.200.

[155] D. E. Zmeev et al. "Observation of Crossover from Ballistic to Diffusion Regime for Excimer Molecules in Superfluid ^{4}He". In: *Journal of Low Temperature Physics* 171.3-4 (Sept. 2012), pp. 207–213. ISSN: 1573-7357. DOI: 10.1007/s10909-012-0720-6. arXiv: 1207.1799 [cond-mat.other].

[156] F. W. Carter et al. "Calorimetric Observation of Single He_2^* Excimers in a 100-mK He Bath". In: *Journal of Low Temperature Physics* 186 (Feb. 2017), pp. 183–196. DOI: 10.1007/s10909-016-1666-x. arXiv: 1605.00694 [cond-mat.other].

[157] Humphrey J. Maris. "Phonon-phonon interactions in liquid helium". In: *Reviews of Modern Physics* 49.2 (Apr. 1977), pp. 341–359. DOI: 10.1103/RevModPhys.49.341.

[158] Gianfranco Vidali et al. "Potentials of physical adsorption". In: *Surface Science Reports* 12 (1991), pp. 133–181. DOI: 10.1016/0167-5729(91)90012-M.

[159] L. Reatto et al. "Novel substrates for Helium adsorption: Graphane and Graphene–Fluoride". In: *Journal of Physics: Conference Series* 400.1 (Dec. 2012), p. 012010. DOI: 10.1088/1742-6596/400/1/012010. arXiv: 1204.3061 [cond-mat.mes-hall].

[160] Simon R. Bandler. "Detection of Charged Particles in Superfluid Helium". PhD thesis. Brown University, Dec. 1994. URL: https://www.osti.gov/servlets/purl/10115891.

[161] R. Agnese et al. "Projected sensitivity of the SuperCDMS SNOLAB experiment". In: *Physical Review D* 95.8 (Apr. 2017). DOI: 10.1103/physrevd.95.082002. arXiv: 1610.00006 [physics.ins-det].

[162] Alan E. Robinson. "Coherent photon scattering background in sub-GeV/c^2 direct dark matter searches". In: *Physical Review D* 95.021301 (Jan. 2017). DOI: 10.1103/PhysRevD.95.069907. arXiv: 1610.07656 [astro-ph.IM].

[163] J. H. Hubbell et al. "Atomic Form factors, incoherent scattering functions and photon scattering cross sections". In: *Journal of Physical and Chemical Reference Data* 4.3 (July 1975), pp. 471–538. DOI: 10.1063/1.555523.

[164] H. Falkenberg et al. "Amplitudes for Delbrück Scattering". In: *Atomic Data and Nuclear Data Tables* 50 (1992), pp. 1–27. DOI: 10.1016/0092-640X(92)90023-B.

[165] Mohamed Omer and Ryoichi Hajima. "Including Delbrück scattering in GEANT4". In: *Nuclear Instruments and Methods in Physics Research B* 405 (Aug. 2017), pp. 43–49. DOI: 10.1016/j.nimb.2017.05.028.

[166] G. V. Turturica et al. "Implementation of photon elastic scattering in GEANT4". In: *Nuclear Instruments and Methods in Physics Research B: Beam Interactions with Materials and Atoms* 436 (Dec. 2018), pp. 68–73. DOI: 10.1016/j.nimb.2018.09.007.

[167] J. Billard, E. Figueroa-Feliciano, and L. Strigari. "Implication of neutrino backgrounds on the reach of next generation dark matter direct detection experiments". In: *Physical Review D* 89.2 (Jan. 2014). DOI: 10.1103/physrevd.89.023524. arXiv: 1307.5458 [hep-ph].

[168] Chris Kouvaris and Josef Pradler. "Probing sub-GeV Dark Matter with conventional detectors". In: *Physical Review Letters* 118.031803 (Jan. 2017). DOI: 10.1103/PhysRevLett.118.031803. arXiv: 1607.01789 [hep-ph].

[169] Simon Knapen, Tongyan Lin, and Kathryn M. Zurek. "Light dark matter in superfluid helium: Detection with multi-excitation production". In: *Physical Review D* 95.5 (Mar. 2017). ISSN: 2470-0029. DOI: 10.1103/physrevd.95.056019. arXiv: 1611.06228 [hep-ph].

[170] T. M. Ito and G. M. Seidel. "Scintillation of liquid helium for low-energy nuclear recoils". In: *Physical Review C* 88.2 (Aug. 2013). DOI: 10.1103/physrevc.88.025805.

[171] W. Guo and D. N. McKinsey. "A Concept for A Dark Matter Detector Using Liquid Helium-4". In: *Physical Review D* 87.2 (June 2013). DOI: 10.1103/PhysRevD.87.115001. arXiv: 1302.0534 [astro-ph.IM].

[172] George Seidel. *Some properties of superfluid helium of relevance to dark matter detection*. Sub-eV Workshop. Lawrence Berkeley National Lab, Dec. 2016. URL: https://indico.physics.lbl.gov/event/298/contributions/755/.

[173] George Seidel. *Properties of Helium of Importance for Dark Matter Detection*. Dark Matter Direct Detection Challenges and Opportunities. Peking University, Oct. 2019. URL: https://indico.ihep.ac.cn/event/10369/session/4/contribution/20.

[174] A. Biekert et al. "Scintillation yield from electronic and nuclear recoils in superfluid ^{4}He". In: *Physical Review D* 105.9 (May 2022). DOI: 10.1103/physrevd.105.092005. arXiv: 2108.02176 [physics.ins-det].

[175] T. A. King and R. Voltz. "The time dependence of scintillation intensity in aromatic materials". In: *Proceedings of the Roayl Society A* 289.25 (Jan. 1966), pp. 424–439. DOI: 10.1098/rspa.1966.0021.

[176] Joseph S. Adams. "Energy Deposition by Electrons in Superfluid Helium". PhD thesis. Brown University, May 2001.

[177] M. E. Dodd et al. "Non-Appearance of Vortices in Fast Mechanical Expansions of Liquid ^{4}He Through the Lambda Transition". In: *Physical Review Letters* 81.3703 (Oct. 1998). DOI: 10.1103/PhysRevLett.81.3703. arXiv: 9808117 [cond-mat.soft].

[178] Andrew Forrester, Han-Ching Chu, and Gary A. Williams. "Exact Solution for Vortex Dynamics in Temperature Quenches of Two-Dimensional Superfluids". In: *Physical Review Letters* 110.16 (Apr. 2013). DOI: 10.1103/physrevlett.110.165303. arXiv: 1211.0661 [cond-mat.stat-mech].

[179] Yu. Ralchenko et al. "Electron-impact excitation and ionization cross sections for ground state and excited helium atoms". In: *Atomic Data and Nuclear Data Tables* 94.4 (July 2008), pp. 603–622. DOI: 10.1016/j.adt.2007.11.003.

[180] Samuel K. Allison. "Experimental Results on Charge-Changing Collisions of Hydrogen and Helium Atoms and Ions at Kinetic Energies above 0.2 keV". In: *Reviews of Modern Physics* 30.4 (Oct. 1958), pp. 1137–1168. DOI: 10.1103/RevModPhys.30.1137.

[181] W. Meckbach and I. B. Nemirovsky. "Charge Equilibrium of Helium Ions in Helium Gas from 60 to 840 keV". In: *Physical Review* 153.1 (Jan. 1967), pp. 13–18. DOI: 10.1103/PhysRev.153.13.

[182] L. I. Pivovar, V. M. Tubaev, and M. T. Novikov. "Electron Loss and Capture by 200 - 1500 keV Helium Ions in Various Gases". In: *Soviet Journal of Experimental and Theoretical Physics* 14.1 (Jan. 1962), pp. 20–24. URL: http://jetp.ras.ru/cgi-bin/e/index/e/14/1/p20?a=list.

[183] Akio Itoh and Fumio Fukazawa. "Equilibrium Charge Distributions of Helium Beams in Various Gases". In: *Journal of the Physical Society of Japan* 50.2 (Feb. 1981), pp. 632–637. DOI: 10.1143/JPSJ.50.632.

[184] L. J. Puckett, G. O. Taylor, and D. W. Martin. "Cross Sections for Ion and Electron Production in Gases by 0.15-1.00-MeV Hydrogen and Helium Ions and Atoms". In: *Physical Review* 178 (Feb. 1969), pp. 271–287. DOI: 10.1103/PhysRev.178.271.

[185] J. M. Sanders et al. "Ionization in fast atom-atom collisions: The influence and scaling behavior of electron-electron and electron-nucleus interactions". In: *Physical Review A* 76.6 (Dec. 2007). DOI: 10.1103/physreva.76.062710.

[186] C. F. Barnett and P. M. Stier. "Charge Exchange Cross Sections for Helium Ions in Gases". In: *Physical Review* 109.1 (Jan. 1958), pp. 385–390. DOI: 10.1103/PhysRev.109.385.

[187] Nobuaki Noda. "Electron Stripping of He and H in Helium, Hydrogen and Nitrogen Gases from 0.2 keV to 5.0 keV". In: *Journal of the Physical Society of Japan* 41.2 (Aug. 1976), pp. 625–632. DOI: 10.1143/JPSJ.41.625.

[188] E. S. Soloviev et al. "Ionization of gases by fast helium atoms and singly-charged helium ions". In: *Soviet Journal of Experimental and Theoretical Physics* 18.2 (Feb. 1964), pp. 342–345. URL: http://www.jetp.ras.ru/cgi-bin/e/index/e/18/2/p342?a=list.

[189] Howard C. Hayden and Nyle G. Utterback. "Ionization of Helium, Neon, and Nitrogen by Helium Atoms". In: *Physical Review* 135.6A (Sept. 1964), pp. 1575–1579. DOI: 10.1103/PhysRev.135.A1575.

[190] R. D. DuBois. "Multiple ionization of He^+–rare-gas collisions". In: *Physical Review A* 39.9 (May 1989), pp. 4440–4450. DOI: 10.1103/PhysRevA.39.4440.

[191] M. E. Rudd et al. "Cross sections for ionization of gases by 10-2000-keV He^+ ions and for electron capture and loss by 5-350-keV He^+ ions". In: *Physical Review A* 32.2 (Aug. 1985), pp. 829–835. DOI: 10.1103/PhysRevA.32.829.

[192] M. B. Shah and H. B. Gilbody. "Single and double ionisation of helium by H^+, H^{2+}, and Li^{3+} ions". In: *Journal of Physics B: Atomic and Molecular Physics* 18.5 (Mar. 1985), pp. 899–913. DOI: 10.1088/0022-3700/18/5/010.

[193] A. C. F. Santos et al. "Absolute multiple-ionization cross sections of noble gases by He^+". In: *Physical Review A* 63.6 (May 2001). ISSN: 1094-1622. DOI: 10.1103/physreva.63.062717.

[194] D. W. Martin et al. "Cross Sections for Ion and Electron Production in Gases by Fast Helium Ions (0.133-1.0-MeV). II. Comparison with Theory". In: *Physical Review* 136.2A (Oct. 1964), pp. 385–392. DOI: 10.1103/PhysRev.136.A385.

[195] V. Kempter, F. Veith, and L. Zehnle. "Excitation processes in low-energy collisions between ground state helium atoms". In: *Journal of Physics B: Atomic and Molecular Physics* 8.7 (Jan. 1975), pp. 1041–1052. DOI: 10.1088/0022-3700/8/7/010.

[196] K. E. Banyard, B. J. Szuster, and G. J. Seddon. "Ground-state correlation effects in He-He inelastic scattering". In: *Journal of Physics B: Atomic and Molecular Physics* 8.12 (Feb. 1975), pp. 2109–2113. DOI: 10.1088/0022-3700/8/12/021.

[197] R. Okasaka et al. "Excitation cross sections in He^+-He collisions: I. Excitation function and potential curve crossing". In: *Journal of Physics B: Atomic and Molecular Physics* 20 (Feb. 1987), pp. 3771–3787. DOI: 10.1088/0022-3700/20/15/023.

[198] Victor Pol, Walter Kauppila, and John T. Park. "Absolute Differential Elastic- and Inelastic-Scattering Cross Section in 25-140 keV He^+ + He Collisions". In: *Physical Review A* 8.6 (Dec. 1973), pp. 2290–3000. DOI: 10.1103/PhysRevA.8.2990.

[199] R. Hippler, K.-H. Schartner, and H. F. Beyer. "Direct and charge-exchange excitation of the 2^1P level in He^+-He collisions". In: *Journal of Physics B: Atomic and Molecular Physics* 11 (Apr. 1978), pp. L337–L341. DOI: 10.1088/0022-3700/11/11/001.

[200] H. O. Folkerts et al. "He^{2+}-He collisions: one-electron capture and target-ion exciation". In: *Journal of Physics B: Atomic and Molecular Physics* 27 (June 1994), pp. 3475–3488. DOI: 10.1088/0953-4075/27/15/022.

[201] M. E. Rudd et al. "Electron production in proton collisions with atoms and molecules: energy distributions". In: *Reviews of Modern Physics* 64.2 (Apr. 1992), pp. 441–490. DOI: 10.1103/RevModPhys.64.441.

[202] J. Lindhard et al. "Integral equations governing radiation effects (notes on atomic collisions, III)". In: *Matematisk-fysiske Meddelelser udgivet af Det Kongelige Danske Videnskabernes Selskab* 33.10 (1963).

[203] D.-M. Mei et al. "A model of nuclear recoil scintillation efficiency in noble liquids". In: *Astroparticle Physics* 30.1 (Aug. 2008), pp. 12–17. DOI: 10.1016/j.astropartphys.2008.06.001. arXiv: 0712.2470 [nucl-ex].

[204] T. M. Ito et al. "Effect of an electric field on superfluid helium scintillation produced by α-particle sources". In: *Physical Review A* 85.4 (Apr. 2012). ISSN: 1094-1622. DOI: 10.1103/physreva.85.042718. arXiv: 1110.0570 [nucl-ex].

[205] J. S. Adams et al. "Simultaneous calorimetric detection of rotons and photons generated by particles in suerfluid helium". In: *Physics Letters B* 341 (Jan. 1995), pp. 431–434. DOI: 10.1016/0370-2693(95)80025-S.

[206] M. J. Berger et al. *ESTAR, PSTAR, and ASTAR: Computer Programs for Calculating Stopping-Power and Range Tables for Electrons, Protons, and Helium Ions.* Gaithersburg, MD: National Institute of Standards and Technology, July 2017. URL: http://physics.nist.gov/Star.

[207] J. W. Keto et al. "Dynamic properties of neutral excitations produced in electron-bombarded superfluid helium. II. Afterglow fluorescence of excited helium molecules". In: *Physical Review A* 10 (Sept. 1974), pp. 887–896. DOI: 10.1103/PhysRevA.10.887.

[208] Huey A. Roberts and Frank L. Hereford. "Luminescence of Helium II Produced by Weak α-Particle Sources". In: *Physical Review A* 7 (Jan. 1973), pp. 284–291. DOI: 10.1103/PhysRevA.7.284.

[209] A. Biekert et al. "Nuclear recoil scintillation linearity of a high pressure ^{4}He gas detector". In: *Journal of Instrumentation* 14.P10028 (Oct. 2019). DOI: 10.1088/1748-0221/14/10/P10028. arXiv: 1907.03985 [physics.ins-det].

[210] R. Chandra et al. "Fast neutron detection with pressurized ^{4}He scintillation detectors". In: *Journal of Instrumentation* 7.3 (Mar. 2012), p. C03035. DOI: 10.1088/1748-0221/7/03/c03035.

[211] David Emmanuel Murer. "He-4 Fast Neutron Detectors in Nuclear Security Applications". PhD thesis. ETH Zurich, 2014. DOI: 10.3929/ethz-a-010111172.

[212] G. L. Morgan and R. L. Walter. "Linearity and energy resolution of a high pressure helium gas scintillation counter". In: *Nuclear Instruments and Methods* 58 (Sept. 1968), pp. 277–281. DOI: 10.1016/0029-554X(68)90477-1.

[213] Ryan P. Kelley et al. "Neutron response function characterization of ^{4}He scintillation detectors". In: *Nuclear Instruments and Methods in Physics Research Section A: Accelerators, Spectrometers, Detectors and Associated Equipment* 793 (Apr. 2015), pp. 101–107. DOI: 10.1016/j.nima.2015.04.011.

[214] R. P. Kelley et al. "Analysis of the scintillation mechanism in a pressurized ^{4}He fast neutron detector using pulse shape fitting". In: *AIP Advances* 5.037144 (Mar. 2015). DOI: 10.1063/1.4916904.

[215] R. Jebali et al. "A first comparison of the responses of a ^{4}He-based fast-neutron detector and a NE-213 liquid-scintillator reference detector". In: *Nuclear Instruments and Methods in Physics Research Section A: Accelerators, Spectrometers, Detectors and Associated Equipment* 794 (Sept. 2015), pp. 102–108. DOI: 10.1016/j.nima.2015.04.058.

[216] *Arktis S-670(e) Detector Series Operating Manual*. v4. Arktis Radiation Detectors. Räffelstrasse 11, 8045 Zürich, Switzerland, July 2016.

[217] J. M. Lewis et al. "Fission signal detection using helium-4 gas fast neutron scintillation detectors". In: *Applied Physics Letters* 105.014102 (July 2014). DOI: 10.1063/1.4887366.

[218] Ting Zhu et al. "Improved fission neutron energy discrimination with ^{4}He detectors through pulse filtering". In: *Nuclear Instruments and Methods in Physics Research Section A: Accelerators, Spectrometers, Detectors and Associated Equipment* 848 (Mar. 2017), pp. 137–143. DOI: 10.1016/j.nima.2016.12.016.

[219] Massimo Caccia et al. "Silicon Photomultiplier Readout of a Scintillating Noble Gas Detector for Homeland Security". In: *3rd International Conference on Advancements in Nuclear Instrumentation, Measurement Methods and their Applications (ANIMMA)*. IEEE, June 2013. DOI: 10.1109/ANIMMA.2013.6727974.

[220] Cathleen Barker et al. "Pulse Shape Analysis and Discrimination for Silicon-Photomultipliers in Helium-4 Gas Scintillation Neutron Detector". In: *EPJ Web of Conferences* 170.07002 (Jan. 2018). DOI: 10.1051/epjconf/201817007002.

[221] Horst Liskien and Arno Paulsen. "Neutron Production Cross Sections and energies for the Reactions T$(p,n)^3$He, D$(d,n)^3$He, and T$(d,n)^4$He". In: *Nuclear Data Tables* 11.7 (June 1973), pp. 569–619. DOI: 10.1016/S0092-640X(73)80081-6.

[222] Guillaume Plante. "The XENON100 Dark Matter Experiment: Design, Construction, Calibration and 2010 Search Results with Improved Measurement of the Scintillation Response of Liquid Xenon to Low-Energy Nuclear Recoils". PhD thesis. Columbia University, 2012.

[223] D. N. McKinsey et al. "Fluorescence efficiencies of thin scintillating films in the extreme ultraviolet spectral region". In: *Nuclear Instruments and Methods in Physics Research Section B: Beam Interactions with Materials and Atoms* 132.3 (Nov. 1997), pp. 351–358. DOI: 10.1016/S0168-583X(97)00409-6.

[224] Christopher Benson, Gabriel D. Orebi Gann, and Victor Gehman. "Measurements of the intrinsic quantum efficiency and absorption length of tetraphenyl butadiene thin films in the vacuum ultraviolet regime". In: *The European Physical Journal C* 78.329 (Apr. 2018). DOI: 10.1140/epjc/s10052-018-5807-z. arXiv: 1709.05002 [physics.ins-det].

[225] X. Zhang et al. "Cryogenic phonon–scintillation detectors with PMT readout for rare event search experiments". In: *Astroparticle Physics* 79 (June 2016), pp. 31–40. DOI: 10.1016/j.astropartphys.2016.02.007. arXiv: 2004.00985 [physics.ins-det].

[226] S.I. Hyodo and A. Nagai. "Helium permeation through glass at low temperatures". In: *Journal of the Faculty of Engineering, University of Tokyo, Series A* 18 (1980).

[227] D. N. McKinsey et al. "Time dependence of liquid-helium fluorescence". In: *Physical Review A* 67.062716 (June 2003). ISSN: 1094-1622. DOI: 10.1103/physreva.67.062716.

[228] E. Segreto. "Evidence of delayed light emission of tetraphenyl-butadiene excited by liquid-argon scintillation light". In: *Physical Review C* 91.3 (Mar. 2015). DOI: 10.1103/physrevc.91.035503. arXiv: 1411.4524 [physics.ins-det].

[229] A. Biekert et al. "A backing detector for order-keV neutrons". In: *Nuclear Instruments and Methods in Physics Research Section A: Accelerators, Spectrometers, Detectors and Associated Equipment* 1039.166981 (Sept. 2022). DOI: 10.1016/j.nima.2022.166981. arXiv: 2203.04896 [physics.ins-det].

[230] P. S. Barbeau, J. I. Collar, and P. M. Whaley. "Design and characterization of a neutron calibration facility for the study of sub-keV nuclear recoils". In: *Nuclear Instruments and Methods in Physics Research Section A: Accelerators, Spectrometers, Detectors and Associated Equipment* 574.2 (May 2007), pp. 385–391. DOI: 10.1016/j.nima.2007.01.169. arXiv: 0701011 [nucl-ex].

[231] T. H. Joshi et al. "Design and demonstration of a quasi-monoenergetic neutron source". In: *Nuclear Instruments and Methods in Physics Research B* 333 (Aug. 2014), pp. 6–11. DOI: 10.1016/j.nimb.2014.04.008. arXiv: 1403.1285 [physics.ins-det].

[232] H. Iimura et al. "Nuclear Data Sheets for A = 124". In: *Nuclear Data Sheets* 80.4 (Apr. 1997), pp. 895–1068. DOI: 10.1006/ndsh.1997.0009.

[233] J. Katakura et al. "Nuclear Data Sheets for A = 125". In: *Nuclear Data Sheets* 70.2 (Oct. 1993), pp. 217–314. DOI: 10.1006/ndsh.1993.1049.

[234] J. Aalbers et al. "A Next-Generation Liquid Xenon Observatory for Dark Matter and Neutrino Physics". In: (2022). arXiv: 2203.02309 [physics.ins-det].